Investigation of thin films properties for HgCdTe based infrared detector

Thesis
Submitted to
Delhi Technological University
in partial fulfilment of the requirements for the degree of
DOCTOR OF PHILOSOPHY
in
APPLIED PHYSICS
By

Mr. Vijay Singh Meena

(Reg. No. 2K17/Ph.D/AP/15)

Under the supervision of

Dr. Mohan Singh Mehata
Assistant Professor

Department of Applied Physics
Delhi Technological University, Shahbad Daulatpur, Bawana Road,
Delhi 110 042, India

July-2023

Dedicated to…..
My lovely parents &
family…..

PREFACE

The whole research work comprised in this thesis entitled **"*Investigation of thin films properties for HgCdTe based infrared detector*"** *was carried out during the year 2017-2022. It was carried out in the Laser-Spectroscopy Laboratory, Department of Applied Physics, Delhi Technological University (DTU), Delhi, and Solid State Physics Laboratory (SSPL), Defence Research & Development Organisation (DRDO), Delhi under the supervision of* ***Dr. Mohan Singh Mehata,*** *Assistant Professor, DTU.* ***Dr. Anand Singh,*** *(Scientist 'E'), of IR Device Group, SSPL, Delhi, provided his constant support to accomplish this research. I am very thankful to* ***Dr. Mohan Singh Mehata*** *(my supervisor) and* ***Dr. Anand Singh*** *(SSPL) for their continuous inspiration as well as support.*

This thesis consists of seven chapters where ***Chapters 1 & 2*** *are introduced for covering the introduction part and the experimental and characterization techniques utilized to accomplish the proposed objectives, respectively.* ***Chapters 3, 4, 5,*** *and* ***6*** *have been published in the form of research papers/publications 1-5 in the reputed international SCI/SCIE journals (as shown in the list of publications: page no.-IX) while* ***Chapter 7*** *is the summary of the thesis. All the published research papers/publications (as per the attached publication list on page no.-IX) include the name of me* ***(Vijay Singh Meena)****, my supervisor* ***(Dr. Mohan Singh Mehata),*** *and five other authors namely,* ***Dr. Anand Singh, Ajay Kumar Saini, Sumit Jain, Dr. Devendra Kumar Rana, and Ranveer Singh****. I was the first author in all these* ***papers no.-1, 2, 4, and 5,*** *respectively while my supervisor played an important role as the corresponding author. All the aforesaid persons have played the role of co-authors in some of these publications.*

For ***Chapter 3****, I,* ***Vijay Singh Meena,*** *prepared the concept/design and plan of the whole study (literature survey/review, writing up the literature-discussion and* *experimentation-framework), acquisition/analysis/interpretation of data, and drafting the manuscript.* **Dr. Mohan Singh Mehata** *wrote the final version of the manuscript after making some certain revisions/editions in the original manuscript and the whole of the study was performed under his direction.* **Chapter 4,** *I,* **Vijay Singh Meena,** *contributed as the first author (literature review/concept formation, planning/execution of the required experiments, collection & analysis of the data/results, and preparing the draft of manuscript/research paper) while* **Dr. Mohan Singh Mehata** *(the guiding/corresponding author) had supervised the whole study and finalized the manuscript/article after applying the definite revisions/editions to the original manuscript. For* **Chapter 5,** *I,* **Vijay Singh Meena,** *participated in all the major areas namely literature survey/conceptualization, planning/execution of the methodology/ experiments, data curation and formal analysis, as well as the composition of the original draft.* **Ajay Kumar Saini, Dr. Anand Singh, Sumit Jain, and Dr. Devendra Kumar Rana** *helped me and contributed as co-authors to perform data curation and formal analysis needed for writing the original draft of the manuscript.* **Dr. Mohan Singh Mehata** *(the supervisory/corresponding author) administered the whole investigation/study and validated/finalized the manuscript after reviewing/editing the original manuscript. I,* **Vijay Singh Meena,** *was the main author for* **Chapter 6** *and was accountable for all the major areas like literature survey, concept/design, planning and implementation of the study, collection, and exploration of the realized data/results, and composition of the original draft of the chapter/research paper.* **Ajay Kumar Saini, Dr. Anand Singh, Sumit Jain, and Ranveer Singh** *significantly contributed as co-authors by helping in the data curation, interpretation/presentation of the corresponding data/results, and formal analysis needed for writing the original draft of the manuscript.* **Dr. Mohan Singh**

***Mehata** (the corresponding author) supervised/directed the whole investigation/study, visualized (reviewed/edited), and validated the original manuscript/chapters.*

During the tenure of my research work, I learned that it is very challenging to accomplish a task without interaction with others/professionals since it can generate some significant/fruitful results or concepts because of the different opinions or approaches of the respective persons. The criticism from others (which could be painful to deal with and a time-consuming course) not only improves our mistakes but also enhances our clarity. I educated lots from others through their expertise and in that way, my research work remained delightful. I am highly grateful to everyone who provided me the professional direction and skillful advice for my research work.

All support from the Department of Applied Physics, DTU, Delhi, and Solid State Physics Laboratory (SSPL), DRDO, Delhi is gratefully acknowledged.

*Finally, I am very grateful to my family (**parents**, wife **Manju**, son **Shreyansh,** and daughter **Astha**) for their affection, endurance, and support during this research work.*

Vijay Singh Meena

July 2023

DECLARATION

I hereby declare that the work presented in this thesis entitled ***" Investigation of thin films properties for HgCdTe based infrared detector"*** submitted to the Delhi Technological University (DTU), Delhi for the award of the degree of ***"Doctor of Philosophy"*** is based on the original research work carried out by me under the supervision of Dr. Mohan Singh Mehata, Assistant Professor, Department of Applied Physics, Delhi Technological University, Delhi and has fulfilled the requirements for the submission of this thesis. I further declare that it has not formed the basis for the award of any degree, diploma, fellowship or associateship, or similar title of any University/Institution. The extent of information derived from the existing literature has been indicated in the body of the thesis at appropriate places giving the references.

Vijay Singh Meena
Research Scholar
(Reg. No. 2K17/Ph.D./AP/15)

Date: **07/07/2023**
Place: **Delhi**

Delhi Technological University
Formerly Delhi College of Engineering
(Under Delhi Act 6 of 2009, Govt. of NCT of Delhi)
Shahbad Daulatpur, Bawana Road, Delhi-110042

CERTIFICATE

This is to certify that the thesis entitled ***"Investigation of thin films properties for HgCdTe based infrared detector"*** submitted to the Delhi Technological University (DTU), Delhi for the award of the degree of "***Doctor of Philosophy***" in Applied Physics is a record of bonafide original research work carried out by ***Mr. Vijay Singh Meena*** under my supervision at Laser-Spectroscopy Laboratory, Department of Applied Physics, Delhi Technological University, Delhi and has fulfilled the requirements for the submission of this thesis. It is further certified that the work embodied in this thesis has neither been partially nor fully submitted to any other university or institution for the award of any degree or diploma.

Dr. Mohan Singh Mehata
Supervisor
Assistant Professor
Department of Applied Physics
Delhi Technological University,
Delhi- 110 042

Submitted Through:

Prof. A. S. Rao
Head
Department of Applied Physics
Delhi Technological University,
Delhi-110 042

ACKNOWLEDGEMENTS

The journey of my research is accomplished with the valuable support of many people. It is a pleasant aspect that I have now the opportunity to express my gratitude to all of them.

At the outset, I would like to express my profound sense of gratitude, indebtedness, and reverence to my supervisor, ***Dr. Mohan Singh Mehata****, Department of Applied Physics, Delhi Technological University, Delhi, who nurtured my research capabilities for a successful scientific research career. It has been an honor to work under an excellent, enthusiastic, and distinguished supervisor. His unremitting encouragement, constant help, meticulous supervision, and constructive criticism throughout my study for carving another milestone in my academic journey. I feel privileged to have worked under such great supervision.*

I further stand ovated to ***Prof. A. S. Rao****, Head, Department of Applied Physics, DTU, for his valuable help and suggestions. My heartfelt recognition to* ***Prof. S. C. Sharma****, DRC Chairman, former Head, Department of Applied Physics, DTU,* ***Prof. Rinku Sharma****, former Head, Department of Applied Physics, DTU, my SRC & DRC committee members* **(*Prof. H. K. Malik,*** *IIT Delhi,* ***Prof. Shyama Rath,*** *University of Delhi***)** *for their enduring support and appropriate propositions. I express my sincere gratitude especially to* ***Dr. Yashashchandra Dwivedi,*** *Department of Applied Physics, NIT, Kurukshetra,* ***Dr. Anand Singh,*** *(Scientist 'E'), IR Device Group, Solid State Physics Laboratory, Delhi, and* ***Prof. M. M. Tripathi,*** *Department of Electrical Engineering, DTU & DG NIELIT, Delhi for their timely advice and support as SRC members. I also express my great thanks to* ***Dr. Amrish K. Panwar,*** *DTU for his fruitful motivation.*

It is my pleasure to express my sincere thanks to all the faculty members of the Department of Applied Physics, DTU for their continuous encouragement and help *during my research work. I am also grateful to technical and non-technical staff for their timely support and cooperation whenever required.*

I especially express my sincere gratitude to my seniors (from Solid State Physics Laboratory: SSPL, DRDO, Delhi) namely **Dr. Anand Singh** *(Scientist 'E')***, Mr. Ajay Kumar Saini** *(Scientist 'E'),* **Mr. Sumit Jain** *(Scientist 'D') and group-mate* **Mr. Ranveer Singh** *(STA'B'), IR Device Group; for their kind support in developing the various thin films. Sincere thanks to* **Dr. Akhilesh Kumar Pandey** *(Scientist 'F'),* **Garima** *(TO 'B'),* **Sandeep Dalal** *(TO 'A') and* **Monika** *(TO 'A'), Characterization Group, SSPL;* **Shashitosh** *(Scientist 'D'), IEEE Group, SSPL; for their help in the evaluation/characterization of developed thin films. I also thank* **Dr. Chanchal** *(Scientist 'D') LPE Group, SSPL for making the availability of HgCdTe epilayers to perform the whole research.*

I sincerely thank my dear former and present lab mates whose support helped in accomplishing my work. It is my great pleasure to express special thanks to my senior **Dr. Ratneshwar Kr. Ratnesh***,* **Dr. Mrityunjay Kumar Singh,** *and lab-mates:* **Dr. Prateek Sharma** *and* **Dr. Vineet Sharma.** *I thank my present lab mates* **Ms. Aneesha, Mr. Aryan, Mr. Vinay Kumar, Mr. Dhananjay, Ms. Aarti, and Ms. Sapna** *for their support and timely help. I would like to thank my friends* **Dr. Devendra Kumar Rana (ARSD College, DU), Mohit Tyagi, Dr. Shankar Subramanian, Mr. Abhishek Bhardwaj, Sandeep Sarpal, Mr. Deepak Kumar, Ms. Namrata Sharma, and Mr. Uday Veer Singh,** *for their timely help, encouragement, and unwavering support during my difficult time. Their friendship has provided a wonderful time along the way. I would also like to thank all the other research scholars of the Department of Applied Physics, Delhi Technological University, Delhi for their help and advice.*

Finally, I thank my family for their support and motivation, at every moment of my research period. With heartfelt gratitude and love, I express my gratefulness to my father ***Late Mr. Kirodi Lal Meena****, mother* ***Mrs. Gyarasi Devi Meena,*** *wife* ***Mrs. Manju Meena,*** *son* ***Shreyansh Jarwal,*** *daughter* ***Astha Jarwal*** *for their continual love and encouragement over the entire course of my life. I am thankful to my in-laws* ***(Mr. Hira Lal Meena & Mrs. Keshanti Devi Meena)****, my brothers* ***Mr. Jay Singh Meena, Mr. Ajay Singh Meena, Mr. Balram Meena and Mr. Roop Singh Meena;*** *co-brother* ***Dr. R. P. Meena*** *and brother-in-law* **Mr. Mukesh Chand Meena** *for their constant encouragement, care, love, blessings and have helped me to achieve what I am today. I am thankful to my extended maternal and paternal family for helping me maintain a positive attitude throughout my studies. I am always thankful to all my beloved friends across the globe for sharing my happiness and sorrow.*

I gratefully acknowledge the volumetric support & facilities provided by the ***Delhi Technological University (DTU)*** *and* **Solid State Physics Laboratory (SSPL)** *to accomplish the whole research work. Various groups of* **SSPL, DRDO, Delhi (IR Device Group:** *HgCdTe epilayers availability, sample preparation, ellipsometry, microscopy, photolithography, and deposition system;* **Characterization& IEEE Groups:** *XRD, SEM, EDX, AFM, FTIR, surface profiler, and CV/IV characterization systems) have given their great/unconditional assistance and amenities to realize this research work. I extend my gratitude to DTU staff in Administration, Accounts, Store & Purchase, Library, and Computer Centre for their help and services.*

I thank one and all for helping me accomplish the successful realization of the thesis.

Thank you all!!!

Vijay Singh Meena

LIST OF PUBLICATIONS

Publications in the PhD thesis

1. **Vijay Singh Meena** and Mohan Singh Mehata, Investigation of grown ZnS film on HgCdTe substrate for passivation of infrared photodetector, **Thin Solid Films 731 (2021) 138751. (IF=2.358).**
2. **Vijay Singh Meena** and Mohan Singh Mehata, Thermally grown Indium (In) thin-film for creating Ohmic contact and In-bumps for HgCdTe-based IR Detectors, **Applied Surface Science 596 (2022) 153501. (IF=7.392).**
3. **Vijay Singh Meena**, Ajay Kumar Saini, Devendra Kumar Rana, Mohan Singh Mehata, Synthesis and characterization of thermally-evaporated CdS thin-films, **Materials Today: Proceedings, 67(5), (2022) 643-647(not included in Thesis)**.
4. **Vijay Singh Meena**, Ajay Kumar Saini, Anand Singh, Sumit Jain, Ranveer Singh and Mohan Singh Mehata, Structural, compositional, morphological and electrical characteristics of thermally evaporated Au Ohmic contact on p-type HgCdTe substrate for possible infrared detectors **Optical Materials 141 (2023) 113943**.
5. **Vijay Singh Meena**, Ajay Kumar Saini, Anand Singh, Sumit Jain, Devendra Kumar Rana and Mohan Singh Mehata, Design and Development of Four-layer Anti-Reflection Coating Stacks (ZnS and YF3 Thin Films) for HgCdTe-based Mid-wave Infrared (MWIR) Detectors **Materials Science in Semiconductor Processing 163 (2023) 107556**.

Publications in conference/workshop proceeding

1. **Vijay Singh Meena** and Mohan Singh Mehata, Optimization of Thermally-evaporated ZnS films for Passivation of HgCdTe Infrared Detectors.1st International Conference on Design and Materials (ICDM 2022) during 30-27 January 2022, Delhi Technological University, Delhi, India.
2. **Vijay Singh Meena**, Ajay Kumar Saini, Devendra Kumar Rana and Mohan Singh Mehata, Synthesis and Characterization of Thermally-evaporated CdS Thin-films International Conference on Recent Advances in Functional Materials (RAFM-2022) from 14 -16th March 2022, Department of Physics, IQAC and Star College Scheme (GoI), ARSD College University of Delhi, Delhi.

CONTENTS

Chapter 2: Experimental and characterization techniques……………………….31-60

Chapter 3: Investigation of thermally evaporated ZnS film on HgCdTe substrate for passivation of infrared photodetector……………..…………………………...61-79

Chapter 4: Study of thermally evaporated indium (In) thin-film for creating ohmic contact and In-bumps for HgCdTe-based IR detectors……………………….....80-118

Chapter 7: Summary and future scope...…………………………………….190-195

LIST OF FIGURES

LIST OF TABLES

Chapter 1

Introduction

The current chapter comprises a brief description of the fundamental concepts of IR radiation/materials & detectors, past/present development of HgCdTe IR detector fabrication technology, and applications/roles of several thin films (such as ZnS, Indium, Au, and ZnS/YF_3-based ARC film stack) in HgCdTe-based IR detector fabrication. It also covers other topics like a short literature review/discussion of the previous experimental results, motivation, and research findings.

1.1. Infrared (IR) radiation: Infrared (IR) radiation was discovered by the astronomer Sir William Herschel in 1800 through an experiment**.** Accordingly, the temperature of each colour was measured in sunlight through the use of a prism and a simple thermometer. He observed the highest intensity of temperature beyond the red which is now termed IR. Maxwell's theory (given in 1864) of electromagnetic radiation categorized the IR as a band existing between the visible and microwave wavelength regions of the electromagnetic spectrum having a wavelength range of 0.75 to 1000 µm [1-4].

All the objects above absolute zero temperature emit IR radiation which can be detected by an electronic detector/infrared detector (it is a tool that can detect thermal/IR radiation emitted in a given environment via the sensing of thermal energy as a function of temperature and emissivity) and detected IR energy is converted into an image that is the temperature/IR energy difference between the objects [5]. IR detection/sensing (that uses the unique features of IR radiation like the visibility of the objects in darkness/opaque conditions/smoke/fog/dust, seeing the hot objects in cooler backgrounds that discharge no visible light, detection of weaknesses in structures, longer wavelength so less likely to scatter than visible light, best transmission through various medium, invisible to human eyes hence useful for security application and small energy i.e. equal to rotational/vibrational energy accordingly beneficial for easy identification of the molecules) is an important phenomenon which conveys the information about the temperature, surface characteristics and atmospheric constituents coming into IR transmission path. Any application measuring the IR radiation is related to the evaluation of the object's properties that emits or reflects the IR radiation and this is the spatial/time-varying mapping of IR radiation intensity [5-7].

IR radiation (0.75-1000 µm) can be divided into different categories namely short-wavelength infrared (SWIR) region: 0.75-3.0 µm, mid-wavelength infrared (MWIR) region: 3.0-5.0 µm, long-wavelength infrared (LWIR) region: 8.0- 14.0 µm, very long wavelength infrared (VLWIR) region: 14-30 µm and far infrared (FIR) region: >30 µm [8-11].

1.2. IR materials/detectors and applications: There are many regions of the IR spectrum (as mentioned earlier) but SWIR, MWIR, and LWIR are the most useful regions because the atmosphere offers high transmissions at these wavelengths with no significant losses. Thus, IR detection in these regions has many applications such as the ability to look into fog/haze, identification of materials, free-space communications, night vision/missile tracking, thermal imaging, medical applications (cancer/tumour identification), IR spectroscopy (analysis of the chemical bonds of molecules/organic compounds), astronomy (for analyzing the stars and exoplanets), airborne mapping of minerals, satellite weather imaging, crop monitoring (since diseased plants have different IR emissivity) and automotive/electronic industry. Thus, IR detectors are highly useful in numerous fields, namely defence, medical, astronomy, industry sectors, environmental safety, and remote sensing [7,8-11,12-14].

IR radiation (wavelength: 0.75 -1000 μm) can be converted into a measurable electronic signal by IR detectors and the first IR detectors were invented by Case in 1917. An extensive range of well-known/popular IR detector materials [7-9,11-18] is displayed in Fig. 1.1 as given below:

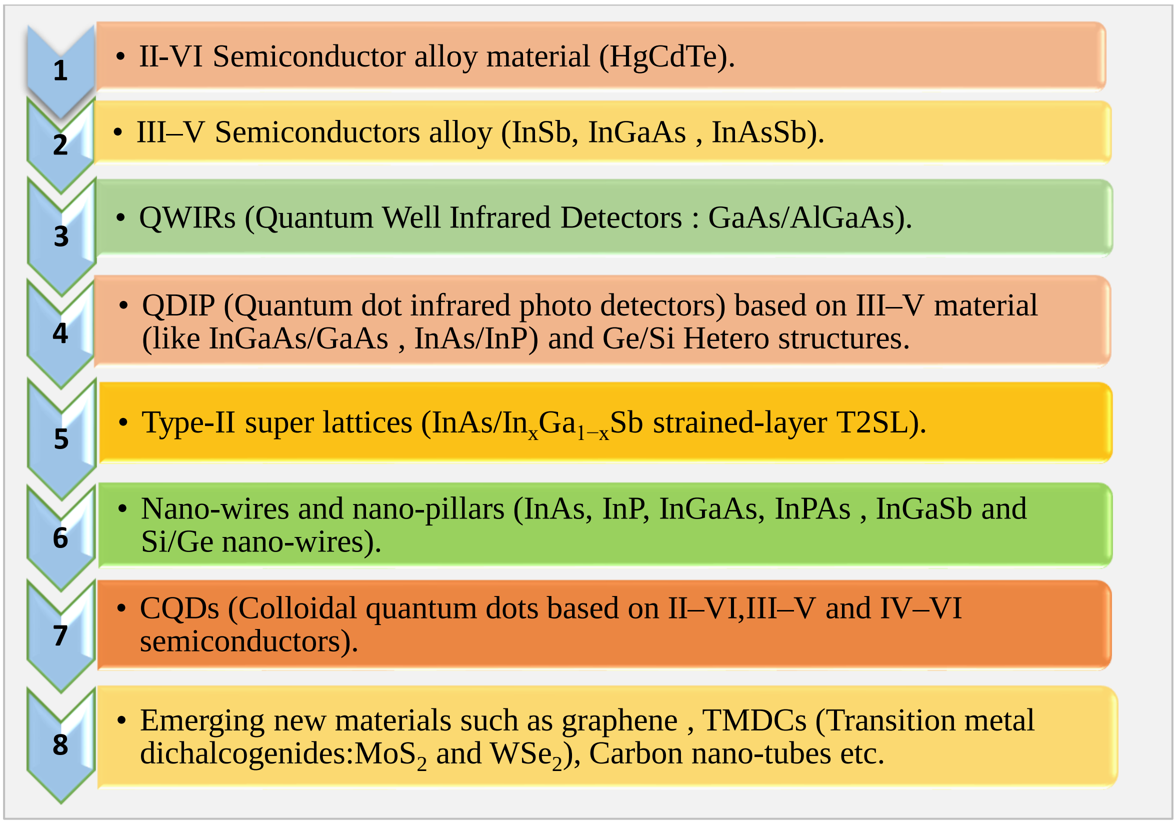

1. II-VI Semiconductor alloy material (HgCdTe).
2. III–V Semiconductors alloy (InSb, InGaAs , InAsSb).
3. QWIRs (Quantum Well Infrared Detectors : GaAs/AlGaAs).
4. QDIP (Quantum dot infrared photo detectors) based on III–V material (like InGaAs/GaAs , InAs/InP) and Ge/Si Hetero structures.
5. Type-II super lattices (InAs/$\mathrm{In_xGa_{1-x}Sb}$ strained-layer T2SL).
6. Nano-wires and nano-pillars (InAs, InP, InGaAs, InPAs , InGaSb and Si/Ge nano-wires).
7. CQDs (Colloidal quantum dots based on II–VI,III–V and IV–VI semiconductors).
8. Emerging new materials such as graphene , TMDCs (Transition metal dichalcogenides:MoS_2 and WSe_2), Carbon nano-tubes etc.

Figure 1.1. Various materials (the most popular, with frequent use and mature/developed) are used for the development of IR detectors.

The history of IR detectors/systems development states that all four generations of IR detectors **(**1st generation: scanning systems, 2nd generation: staring systems with electronic scanning, 3rd generation: staring system with a large number of pixels and two-color operation, and 4th generation: staring systems having a very large number of pixels, multi-colour operation, 3D ROIC, and other on-chip functions) with various architectures/structures were developed gradually using a variety of materials [2,5,6,9,13,15,19,20].

1.3. HgCdTe as IR detector: Although, several efficient IR detector materials (as mentioned in Fig. 1.1) have been explored by the researchers which are potentially manufacturable/more economical where no one can outperform HgCdTe (mercury cadmium telluride: MCT) in terms of material's fundamental physical properties (electronic and optical), IR detectors/focal plane arrays (FPA) performance and multi-colour operability/hyperspectral functionality [7,10].

1.3.1. HgCdTe material's unique properties: HgCdTe (MCT) is the most promising IR detector/FPA material [8,11,21] that was developed in 1959 and HgCdTe-based first detector was formed in 1962. HgCdTe is a pseudo-binary semiconductor alloy with a zinc blende crystalline structure which is a mixture of HgTe (semimetal) and CdTe (semiconductor) compounds. It has unique fundamental properties, namely (a) composition-dependant band gap (varies between HgTe: -0.3 eV and CdTe: 1.6 eV)/adjustable band gap ranging from 0.7 to 30 µm; (b) direct band gap having high absorption coefficient; (c) availability of various lattice-matched substrates for HgCdTe epilayer growth, and (d) moderate thermal coefficient of expansion and dielectric constant. Some other specific properties of HgCdTe material are high-quality layered material with matured growth technology, high detection sensitivity/quantum efficiency (>70%), the fast response time (i.e., order of nanosecond), low biasing voltage, favourable inherent recombination mechanisms (accountable for long carrier lifetime and high working temperature), high thermal resolution/other on-chip functions, the capability of achieving both the low and high carrier concentrations and high mobility of electrons, etc., which make it very popular among all the available IR detector materials [1,3,6,7,8-10,12,13,20,22-28].

A brief description of some key features of HgCdTe material is as follows:

(a) Crystal structure (lattice constant): $Hg_{1-x}Cd_xTe$ is a pseudobinary alloy semiconductor with a zinc blende crystal structure consisting of two interpenetrating *fcc* lattices offset by (1/4, 1/4, 1/4)a_o in its unit cell/primitive cell. Te anions form purple colored sublattice and Hg/Cd cations form yellow colored sublattice. Since the band gap (which corresponds to cut-off wavelengths in the SWIR to VLWIR spectral regions) of HgCdTe material is related to a small change in the value of composition x of element Cd. Moreover, the lattice constant of HgCdTe shows nominal changes (≤0.3%) for the entire composition range x (since it varies between the lattice constants of HgTe: 6.46Å and CdTe: 6.46Å) which is very advantageous for attaining an approximately perfect lattice-matching of HgCdTe with cadmium zinc telluride (CdZnTe) substrate and dislocation-free HgCdTe epilayer grown on the CdZnTe substrate. Accordingly, complex heterostructures and high-quality layered/graded gap structures are created; which are very useful for developing IR detectors with numerous operating modes (such as photovoltaic, photoconduction, and metal-insulator-semiconductor: MIS) and advanced/high performance.

(b) Band structure (energy band gap) and absorption coefficient: $Hg_{1-x}Cd_xTe$ is a direct band gap pseudobinary alloy semiconductor (made from two compounds i.e. CdTe: semiconductor with a band gap of 1.6 eV and HgTe: semimetal having a band gap of -0.3 eV) with zinc blende crystal structure. The energy band gap of $Hg_{1-x}Cd_xTe$ (as a function of composition x as well as temperature T) can be expressed by (a well-known expression given by Hansen et al) equation 1

$$E_g = -0.302+1.93x-0.81x^2+0.832x^3+5.35\times10^{-4}(1-2x)\,T \quad (1)$$

Where: E_g (in eV), x: composition of MCT, and T: temperature (in Kelvin).

$Hg_{1-x}Cd_xTe$ material with adjustable or tuneable band gap (-0.3 eV to 1.6 eV) can be grown by varying the Cd element composition x as a function of temperature T; which makes it an extremely useful material for various applications lying in the different IR ranges from SWIR to VLWIR (spectral response/cut-off wavelength $\lambda_c = 1.238/E_g$ is a function of the band gap).

The direct band gap nature of HgCdTe results in a strong optical absorption (high absorption coefficient) for the given photon energies and it allows a high percentage absorption of the incoming photons/IR signals by the HgCdTe-detector with reasonably thin (10-20 µm) active layer. Although, the thin active layer is not so necessary but the minimum thickness of the detector is very helpful in reducing the noise and thermal excess carriers [3,7,11].

(c) Wide band gap substrates for epilayer growth: The other important property of HgCdTe material is the availability of lattice-matched substrates required for epitaxial growth and it has been frequently utilized for HgCdTe-based IR detector array production. The lattice-constant mismatch between substrate and epilayer can affect the crystal perfection/surface morphology of the grown epitaxial layer. A wide range of substrates is available for the growth of HgCdTe epilayers such as Si, Ge, GaAs, GaSb, and CdZnTe. Although the other four substrates (Si, Ge, GaAs, and GaSb) have the properties like low cost, easy availability, large available area, and minimum defect density that are not present in CdZnTe but the lattice-mismatch of all these substrates (Si: 19.47%, Ge: 14.3%, GaAs: 14.4% and GaSb: 6.1%) with the HgCdTe is large compared to CdZnTe substrate (where substrate-epilayer lattice mismatch $\leq 1\%$). So, CdZnTe is still the substrate of choice to grow the HgCdTe epilayer and it is necessary for current state-of-the-art IR technologies. This was discovered by adding about 4% ZnTe to CdTe for tuning/matching the substrate's lattice constant with the HgCdTe epilayer and the lattice constant can be varied in a narrow range (from CdTe to HgTe) for this II-VI alloy system [11,29].

(d) Dielectric constant: HgCdTe is a suitable material with a moderate dielectric constant which is very necessary to generate the low capacitance photovoltaic IR detectors of features like fast response time, minimum ROIC noise, and lowest smearing in scanned-image.

(e) Thermal coefficient of expansion (TCE): IRFPA is the hybrid structure consisting of a detector array and Si-based read-out integrated circuit (ROIC) which are interconnected via indium-bump (circular columns of indium). Successful interconnection of the detector array with ROIC depends on the TCE (thermal coefficient of expansion) difference between them (i.e. ROIC and detector array) since large TCE mismatch/difference can lead to failure of the indium bumps during repetitive thermal cycling (from room temperature to the cryogenic temperature) of IR detector operation. HgCdTe has a moderate thermal coefficient of expansion (TCE) because of TCE mismatch (3.53%) between the HgCdTe-based detectors (since CdZnTe substrate has nearly perfect lattice-matching with HgCdTe) and Si-based ROIC is minimum [7,29,30].

(f) Thermal generation and recombination processes: Carrier generation leads in the reverse biasing mode, especially for photo detectors that can alter the photon-generated signal-to-noise ratio. It significantly contributes to the dark current which affects the detector's performance. There are three important generations and recombination (G-R) bulk processes namely Shockley-Read-Hall, radiative, and Auger generation which are very significant for the HgCdTe (narrow band gap semiconductors) material. The favourable inherent recombination mechanism which is the function of the intrinsic material properties (such as diffusion current because of Auger or radiative recombination processes in the n-region/p-region and band-to-band tunnelling current) that also leads to IR detector operability at high temperatures.

(g) Mobility and carrier concentration: HgCdTe can obtain both low and high carrier concentrations. HgCdTe has high mobility of electrons and low mobility of holes (small effective masses of the electron responsible for its high mobility while heavy holes have relatively very low mobilities). Mobility and concentration also affect the dark current/photocurrent which is part of detector performance. The involvement of holes in electrical conduction is comparatively low (because of their low mobility) than the electrons and a few studies associated with hole transport properties have been reported [3,7,30].

1.3.2. HgCdTe material growth:

(a) Growth technology: Although single-crystal HgCdTe growth is very challenging (because the comparatively high vapour pressure of the Hg element creates problems in controlling the stoichiometry/composition of the HgCdTe material during its growth and any successive thermal treatment) yet the HgCdTe growth technology has been reached in very advanced phase since its discovery in 1959 to till today [1,3,28-32] where the various growth methods (starting from bulk crystal growth to epitaxial growth) have been established gradually for producing the crystalline HgCdTe material.

The epitaxial growth method is superior to the bulk growth since it can generate high-quality HgCdTe layers (with a high crystalline quality, good homogeneity, complex composition controlled doping profile/layer thickness, and minimum native defect/ inter diffusion because of low growth temperature) which are necessary for fabricating the high-performance IR detectors of large-area and complex device architecture. Generally, two types of epitaxial growth techniques namely liquid phase epitaxy (LPE) as well as vapour phase epitaxy (metal-organic chemical vapour deposition: MOCVD and molecular beam epitaxy: MBE) are available in the literature [1,11,20,28,30]. All these techniques have been used to grow single-crystal HgCdTe material/epilayer but the LPE is a mature, traditional, and popular growth method that can be used to realize the HgCdTe epilayers of higher crystalline quality as well as growth efficiency; over the lattice-matched CdZnTe (cadmium zinc telluride: CZT) substrates with orientation (111) that has 4 % Zn element and 96 % CdTe compound in its composition [1,6,7,33]. The LPE-grown high-quality HgCdTe-epilayers having the crystalline parameters such as X-ray diffraction full-width half-maximum (XRD FWHM): 25-40 arc sec, an etch pit density (EPD): 1×10^{4} –1×10^{5} cm^{-2}, and residual doping: 1×10^{15} cm^{-3}; were utilized to develop the high-performance IR detectors of current as well as futuristic technological requirements [1,3,6,7,29,33].

(b) Progress and limitations of HgCdTe material/detector: HgCdTe material with tailored/ adjustable band gap (multispectral material like SWIR, MWIR, and LWIR can be grown via a precise tuning of cadmium (Cd) concentration at the time of epilayer growth) has been reached in a developed phase and it is very useful for fabricating the multispectral/multicolour IR detector which can operate in the temperature range of liquid nitrogen to room temperature. Some other qualities of the HgCdTe IR detector, which have been upgraded by researchers in the last two decades of the XX century are; higher frame rate, better thermal resolution, higher resolution/a larger number of pixels, and on-chip functions [8-11,13,21,34,35]. The modern defence surveillance system, space imaging system, and laser-based detection system require such IR sensors, which must have unique features like high visibility (3D imaging of a scene in all types of environments, say haze, fog, dust, smoke and night, etc.), high sensitivity/accuracy in scene detection, rapid response, identification of attenuated/weak optical flux/distant target and thermal stability within all the appropriate IR windows. Thus, HgCdTe-based

IR sensors (work based on thermal imaging application) are the most suitable sensors that can simultaneously offer all the features required by the aforesaid detection systems [3,8,11,36-38].

Although HgCdTe-based IR sensors have all the unique properties needed by the above-mentioned technological applications (defence surveillance system, space imaging system, and laser-based detection system) but some limitations [1,3,11,36,38] namely high cost, limited array size, low operational temperature, high fragility of the material, compositional non-uniformity, the thermal coefficient of expansion (TCE) difference between CdZnTe substrates as well as silicon-based readout integrated circuit (ROIC), difficulty to grow on silicon, a health-hazardous technology, etc., have reduced the speed of HgCdTe-IR technology development. Several other challenges like low cost, p-type doping control, and advanced plasma dry etching control have also been faced in the HgCdTe (MCT) IR technology [1,3,8,11,39] and thus it has drawn the attention of researchers towards the HgCdTe IR technology advancement.

1.4. HgCdTe-based IR detector/FPA technology:

1.4.1. Structure and working: IRFPAs (with the higher format and 2D structure) have become extremely useful for high-quality imaging applications since these are the photodetectors (p-n junction diodes) working under reverse bias conditions which offer high impedance and low power dissipation. Besides these advantages, the photodetectors also have some other useful features such as negligible 1/f noise, easy multiplexing with Si-based ROIC, and linear photo response over a high range of photon- flux; which are necessary for high-performance IR photo detectors [1,3,39].

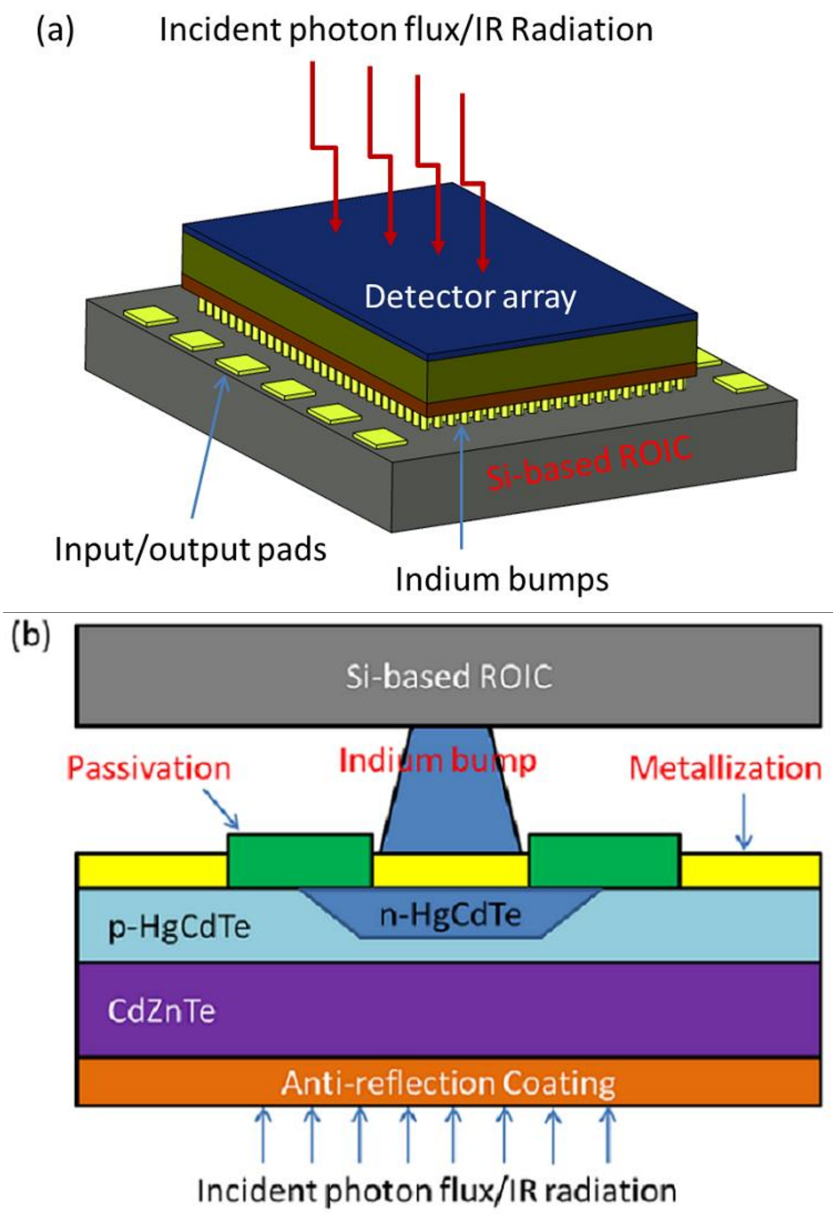

Figure 1.2. Schematic of HgCdTe-based IRFPA: (a) Hybrid structure of IRFPA consists of detector and ROIC (b) cross-sectional view of the single element detector array.

Fig. 1.2 demonstrates the schematic of HgCdTe-based IRFPA which is a 2D hybrid structure of the detector array and readout integrated circuit (ROIC) array in which both are interconnected via indium (In) bump array by flip-chip bonding technique. This indium (In) bump array serves as an electrical, mechanical, and thermal interface between them. In the working of hybrid IRFPA, the incident photon flux with minimum reflectance (through the use of anti-reflection coating (ARC) film at air/CdZnTe-HgCdTe interface) enters the backside of the detector via CdZnTe (CZT) face. Subsequently, electron-hole pairs (electrical signals) along the detector (p-n junction) are created, which are further transferred to the multiplexer (ROIC) via indium bump and the resultant video signal is achieved across the ROIC output driver. The output signal contains all the relevant information inside the IRFPA's field of view (FOV: a solid angle via a detector realizes the scene) and the detectors with back-illuminated configuration have the benefit of choosing the most suitable detectors/ ROICs that are needed in the hybridization-process [3,10,11,39].

1.4.2. HgCdTe-based IR detector (IRFPA) processing:

The processing of HgCdTe-based backside-illuminated devices is challenging because of their low damage threshold which can considerably affect the uniformity, device yield, and performance of the detector. IR photodetector array fabrication process is started from the growth of a p-type $Hg_{1-x}Cd_xTe$ (x=0.29-0.31) epilayer over a lattice-matched CdZnTe (CZT) substrate. It consists of several unit processing steps [8,11,16,33,39] like HgCdTe-surface preparation (for achieving the desired dimensions/thickness:10 µm), passivation (to minimize dark current), metallization (p-contact), p-n junction formation (via Boron ion implantation), etching of passivation, growth of In-bump (on detector array/ROIC for their integration and formation of n-contact using In), ARC film-stack (single/multilayer film over the polished CdZnTe substrate to minimize the reflection losses of incident photon flux/ increase the quantum efficiency of IR detector array), etc.; which are shown in Fig. 1.3. Hence, the HgCdTe-based IR photo detector array is fundamentally a multi-layer structure [1,8,11,39] that consists of contact metal, photon-absorbing material, and a substrate.

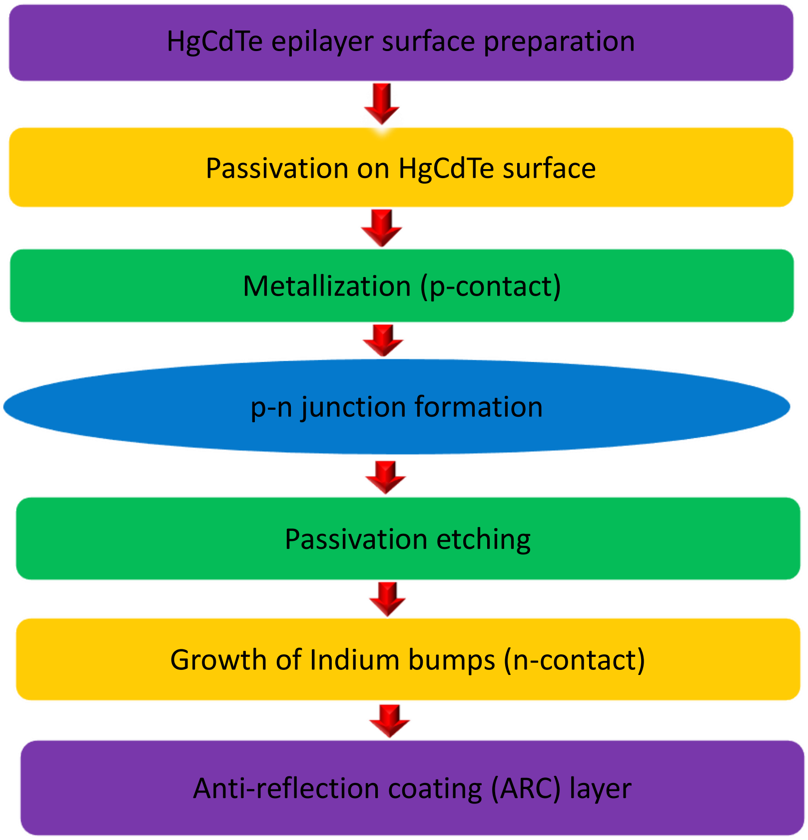

Figure 1.3. Process-flow chart of HgCdTe-based IR photodetector array fabrication.

Since the junction formation has an important role in the fabrication of the HgCdTe-IR detector and so it can be described in detail. Various techniques like thermal oxidation, diffusion, reactive ion etching (RIE), ion beam milling (IBM), and ion-implantation can be used to create a p-n junction on the HgCdTe epilayer but the ion-implantation technique is the most effective/suitable technique that creates a homo-junction (n/p) of desired junction depth since this technique has precise control over junction formation. Sensitive HgCdTe (MCT) material suffers negligible/severe heating during the junction formation process because it occurs at very low temperature (room temperature) and angle of incidence. Typically impurity boron ions of desired energy/dose are directly implanted into HgCdTe crystal for creating Hg vacancies/defects, which behave like a donor atom and finally, the n^+/p region in p-type

HgCdTe epilayer is created. Boron is the most suitable ion that is used to generate the n+/p region in the photodetectors since it has light mass/slow diffusion (responsible for creating lesser native defects in the HgCdTe lattice and type conversion i.e. p-region converts into an n+ region) and a p-n junction with the junction depth of 1-1.5 µm can be achieved at the desired energy (30-140 KeV)/dose (10^{14} atoms/cm^2) of the boron ion [11,20,31,33,40].

1.5. Literature review/role of ZnS, In, Au, and ZnS/YF_3 (ARC) in HgCdTe IR detector: The high-performance HgCdTe IR detectors (low dark current, high photocurrent, high interconnection yields of detector-ROIC, high IR signal transmission/quantum efficiency, low crosstalk and noise) can be fabricated using the optimum passivation, metallization/p-contact, Indium bump (detector-ROIC interconnection metal)/n-contact metal and ARC films; which can minimize all the aforesaid factors responsible for the degraded/lower performance of IR detectors. HgCdTe-based IR detector array fabrication has many unit processing steps/photolithography (PLG) steps (passivation, p-contact metallization, Indium bump/n-contact metal and ARC films as mentioned in **section 1.4**) which are completed through the use of various thin films like ZnS, In, Au and ZnS/YF_3-based ARC and each of them have its equal significance in the HgCdTe-based IR photodetector array fabrication technology. Thus, different thin films of varying thicknesses (ranging from a few nm to several µm) have been used to produce high-performance IR detectors and thin film formation has played an important role in IR detector fabrication technology. Thin films are 2-dimensional layers of solid or liquid materials grown on a substrate (in which one dimension is of nm size that is created by condensation of atomic/molecular/ionic species one by one and its thickness typically ranges from a few nm to several µm); which have significantly different properties from that of bulk material. The specific properties of thin films are due to their increased surface-to-volume ratio compared to the bulk material. Some of the unique properties of thin films are such as high surface-to-volume ratio, specified crystalline orientation, different defect structures from bulk, surface and interface effects, enhanced optical transmission/mechanical strength, thickness-dependent resistivity, etc.

The unit processing steps of IR detector fabrication are mentioned as follows:

1.5.1. ZnS as passivation: The HgCdTe-based IR detectors of high performance can be developed through the utilization of a suitable passivation film that has an appropriate thickness. Since HgCdTe-epilayer with a large number of fixed charges, oxide charges, interface states, and defects; can produce IR detectors of degraded performance (in terms of high surface leakage current/dark stability as well as poor electrical insulation of substrate-metal interconnects) and current, increased generation-recombination centres, reduced thermal stability/chemical the passivation of the p-type HgCdTe surface is moderately problematic. Even if, several passivation materials such as native films (sulphides, oxides, and fluorides), deposited dielectric films (CdTe, CdS, SiO_2, Si_3N_4, CdTe/ZnS, ZnS, and polymers), and in-situ grown extensive band gap materials (CdTe and CdZnTe); have been used to develop the HgCdTe IR detector [8,11,12,20,22,31] but ZnS is a conventionally used passivation agent for fabricating the HgCdTe-based IR detectors that have also been applied as an ARC material in HgCdTe-IR detector fabrication. It is an excellent passivation material that has nearly ideal properties namely insulating dielectric material/electrically inert, low values of slow state density/fast state density (needed for the optimal band-bending at the surface), compatibility with the device processing chemicals, reasonable chemical/thermal stability, small stress, well-matched crystalline properties (since ZnS and HgCdTe have nearly same crystalline parameters i.e. ZnS: cubic zinc-blende structure, lattice constant- 5.409 Å; HgCdTe:

cubic zinc blend structure, lattice constant- 6.464 Å). Consequently, ZnS material could be an effective and appropriate passivation film/layer for achieving the HgCdTe-based IR detectors of high performance [8,11,12,31,41].

1.5.2. Au as p-contact: High-performance/reliable IR photodetectors (having the capabilities of fulfilling current and future technology requirements) can be fabricated by creating a thermally stable metal-contact/HgCdTe interface with ohmic nature (that shows linear current-voltage characteristics and low contact resistance) and good reproducibility. Ohmic contact formation on HgCdTe (MCT) semiconductors [1,14,31,33,41,42] is slightly challenging since it has many issues like long-term thermal stability, I/f noise, uniformity, reliability in a high operating temperature, and cleanliness of contact surface, etc., Particularly for p-type HgCdTe material ohmic contact formation is relatively more problematic (that shows non-ohmic behavior) because of its delicate nature (weak Hg–Te bond) and HgCdTe material stability relating to time & temperature. Various metals like Al, Ag, Cu, Ti, Pd, Pt, Ge, HgTe, Sn, Cr, and Au [15,33,41,42] are used to form p-contact (common contact) on HgCdTe-based IR detectors. Metals Ag, Cu, Pd, Pt, Sb, and Ge exhibit rectifying behaviour while HgTe metal can create ohmic contact that is not so economical because complicated growth equipment (like metal-organic chemical vapour deposition (MOCVD) and molecular beam epitaxy techniques (MBE)) of high-cost are required for the growth of this metal. The metals Al, Cr, Sn, and Au have also been utilized for creating p-contact with a nearly ohmic nature. Among all these metals, Au is the metal that has some unique features [8,22,40,42] like high electrical conductivity, noble metal, anticorrosive/prevents oxidation, and soft and good ductility; which make it highly suitable/effective metal for creating ohmic p-contact on HgCdTe-based IR detectors. The generated ohmic contact (it offers minimum signal-to-noise-ratio/negligible power dissipation) is responsible for the high performance of the IR photo detector.

1.5.3. In as indium bump/n-contact: The maximum interconnection yields of detector-ROIC and ohmic n-contact formation are necessary to achieve high-performance HgCdTe-based IR detectors. Different materials namely Cu/Ni/Sn, Ti/Pt/Au/Ep/In, Ti/Pt/Au/In, and In are utilized for the fabrication of bumps. Indium (In) metal is one of the most suitable/frequently used interconnection materials for the detector-ROIC interface which has some unique properties such as cryogenic stability, appropriate mechanical/electrical belongings, high ductility, low melting point (156 °C), excellent plasticity with easy cold-welding, easy creation of small/high-density interconnection bumps and optimum TCE (thermal coefficient of expansion) mismatch. It has been applied to generate the In-bumps (circular columns of an optimized height: 5-6 μm) on the detector and ROIC. The flip-chip bonding technique is used to integrate the detector and ROIC; where the grown In-bumps (on the detector and ROIC) act as an electrical/mechanical interface between them. The readout electronics with In-bumps offer multiplexing of the signals (coming from thousands/millions of pixels to a small number of output lines). The In-bumps also simplify the interface between the vacuum-enclosed cryogenic IR sensor/detector as well as the system electronics significantly [2,7,9,33,35,39,43-45]. The ohmic contact (low resistance/minimum power dissipation, thermally stable, low noise level) is essential for the effective functioning/maximum efficiency of IRFPA. Numerous single/double/triple metal layers namely Al, Au, Ti, Ni, Cr, In, Mo/Au, Mo/In, HgTe/In/Au, and Ti/Pt/Au are being used to form ohmic electrical contact on n-HgCdTe based IR photodetectors. In is the renowned/conventional material that can form an ohmic n-contact (low-temperature deposition/high adhesion layer and low noise level of grown In-contact) on individual diodes of the HgCdTe-based detector array to make their connections from the external world [2,9,35,39,43]. Thus, In metal can create the bumps of high-density/maximum interconnections on HgCdTe-detector/Si-ROIC and ohmic n-contact to HgCdTe; which are necessary for realizing the high performance/ reliability HgCdTe-IR detectors.

1.5.4. ZnS/YF_3-based ARC film-stack: The back-illuminated HgCdTe detectors are usually fabricated on the lattice-matched CdZnTe (CZT) substrates that reflect about one-fourth (21%) of incident IR flux entering via the transparent CdZnTe (CZT) substrate due to reflection losses (since the refractive index of CdZnTe: 2.7 is higher than the refractive index of air: 1 and this mismatch of refractive indices are liable to generate high Fresnel reflection losses at the air-CdZnTe interface) and it passes only three-fourths (79 %) of incident IR radiation to the active area of HgCdTe where electron-hole pairs are created. The loss of incident IR signals affects the detector performance in terms of reduced quantum efficiency, increased noise/cross-talk, and poor image contrast [8,11,40,46-49].

The realization of maximum photo-signal/IR signal (with minimum reflectance and maximum transmission) along the air/CdZnTe interface is a very critical issue and it can be achieved by the use of ARC layers on CdZnTe substrate which minimizes the reflection losses of the photo signals across the CdZnTe substrate/CdZnTe-HgCdTe assembly. Several ARC materials/designs such as ZnS-based single-layer ARC, four-layer ARC (CdTe/Si_3N_4/BaF_2/diamond), ZnS/Ge-based 5-layer ARC microstructures (1.53-3.4 μm) and ZnS/YF_3-based two-layer ARC on CdZnTe (reflection≤1%) substrate/CdZnTe-HgCdTe assembly; were applied to minimize the reflection losses of IR photo signals through this substrate [4,12,20,47-49]. ZnS/YF_3-based ARC design (having the least number of layers, lowest optical thickness with coverage of the whole spectral region, good stability/durability, high adhesion/better bond, and minimum stress) is the most effective/suitable one among the above-mentioned designs/layers and it can be applied on

CdZnTe substrate or HgCdTe-CdZnTe assembly for reducing the reflection-losses of the incident IR signals. It could be advantageous in the development of high-performance (high spectral response/quantum efficiency, minimum reflectance, low noise, high stability, and low cross-talk) HgCdTe-based IR detectors [4,8,11,48,49].

Various thin films namely ZnS (passivation), In (bumps/ohmic n-contact), Au (ohmic p-contact), and ZnS/YF_3-based ARC; have significant roles in the fabrication of HgCdTe-based IR detectors. Over the past decades, researchers have utilized the aforesaid thin films in the HgCdTe-based IR detector fabrication technology and a short literature review of all the thin films (i.e. ZnS, In, Au, and ZnS/YF_3-based ARC) is given in Table 1.1 as follow:

Table 1.1 Utilization/role of various thin films like ZnS, In, Au, and ZnS/YF_3-based ARC films in HgCdTe-based IR detector fabrication.

Name of Grown thin film	**Application/purpose of film and properties studied**	**A substrate on which film grown**	**Deposition technique**	**References**
ZnS	Passivation, electrical	HgCdTe	Thermal evaporation	[41]
ZnS	Passivation, electrical	HgCdTe	Thermal evaporation	[50-51]
ZnS	Passivation, electrical	HgCdTe	Thermal evaporation	[52]
ZnS	Passivation, electrical	HgCdTe	Thermal evaporation	[53]
ZnS	Passivation, electrical	HgCdTe	Thermal evaporation	[54]

ZnS	Passivation; electrical and compositional	HgCdTe	Thermal evaporation	[55]
Au	p-contact; electrical	HgCdTe	Thermal evaporation	[42]
Au	p-contact; electrical and compositional	HgCdTe	Thermal evaporation	[56]
Mo/Au	p-contact, electrical	HgCdTe	Thermal evaporation	[57]
Ti/Pt/Au	p-contact, electrical	HgCdTe	Thermal evaporation	[58]
Au	p-contact; electrical and compositional	HgCdTe	Electroless deposition	[59]
Au	p-contact; electrical and compositional	HgCdTe	Thermal evaporation/ electroless deposition	[60]
In	Indium bump; microstructural and morphological	Epi-ready sapphire	Thermal evaporation	[61]
In	Indium bump, microstructural	HgCdTe	Thermal evaporation	[44]
In	Indium bump; structural, compositional, and microstructural	Si	electroplating	[62]
In	n-contact; electrical and compositional	HgCdTe	Thermal evaporation	[43]
Mo/In	n-contact, electrical	HgCdTe	Thermal evaporation	[57]
In	n-contact; electrical and compositional	CdTe	Thermal evaporation	[63]

ZnS/Ge/ZnS/YF$_3$	Anti-reflection coating (ARC), optical	InP	Electron beam	[31]
ZnS/YF$_3$ and ZnS/YF$_3$/ZnS/YF$_3$	Anti-reflection coating (ARC), optical	HgCdTe	Thermal evaporation	[38]
ZnS	Anti-reflection coating (ARC), optical	HgCdTe	Sputtering	[46]
ZnS/YF$_3$/ZnS/YF$_3$	Anti-reflection coating (ARC), optical	ZnSe	Electron beam	[48]
ZnS/YF$_3$	Anti-reflection coating (ARC), optical	HgCdTe	Thermal evaporation	[49]
ZnS/YF$_3$	Anti-reflection coating (ARC), optical	HgCdTe	Thermal evaporation	[64]

Although the literature (Table 1.1) covers all the essential properties of these thin films (ZnS passivation, In bumps, Au ohmic p-contact, and ZnS/YF$_3$-based ARC) but it would be more beneficial for the further advancement of HgCdTe-based IR technology if all the other properties like structural, compositional, morphological, microstructural, electrical and optical were there within the individual films. Since all the properties of thin films are interrelated to each other and a small variation within any individual property can affect the performance of the IR detector.

1.6. Motivation and findings of the research: The collective benefit of HgCdTe-based IR detector (like unique/fundamental properties, popular/mature IR technology, and various applications as mentioned in **sections 1.2 and 1.3**) and utilization of various thin films (passivation, p-contact, metal bumps as detector-ROIC interconnection interface/n-contact and ARC film stack as an agent that minimizes the IR signal's reflection losses; as described in **section 1.5**) in the HgCdTe-based IR detector fabrication technology;

have motivated us for making the further investigations of these thin films (ZnS: passivation, In: as metal bumps (detector-ROIC interconnection interface)/ohmic n-contact, Au: ohmic p-contact and ZnS/YF_3-based ARC: to minimize the reflectance of incident photon flux/IR signals), which are extremely essential to develop the highly demanded IR detector technology. The proposed investigation is based on the elimination/improvement of the shortcomings (limitations) in earlier published literature and the relation of detector performance with the varying properties of numerous thin films. Accordingly, this might be very advantageous for the further advancement of highly demanding, critical, and challenging HgCdTe-based IR photodetectors technology.

In the present thesis, various thin films namely ZnS (passivation), indium (as ohmic n-contact/detector-ROIC interconnector), Au (ohmic p-contact), and ZnS/YF_3 (four-layer ARC to minimize IR signal reflectance) were synthesized using thermal evaporation technique. Accordingly, the characterization techniques such as X-ray diffraction (XRD), atomic force microscopy (AFM), scanning electron microscope (SEM), energy-dispersive X-ray analysis (EDX), surface profiler (Dektak), ellipsometry, microscopy, non-contact sheet resistance measurement were used to produce the optimized thin films. The effectiveness/usefulness of these optimized films was further examined by fabricating various test structures/devices namely metal-insulator-semiconductor (MIS) device with the configuration of Au-Cr/ZnS/p-HgCdTe, In bumps/HgCdTe structure, transfer length method (TLM) structure (configuration: In/n/p-HgCdTe), TLM structure (Au/p-HgCdTe), ARC film stack/structure (configuration: YF_3/ZnS/YF_3/ZnS/CdZnTe-HgCdTe) using these films. Subsequently, the characterization techniques namely scanning electron microscope (SEM), capacitance-voltage (C-V)/current-voltage (I-V) measurements, and Fourier transform infrared (FTIR) spectroscopy were used to prove the suitability of the fabricated structures/devices for the HgCdTe-based IR detector fabrication. The thin films like ZnS (passivation layer with low surface leakage current/dark current), In (ohmic In/n-HgCdTe interface with low specific contact resistance; In-bumps: with optimum uniformity, height, diameter, and stress), Au (ohmic Au/p-HgCdTe interface with low specific contact resistance), and ZnS/YF_3-based ARC (with reflection≤1.0 % within the MWIR spectral region:3.2 - 4.3 µm); were found with optimum features and those might be treated as the corresponding applications of the thin films in the fabrication of HgCdTe-based IR detectors.

References:

[1] A. Rogalski, J. Antoszewski, and L. Faraone, Third-generation infrared photodetector arrays, J. Appl. Phys. 105 (2009) 091101.

[2] A. Rogalski, Infrared detectors: status and trends, Prog. Quantum Electron. 27 (2003) 59-210.

[3] M. Vaghayenegar, Characterization of HgCdTe and related materials for third generation infrared detectors, PhD thesis, Arizona State University, 2017.

[4] A. Rogalski, Progress in focal plane array technologies, Prog. Quantum Electron. 36 (2012) 342-473.

[5] O. Gravrand, J. Rothman, P. Castelein, C. Cervera, N. Baier, C. Lobre, E. De Borniol, J. P. Zanatta, O. Boulade, V. Moreau, B. Fieque, P. Chorier, Latest achievements on MCT IR detectors for space and science imaging, Infrared Technology and Applications XLII, Proc. of SPIE 9819 (2016) 98191W.

[6] A. Rogalski, Infrared detectors for the future, Acta Phys. Pol. A 116 (2009) 389-406.

[7] A. Rogalski, HgCdTe infrared detector material: history, status and outlook, Rep. Prog. Phys. 68 (2005) 2267-2336.

[8] C. L. Tan, H. Mohseni, Emerging technologies for high performance infrared detectors Nanophotonics 7 (2018) 169-197.

[9] A. Rogalski, New material system for third generation infrared photodetectors, Opto-Electron. Rev. 16 (2008) 458-482.

[10] R. K. Bhan, V. Dhar, Recent infrared detector technologies, applications, trends and development of HgCdTe based cooled infrared focal plane arrays and their characterization, Opto-Electron. Rev. 27 (2019) 174-193.

[11] W. Lei, J. Antoszewski, L. Faraone, Progress, challenges, and opportunities for HgCdTe infrared materials and detectors, Appl. Phys. Rev. 2 (2015) 041303.

[12] C. Downs and T. E. Vandervelde, Progress in Infrared photodetectors since 2000, Sensors 13 (2013) 5054-5098.

[13] S. Bianconi and H. Mohseni, Recent advances in infrared imagers: toward thermodynamic and quantum limits of photon sensitivity, Rep. Prog. Phys. 83 (2020) 044101.

[14] B. Chen, Y. Chen and Z. Den, Recent Advances in high speed photodetectors for eSWIR/MWIR/LWIR applications, Photonics 8 (2021) 14.

[15] A. Rogalski, P. Martyniuk, M. Kopytko, W. Hu, Trends in performance limits of the HOT infrared photodetectors. Appl. Sci. 11 (2021) 501.

[16] A. Rogalski, Assessment of HgCdTe photodiodes and quantum well Infrared photoconductors for long wavelength focal plane arrays, Infrared Phys. Technol. 40 (1999) 279-294.

[17] J. Philips, Evaluation of the fundamental properties of quantum dot infrared detectors, J. Appl. Phys. 91 (2002) 4590.

[18] S. B. Hafiz, M. Scimeca, A. Sahu, D. K. Ko, Colloidal quantum dots for thermal infrared sensing and imaging, Nano Converg. 6 (2019) 7.

[19] A. Rogalski, Infrared detectors: an overview, Infrared Phys. Technol. 43 (2002) 187-210.

[20] A. Rogalski, Recent progress in infrared detector technologies, Infrared Phys. Technol. 54 (2011) 136-154.

[21] R. S. Saxena, R. Nokhwal, R. K. Bhan, R. K. Sharma, Electrical characteristic signatures for non-uniformity analysis in HgCdTe photodiode arrays, Infrared Phys. Technol. 56 (2013) 69-75.

[22] Titu-Marius I. Băjenescu, Infrared detectors, J. Eng. Sci. XXV (3), (2018) 29-40.

[23] M. S. Cabrera, C. W. McMurtry, M. L. Dorn, W. J. Forrest, J. L. Pipher, and D. Lee, Development of 13-μm cutoff HgCdTe detector arrays for astronomy, J. Astron. Telesc. Instrum. Syst. 5 (2019) 036005.

[24] V. Srivastav, R. K. Sharma, R. K. Bhan, V. Dhar, V. Venkataraman, Exploring novel methods to achieve sensitivity limits for high operating temperature infrared detectors, Infrared Phys. Technol. 61 (2013) 290-298.

[25] O. Gravrand and J. Rothman, HgCdTe quantum detection: from Long-Wave IR down to UV, J. Electron. Mater. 40 (2011) 1781-1784.

[26] N. Vanamala, K. C. Santiago, and N. C. Das, Enhanced MWIR absorption of HgCdTe (MCT) via plasmonic metal oxide nanostructures, AIP Adv. 9 (2019) 025113.

[27] Y. F. Lao, A. G. Unil Perera, and P. S. Wijewarnasuriya, Optical study of HgCdTe infrared photodetectors using internal photoemission spectroscopy, Appl. Phys. Lett. 104 (2014) 131106.

[28] A. Rogalski, 7 - HgCdTe photodetectors, Mid-infrared optoelectronics, In Woodhead Publishing Series in Electronic and Optical Materials, Woodhead Publishing (2020) 235-335.

[29] P. Norton, HgCdTe infrared detectors, Opto-Electron. Rev. 10 (2002) 159-174.

[30] A. M. Itsuno, Bandgap-Engineered HgCdTe Infrared detector structures for reduced cooling requirements, PhD thesis, The University of Michigan, 2012.

[31] J. Kenion White, Mid-wave infrared HgCdTe photodiode technology based on plasma induced p-to-n type conversion, PhD thesis, The University of Western Australia, 2005.

[32] D. Eich, W. Schirmacher, S. Hanna, K. M. Mahlein, P. Fries, and H. Figgemeier, Progress of MCT detector technology at AIM towards smaller pitch and lower dark current, J. Electron. Mater. 46 (2017) 5448-5457.

[33] M. Kimata, Development of infrared focal plane arrays, Sens. Mater. 30 (2018) 1221-1230.

[34] A. Chatterjee, J. Balakrishnan, N. B. Pendyala, K. S. R. Koteswara Rao, Room temperature operated HgCdTe colloidal quantum dot infrared focal plane array using shockwave dispersion technique, Appl. Surf. Sci. Adv. 1 (2020) 100024.

[35] J. A. Montoya, Z. B. Tian, S. Krishna, and W. J. Padilla, Ultra-thin infrared metamaterial detector for multicolor imaging applications, Opt. Express 25 (2017) 23345-23355.

[36] H. Figgemeier, S. Hanna, D. Eich, K.-M. Mahlein, W. Fick, W. Schirmacher, R. Thöt, State of the art of AIM LWIR and VLWIR MCT 2D focal plane detector arrays for higher operating temperatures, Infrared Technology and Applications XLII, Proc. of SPIE 9819 (2016) 98191C.

[37] A. Rogalski and R. Ciupa, Theoretical modeling of long wavelength n+-on-p HgCdTe photodiodes, J. Appl. Phys. 80 (1996) 2483.

[38] A. Singh and R. Pal, Performance of Hg1-xCdxTe infrared focal plane array at elevated temperature, Semicond. Sci. Technol. 32 (2017) 045011.

[39]A. Rogalski, Toward third generation HgCdTe infrared detectors, J. Alloys Compd. 371 (2004) 53-57.

[40] A. Singh, V. Srivastav, R. Pal, HgCdTe avalanche photodiodes: A review, Opt. Laser Technol. 43 (2011) 1358-1370.

[41] R. K. Bhan, V. Srivastava, R. S. Saxena, L. Sareen, R. Pal, R. K. Sharma, Improved high resistivity ZnS films on HgCdTe for passivation of infrared devices, Infrared Phys. Technol. 53 (2010) 404-409.

[42] W. A. Beck, G. D. Davis, and A. C. Goldberg, Resistance and 1/f noise of Au, Al, and Ge contacts to (HgCd)Te, J. Appl. Phys. 67 (1990) 6340.

[43] P. W. Leech, G. K. Reeves, Specific contact resistance of indium ohmic contacts to n-type $Hg_{1-x}Cd_xTe$, J. Vac. Sci. Technol. A 10 (1992) 105.

[44] J. Jiang, S. Tsao, T. O'Sullivan, M. Razeghi, G. J. Brown, Fabrication of indium bumps for hybrid infrared focal plane array applications, Infrared Phys. Technol. 45 (2004) 143-151.

[45] T. V. Blank and Y. A. Goldberg, Mechanisms of current flow in metal-semiconductor Ohmic Contacts, Semiconductors 41 (2007) 1263-1292.

[46] Q. J. Liao X. N. Hu, The study of improving the performance of HgCdTe photovoltaic detectors with antireflection coating, 2006 Joint 31st International conference on infrared millimeter waves and 14th international conference on terahertz electronics, IEEE Xplore, 23524110 (2006) 132.

[47] V. Gopal, Effect of anti-reflection coating on the performance of 0.1 eV HgCdTe photoconductive detectors, Infrared Phys. 23 (1983) 307-310.

[48] F. Lemarquis, G. Marchand, and C. Amra, Design and manufacture of low-absorption $ZnS-YF_3$ anti-reflection coatings in the 3.5-16 μm spectral range, Appl. Opt. 37 (1998) 4239-4244.

[49] A. K. Saini, A. Singh, V. S. Meena, S. K. Gaur, R. Pal, Design and development of double-layer anti-reflection coating for HgCdTe based mid-wave infrared detector, Mater. Sci. Semicond. Process. 147 (2022) 106749.

[50] J. K. White, C. A. Musca, H. C. Lee, L. Faraone, Hydrogenation of ZnS passivation on narrow-band gap HgCdTe, Appl. Phys. Lett. 76 (2000) 2448-2450.

[51] I. Madni, Characterization of MBE-grown HgCdTe and related II-VI materials for next generation infrared detectors, PhD thesis, The University of Western Australia, 2017.

[52] J. K. White, J. Antoszewski, R. Pal, C. A. Musca, J. M. Dell, L. Faraone, and J. Piotrowski, Passivation effects on reactive-ion-etch-formed n-on-p junctions in HgCdTe, J. Electron. Mater. 31 (2002) 743-748.

[53] Q. Lu, X. Wang, S. Zhou, R. Ding, L. He and C. Lin, Effects of different passivation layers on RV characteristics of long-wave HgCdTe gate controlled diodes, Semicond. Sci. Technol. 35 (2020) 095003.

[54] F. S. Juang, Y. K. Su, S. J. Chang, S. M. Chang, F. S. Shu, C. D. Chiang, Y. T. Cherng, and T. P. Sun, Dark Currents in HgCdTe Photodiodes Passivated with ZnS/CdS, J. Electrochem. Soc. 146 (1999) 1540-1545.

[55] Y. C. Jung, S.Y. An, S. H. Suh, D. K. Choi, J. S. Kim, Ammonium sulfide treatment of HgCdTe substrate and its effects on electrical properties of ZnS/HgCdTe heterostructure, Thin Solid Films 483 (2005) 407-410.

[56] F. Sizov, Z. Tsybrii, M. Apats'ka, N. Dmytruk, V. Slipokurov, S. Bunchuk, Yu Bezsmolnyy, V. Popovych, M. Wiertel and N. Mikhailov, Ohmic metal/$Hg_{1-x}Cd_xTe$ ($x \approx 0.3$) contacts, Semicond. Sci. Technol. 35 (2020) 125030.

[57] Z. Tsybrii, Y. Bezsmolnyy, K. Svezhentsova, M. Vuichyk, I. Lysiuk, M. Apatska, M. Smolii, N. Dmytruk, S. Bunchuk, K. Andreeva, F. Sizov, HgCdTe/CdZnTe LPE epitaxial layers: from material growth to applications in devices, J. Cryst. Growth 529 (2020) 125295.

[58] V. Srivastav, R. Pal, B. L. Sharma, V. Mittal, V. Gopal, and H. P. Vyas, Electrical properties of titanium-HgCdTe contacts, J. Electron. Mater. 34 (2005) 225-231.

[59] A. Singh, A. K. Shukla, S. Jain, B. S. Yadav, R. Pal, Electrical characteristics of electroless gold contacts on p-type $Hg_{1-x}Cd_xTe$, Mater. Sci. Semicond. Process. 26 (2014) 294-300.

[60] V. Krishnamurthy, A. Simmons, C. R. Helms, Oxide interfacial layers in Au ohmic contacts to p-type $Hg_{1-x}Cd_x$ Te, Appl. Phys. Lett. 56 (1990) 925.

[61] P. Kozłowski, K. Czuba , K. Chmielewski , J. Ratajczak, J. Branas, A. Korczyc, K. Regi´nski and A. Jasik, Indium-based micro-bump array fabrication technology with added pre-reflow wet etching and annealing, Materials 14 (2021) 6269.

[62] Q. Huang, G. Xu, Y. Yuan, X. Cheng and L. Luo, Development of indium bumping technology through AZ9260 resist electroplating, J. Micromech. Microeng. 20 (2010) 055035.

[63] S. Nozaki and A. G. Milnes, Specific contact resistivity of indium contacts to n - type CdTe, J. Electron. Mater. 14 (1985) 137-155.

[64] A. Singh, A. K. Shukla, and R. Pal, HgCdTe e-avalanche photodiode detector arrays, AIP Adv. 5 (2015) 087172.

Chapter 2

Experimental and characterization techniques

Introduction

This chapter presents an overview of the experimental and characterization techniques utilized to accomplish the proposed objectives of the thesis. The experimental techniques/methodology involves the HgCdTe sample preparation and deposition of various thin films (ZnS, Indium, Au, and ZnS/YF_3-based ARC film stack) on these samples. On the other hand, the main characterization techniques which have been used for evaluating the properties of grown thin films are X-ray diffraction (XRD) analysis, atomic force microscopy (AFM), scanning electron microscope (SEM), energy-dispersive X-ray analysis (EDX),capacitance-voltage (C-V)/current-voltage (I-V) measurements, Fourier transforms infrared (FTIR) spectroscopy, surface profiler (Dektak), ellipsometry, microscopy, and non-contact sheet resistance measurement.

A brief description of experimental techniques/methodology (sample preparation and thermal evaporation vacuum technique) and characterization techniques are given below:

2.1. Sample preparation

Sample surface plays a vital role in deciding the quality of deposited thin films. Accordingly, surfaces of all the $Hg_{1-x}Cd_xTe$ samples ($x \approx 0.29$, used in the research) were prepared by use of many standard and sequential processes/methods (like Mechanical/chemo-mechanical polishing, etching, cleaning, washing, drying, baking, etc.) before deposition/formation of thin films over these samples/substrates where different chemicals (in the form of solid, liquid and gases) of semiconductor/electronic grade had been utilized in these processes of sample preparation [1-5].

Aforesaid processes and used chemicals are mentioned as follows:

- Mechanical polishing (via 0.05 μm alumina powder) of the samples/epilayers for achieving their desired dimension.
- Chemical polishing to achieve the surface with a minimum amount of native oxides and desired surface morphology where the solution (I_2:KI: $C_2H_6O_2$)**::** (1g:4g: 10 ml) + few drop of KOH solution was used in this procedure.
- Cleaning of epilayers by a standard procedure (5 min heating of epilayers in each chemical sequentially, i.e., in trichloroethylene, acetone, and methanol) to remove the oil vapours and greasy impurities from the surfaces of samples.
- Chemical etching (for 20 sec by 0.1% bromine in methanol solution) to achieve the oxide-free/fresh surface or procedure of washing (DI water), drying (highly pure N_2), and baking (in N_2 gas ambient 5 min at 90 °C) depending on the specific thin film formation to remove the chemical residues/water vapours from the sample's surface.
- Examination of the surface quality of the samples/epilayers through microscopy observation/ellipsometry measurement.
- Finally, samples/epilayers were utilized for the depositions of proposed thin films as mentioned further.

2.2. Thin film growth techniques

All the aforesaid films (ZnS, Indium, Cr-Au, and ZnS/YF_3-based ARC film stack) can be fabricated through the deposition techniques like successive ionic layer adsorption and reaction (SILAR) techniques, thermal evaporation, atomic layer deposition [6-8], electroplating, electro-deposition[9-11], ion beam sputtering, electroless deposition [12-15], electron beam, magnetron sputtering [13,16-20], etc. Among all the deposition techniques, thermal evaporation is the standard/conventional, economical (in terms of deposition material and power consumption), and matured technique that has many benefits [21-25] in film deposition, namely directional deposition, least impurities, high deposition rate, precise control over the deposited film thickness/deposition rate and substrate temperature, etc. Thermally grown films also have reasonable crystalline (homogeneous growth, smoothness/low roughness, and pin-hole-free film) and electrical/optical (low resistance, reflectance/transmission) properties required for high-performance IR detectors. Here, we have synthesized numerous films like ZnS (passivation), indium (as ohmic n-contact/detector-ROIC interconnector), Au (ohmic p-contact), and ZnS/YF_3 (four-layer ARC to minimize IR signal reflectance) films by thermal evaporation vacuum technique.

2.2.1. Thermal evaporation and growth mechanism

The thermal evaporation technique is one of the most popular, well-known, and simple technique that can be utilized for evaporating different kinds of materials on numerous substrates of semiconductors as well as industrial applications. In this technique, at first, the solid source material (available in different shapes like chunks/powder, pellets/wire/coins) is put into a boat/filament/basket made from refractory metals like molybdenum, tungsten, and tantalum. Afterward, it is heated to a sufficient temperature by resistive heating/an electric current source under optimum/desired vacuum conditions which are achieved in the vacuum chamber with the help of a turbo-molecular pump supported by a rotary pump. Thus, the created vapour flux (vapour stream) is transported directly towards the substrate through the high vacuum environment without making a collision with the other background gases/residual gases and after the condensation of these vapours onto the substrate a thin film of the desired material is achieved. The high vacuum enhances the mean free path of the evaporants and the created vapour atoms travel toward the substrate in a straight path/trajectory. So, this deposition process is termed a line-of-sight process and there is a minimum possibility of contamination within the deposited film. The mean free path (of the evaporated atoms) also decides the distance between source and substrate that is normally fixed to a range of 10-50 cm at an optimum vapour pressure but in the proposed research work it has been taken as 30 cm

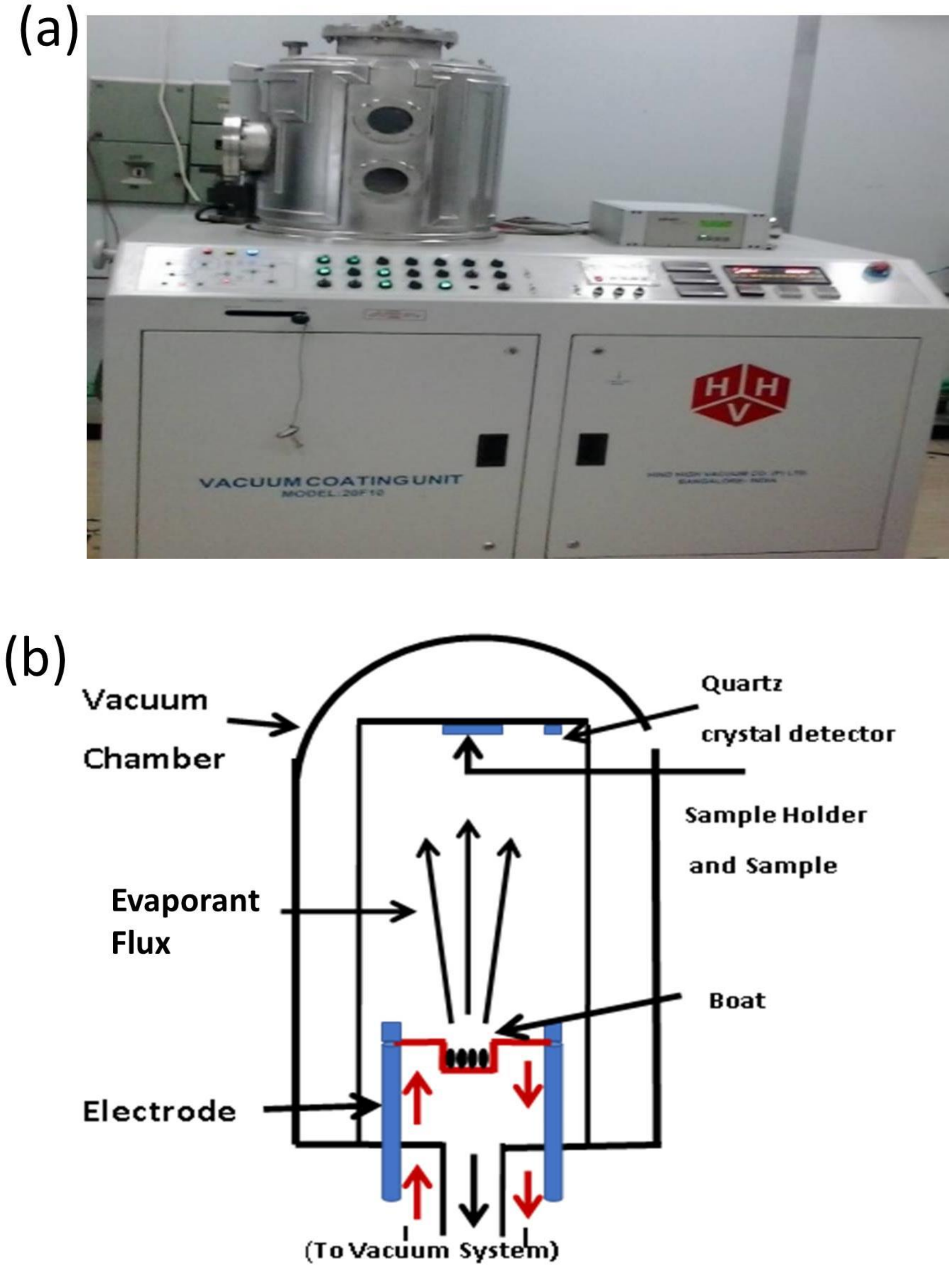

Figure 2.1. Experimental set-up and growth mechanism/process: (a) a photograph of the thermal evaporation vacuum system and (b) the schematic diagram.

for that reason. The experimental set-up and growth mechanism/process (with thermal evaporation system and its schematic diagram) are shown in Fig. 2.1.

Here, the film of desired thickness can be grown on the substrate at the optimized process parameters (deposition rate and evaporation current) and accordingly, the auto rate controller/quartz crystal monitor fitted in the vacuum coating system can regulate these parameters very precisely.

2.2.2. Steps and parameters for the growth of thin films

Various thin films have been grown on the $Hg_{1-x}Cd_xTe$ samples ($x \approx 0.29$) to accomplish the proposed research objectives. The fundamental sequential steps to grow these thin films are mentioned as follows:

- HgCdTe-epilayers are put into a vacuum chamber of a coating unit after completing their sample preparation followed by a surface quality examination.
- Desired source materials (since different materials may have numerous shapes like chunks/powder, pellets/wire/coins) are put into the molybdenum boat.
- Chamber is evacuated to an ultimate vacuum through different vacuum pumps (rotary and turbo molecular pumps) needed to grow a thin film of an individual material on the substrate and every material has a different deposition pressure/vacuum.
- Films (ZnS, In bumps, Cr-Au, and ZnS/YF_3-based ARC) of desired thickness (which are different for every film) were deposited on the HgCdTe-epilayers.
- The deposition process at the optimized process parameters (rate of deposition: Å/sec, film thickness, and process temperature: room temperature) and every film has different growth parameters.
- Thickness and deposition rate are monitored by an auto rate controller (quartz crystal monitor) that is fitted with a coating unit.

- Samples/epilayers are taken out from the vacuum chamber after the completion of the deposition process. Consequently, these deposited samples with various thin films are evaluated by various characterization/measurement techniques as mentioned further. The deposition parameters of different films are shown in Table 2.1 as given below:

Table 2.1. The optimized deposition/growth parameters for various thin films.

Deposited films/materials	Film thickness (nm/ µm)	Deposition rate (Å/sec or nm/sec)	Evaporation current (A)	Vacuum level (Torr)	Process temperature (°C)
ZnS	300 ± 5 nm	1.0-1.2 Å/sec	60-65	2×10^{-7}	room temperature: 25
In	4.5 ± 0.5 µm	2.7 nm/sec	170-200	4.0×10^{-7}	room temperature: 24
Au	200 ± 5 nm	10 Å/sec	122-130	6×10^{-7}	room temperature: 25
ZnS/YF_3-based four-layer ARC	699 ± 2.6 nm	2 -5 Å/sec	77-103	2×10^{-7}	room temperature: 21

2.3. Characterization techniques

Numerous characterization/measurement techniques like XRD, AFM, SEM, EDX, C-V)/I-V measurements, FTIR spectroscopy, Dektak surface profiler, ellipsometry, microscopy, and non-contact sheet resistance measurement (eddy current inspection technique) were applied to evaluate the properties of the grown films namely ZnS, Indium, Au, and ZnS/YF_3-based ARC film stack, etc. An extensive explanation of the aforesaid techniques is given below:

2.3.1. X-ray diffraction (XRD)

The discovery of X-rays was done by Wilhelm Roentgen in 1895 through the Crookes tube experimentation and he found that these are part of electromagnetic radiation lying between gamma rays as well as ultraviolet radiations. The wavelength of X-rays (0.5-2.5 Å) is comparable to the interatomic distance/interplanar spacing of the crystalline solids and hence the phenomenon of X-ray diffraction (XRD) occurs when the X-ray beam strikes a crystal. The crystals (have a periodic arrangement of atoms with a fixed interatomic distance) act as the best scattering centres/diffraction gratings source for the incident X-rays. Each crystalline material owns its unique characteristic X-ray powder pattern which may be utilized for knowing its existence and crystal structure. Thus, X-ray diffraction has become one of the most popular characteristics tools which are used in the field of solid-state physics, chemistry, and materials science [26-29]. This is a renowned, advanced, and non-destructive technique that has a wide range of applications analyzing unknown crystalline solids/materials (semiconductors, metals, and grown thin films: crystal structure/phase, lattice constant/unit cell dimensions, grain size, and its orientation in a polycrystalline sample, impurity/defects in sample and stress level), minerals/inorganic compounds (identification of the clays/mixed layer clays with very fine grain size, determination of the number of minerals via quantitative analysis), fingerprint materials & their structure**,** catalysts, polymers, plastics, fluids ceramics and pharmaceuticals, etc. [26-28].

The interaction of incident monochromatic X-ray waves with the periodically arranged atoms/crystallographic planes of a material’s crystal is shown in Fig. 2.2. This interaction produces a constructive interference /diffraction phenomenon which is governed by the Equation given below:

$$2d \sin \theta = n\lambda \qquad (2.1)$$

Where the parameters, θ: diffraction angle, n: order of diffraction, λ: wavelength of incident X-rays, and d: interplanar spacing/interatomic distance.

Eq^{n} 2.1 is termed Bragg's Law which defines the relation among the parameters namely incident X-ray wavelength, diffraction angle, and interplanar spacing/interatomic distance in a crystalline solid.

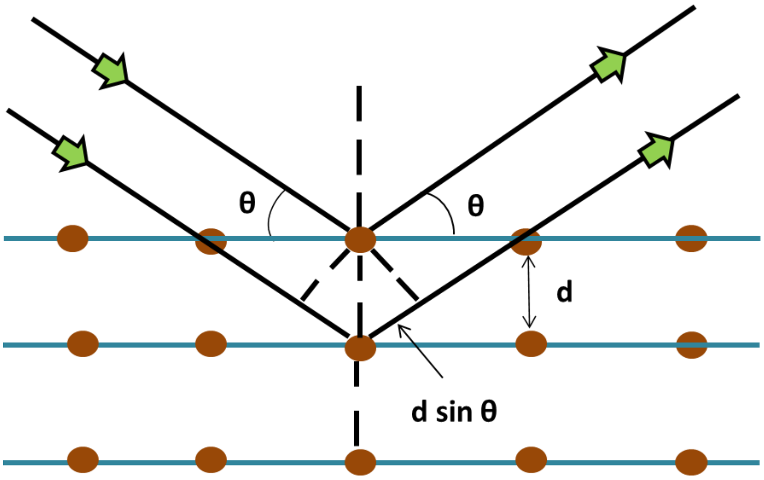

Figure 2.2. Schematic representation of X-ray diffraction.

A standard XRD diffractometer consists of three main elements namely an X-ray source, a sample (to be analyzed), and a detector; where the most common X-ray source is copper ($CuK\alpha$) with the characteristic wavelength λ = 1.542Å. When the incident X-ray beam strikes a sample/specimen and it produces diffraction in every possible direction/orientation 2θ. The movable detector is used to detect the diffracted beam while the counter (mounted to a goniometer) measures the intensity of the X-ray. The sample as well as the counter is both rotated where the counter makes its rotations along the circle of the diffractometer. The counter with a scanning range of 2θ =20-80° (at a fixed/constant angular velocity and scanning speed) is sufficient to collect the most significant XRD pattern for a developed sample but it can vary according to the sample’s specifications. All the resultant XRD patterns (diffraction peaks with specific intensity and position) are compared with the standard data files (JCPDS: Joint Committee on Powder Diffraction Standard) to identify the specimen’s material since each standard crystalline material/solid has the diffraction peaks with definite intensity/ peak position.

Figure 2.3. Photograph of X-ray diffraction system of PANalytical B.V.-X'Pert PRO MRD (Material research diffractometer).

The resultant FWHM (full width at half maximum) of the material can be utilized to evaluate its grain size with the help of the well-known Debye Scherrer formula (Eq^{n}. 2.2) as follows:

$$D = \frac{K.\lambda}{\beta \cos\theta} \tag{2.2}$$

The parameters β, θ, and K represent the diffraction peak's FWHM, angle of diffraction, and constant respectively; where the constant K usually has values in the range of 0.89-1.39 but for most cases it is nearly close to 1(K=0.94).

XRD measurements of the thermally grown thin films were performed by a PANalytical (B.V.-X'Pert PRO MRD) diffractometer system consisting of a copper ($CuK\alpha$) radiation source (with the wavelength λ = 1.542Å) and Xe-proportional counter shown in Fig. 2.3. All the useful/significant data of the developed thin films were collected within the scanning range of 2θ =20-90°.

2.3.2. Atomic force microscopy (AFM)

Atomic force microscopy (AFM)/scanning force microscopy (SFM)/scanning probe microscopy (SPM) was developed in 1986 (by Binnig et al.) for eliminating the condition of a conductive sample (prepared via metal coating on the surface of a sample that causes the damages/alterations of its surface and also the charging artifacts may appear in the final image) similar to the scanning tunnelling microscopy (STM) which has a very high resolution (order of divisions of a nanometre/1000 times the diffraction limit) and thus this is the superior characterization technique than the electron/conventional optical microscopes. AFM does not need a specific vacuum environment similar to the electron microscope but it can operate in any type of environment namely ambient air/ even a liquid environment and this feature makes the study of the biological macromolecules/ living organisms easier. It is one of the primary techniques/tools that is used to measure the surface morphology/topography (roughness, grains, and density) of various materials (like ceramic, polymer, metallic, and organic/inorganic mixtures) as well as for imaging (2D and 3D-images)/deploying the materials at the scale of nanometre [30].

AFM instrument contains a cantilever (with a silicon/silicon nitride sharp tip on its end where the radius of curvature of the tip: is nanometre order) which is used for scanning/probing of the sample/specimen surface. The sample is mounted on the piezoelectric actuator/tube while the cantilever is supported with detector & feedback electronics. When the tip is moved across the sample surface, then the forces (mechanical contact force) between the tip and sample generate a deflection of the cantilever under Hooke's law. A laser spot reflected from the top of the cantilever is used to measure the deflection through the help of photodiodes connected to the feedback electronics. The constant forces between the tip and sample are maintained by adjusting the tip-to-sample height with the help of a feedback mechanism since the sample can be damaged in the situation of varying tip-to-sample height. AFM is operated in three imaging modes namely contact mode, non-contact mode, and tapping/intermittent mode [31]. A brief discussion of these imaging modes is given below:

(a) Contact mode: The distance between tip and sample remains fixed during scanning of the sample surface and the cantilever deflection generated due to sample-tip interaction force is utilized to produce an image. However, close to the surface of the sample, attractive forces can be quite strong, causing the tip to "snap in" to the surface. In this mode, the cantilever is very close to the specimen/sample surface where generally the force is repulsive, and typically this is termed "contact mode".

(b) Non-contact mode: In this mode, the cantilever tip does not make contact with the sample surface but oscillates at its resonant frequency (frequency modulation)/just beyond at some small distance/height above the sample surface where amplitude modulation occurs (oscillation amplitude lying between a few nanometres (say <10 nm) to few picometres). The signal applied to the piezoelectric actuators needed to keep the resonant frequency constant is then used to generate a topographic image. The constant oscillation amplitude/frequency is maintained by the feedback detector/electronics system via adjusting the typical tip-to-sample distance and the scanning software form a sample's topographic image.

(c) Intermittent mode: The cantilever first oscillates at its resonance frequency but at amplitudes higher than those used in non-contact mode. Cantilever-tip creates contact with the sample's surface when it is taken near to the sample by reducing its oscillation amplitude and thus it is the most favoured imaging mode [30,31].

In this work, the AFM system/instrument (with the detail: Model-5600LS, AC Model III Module, Agilent Technologies) was used to measure the surface morphological properties of thermally grown thin films and it is shown in Fig. 2.4. All the samples were scanned/measured in tapping/intermittent mode to achieve better imaging and minimize the risk of sample surface damaging.

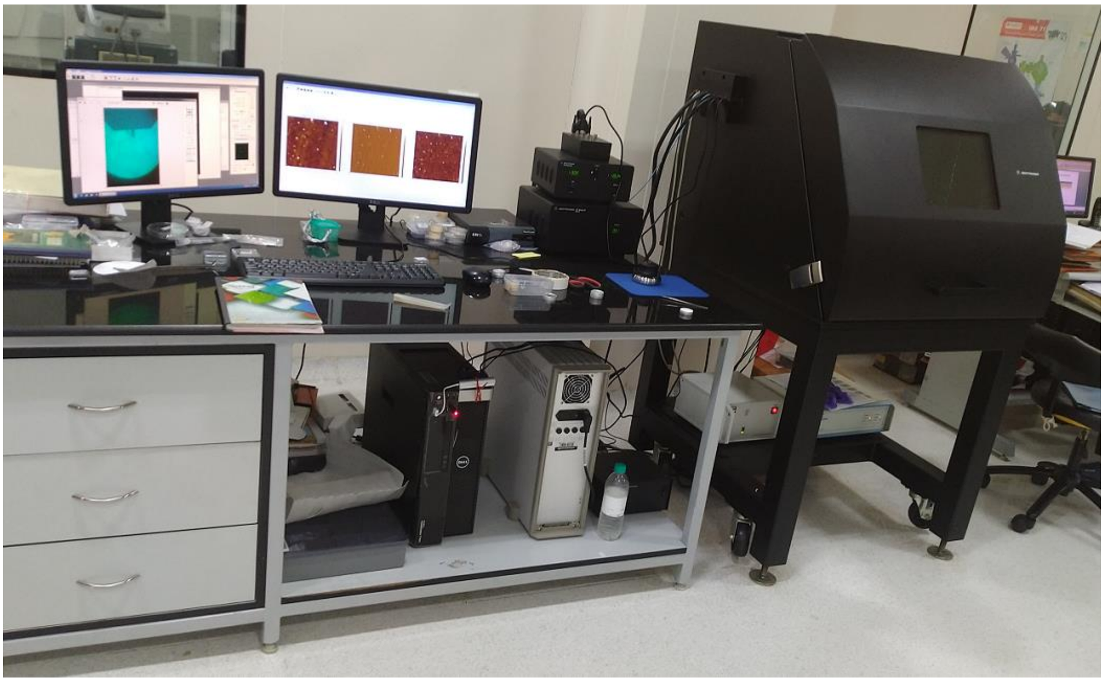

Figure 2.4. AFM system used for measuring the surface morphological properties of the thermally grown thin films.

2.3.3. SEM and EDX systems

SEM and EDX characterization techniques are used to evaluate the microstructural (grain size, continuity, and density/orientation of film-forming particles) and compositional (elemental information/stoichiometry and purity) features of the samples/specimen/films. A brief description of these techniques is as follows:

(a) Scanning electron microscope (SEM)

This is a type of electron microscope that is used to create the sample/specimen image via the scanning of the sample via a high-energy electron beam. When the high energy electron beam hit the surface of the sample and its interaction with the sample's atoms results in various signals (namely secondary electrons, backscattered electrons, and characteristic X-rays) which comprise information about the sample's surface topography/microstructures and chemical composition/elemental mapping. A typical SEM system consists of an electron gun/source (in vacuum condition) that generates an accelerated electron beam (0-30 kV) and its moving direction/size (electron amount) is controlled with the help of a series of electromagnetic lenses (condenser lens: reduce the main beam size to a suitable size, objective lens: focus the electron beam to sample). Finally, the electron beam hits the specimen surface by entering into the scanning coil path which can scan the desired window of the sample (their rectangular area) since the electron beam is deflected horizontally/vertically over the sample surface. The electronic devices (secondary electron detector: surface topography and backscattered electron detector: chemical and phase information) are utilized to achieve high-resolution images after processing various signals emitted from the sample surface due to their interaction with the electron beam [26,32].

(b) Energy-dispersive X-ray (EDX) analysis

This is a technique that works in conjunction with SEM which provides information about the chemical composition (elements and their proportions at different energy positions) and global mapping of the sample through the utilization of the emitted characteristics X-rays from the specimen surface. EDX spectrometer comprises a solid state detector (generally made of lithium-drifted silicon (Si-Li) as well as signal processing electronics) that is fitted within the SEM chamber and it has a design to view the samples with specified conditions while the minimum working distance (10 mm) can be adjusted. The electron beam (with 10-20 kV) strikes the sample surface and the characteristic X-rays are emitted from the specimen surface. The electron beam is moved across the whole area of the specimen to achieve the image of each element present in the sample and it takes several hours since the intensity of these X-rays is very low. Thus, the Si-Li detector processes (detects/converts) the emitted X-rays to produce the EDX spectra (X-ray energy histogram: the intensity of detected X-ray (X-ray count) along the Y-axis and energy (keV) along the X-axis) which involve a series of peaks of the representative element with their relative atomic composition [28,32].

(c) SEM/EDX instrument

The SEM (Model-Carl Zeiss SUPRA55VP, operating voltage: 5-20 kV) system supported with Oxford Instrument X-MAX EDX Spectrometer was utilized to evaluate the microstructural and compositional features of the thermally grown thin films on the HgCdTe samples and it is shown in Fig. 2.5.

Figure 2.5. Photograph of SEM system supported with EDX spectrometer.

2.3.4. CV and IV measurements

These measurements are very suitable tools that are used to evaluate the electrical properties of semiconductor devices (thermally grown passivation layer: the flat band voltage: $V_{FB,}$ fixed charge density, hysteresis width, slow state density, and fast interface states/interface traps) and electrical ohmic contacts (contact resistance, ohmicity, and current mechanism) where a brief description of these techniques is given below:

(a) CV measurement

In the CV measurement technique, two types of voltages (an AC voltage and a DC voltage) are applied on a semiconductor device (under test) simultaneously where AC voltage remains fixed (in magnitude and frequency) and DC voltage is swept in time. The capacitance of the device changes with variation of applied DC voltage (this is used for sampling of the material/device) and thus the capacitance measurement at a given depth of the device can be performed through the applied fixed AC voltage which provides a small-signal bias.

The MIS device/capacitor has an important property in that its capacitance varies with the applied DC voltage which leads to the operation of the MIS device in different modes namely accumulation, depletion, as well as inversion regions. The C-V characteristics for different capacitors of fabricated MIS device/structure were obtained at a frequency of 1.0 MHz, temperature 80 ± 3 K, and 30 mV AC voltage (rms) where a DC bias (ranging from 5.0 to -3.0 V and -3.0 V to 5.0 V) was applied for probing/sweeping of each capacitor of the device. The C-V characteristics of typical capacitors were used for extraction of various parameters (namely the flat band voltage: V_{FB}/fixed charge density, hysteresis width/ slow state density, and fast interface states/traps at ZnS/HgCdTe interface) through the help of MIS theory which provides the information about the effectiveness/suitability of thermally grown passivation layer (ZnS) in the fabrication of MIS structure/IR detector [3,33,34].

(b) IV measurement

I-V measurements for the fabricated TLM structures (Au and In contacts) were performed at 80 ± 3 K where the two probes are put on various pairs of metal contact pads with the applied voltage range -2 to 2 V (Au contact), -0.5 to 0.5 V (In contact) respectively. The corresponding current flows in the contact pads and thus an I-V curve for different pairs of various spacing is obtained which is used to extract the resistance for the pair of two contact pads. Similarly, resistances for all the contact pads were extracted with the help of their resultant IV curves. Subsequently, a plot of total resistance R_T *vs*. interspacing (d) was constructed which is utilized to estimate the electrical parameters sheet resistance (R_{sh}), transfer length (L_T), contact resistance (R_c), and specific contact resistance (ρ_c) respectively. Thus, the IV curves were used to confirm the ohmicity of the contacts/current mechanism and for evaluating the various electrical parameters of the fabricated ohmic contacts of Au-based/In-based TLM structures [5,11,12,28,33].

(c) CV/IV measurement system

A low-temperature Cryo-prober (Keithley parametric analyzer, Model-4200 with integrated 4200-CUV card) system was used to perform the C-V measurement of fabricated ZnS-based MIS device. The photograph of the Cryo-prober is shown in Fig. 2.6.

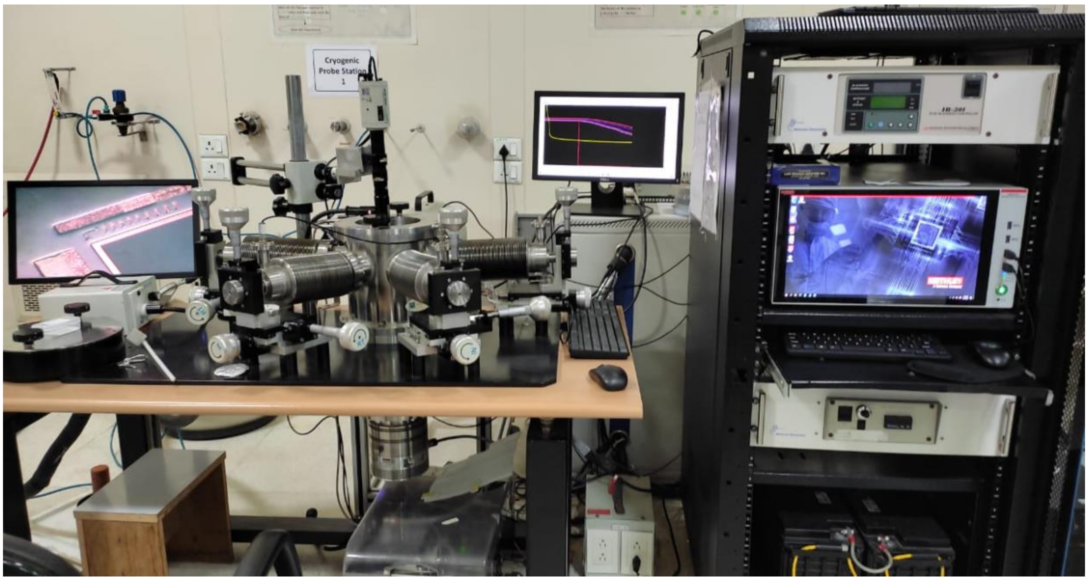

Figure 2.6. Keithley Cryo-prober to perform the CV/IV measurements of thermally grown MIS device (ZnS) and In-based/Au-based TLM structures.

The same system was also utilized to perform the current-voltage (I-V) measurements of In/HgCdTe-based TLM structure and Au/p-HgCdTe-based TLM structure for evaluating the electrical properties of Au/p-HgCdTe contact and In/n-HgCdTe contact, respectively.

2.3.5. Fourier transforms infrared (FTIR) spectroscopy

Fourier transforms infrared (FTIR) spectroscopy is an analytical technique that is used to evaluate the properties of materials (solid, liquid, and gas) with the help of infrared (IR) light. It has been utilized in many applications like measuring the reflection, transmission, and absorption of materials via shining a narrow IR beam of various wavelengths on the material. The response of each wavelength to the material is detected in the form of data (interferogram) which is converted into useful digital information by applying a mathematical algorithm termed the “Fourier transform” on it [35].

The main component of an FTIR spectrometer is a Michelson interferometer that consists of a broadband IR source, a beam splitter, a fixed mirror (M1), a moving mirror (M2), and an IR detector. When a collimated IR light/beam from the IR light source hits the beam splitter then it is split into two beams of equal amplitude. Continuously, one-half portion of the beam is reflected towards mirror M1 and the other half is transmitted via the beam splitter to mirror M2. Now, both the beams are reflected to the beam splitter from the corresponding mirrors and those light beams interact with each other for producing the constructive or destructive interference pattern accordingly since it depends on the path difference/phase difference (created by the changing the position of mirror M2) between the two returning light beams. This interference pattern is known as an interferogram that designates the intensity of the IR light beam/signal reaching the detector as a function of the path difference. In the end, one-half of the returning light is focused toward the IR detector for measuring the intensity of the interference pattern, and the rest half is transported back to the IR source. Finally, a plot of the intensity of the recombined beam as a function of the wavenumber is produced by applying a Fourier transform on the resultant interferogram, and for a well understanding, the wavenumber unit can also be changed to wavelength unit [35,36].

The FTIR Spectrometer system (model: Varian 680-IR, range = 0.5-100 μm, resolution = 0.01 cm^{-1}) was utilized to measure the reflection of thermally grown ARC film stacks over the HgCdTe-CdZnTe samples where the measurement was performed at room temperature (300 ± 3 K) and it is shown in Fig. 2.7.

Figure 2.7. FTIR spectrometer used for measuring the reflectance of thermally grown ARC film stacks (YF_3/ZnS/YF_3/ZnS/CdZnTe-HgCdTe).

2.3.6. Surface profiler

A surface profiler is an instrument that is used to measure the thickness and surface roughness of thin films. In the surface profiler, there is a diamond tipped-stylus of radius-12.5 µm which is moved vertically in contact with a sample and then moved horizontally across the sample's surface while the parameters like distance/scan length, speed, and contact force are programmed by the user. The stylus is attached to a linear variable differential transformer (LVDT) that can precisely measure the small surface variations (vertical displacement of the stylus as a function of height/position) and now those are changed into the form of an analog electrical signal. Sequentially, this signal is digitized, stored, displayed, and analyzed. The surface profiler can measure the thicknesses ranging from 10 nm to 65 µm [26,37,38] and the surface profiler (Model: Alpha Step* D-500) that was used to measure the thicknesses of thermally evaporated thin films is shown in Fig. 2.8.

Figure 2.8. Photograph of the surface profiler (Model: Alpha Step* D-500) used for measuring the thicknesses of thin films.

2.3.7. Ellipsometry

Ellipsometry is a well-known, reliable, sensitive, non-contact, and non-destructive optical measurement technique that can be used to evaluate the optical properties (like film thickness, refractive index, composition, and structure) of a sample material via the utilization of reflected light. It measures the alterations in the polarization state of the incident light (oblique incidence) to a surface/sample after its reflection/transmission from that sample's surface. The polarization state of a linearly polarized light (that incident to a surface at an oblique incidence angle of 40-90°) alters to an elliptically polarized light after its reflection from the sample's surface which is why it is termed" ellipsometry". Ellipsometry is usually used to measure the thickness of thin films grown on a substrate/sample. Since changes in the sample's thickness/ material composition lead to a change in its reflective properties. If the values of refractive indices of the substrate and film are known then ellipsometry is useful to evaluate the thin film thickness. Thus, ellipsometry has extensively been used for the investigation of materials as well as surfaces [39].

The well-known ellipsometric expressions can be written by equations 2.3 and 2.4 as follow:

$$\rho = \frac{r_p}{r_s} = \tan\Psi \cdot e^{i\Delta} \tag{2.3}$$

$$\Delta = \delta_p - \delta_s \tag{2.4}$$

Where the symbols r_p and r_s denote the parallel and perpendicular reflection coefficients respectively; which are taken concerning the plane of incidence. While tan Ψ and Δ represent the amplitude ratio as well as phase difference. Here δ_p and δ_s, represent the phase changes corresponding to the p and s components of light [39].

An ellipsometer (model: Gartner LSE-MS stokes microspot ellipsometer) with a He-Ne laser light source (single wavelength: 632.8 nm) was used to observe the HgCdTe sample's qualities (composition, oxide/impurity layers: presented on their top surfaces of samples and surface roughness) where the light has an oblique incidence angle of 70°. The experimental set-up/photograph is shown in Fig. 2.9. It consists of a sample-table (with a manual tilt and adjustable height), a laser beam (dia-15µm), a camera (to view the measuring area on a PC screen), and a manual XY micrometer. The laser light source is very beneficial because of its stability, spectral precision, and long lifetime. Thus, the ellipsometric measurement can be performed very precisely as well as rapidly using this advanced instrument that has no moving parts/no modulators.

Figure 2.9. Photograph of the ellipsometer used to examine the surface quality of HgCdTe samples.

2.3.8. Microscopy

This is one of the most popular/convenient characterization tools for the HgCdTe epilayers. The HgCdTe samples were immediately inspected by a Nomarski microscope in contrast imaging mode (since it provides higher resolution/better clarity than the conventional optical microscopy during the time of inspection) after performing their surface cleaning process and it was developed by the scientist ‘Georges Nomarski’ in the mid-1950s. This can deliver information about the planarity (through the variation of height/refractive index), 3D features/ macro-defects (within the sample’s surface like Te precipitates appearing at large crystallites and crosshatches: accountable for generating strain in the sample because of lattice mismatch), contaminations, and estimated surface roughness of the samples under testing/inspection. Thus, the Nomarski imaging mode is quite sufficient as a primary approximation to find out the defects and surface roughness of the samples [40].

Figure 2.10. Nomarski microscope used for the inspection of HgCdTe samples surfaces.

The experimental set-up/photograph of the microscope is shown in Fig. 2.10. It works on the concept of polarization according to which one polarized light beam is separated by a Wollaston prism while the polarized beam is created by a lamp and then passes through a polarizer that splits it into two orthogonally polarized beams. The split light beams travel into the sample's surface and recombine with each other via another Wollaston prism. If the parameters of the sample like thickness and reflective index are changed then an optical path difference between two beams will be created and the beams are unable to interfere with each other. When the beams are taken into the same plane via adding a polarizer to produce zero optical path difference between them (using a variable offset phase design); a spatial interference pattern is generated. This (the contrast) is recorded as the shear distance and marked in equivalent intensity/colour [41].

2.3.9. Non-contact sheet resistance measurement (eddy current technique)

The sheet resistance of the metal thin films can be realized via a non-destructive and non-contact eddy current technique which is based on Faraday's electromagnetic induction law. Faraday exposed that currents in an electrical conductor are induced by a time-varying magnetic induction flux density while the electromotive force is directly proportional to the time-rate change of the magnetic induction flux density [42].

Hence, when an alternating current (AC) flows in a coil then its time-varying magnetic field induces circulating/eddy currents within the sample under inspection /measurement. This measurement is the measurement of the material's electrical loss in which the measuring head/sensor moves above the sample (under measurement/test) at a constant height without making any physical contact/touch to the sample. The measured signal is a function of the sample's sheet resistance as well as a sample to probe distance while a built-in distance sensor (based on capacitance measurement) detects in a similar spot like an eddy sensor. Hence, the sheet resistance can be achieved via the measured values of distance and eddy signal. Continuously, the conductivity, as well as the chemical composition of the test sample, can also be revealed using this specific information. Thus, this non-destructive technique is very useful in the metal industry as well as in science for evaluating the properties of numerous materials without creating any damage [43].

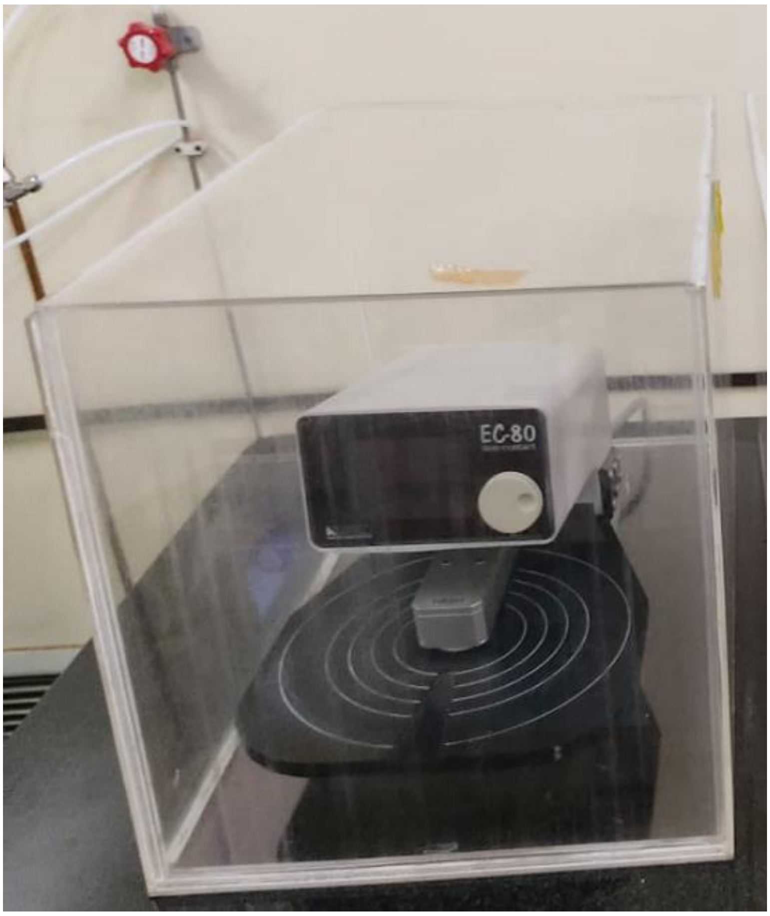

Figure 2. 11. Non-contact sheet resistance measurement system used to evaluate the sheet-resistance/conductivity of the thermally grown Au and In films on HgCdTe sample.

The non-contact sheet resistance measurement system (model: EC80) that was used to measure the sheet resistance/conductivity of thermally evaporated metal films (Au and In) is shown in Fig. 2.11.

References

[1] R. Nokhwal, V. Srivastav, A. Goyal, B. L. Sharma, S. A. Hashmi, and R. K. Sharma, Surface Studies on HgCdTe Using Non-aqueous Iodine-Based Polishing Solution, J. Electron. Mater. 46 (2017) 6795-6803.

[2] Yong-Chul Jung, Seok-Jin Yoon, Sang-Hee Suh, Jin-Sang Kim, The effect of ammonium sulfide treatment on interfacial properties in ZnS/HgCdTe heterostructure, J. Electroceram. 17(2006) 1041-1045.

[3] V. S. Meena, M. S. Mehata, Investigation of grown ZnS film on HgCdTe substrate for passivation of infrared photodetector, Thin Solid Films 731(2021)138751.

[4] J. Sun, L. Fu, Z. Nie, Y. Shi, L. Yapeng, The effect of chemical polishing on the interface structure and electrical property of Au/$Cd_{0.9}$ $Zn_{0.1}$Te contact, Appl. Phys. A 115 (2013) 1309-1316.

[5] V. S. Meena, M. S. Mehata, Thermally grown indium (In) thin-film for creating ohmic contact and In-bumps for HgCdTe-based IR detectors, Appl. Surf. Sci. 596 (2022)153501.

[6] K. Priya, V.K. Ashith, G.K. Rao, G. Sanjeev, A comparative study of structural, optical and electrical properties of ZnS thin films obtained by thermal evaporation and SILAR techniques, Ceram. Int. 43 (2017) 10487–10493.

[7] C.H. Sun, P. Zhang, T.N. Zhang, X. Chen, Y.Y. Chen, Z.H. Ye, ZnS thin films grown by atomic layer deposition on GaAs and HgCdTe substrates at very low temperature, Infrared Phys. Technol. 85 (2017) 280–286.

[8] N. Bouguila, D. Bchiri, M. Kraini, A. Timoumi, I. Halidou, K. Khirouni, S. Alaya, Structural, morphological and optical properties of annealed ZnS thin films deposited by spray technique, J. Mater. Sci. Mater. Electron. 26 (2015) 9845–9852.

[9] J. Jiang, S. Tsao, T. O'Sullivan, M. Razeghi, G. J. Brown, Fabrication of indium bumps for hybrid infrared focal plane array applications, Infrared Phys.Technol.45 (2004) 143–151.

[10] Q. Huang, G. Xu, Y. Yuan, X. Cheng and L. Luo, Development of indium bumping technology through AZ9260 resist electroplating, J. Micromech. Microeng. 20 (2010) 055035.

[11] B.K. Kim, T.H. Kim, D.H. Choi, H. Kim, K. Watanabe, T. Taniguchi, H. Rho, J.J. Kim, Y.H. Kim and M.H. Bae, Origins of genuine Ohmic van der Waals contact between indium and MoS_2, NPJ 2D Mater. Appl. 5 (2021) 9.

[12] A. Singh, A. K. Shukla, S. Jain, B. S. Yadav, R. Pal, Electrical characteristics of electroless gold contacts on p-type Hg1_xCdxTe, Mater. Sci. Semicond. Process. 26 (2014) 294–300.

[13] Y. Tang, Jia Jia, H. Qiao, Y. Zhang, X. Li, Application of Au/Sn in the formation of p-HgCdTe photoconductive detectors electrodes, 6th International Symposium on Advanced Optical Manufacturing and Testing Technologies: Optoelectronic Materials and Devices for Sensing, Imaging, and Solar Energy, Proc. of SPIE, 8419 (2012) 84190Z.

[14] Z. Tsybrii, Y. Bezsmolnyy, K. Svezhentsova, M. Vuichyk, I. Lysiuk, M. Apatska, M. Smolii, N. Dmytruk, S. Bunchuk, K. Andreeva, F. Sizov, HgCdTe/CdZnTe LPE epitaxial layers: from material growth to applications in devices, J. Cryst. Growth 529 (2019) 125295.

[15] G. Bahir, R. Adar, and R. Fastow, The electrical properties of metal contact Au and Ti on p type HgCdTe, J. Vac. Sci. Technol. B 9 (1991) 266.

[16] Y. Matsuoka, S. Mathonneire, S. Peters, and W. T. Masselink, Broadband multilayer anti-reflection coating for mid-infrared range from 7 µm to 12 µm, Appl. Opt. 57 (2018) 1645-1649.

[17] M. Gholampour, A. Miri, S. I. Karanian and A. Mohammadi, Design and fabrication of multi-layers infrared anti-reflection nanostructure on ZnS substrate, Acta Phys. Pol. A 136 (2019) 527-530.

[18] M. B. Kala, P. K. Bandyopadhyay, B. B. Nautiyal, Thorium free anti-reflection coating in MWIR region on silicon optics, Infrared Phys. Technol. 55 (2012) 409-411.

[19] A. Behranvand, M. D. Darareh, M. Jannesari, M. Mahdavi, Design and fabrication of PbTe/BaF_2 hydrophobic high-efficiency broad-band anti-reflection coating on Ge substrate in long-wave infrared region, Infrared Phys. Technol. 92 (2018) 163-165.

[20] F. Lemarquis, G. Marchand, and C. Amra, Design and manufacture of low-absorption ZnS–YF_3 anti-reflection coatings in the 3.5-16 µm spectral range, Appl. Opt. 37 (1998) 4239-4244.

[21] D. Suthar, S. Chuhadiya, R. Sharma, Himanshu and M. S. Dhaka, An overview on the role of ZnTe as an efficient interface in CdTe thin film solar cells: a review, Mater. Adv. 3 (2022) 8081.

[22] P. Rahi, Challenges in PVD technique (Thin film formation by thermal evaporation), Int. J. Adv. Res. Dev. 2 (2017) 30-37.

[23] J. T. Gudmundsson, A. Anders, and A. von Keudell, Foundations of physical vapor deposition with plasma assistance, Plasma Sources Sci. Technol. 31 (2022) 083001.

[24] O. O. Abegunde, E. T. Akinlabi, O. P. Oladijo, S. A. and A. U. Ude, Overview of thin film deposition techniques, AIMS Mater. Sci. 6 (2019) 174–199.

[25] P. A. Savale, Physical Vapor Deposition (PVD) Methods for Synthesis of Thin Films: A Comparative Study, Arch. Appl. Sci. Res. 8 (2016) 1-8.

[26] A.V. Rajgure, Synthesis and characterization of nanocrystalline ZnO gas sensor, PhD thesis, Solapur University, India, 2014.

[27] A. A. Bunaciu, E. G. Udristioiu, and H.Y. Aboul-Enein, X-Ray diffraction: Instrumentation and applications, Crit. Rev. Anal. Chem. 45 (2015) 289–299.

[28] D. G. Diso, Research and development of CdTe based thin film PV solar cells, PhD thesis, Sheffield Hallam University, 2011.

[29] A. K. Ghatage, S. G. Kanitkar, Characterization of materials by X-Ray diffraction, Int. J. Eng. Res. Technol. 8 (2019).

[30] J. A. Last, P. Russell, P. F. Nealey, and C. J. Murphy, The Applications of atomic force microscopy to vision science, Invest. Ophthalmol. Vis. Sci. 51 (2010) 6083–6094.

[31] K. W. Shinato, F. H. and Y. Jin, Principle and application of atomic force microscopy (AFM) for nanoscale investigation of metal corrosion, Corros. Rev.38 (2020) 423–432.

[32] M. Joshi, A. Bhattacharyya, S.W. Ali, Characterization techniques for nanotechnology applications in textiles, Indian J. Fibre Text. Res. 33(2008) 304-317.

[33] J. Zhang, A Fundamental study of interface effects in HgCdTe materials and devices, PhD thesis, The University of Western Australia, 2015.

[34] A. K. Saini, V. Srivastav, S. Gupta, B. L. Sharma, M. Asthania, N. Singh, S. K. Gaur, V. S. Meena, R. Thakur, Chanchal, V. Sharma, R. K. Sharma, Improvement of electrical properties of ZnS/CdTe-HgCdTe interface by (NH4)2S treatment, Infrared Phys. Technol. 102 (2019) 102988.

[35] K. T. Ojala, E. Koski, and M. J. Lampinen, Reflection and transmission measurements with an integrating sphere and Fourier-transform infrared spectrometer , Appl. Opt. 31(1992) 4582-4589.

[36] C. Xie, A novel monolithic focal plane array for mid-IR imaging, PhD thesis, The University of Glasgow, 2016.

[37] A. Piegari and E. Masetti, Thin film thickness measurement: A comparison of various techniques, Thin Solid Films 124 (1985) 249-257.

[38] B. J. Mrstik, P. J. McMarr, J. R. Blanco, J. M. Bennett, Measurement of the thickness and optical properties of thermal oxides of Si using spectroscopic ellipsometry and stylus profilometry, J. Electrochem. Soc. 138 (1991) 1770-1778.

[39] L. Z. Maulana, K. Megasari, E. Suharyadi, R. Anugraha, K. Abraha and I. Santoso, Inexpensive home-made single wavelength ellipsometer (λ = 633 nm) for measuring the optical constant of nanostructured materials, IOP Conf. Ser.: Mater. Sci. Eng. 202 (2017) 012031.

[40] I. Madni, Characterization of MBE-grown HgCdTe and related II-VI materials for next generation infrared detectors, PhD thesis, The University of Western Australia, 2017.

[41] M. B. Dowell, C. A. Hultman, and G. M. Rosenblatt, Determination of slopes of microscopic surface features by Nomarski polarization interferometry, Rev. Sci. Instrum. 48 (1977) 1491.

[42] W. Wejgaard and V. S. Tomar, Contactless measurement of electrical resistivity by eddy current methods: discussion and a new technique, J. Phys. E: Sci. Instrum.7 (1974) 395.

[43] J. García-Martín, J. Gómez-Gil and E. Vázquez-Sánchez, Non-destructive techniques based on eddy current testing, Sensors 11(2011) 2525-2565.

Chapter 3

Investigation of thermally evaporated ZnS film on HgCdTe substrate for passivation of infrared photodetector

3.1. Introduction

Infrared (IR) photodetectors have become a handy tool because of their various applications in the modern world. Currently, these are utilized in different sectors like defense (for night vision, weapons detection, and thermal imaging), remote sensing of earth and planetary, medical (diagnosing cancer and tumor), astronomy, environmental monitoring, and meteorology [1]. Various materials were used to fabricate infrared detectors, namely II-VI semiconductors, mercury cadmium telluride (HgCdTe), quantum well infrared photodetector (gallium arsenide/aluminium gallium arsenide, type-II superlattices (indium arsenide/indium gallium antimonide strained layer), etc. [2]. HgCdTe is one of the most popular, industrial, and matured materials for IR photodetector fabrication because it has a tunable energy bandgap for the spectral range of 1–30 μm. It can be used to fabricate detectors operating in various wavelength ranges like short-wavelength infrared (SWIR), mid-wavelength infrared (MWIR), and long-wavelength infrared (LWIR). The other specific properties of HgCdTe are composition-dependent high-quality layered material growth, high mobility, moderate dielectric constant, high sensitivity, large optical coefficients, high quantum efficiency (>70%), and fast response time (in nanosecond range), etc. HgCdTe is a highly suitable material to fabricate IR detectors of high quality, higher area format, and high resolution, which may be useful for current and future technology requirements [2–5].

---

[*] *Part of this work has been published in* ***Thin Solid Films 731 (2021) 138751 (Elsevier)***.

The detector array fabrication includes many unit steps like epilayer surface preparation, passivation, junction formation, metallization, indium bump growth, anti-reflection coating, etc. Surface passivation has an essential role in IR detector fabrication technology. The increasing dark current across the p-n junction is responsible for the degradation of the performance of the photodetectors. The detector performance can be improved significantly by using an appropriate passivation layer (film) with properties, i.e., well adhesion with the substrate, compatibility with the processing chemicals, stoichiometric compositions, insulating dielectric material, and electrically inert. The layer must protect the devices from environmental conditions (temperature, humidity, etc.). Different passivation materials have been used to fabricate HgCdTe-based IR detectors, namely anodic oxide, cadmium telluride (CdTe), zinc sulfide (ZnS), CdTe/ZnS, silicon oxide, silicon nitride, cadmium sulfide (CdS), etc. [4,6-9]. ZnS is the most commonly used passivation material for the HgCdTe-based detectors because it has nearly ideal properties that a passivation layer must possess, like insulating dielectric material, the low value of slow state density and fast state density (for the optimal band-bending at the surface), compatible with the HgCdTe layer, low stress, desired chemical and thermal stability [10-12]. Crystalline parameters of ZnS (cubic zinc-blend structure, lattice constant 5.409 Å) are well-matched with HgCdTe (cubic zinc blend structure, lattice constant 6.464 Å). Hence, ZnS is an excellent IR material that exhibits good compatibility with HgCdTe photodetector materials [13,14]. Some reports [15-17] present structural, morphological, and optical parameters of ZnS film grown over glass and HgCdTe substrates using various techniques, including atomic layer deposition (ALD), and implemented for various applications. These reports do not thoroughly study structural, morphological, compositional, mechanical, and electrical properties, which need to be explored further in device configurations.

In this chapter, ZnS films were grown on the HgCdTe substrate (epilayer or surface) by the thermal evaporation deposition method. Various characterization techniques evaluated the structural, morphological, and compositional parameters. The ZnS films were further used to fabricate the metal-insulator-semiconductor (MIS) device with the configuration of Au-Cr/ZnS/p-HgCdTe. Accordingly, capacitance-voltage (C-V) analysis was performed to investigate the electrical properties of the ZnS/HgCdTe-based MIS device. The study predicts that the quality of ZnS passivation film is acceptable as an efficient and suitable passivation layer for IR photodetector fabrication [18].

3.2. Material and methods

3.2.1. HgCdTe sample preparation and growth of ZnS film

The p-type $Hg_{1-x}Cd_xTe$ epilayers were grown on lattice-matched cadmium zinc telluride substrate (111) by the in-house vertical dipping liquid phase epitaxy (VD-LPE) growth method. The p-type $Hg_{1-x}Cd_xTe$ epilayers of the parameters (dimensions 25×25 mm^2; thickness 10 μm; composition x=0.29; carrier concentration 1×10^{16} cm^{-3} and carrier mobility 416 $cm^2 \times V^{-1} \times s^{-1}$) were used in this study of ZnS thin film. The HgCdTe epilayers (substrates) were carried out through a mechanical polishing process using an alumina powder (suitable abrasive) of 0.05 μm. Successively, a chemical-mechanical polishing was performed with the solution of (I_2:KI: $C_2H_6O_2$) :: (1 g :4 g: 10 mL) and a few drops of KOH. Then, de-ionized water and highly pure N_2 gas were used to wash and dry the epilayers. After this process, the surface quality of the substrate was examined with ellipsometry measurement. Immediately, HgCdTe epilayers were shifted into a vacuum chamber of the coating unit (MODEL: HHV 20F10) for the deposition of ZnS film. The ZnS crystals (purity of 99.99%, dimension of 6 mm and less) were put into the molybdenum boat. The distance between the source (evaporant) and the substrate was fixed to be 30 cm. The vacuum chamber was evacuated to a pressure of 2×10^{-7} Torr (2.6

$\times 10^{-5}$ Pa). Subsequently, ZnS films of thickness 300 ± 5 nm were grown on the samples (epilayers) with the optimized process parameters (deposition rate: 1.0-1.2 Å/sec, evaporation current: 60-65 A with a bias of 10 V). Processing parameters were optimized to get uniform, dense, and stoichiometric ZnS film with low roughness. The optimized deposition rate was 1.0-1.2 Å/sec, at which desired value of resistivity (8×10^{10} Ω·cm) of ZnS film was achieved. The deposition rate was monitored with an auto rate controller (supported by a quartz crystal) by adjusting the current from the power supply. The whole process of ZnS thin film formation was completed at room temperature (25 °C). The grown films were used for further investigation and applications.

3.2.2. Characterization techniques

A high-resolution X-ray diffraction system of PANalytical B.V.-X'Pert PRO MRD (Material research diffractometer) having a CuKα (λ=1.542 Å) radiation source and Xe-proportional counter was used to evaluate the structural parameters of ZnS film. X-ray diffractogram of the film was achieved by keeping the grazing angle fixed at 2° and varying the scanning range between 20-70°on on the 2θ drive axis. The morphology and compositional analysis of the grown thin films were carried out using Atomic Force Microscopy (AFM; Model-5600LS, AC Model III Module, Agilent Technologies) and Energy Dispersive X-rays (EDX; Model-FESEM Carl Zeiss SUPRA55VP with Oxford Instrument X-MAX EDS Spectrometer, Operating voltage: 5-12 kV) microanalysis system. C-V measurement of the ZnS-based MIS device was performed using a low-temperature Cryo-prober of Keithley parametric analyzer (Model-4200 with integrated 4200-CUV card), and C-V data for the individual capacitors of the device was recorded at a frequency of 1.0 MHz and temperature 80 ± 3 K.

3.3. Results and discussion

3.3.1. Structural characterization

Structural parameters of ZnS film have been investigated by the X-ray diffraction (XRD) technique. The XRD pattern of ZnS film grown over the HgCdTe substrate (epilayer) is shown in Fig. 3.1. Three diffractions peaks at 2θ of 28.62°, 47.98°, and 56.91° were observed in the diffractogram. The analysis of the diffraction peaks with an international diffraction data standard JCPDS indicates (111), (220), and (311) planes of ZnS. The first diffraction peak is more intense than the other two peaks. This reflects that ZnS is polycrystalline, having a preferred orientation along (111) plane. It also reveals the cubic zinc blend structure of ZnS. Besides these three peaks, a peak at 23.82° was also observed in the XRD pattern, which has been assigned to the (111) plane of the HgCdTe substrate.

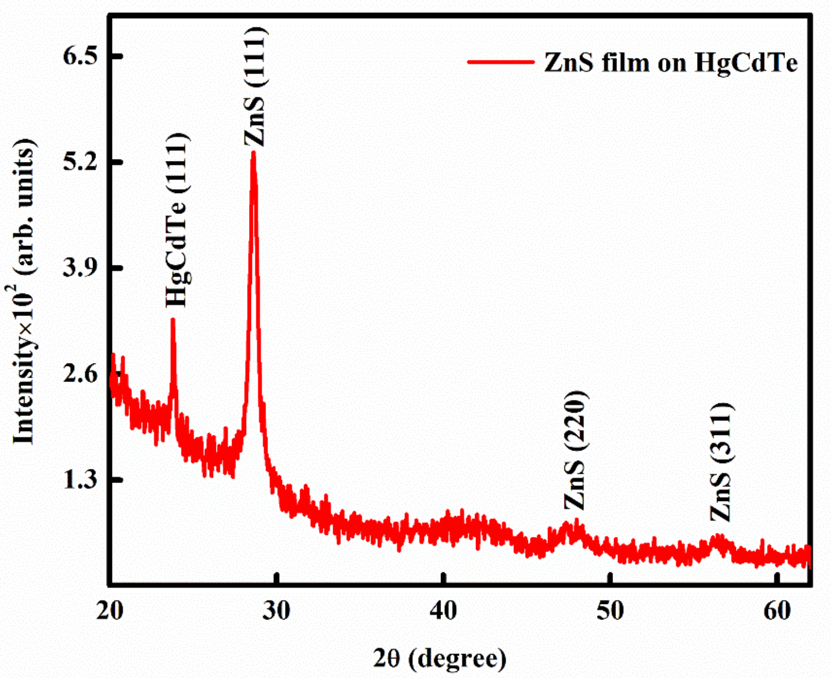

Figure 3.1. XRD diffractogram of ZnS thin film deposited on the surface of HgCdTe substrate.

The lattice constant (a) and interplanar distance (d) of ZnS were calculated from Eqs. (3.1) and (3.2) as given below [19,20]:

$$a = \frac{\lambda\sqrt{h^2+k^2+l^2}}{2\sin\theta} \quad (3.1)$$

$$d = \frac{a}{\sqrt{h^2+k^2+l^2}} \quad (3.2)$$

Where λ is the wavelength of the incident x-ray, θ is the diffraction angle and h, k, l represents the miller coordinates corresponding to crystalline planes. The details of the measured data (2θ, diffraction peaks, lattice plane and FWHM: full-width at half-maximum) and estimated XRD lattice parameters (d: interplanar spacing, a: lattice constant) are described in Table 3.1. The experimental and standard values of interplanar spacing and lattice constants are in good agreement, which indicates that the properties of ZnS films and bulk ZnS material are identical. Experimentally obtained values of lattice parameters (a and d) of thermally evaporated ZnS film were found to be relatively close to the reported values [20-23]. These_results further reveal that thermally evaporated ZnS film's crystalline properties are comparable to those of the ZnS films prepared by other techniques.

Table 3.1: Structural parameters obtained from XRD analysis of ZnS/HgCdTe sample and comparison of experimental *vs.* standard lattice parameters (**d**: interplanar spacing, **a**: lattice constant).

2θ (degree)	**Lattice plane (hkl)**	**FWHM (degree)**	**Experimental d (Å)**	**Standard d (Å)**	**Experimental a (Å)**	**Standard a (Å)**
28.62	(111)	0.59	3.121	3.123	5.407	5.406
47.98	(220)	1.91	1.897	1.912	5.366	5.406
56.41	(311)	2.08	1.631	1.633	5.410	5.406

It may be noted that the thermal evaporation technique is well established, which produces the film of desired crystalline quality. The average crystallite size (D) of ZnS film was estimated using Eq. 3.3 [24,25].

$$\mathrm{D} = \frac{0.94\lambda}{\beta \cos\theta} \tag{3.3}$$

Here, β is the FWHM of diffraction peaks and θ is the diffraction angle. The calculated values of β are shown in Table 3.1.

Strain (ε) of the grown film is defined as the ratio of $(\mathrm{a} - \mathrm{a}_0)/\mathrm{a}_0$, where a and a_0 are the lattice constants of ZnS film and bulk ZnS material, respectively. The value of ε was estimated from the following Eq. 3.4 [22,26].

$$\varepsilon = \frac{\beta}{4\tan\theta} \tag{3.4}$$

The length of dislocation lines per unit volume is termed dislocation density (δ), and it can be evaluated using Eq. 3.5 [22,26].

$$\delta = \frac{1}{\mathrm{D}^2} \tag{3.5}$$

D is the average crystallite size of the thin film. The stress of ZnS film can be evaluated using Eq. 3.6 [20].

$$\sigma_s = \frac{\mathrm{Y}(\mathrm{a}-\mathrm{a}_o)}{2\mathrm{a}_o\gamma} \tag{3.6}$$

where Y is Young's modulus of ZnS in GPa, which is 75 GPa, a is the measured value of lattice constant using XRD analysis, a_0 is the standard value of lattice constant (5.406 Å) for bulk material and γ represents the Poisson's ratio (0.28) for ZnS. The estimated values of structural parameters like lattice constant, average crystallite size, dislocation density, strain, stress, etc., of ZnS thin film for the preferred plane (111) are summarized in Table 3.2. Comparison of the calculated values of structural parameters (average crystallite size of 14.5 nm, dislocation density, strain, and stress) with the best-reported results [20-22,26] revealed that the achieved values of structural parameters are acceptable and favorable for a well-crystalline film. Thus, the structural parameters are closely related to the properties of a passivation film.

It is to be noted that the lattice constant of the deposited film closely matches the bulk ZnS material. Dislocation and stress generated at the HgCdTe-ZnS interface due to the lattice mismatch between HgCdTe- ZnS are within acceptable limits, which are the major factors that influence the magnitude of the interface trap density and fixed charge density present at the semiconductor-passivant interface.

Table 3.2: Structural parameters of ZnS thin film estimated for the preferred orientation plane (111).

Structural parameters	Estimated values
2θ (degree)	28.62
Lattice plane (hkl)	(111)
FWHM (degree)	0.59
The lattice constant, a (Å)	5.407
Average crystallite size, D (nm)	14.5
Dislocation density, δ ($\times 10^{11}$ Line.cm^{-2})	4.7
Strain, ε ($\times 10^{-4}$)	6.55
Stress, σ_s (GPa)	0.113

Thus, ZnS film's structural properties enable us to determine that this may be a strong passivation material having good compatibility with HgCdTe.

3.3.2. Morphological analysis

The surface morphology of thermally deposited ZnS film is being analyzed with the AFM method. The AFM images (2 and 3-dimensional) of ZnS film (thickness: 300 nm, scanning area: 2.01 μm × 2.01 μm) are shown in Figs. 3.2 and 3.3, respectively. The AFM images revealed that the grown thin film contains many high-density islands separated by small paddy-like crystallites. These crystallites are uniformly distributed over the surface. The measured root-mean-square (rms) roughness of ZnS film is 1.6 ± 0.05 nm. This value of *rms* roughness of ZnS thin film is quite close to earlier reported values [22,27].

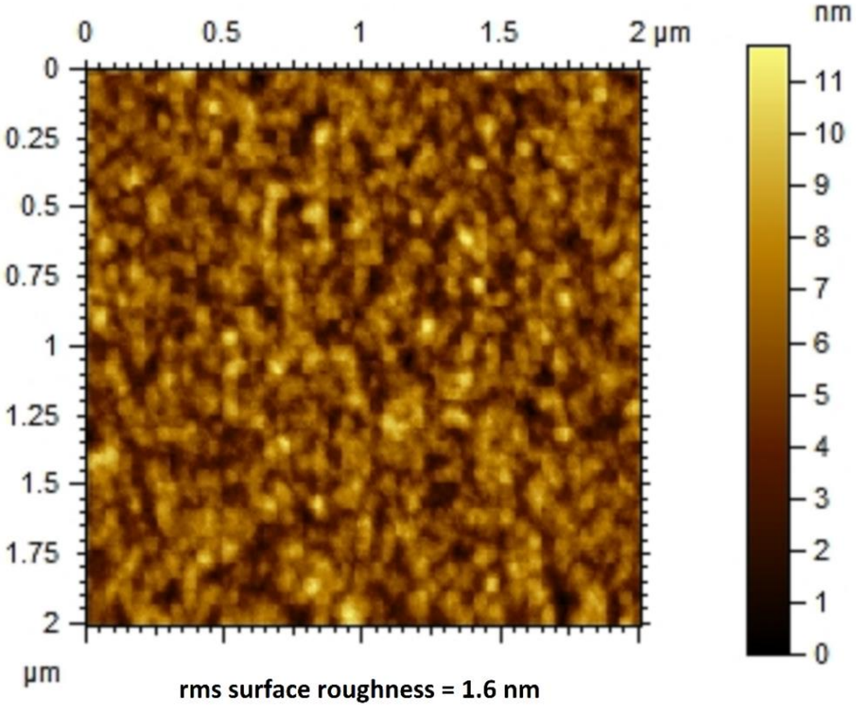

Figure 3.2. AFM image (2-dimensional) of ZnS thin film deposited on the surface of HgCdTe substrate.

The measured rms roughness value also shows its dominance over the rms roughness values of thin film deposited on HgCdTe substrate by ALD and thermal evaporation methods [17]. It can be motioned that the ZnS film is uniform, densely packed, and smooth (low roughness), which emphasizes that the morphological parameters of ZnS thin film could be acceptable for device fabrication since the surface morphology is essential for the quality and performance (in terms of electrical parameters) of the fabricated device. The electrical results of the MIS device also confirm the excellent surface morphology of ZnS thin film that can be used as a passivation agent.

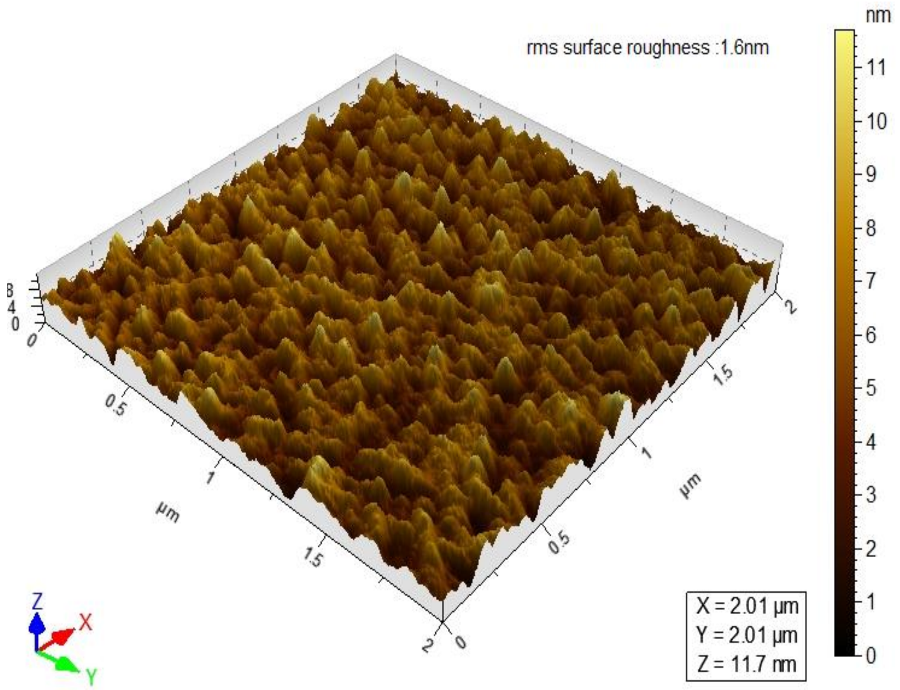

Figure 3.3. AFM image (3-dimensional) of ZnS thin film deposited on the surface of HgCdTe substrate.

3.3.3. Compositional analysis

The EDX analysis determines the chemical composition of ZnS thin films prepared on the HgCdTe surface. A typical EDX spectrum of the thin film is shown in Fig. 3.4. The spectrum shows peaks corresponding to the Zn and S elements. Approximately equal counts of Zn and S elements in the spectrum indicate that the film is stoichiometrically good. The obtained experimental values reveal that the thin film has two elements, Zn (51 %) and S (49 %) in its composition. The average Zn/S ratio for this film is 1.04, which further confirms its better stoichiometric composition. Various reports [28,29] described that the thermally evaporated ZnS thin films have nonstoichiometric compositions due to the vapor pressure difference between their constituent elements Zn and S. However, in the present case, the obtained stoichiometry result is comparable to the best-reported stoichiometry result [21] of ZnS thin film developed by the thermal evaporation vacuum technique. Several reports [20,30] support compositional uniformity (stoichiometry) of the thermally grown thin film.

Since nonstoichiometric and contaminated passivation films [31] create electrically active defects in the passivation semiconductor interface region, which are generally responsible for increased dark current, weak signal level, and more noise in the fabricated photodetectors, due to this, the photodetector performance degraded.

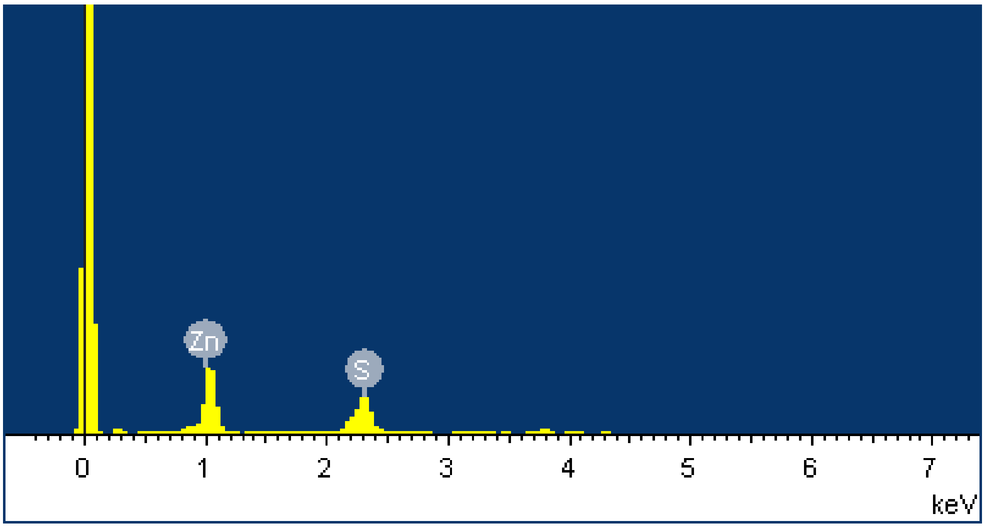

Figure 3.4. EDX spectrum of ZnS thin film grown on the surface of the HgCdTe sample.

Hence, it is necessary to maintain the stoichiometry of the passivation film during the deposition process. The electrical characterization of ZnS/HgCdTe-based MIS device reveals that the calculated value of densities of fixed charges and slow interface traps are in good agreement with earlier reported results of the photodetector. It concludes that the prepared ZnS film has excellent stoichiometry, which is essential for passivation film.

3.3.4. Electrical measurement of ZnS/HgCdTe based MIS device

The electrical properties of the ZnS thin film were obtained with a C-V measurement of a ZnS/HgCdTe-based MIS device. For performing MIS device fabrication, at first, the HgCdTe sample (surface) was treated with the iodine (I_2)-potassium iodide (KI) and dried with highly pure N_2 gas. Now thin film of ZnS (300 ± 5 nm) was grown on the HgCdTe sample. Gate metal contacts in the form of circular dots of Cr (30 ± 0.5 nm), Au (200 ± 4 nm) with dia of 200 μm were formed on ZnS/HgCdTe surface by thermal evaporation, where the ultimate vacuum is of the order of 1 × 10^{-6} Torr (1.3 × 10^{-4} Pa). The same metals (Cr-Au) were also used to form p-contact (ohmic contact) on the HgCdTe sample. The schematic of the fabricated MIS device is shown in Fig. 3.5. A cryo-prober was used for the C-V measurement of the MIS device.

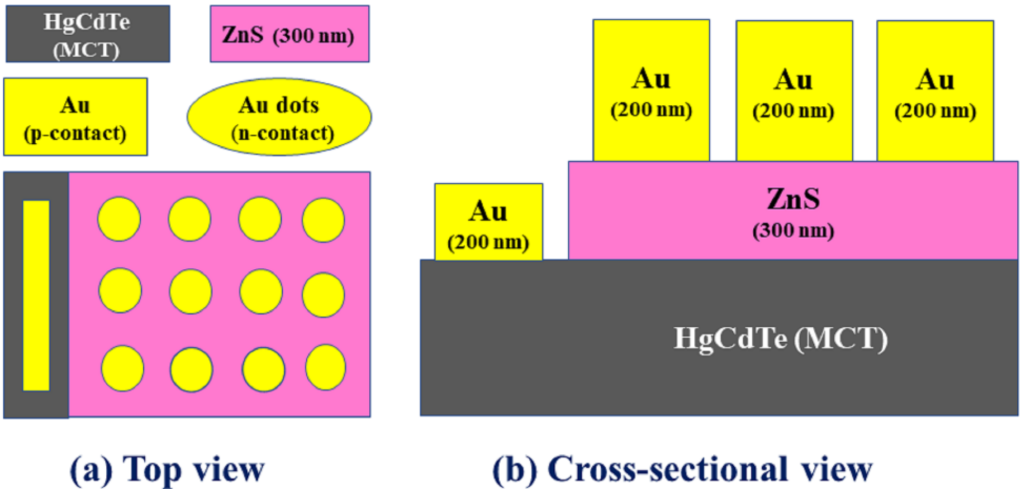

(a) Top view

(b) Cross-sectional view

Figure 3.5. Schematic of fabricated MIS device (Au-Cr/ZnS/p-HgCdTe, x=0.29), the top view (a) and cross-sectional view (b).

The C-V characteristics for different MIS capacitors were obtained at a frequency of 1.0 MHz, temperature 80 ± 3 K, and ac voltage (rms) of 30 mV. Each capacitor of the MIS device was swept by a DC bias of ranges from 5.0 to -3.0 V and -3.0 V to 5.0 V. The resulting C-V characteristics of typical capacitors are shown in Figs. 3.6 and 3.7, respectively. The extraction of parameters can be done by comparing the resulting C-V curve with the standard theoretical curve, as mentioned in MIS theory [32,33]. From the experimental curve (Fig. 3.6), the flat band voltage (V_{FB}) was obtained to be -0.2 V, which can be further utilized to evaluate the fixed charge density. The calculated value of the fixed charge density is 4.98 × 10^{10} cm^{-2}. The hysteresis in the C-V curve can be estimated from the width of the loop of the measured C-V curve at flat band voltage. Fig. 3.7 shows that the measured hysteresis width of the curve is 0.32 V and the calculated value of slow state density is 4.22 × 10^{10} cm^{-2}. Thus, the resulting fixed charge density and slow state density for the prepared MIS device were found within the acceptable or comparable limit of the best-reported values of p-HgCdTe-based IR detectors [30,34,35], since the surface passivated film has a crucial role in deciding the performance of photodetectors.

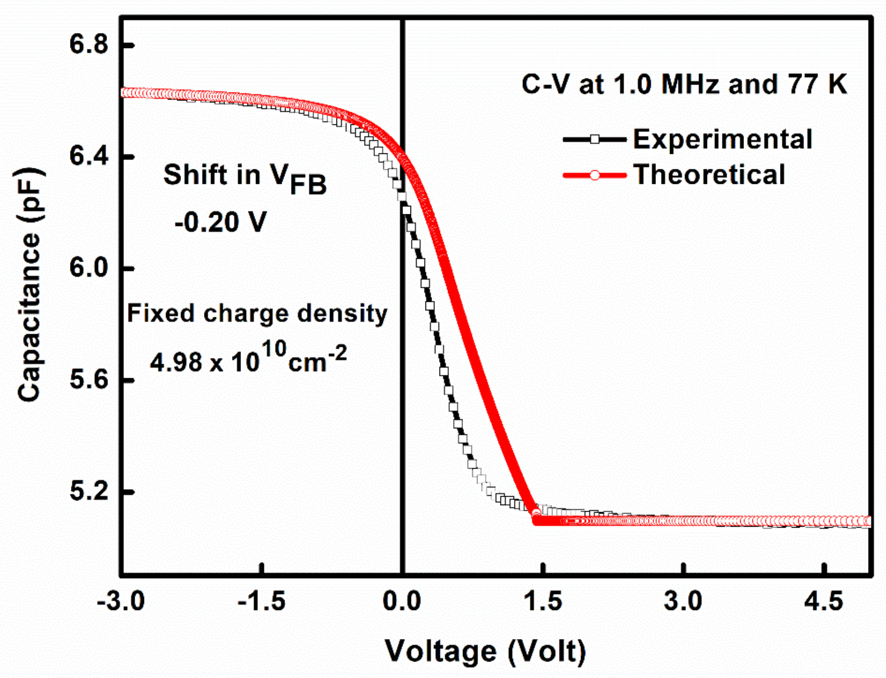

Figure 3.6. Experimentally measured C-V characteristics of the MIS device (Au-Cr/ZnS/p-HgCdTe, x = 0.29) along with the theoretically estimated C-V curve.

A layer consisting of a high density of fixed charges and slow states is generally responsible for increasing the dark current and noise level in the infrared photodetector, causing the degradation of photodetector performance [35]. As the resulting value of fixed charge density is relatively low, thus, the dark current (leakage current) of the p-type HgCdTe-based IR device is small. On the other hand, the hysteresis existence in the C-V curve is due to the slow traps (slow states) residing within the insulating passivation layer. The obtained slow state density, which is very low in the presented system, reduces the photo detector's noise level.

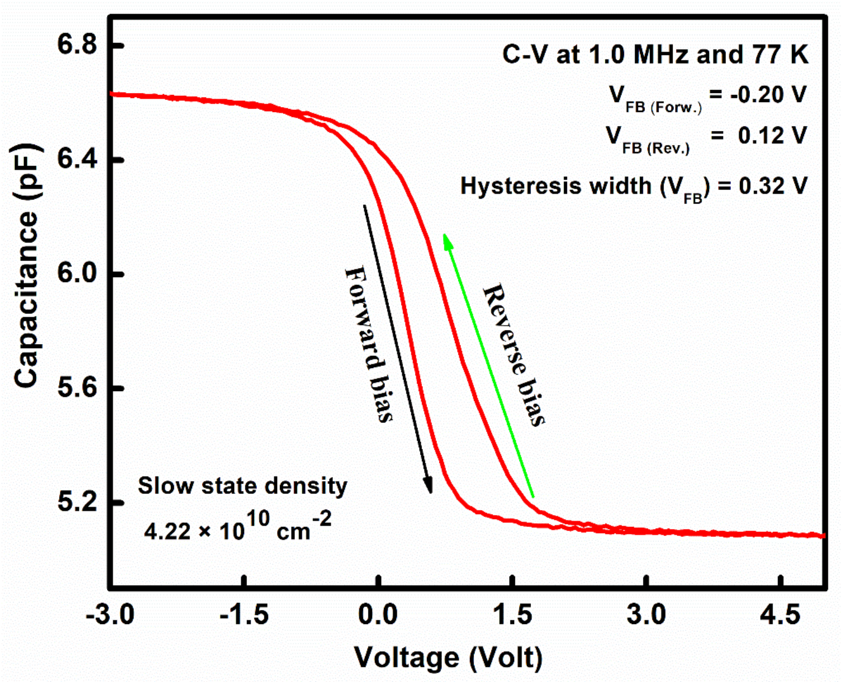

Figure 3.7. The experimentally measured value of hysteresis width and slow state density of the MIS device (Au-Cr/ZnS/p-HgCdTe, x = 0.29).

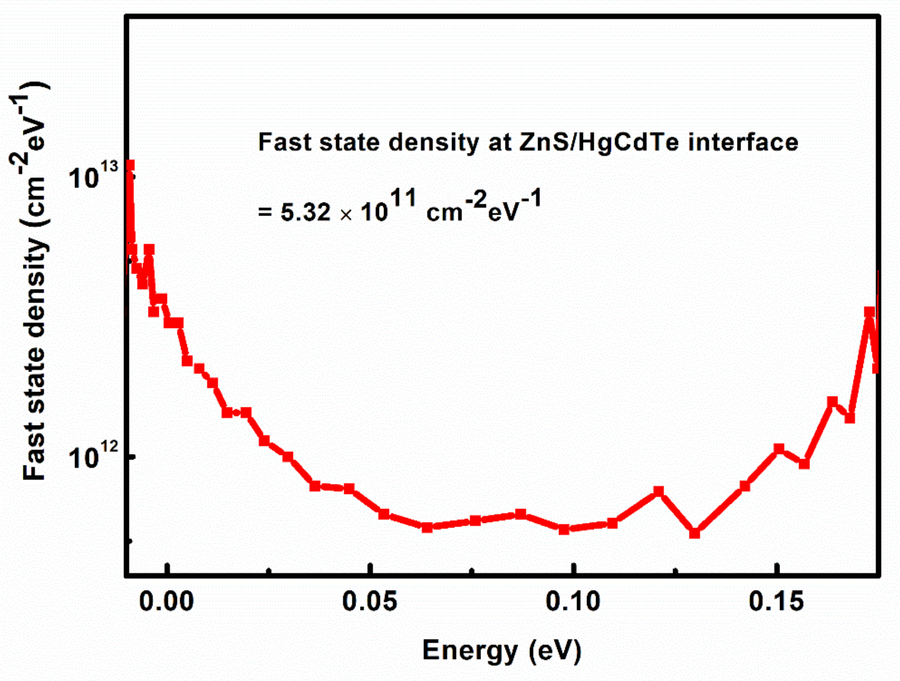

Figure 3.8. The experimentally measured value of fast interface states as a function of energy for MIS device (Au-Cr/ZnS/p-HgCdTe, x = 0.29). Distribution of fast interface states (fast state density) at ZnS/HgCdTe interface determined by Terman method (using C-V analysis results of HgCdTe based MIS device).

The distribution function of fast interface states (interface trap) at the ZnS/HgCdTe interface can be derived by the Terman method [36,37] using the experimental C-V characteristics. The distribution of fast interface states is shown in Fig. 3.8, and it is clear from the curve that the minimum value of interface trap density (fast state density) at mid energy gap is 5.32×10^{11} cm^{-2} eV^{-1}. This result is quite close to the result reported for the MIS device of the HgCdTe substrate, which was passivated with thin CdS film [38]. Thus, the ZnS film may be used as a suitable passivation material for the HgCdTe-based detector fabrication.

3.3.5. Testing of ZnS film's adhesion and its compatibility for HgCdTe device fabrication

The tape test of ZnS film confirmed its good strength of adhesion on the HgCdTe surface. ZnS film is also compatible with the PLG Lift-off process of device fabrication.

3.4. Conclusions

The work describes a study of the thermally deposited crystalline ZnS films on the HgCdTe epilayer. The structural measurement confirmed the cubic structure of polycrystalline ZnS films and the preferred orientation along the (111) direction. The surface morphology indicates that the film is uniform, dense, and of low roughness. The atomic ratio of Zn/S in the grown film is 1.04, confirmed by EDX analysis. The calculated values of fixed-charge density, slow state density, and fast state density are 4.98×10^{10} cm^{-2}, 4.22×10^{10} cm$^{-2,}$ and 5.32×10^{11} cm^{-2} eV^{-1}, respectively. The ZnS film has good adhesion with HgCdTe and is also compatible with the PLG lift-off process of device fabrication. Thus, based on the parameters (structural, morphological, compositional, and electrical), the ZnS films qualify all the conditions followed by a good passivation film. Hence, it could be an effective passivation agent for HgCdTe-based IR photodetector fabrication.

References

[1] C. Downs, T. Vandervelde, Progress in Infrared Photodetectors Since 2000, Sensors. 13 (2013) 5054–5098.

[2] A. Rogalski, Recent progress in infrared detector technologies, Infrared Phys. Technol., 54 (2011) 136–154.

[3] C.L. Tan, H. Mohseni, Emerging technologies for high performance infrared detectors, Nanophotonics 7 (2018) 169–197.

[4] A. Rogalski, Infrared detectors: Status and trends, Prog. Quantum Electron. 27 (2003) 59–210.

[5] A. Rogalski, J. Antoszewski, L. Faraone, Third-generation infrared photodetector arrays, J. Appl. Phys. 105 (2009) 91101.

[6] R. Singh, A.K. Gupta, K.C. Chhabra, Surface passivation of mercury-cadmium-telluride infrared detectors, Def. Sci. J. 41 (1991) 205–239.

[7] W. Lei, J. Antoszewski, L. Faraone, Progress, challenges, and opportunities for HgCdTe infrared materials and detectors, Appl. Phys. Rev. 2 (2015) 041303.

[8] M.S. Mehata, R.K. Ratnesh, Luminescence properties and exciton dynamics of core-multi-shell semiconductor quantum dots leading to QLEDs, Dalt. Trans. 48 (2019) 7619–7631.

[9] Y. Nandan, M.S. Mehata, Wavefunction Engineering of Type-I/Type-II Excitons of CdSe/CdS Core-Shell Quantum Dots, Sci. Rep. 9 (2019) 2.

[10] Y. Nemirovsky, D. Rosenfeld, R. Adar, A. Kornfeld, Tunneling and dark currents in HgCdTe photodiodes, J. Vac. Sci. Technol. A Vacuum, Surfaces, Film. 7 (1989) 528–535.

[11] Y. Nemirovsky, R. Adar, A. Kornfeld, I. Kidron, Gate-controlled $Hg_{1-x}Cd_xTe$ photodiodes passivated with native sulfides, J. Vac. Sci. Technol. A Vacuum, Surfaces, Film.4 (1986) 1986–1991.

[12] Y. Nemirovsky, G. Bahir, Passivation of mercury cadmium telluride surfaces, J. Vac. Sci. Technol. A Vacuum, Surfaces, Film. 7 (1989) 450–459.

[13] P.W. Kruse, The Emergence of $Hg_{1-x}Cd_xTe$ as a Modern Infrared Sensitive Material, Semicond. Semimetals. 18 (1981) 1–20.

[14] A.H. Johnstone, CRC Handbook of Chemistry and Physics-69th Edition Editor in Chief R. C. Weast, CRC Press Inc., Boca Raton, Florida, 1988, pp. 2400.

[15] R.K. Bhan, V. Srivastava, R.S. Saxena, L. Sareen, R. Pal, R.K. Sharma, Improved high resistivity ZnS films on HgCdTe for passivation of infrared devices, Infrared Phys. Technol.53 (2010) 404–409.

[16] K. Benyahia, A. Benhaya, M.S. Aida, ZnS thin films deposition by thermal evaporation for photovoltaic applications, J. Semicond. 36 (2015) 103001.

[17] C.H. Sun, P. Zhang, T.N. Zhang, X. Chen, Y.Y. Chen, Z.H. Ye, ZnS thin films grown by atomic layer deposition on GaAs and HgCdTe substrates at very low temperature, Infrared Phys. Technol.85 (2017) 280–286.

[18] V. S. Meena, M. S. Mehata, Investigation of grown ZnS film on HgCdTe substrate for passivation of infrared photodetector, Thin Solid Films 731(2021)138751.

[19] S.Z. Rahchamani, H.R. Dizaji, M.H. Ehsani, Study of structural and optical properties of ZnS zigzag nanostructured thin films, Appl. Surf. Sci. 356 (2015) 1096–1104.

[20] Y.P.V. Subbaiah, P. Prathap, K.T.R. Reddy, Structural, electrical and optical properties of ZnS films deposited by close-spaced evaporation, Appl. Surf. Sci. 253 (2006) 2409–2415.

[21] K. Priya, V.K. Ashith, G.K. Rao, G. Sanjeev, A comparative study of structural, optical and electrical properties of ZnS thin films obtained by thermal evaporation and SILAR techniques, Ceram. Int. 43 (2017) 10487–10493.

[22] P. Chelvanathan, Y. Yusoff, F. Haque, M. Akhtaruzzaman, M.M. Alam, Z.A. Alothman, M.J. Rashid, K. Sopian, N. Amin, Growth and characterization of RF-sputtered ZnS thin film deposited at various substrate temperatures for photovoltaic application, Appl. Surf. Sci. 334 (2015) 138–144.

[23] M.H. Doha, M.J. Alam, J. Rabeya, K.A.M.H. Siddiquee, S. Hussain, O. Islam, M.A. Gafur, S. Islam, N. Khatun, S.H. Sarkar, Characterization of chemically deposited ZnS thin films on bare and conducting glass, Optik 126 (2015) 5194–5199.

[24] J. Kennedy, P.P. Murmu, P.S. Gupta, D.A. Carder, S. V. Chong, J. Leveneur, S. Rubanov, Effects of annealing on the structural and optical properties of zinc sulfide thin films deposited by ion beam sputtering, Mater. Sci. Semicond. Process. 26 (2014) 561–566.

[25] P. Prathap, Y.P.V. Subbaiah, K.T. Ramakrishna Reddy, R.W. Miles, Influence of growth rate on microstructure and optoelectronic behaviour of ZnS films, J. Phys. D. Appl. Phys. 40 (2007) 5275–5282.

[26] N. Bouguila, D. Bchiri, M. Kraini, A. Timoumi, I. Halidou, K. Khirouni, S. Alaya, Structural, morphological and optical properties of annealed ZnS thin films deposited by spray technique, J. Mater. Sci. Mater. Electron. 26 (2015) 9845–9852.

[27] X. Wu, F. Lai, L. Lin, J. Lv, B. Zhuang, Q. Yan, Z. Huang, Optical inhomogeneity of ZnS films deposited by thermal evaporation, Appl. Surf. Sci. 254 (2008) 6455–6460.

[28] D.H. Hwang, J.H. Ahn, K.N. Hui, K.S. Hui, Y.G. Son, Structural and optical properties of ZnS thin films deposited by RF magnetron sputtering, Nanoscale Res. Lett. 7 (2012) 26.

[29] B. D. Cullity, Elements of X-Ray Diffraction, Addison-Wesley Publishing Company, Inc., Boston, 1956.

[30] P. Xu, G. Xu, K. Chu, N. Wang, Q. Zhou, Y. Tang, K. Zhang, X. Li, Properties study of ZnS thin films deposited on HgCdTe substrate by different methods, Proc. SPIE, Int. Symp. Photoelectronic Detection Imaging 2013: Infrared Imaging Appl. 8907 (2013) 890742.

[31] V. Kumar, R. Pal, P.K. Chaudhury, B.L. Sharma, V. Gopal, A CdTe passivation process for long wavelength infrared HgCdTe photo-detectors, J. Electron. Mater. 34 (2005) 1225–1229.

[32] S.M. Sze, Physics of Semiconductor Devices, John Wiley & Sons Inc., New York, 1982.

[33] H.Wieder, MOS (Metal Oxide Semiconductors) Physics and Technology by E. H. Nicollianand J. R. Brews. , Journal of Vacuum Science and Technology, 21 (1982) 1048–1049.

[34] J.K. White, C.A. Musca, H.C. Lee, L. Faraone, Hydrogenation of ZnS passivation on narrow-band gap HgCdTe, Appl. Phys. Lett. 76 (2000) 2448–2450.

[35] Y.C. Jung, S.Y. An, S.H. Suh, D.K. Choi, J.S. Kim, Ammonium sulfide treatment of HgCdTe substrate and its effects on electrical properties of ZnS/HgCdTe heterostructure, Thin Solid Films. 483 (2005) 407–410.

[36] L.M. Terman, An investigation of surface states at a silicon/silicon oxide interface employing metal-oxide-silicon diodes, Solid State Electronics 5 (1962) 285.

[37] N. Novkovski, Modification of the Terman method for determination of interface states in metal-insulator-semiconductor structures, J. Phys. Commun. 1 (2017) 035006.

[38] R.R. Singh, D. Kaushik, D. Gupta, R.K. Sharma, R.K. Pandey, Investigation of Passivation Processes for HgCdTe/ CdS structure for Infrared application, Thin Solid Films 510 (2006) 235– 240.

Chapter 4

Study of thermally evaporated indium (In) thin-film for creating ohmic contact and In-bumps for HgCdTe-based IR detectors

4.1. Introduction

The most remarkable progressive infrared (IR) technologies have proposed various photon and thermal detectors as a function of their performance, spectral range, and working temperatures. IR materials like type II superlattices (T2SLs), lead salt alloys, InSb, and quantum well-infrared photodetector (QWIP) exist. But mercury cadmium telluride (HgCdTe) is still a leading IR detector material among high-performance IR materials. It has been used to fabricate hybrid IR focal plane arrays (FPA), which operate in various spectral regions lying between 3 -14 μm wavebands of the IR spectrum. IRFPAs (IR detectors) have numerous applications like night-vision, missile tracking, environmental sensing, fires control, medical imaging, etc. [1-4]. The successful operation of electronic and optoelectronic devices is possible when the ohmic contact of devices has low resistance to work at lower voltages with the least power dissipation. This results in improved efficiency and reduced operating temperatures. An effective ohmic contact formation occurs when the height and width of the interfacial barrier are minimal so that the current transport can be dominated through a huge tunneling component**.** This is easy to form the ohmic metallic contact on elemental semiconductors, but in compound semiconductors, it is relatively more challenging since pinning of Fermi level in the mid-gap region leads to the generation of high interfacial barrier width [4-6].

---

[*] *Part of this work has been published in* ***Applied Surface Science 596 (2022)153501 (Elsevier)***.

Although such ohmic contacts on n-type HgCdTe are required for the detectors, which are used for production purposes only. Since HgCdTe is a fragile material (due to its weak HgTe bond), when the metals are deposited on HgCdTe at room temperature, there may be a lattice disruption that causes intermixing. The local impurity levels are generated in HgCdTe due to diffusion of high energy (several eVs) metal atoms into HgCdTe surface (decomposition of HgCdTe occurs particularly, HgTe). The inverse diffusion of components of HgCdTe (Hg, Te) substrate into the metallic layer creates an accumulation at the HgCdTe/metal interface responsible for a band bending in the surface layer. These factors (doping and accumulation) may alter the electrical properties of the metallic contact in terms of contact degradation, thermal instability (during packaging and usage), and timely surface dissociation. The threshold characteristics of photodetectors are defined by the electrical contacts with low noise levels [2,5].

Various metal schemes have been proposed [3-5] in the form of single/double/triple metal layers to form ohmic electrical metal contact on HgCdTe-based IR photodetector/devices like Cr, In, Al, Au, Ti, Ni, etc. Raisanen et al. [3] have applied a simple metal/Yb/ HgCdTe or transition metal/Yb/HgCdTe) scheme for the formation of stable ohmic contact where the Yb interlayer acts as an active diffusion barrier to reduce the factors like metal-Te interaction, out-diffusion of Te, and depletion of Hg near-surface region. A report has suggested [6] the use of indium (In-100 nm) to achieve good ohmic contact for the In/n-ZnSe interface [3,5-7]. The other reported ohmic contact schemes are In/n-HgCdTe, HgTe/In (30 nm)/Au (200 nm)/HgCdTe, Ti/Pt/Au/HgCdTe and organic (3,4-polyethylene-dioxythiophene) poly (styrene sulfonate) (PEDOT: PSS) /HgCdTe [4,8-10]. The I-V characteristics of all interfaces were ohmic except PEDOT: PSS /n-type HgCdTe interface, which has shown a weak rectifying behaviour [10]. The HgCdTe-based injection laser (light-emitting device) was fabricated using the n type-In (1.4 µm) metal layer with well-behaved electrical characteristics. Similarly, In and In (20 nm)/indium tin oxide (ITO-200 nm) based metal schemes were implemented for realizing high-quality ohmic contacts on InGaN light-emitting diodes (LEDs). The specific contact resistances of In and In (20 nm)/ITO (200 nm) based interface were found to be 2.2 x 10^{5} $\Omega\cdot\text{cm}^{2}$, $1.8 \times 10-3$ $\Omega\cdot\text{cm}^{2,}$ respectively [11-13]. Palimar *et al.* [14] have attained a smooth surface topography for the metallic indium/indium oxide/ZnO interface.

Two-layered metal contacts (Mo/Au and Mo/In contacts) were utilized in the fabrication of different IR detectors (Mo/Au contact: ohmic contact in discreet detectors, Mo/In contact: indium bumps for multielement FPA) as reported in the literature [2]. The recent report [15] states that the ultraclean ohmic van der Waals (vdW) contacts on molybdenum disulphide (MoS_2) were fabricated using the thermally grown (In -100 nm) film, where the specific contact resistance (ρ_c) of In/MoS_2 interface was $5.0 \times 10^{-6} - 5.0 \times 10^{-7}$ $\Omega\cdot\text{cm}^{2}$ with a uniform surface morphology of In film. Therefore, indium (In) is a well-known material to form ohmic contact on n-type HgCdTe. The electrical properties of metallic contacts are associated with the deposition conditions, substrate/metal interaction, surface treatments (during processing), etc. So, the formation of ohmic electric contacts to HgCdTe-based photodetector can be accomplished by maintaining the factors like a low-temperature deposition, metallic layer with high adhesion, and low noise level [2,15].

The requirement for high-performance IRFPAs is continuously increasing in the current scenario of the technological world, and it is associated with their fabrication steps. There are many processing steps in IRFPA fabrication, including interconnection (integration) of FPA with Si read-out integrated circuits (ROICs), which is one of the major steps responsible for the performance of FPA. The interconnection may be performed by various techniques like wire bonding and flip-chip bonding [16,17], but

Flip-chip bonding technology is the leading (efficient) one that has been frequently used to achieve high performance as well as miniature products since there is a maximum possibility of interconnections between every pixel to a-Si- ROIC in this technology compared to the wire bonding technique [16-19]. Various types of bump materials have been used for the interconnection of HgCdTe and ROIC, like Cu/Ni/Sn-based bumps, under-bump metallurgy (UBM) based bumps (Ti/Pt/Au/In, Ti/Pt/Au/Ep /In), and indium-based bumps (different height of bumps like 4 μm, 6 μm), etc. The films of (In-Sb)/ (In-Mo foil) having desired crystalline properties (continuous, smooth, dense, low roughness, electronic grade purity of In (1 μm)/Mo foil interface) were also applied in the IR detector fabrication [16,17,19-23].

Indium is an attractive interconnection material because of its features like cryogenic stability, appropriate mechanical and electrical properties, high ductility/malleability, low melting point (156 °C), excellent plasticity/easy cold-welding, relative easiness of small solder bumps formation (high-density interconnections), etc. [17-19,21]. The indium bump formation is a process in which the ball-shaped indium columns are grown on detector/ROIC under the effect of surface tension of the melted In-metal. Accordingly, the indium bumps must have the properties like uniformity, small diameter, tall bump, small pitch, minimum defects in pixels, optimum thermal expansion mismatch, low-temperature bonding, etc., [17-19,24,25]. Thus, IR detectors with high reliability and performance can be fabricated by generating ohmic metal contact on the HgCdTe substrate and high-density interconnection indium bumps (HgCdTe -detector with Si-ROIC). There is no available study of the indium/HgCdTe structure, including all structural, compositional, morphological, and electrical properties.

In the present research work [26], an effort has been made to cover all the issues mentioned above and achieve the theme's goal. Accordingly, indium (In) metal films were deposited over HgCdTe samples using the thermal evaporation technique. Numerous characterization techniques like X-ray diffraction (XRD), energy dispersive x-ray (EDX), Atomic force microscopy (AFM), and Scanning electron microscopy (SEM) were applied to evaluate the properties of thermally grown In films. The results reveal that the grown In films are optimized and employed in fabricating In bumps (configuration: In/n-HgCdTe) and Transfer length method (TLM, configuration: In/n/p-HgCdTe) structures. The microstructural parameters of the (In bumps/HgCdTe) interface were evaluated by SEM analysis. The fabricated TLM structure has been examined through current-voltage (I-V) and resistance measurements. The resultant electrical parameters of In/HgCdTe interface show ohmic behaviour with low contact resistance. Accordingly, the findings of thermally evaporated In films enable us to conclude that this is the most suitable material for forming ohmic contact and indium-bump (flip-chip bonding) in IR photodetector fabrication technology.

4.2. Experimental methods

4.2.1. HgCdTe sample-preparation and deposition of In film

The p-type $Hg_{1-x}Cd_xTe$ epilayers (samples) were utilized to perform the study of In thin films and a domestic growth method, namely vertical dipping liquid phase epitaxy (VD-LPE), was employed to produce the epilayers on lattice-matched CdZnTe (111) substrate. Seven epilayers (A, B, C, D, E, F, and G) having the specifications (dimensions: 30×30 mm^2, thickness = 10 µm, composition $x = 0.29$, concentration = 1×10^{16} cm^{-3}, mobility = 416 cm^{-2} V^{-1} s^{-1}) were applied to accomplish the proposed research work. The process of mechanical/chemical-mechanical polishing of the HgCdTe epilayers (A, B, C, D, E, F, and G) was completed using an alumina powder (0.05 µm), the (I_2:KI: $C_2H_6O_2$) :: (1g:4g: 10 ml) solution and some drops of KOH, respectively. The epilayers were washed and dried carefully with de-ionized (DI) water and highly pure N_2. The epilayers (A, B, and

C) were chopped into three-2 pieces of the same dimensions 10×10 mm^2 (namely A1, A2, A3, B1, B2, B3, C1, C2, C3), and the optimized In the thin film was achieved using the epilayers (A (A1, A2, A3), B (B1, B2, B3), C (C1, C2, C3), D, E, and F) where the indium thin films were grown on the epilayers at different deposition rates. First of all, Samples A1, B1, C1, and D were carried out through the processes of cleaning (standard and prolonged cleaning procedure: 5 min heating of samples in each chemical sequentially, i.e., in trichloroethylene, acetone, and methanol) and chemical etching (20 sec using 0.1% bromine in methanol solution). Then, the washing, drying, and baking (5 min at 90 °C) of the epilayers were completed successfully. The defect and contamination-free surface of the samples were revealed through microscopic and ellipsometry measurements. Immediately, the samples were put into the coating unit's vacuum chamber (model**:** HHV 20F10). In-material (purity: 99.99 %) was put into boats and the source-to-sample distance was fixed at 30 cm**.** The ultimate pressure of the order of 4×10^{-7} Torr was achieved within the vacuum chamber and then the deposition process of In film (thickness: 4.5 ± 0.5 μm) formation was performed at the parameters (deposition rate: 1.4 nm/sec, the evaporation current: 120-150 A). An in-built auto rate controller (attached to the quartz crystal monitor) monitors the deposition rate and film thickness. The entire process of In film deposition was finished at room temperature (24 °C). Samples A2, B2, C2, and E were also carried out through a similar treatment (cleaning, etching, and surface quality examination) as the Samples A1, B1, C1, and D were given and In films of the same thickness were grown on these samples at the parameters (deposition rate: 2.7 nm/sec, the evaporation current: 170-200 A). Consequently, In films of the same thickness were grown on Samples A3, B3, C3, and F at the different parameters (deposition rate: 15 nm/sec, the evaporation current: 200-240 A), whereas other parameters (cleaning, etching and surface quality examination) were identical to the parameters of Samples (A1, B1, C1, D, A2, B2, C2 and E). Afterward, the deposited indium films were characterized (using XRD, AFM, EDX, SEM, and resistivity measurement), and it was revealed that the desired value of conductivity (2.72 × 10^4 mho/cm) could be achieved for the In films, which were grown at a deposition rate of 2.7 nm/sec. In films deposited by a deposition rate of 2.7 nm/sec also hold other essential properties like desired structural parameters (cubic structure), composition (purity), and morphology (highly dense film with low roughness, optimum grain size). Thus, the deposition rate of 2.7 nm/sec is an optimized deposition rate for the growth of In films, and the optimized deposition parameters will further be used for investigations of epilayer-G. The epilayer G was chopped into two pieces of the same dimensions, 15×15 mm^2 (namely G1, G2). The deposition of In films (4.5 ± 0.5 μm) on Sample-G1 (having photolithography pattern of bumps) was accomplished at the optimized process parameters (pressure: 4.0 × 10^{-7} Torr, deposition rate: 2.7 nm/sec, the evaporation current: 170-200 A) and a photolithography lift-off (using acetone solvent) process was followed to achieve the desired features of indium bump on the HgCdTe sample. The SEM measurement was carried out to determine the surface morphology and microstructural features of indium bumps (In film). The electrical properties of thermally grown In films were investigated by using the optimized In films to fabricate HgCdTe (Sample-G2) based TLM structure. In this continuation, all the similar treatments (like chemo-mechanical polishing, prolonged cleaning, chemical etching, etc.) were also given to the HgCdTe (Sample-G2). The defect and contamination-free surface of the HgCdTe Sample-G2 were confirmed by microscopic and ellipsometry observations. An n/p region was created on the sample by an ion- implantation technique in which boron ions are diffused into the HgCdTe substrate slowly to generate the native defects responsible for type conversion with a controlled junction depth junction (1.0-1.5 μm). The implantation process is typically performed (angle of incidence: 7°, implantation dose: 5 x 10^{14} atom/$cm^{2,}$ and ion energy: 50-140 KeV) at room temperature. Then, a photolithography process was executed on HgCdTe Sample-G2 to achieve the desired TLM structure pattern. Subsequently, the epilayer was carried out through a descum process (pressure: 10^{-1} - 10^{-2} Torr, power: 100 W, O_2 flow rate: 200 mL/min) using oxygen plasma for 30 sec and subsequently transferred into the vacuum chamber of the coating unit. After obtaining the ultimate chamber vacuum, i.e., 4.0×10^{-7} Torr, the thin film of In (4.5 ± 0.5 μm) was grown on the HgCdTe Sample-G2 by a thermal evaporation deposition technique, and the resulting TLM structure was achieved after finishing a photolithography lift-off process (in acetone) of the deposited sample.

4.2.2. Characterization techniques

An XRD system of high-resolution (Model: Analytical B.V.-X'Pert PRO MRD (Material Research Diffractometer), radiation source: CuKα (λ = 0.1542 nm) and Xe-proportional counter) was employed for evaluation of the structural parameters of thermally evaporated In films. The morphology statistics of thin films were attained at the parameters (grazing angle =3° and 2θ=20-85°) using the AFM (Model-5600LS, Agilent Technologies) system. A FESEM (Model-Carl Zeiss SUPRA55VP supported with Oxford Instrument X-MAX EDX Spectrometer, operating voltage: 5-20 kV) characterization was performed to find the microstructural and compositional features of In films grown on HgCdTe. The current-voltage (I-V) and resistance measurements of In/HgCdTe-based TLM structure were performed by a cryo-prober (Make: Keithley Parametric analyzer, Model-4200 having integrated 4200-CUV card). I-V characteristics of the HgCdTe-based TLM structures were recorded at a temperature of 80 ± 3 K.

4.3. Results and discussion

4.3.1. X-ray diffraction (XRD) measurement

The structural properties of In films grown on HgCdTe samples through various deposition rates (Fig. 4.1(a): Sample-A1 with rate -1.4 nm/sec), (Fig. 4.1(b): Sample-A2 with rate -2.7 nm/sec) and (Fig. 4.1(c): Sample-A3 with rate -15 nm/sec) were evaluated by XRD measurement and the observed XRD patterns (2θ-Intensity curve) are shown in Fig. 4.1(a, b, c). Sample-A1 (Fig. 4.1a) shows diffraction peaks at $2\theta = 32.96^{\circ}$, 36.28°, 39.16°, 54.44°, 56.52°, 63.16°, 67.00°, 69.08° and 77.04° corresponding to the diffraction planes (101), (002), (110), (112), (200), (103), (211), (202) and (004), respectively (JCPDS no. 85-1409) and exhibits bcc structure of tetragonal indium (In) phase [26-31]. Sample-A2 also identified with a typical bcc structure of tetragonal indium (In) phase consisting of (101), (002), (110), (112), (200), (103), (211) and (213) planes (Fig. 4.1b). The aforesaid planes could be related to the diffraction peaks $2\theta = 32.94^{\circ}$, 36.30°, 39.10°, 54.50°, 56.54°, 63.18°, 67.06°, and 89.98°, respectively along 2θ axis (JCPDS no. 85-1409) [27-32].

Similarly, Sample-A3 (Fig. 4.1c) exhibited diffraction peaks at $2\theta = 32.92^{\circ}$, 63.20° and 67.04° corresponding to (101), (103), and (211), respectively, planes of a typical bcc structure of tetragonal indium (In) phase (JCPDS no. 85-1409) [22,27-31]. All three films (Samples A1, A2 and A3) have also exhibited the substrate peaks (at $2\theta = 44.52^{\circ}$- 44.60°), as shown in Fig. 4.1(a, b and c). Some unknown peaks were also detected in all three samples, possibly due to the formation of In_2O_3 during their environmental exposure. Table 4.1 compares structural parameters, experimental 2θ and (hkl) plane with standard 2θ and (hkl) plane of thermally grown indium films.

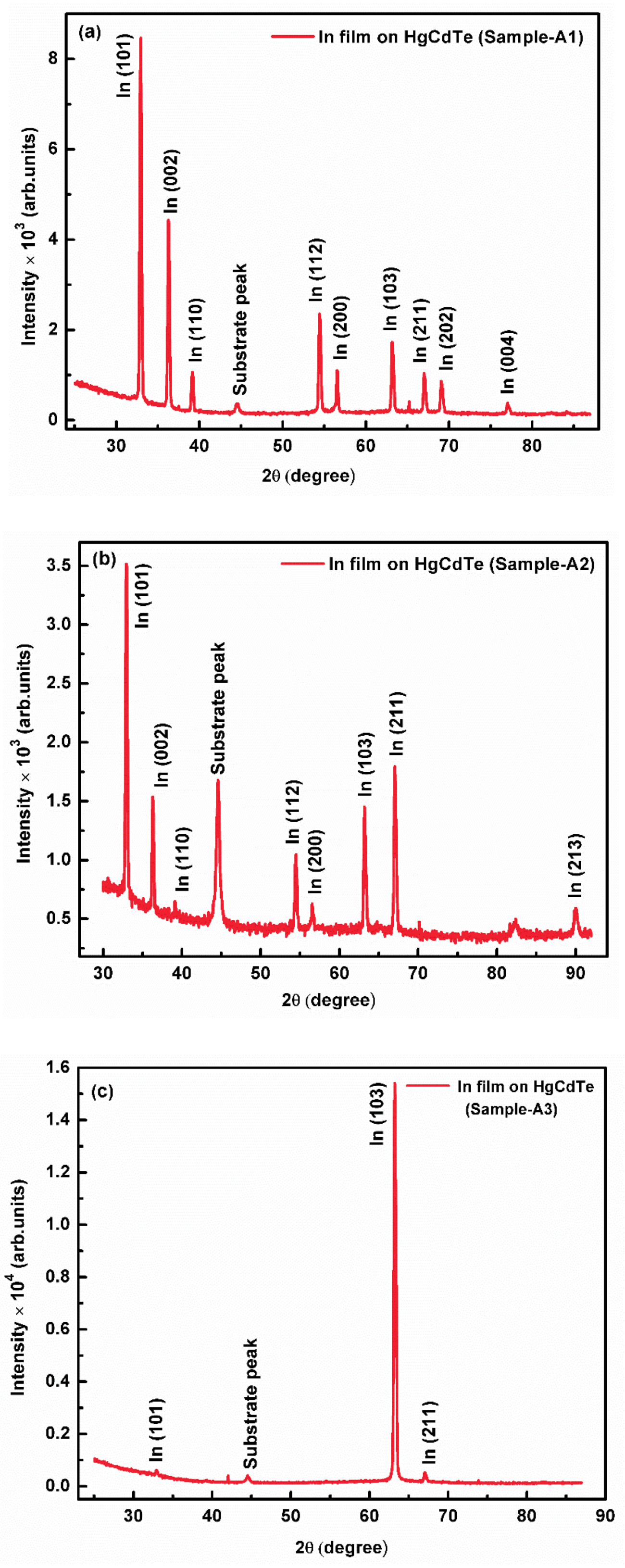

Figure 4.1. XRD patterns of thermally grown In thin films on different HgCdTe samples by various deposition rates: (a) Sample-A1 with a rate of 1.4 nm/sec, (b) Sample-A2 with a rate of 2.7 nm/sec, and (c) Sample-A3 with a rate of 15 nm/sec

Table 4.1: Experimental and standard structural parameters of deposited In film on HgCdTe samples at various deposition rates (Samples A1: 1.4 nm/sec, A2: 2.7 nm/sec and A3: 15 nm/sec).

Sr no.	**Standard values of 2θ and (hkl)**	**2θ and (hkl) by XRD for Sample-A1**	**2θ and (hkl) by XRD for Sample-A2**	**2θ and (hkl) by XRD for Sample-A3**
1	32.94° (101)	32.96° (101)	32.94° (101)	32.92° (101)
2	36.30° (002)	36.28° (002)	36.30° (002)	63.20° (103)
3	39.15° (110)	39.16° (110)	39.10° (110)	67.04° (211)
4	54.45° (112)	54.44° (112)	54.50° (112)	-
5	56.57° (200)	56.52° (200)	56.54° (200)	-
6	63.19° (103)	63.16° (103)	63.18° (103)	-
7	67.04° (211)	67.00° (211)	67.06° (211)	-
8	69.10° (202)	69.08° (202)	89.98° (213)	-
9	77.08° (004)	77.04° (004)	-	-
10	84.16° (220)	-	-	-
11	89.89° (213)	-	-	-

Thus, Fig. 4.1 (a, b, c) and Table 4.1 indicate that the indium film grown on Samples (A1, A2) bear tetragonal phase (bcc lattice), polycrystalline nature and preferred orientation along a (101) plane, while the film grown on Sample-A3 has also tetragonal phase (bcc lattice) and polycrystalline nature, but its preferred orientation (103) is different from the Samples (A1 and A2) and standard indium film. The XRD pattern of the Sample-A3 film does not contain the desirable diffraction peaks as the standard one, which means some of the diffraction peaks are absent. Thus, the structural properties of Sample-A3 film (Fig. 4.1c) may vary with standard indium film. HgCdTe Samples (A1 and A2) have shown a perfect coincidence (in terms of 2θ and (hkl) plane) with the standard indium film (JCPDS no. 85-1409) as reported in the literature [22,27-31].

Fig. 4.1(a, b) and Table 4.1 are also indicating that the 2θ-position of the intense diffraction peak of Sample-A2 ($2\theta = 32.94^{\circ}$) is the same as the XRD peak position (intense peak) of standard bulk In material. In contrast, Sample-A1 ($2\theta = 32.96^{\circ}$) has a minor deviation from the standard bulk material. So, the deposition rate -2.7 nm/sec (Sample-A2) can be taken as the optimized deposition rate to yield the indium film of desired crystalline properties.

The lattice constants **(a)** and **(c)** of the bcc tetragonal phase of In can be evaluated using the familiar Eq. 4.1:

$$\frac{1}{d^2} = \frac{h^2+k^2}{a^2} + \frac{l^2}{c^2}, \qquad (4.1)$$

where $d = \frac{\lambda}{2\sin\theta}$

Here d is interplanar spacing, λ is x-ray wavelength, θ is diffraction angle, and h, k, l are miller indices of respective crystal planes. The average crystallite size (D) of In film **is** evaluated by the well-known Debye Scherrer formula (Eq. 4.2) as follows:

$$D = \frac{0.94\lambda}{\beta\cos\theta} \qquad (4.2)$$

Where β is full-width at half-maximum (FWHM) of diffraction peaks and θ is the diffraction angle. The strain (*ε)* of In film can be calculated using the famous Eq. 4.3 as given below:

$$\varepsilon = \frac{\beta}{4\tan\theta} \tag{4.3}$$

The dislocation density (δ) of In material can be estimated using Eq. 4.4

$$\delta = \frac{1}{D^2} \tag{4.4}$$

Where D represents the average crystallite size of the grown In film.

The expression (Eq. 4.5) was used to calculate the stress of the deposited In film.

$$\sigma_s = \frac{Y\,(a - a_o)}{2a_o\gamma} \tag{4.5}$$

Here values of In parameters are Y: Young's modulus of In (12.7 GPa), a: lattice constant measured by XRD, a_o the lattice constant of bulk In, and γ: Poisson's ratio (0.45) of In. Table 4.2 displays the estimated structural parameters (β: FWHM, a: lattice constant, D: Average crystallite size, ε: strain, stress: σ and dislocation density: δ) of optimized In film (deposition rate -2.7 nm/sec) where the calculation of these structural parameters has been done using the measured XRD parameters (2θ, diffraction peaks, lattice plane). A good agreement between experimental and standard values of lattice constant was found as shown in Table 4.2.

Thus, the properties of In film and bulk In material are identical. The evaluated structural parameters (D, **ε**, σ, and δ) of thermally grown In films were found comparable and acceptable to the best-reported values of In films [27,31-34]. Thus, the thermal evaporation technique is a conventional and well-established technique that can yield the In metal film of desired crystalline quality.

Table 4.2: Structural parameters of optimized In film (Sample-A2: 2.7 nm/sec) calculated for the preferred orientation plane (101).

Structural parameters	**Estimated values**
2θ (degree)	32.94
Lattice plane (hkl)	(101)
FWHM β (rad)	0.0039
Lattice constant, a (Å) and c (Å)	3.33, 4.71
Average crystallite size, D (nm)	39.31
Stress σ for lattice constants a and c (GPa)	0.23, 0.68
Strain, **ε**	0.0033
Dislocation density **δ** (x 10^{11} lines/cm^2)	0.65

4.3.2. Atomic force microscopy (AFM) analysis

The surface morphology of thermally evaporated In films on different HgCdTe samples (Sample-B1, Sample-B2, and Sample-B3) with varying deposition rates of In (rate-1.4 nm/sec, rate -2.7 nm/sec and rate-15 nm/sec) were examined by the AFM measurement. The scanning of In-HgCdTe interfaces (samples) was carried out in an intermittent or tapping mode at high resolution to protect the delicate surface of HgCdTe samples (like soft, fragile, and adhesive) from damage during the measurement. Fig. 4.2(a, b, c, d, e, and f) show the 2D and 3D image profiles of grown In films (thickness = 4.5 ± 0.5 µm, scanning area: 5.0 µm × 5.0 µm).

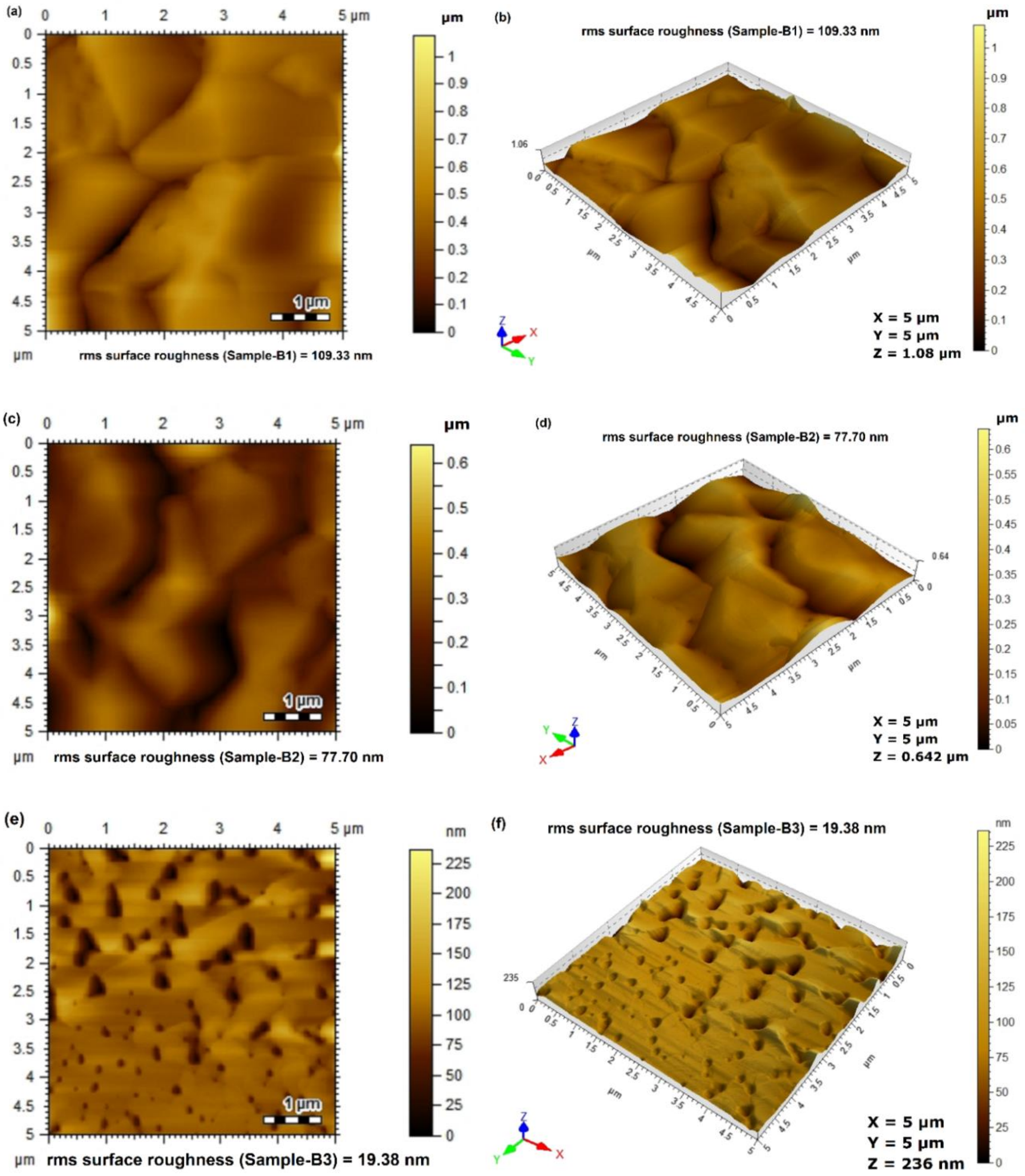

Figure 4.2. Surface morphologies of In thin films grown on different HgCdTe samples with different deposition rates of In (Sample-B1: rate of 1.4 nm/sec, Sample-B2: rate of 2.7 nm/sec and Sample-B3: rate of 15 nm/sec) measured by AFM. 2D image of Sample-B1 (a) 3D image of Sample-B1 (b), 2D image Sample-B2 (c), 3D images of Sample-B2 (d), 2D image of Sample-B3 (e) and 3D image of Sample-B3 (f).

Accordingly, it is estimated that the grown In film on Sample-B1 (rate - 1.4 nm/sec) and Sample-B2 (rate -2.7 nm/sec) are dense, uniform, and continuous (Fig. 4.2(a, b, c and d)). There are 2D layers, many high-density islands (conical islands, elongated), and nanoclusters within the film that are interconnected. The measured root-mean-square (RMS) roughness of Sample-B1 and Sample-B2 are 109.33 ± 0.53 nm and 77.70 ± 0.32 nm, respectively. However, the In film of Sample-B3 (Fig. 4.2e & 4.2f) prepared with deposition rate (15 nm/sec) appears more continuous and dense compared to Samples (B1 and B2). The film has interconnected 2D layers, high-density islands (conical islands, elongated), and nanoclusters. The measured root-mean-square (RMS) roughness of Sample-B3 (19.38 ± 0.12) nm is also lower than the RMS roughness of Sample-B1 and Sample-B2, but it contains many trenches (of various sizes: small, medium, and big), which may be responsible for undesirable porous In film. The different surface morphology of Sample-B3 may be due to the relatively high deposition rate at which film-forming In atoms (high energy) do not have sufficient time to achieve the optimal low energy states (nucleation sites) in the formation of local lattice structure before new atoms arrive at the substrate (sample) surface.

From the comparative analysis of all three Samples (B1, B2, and B3), it is concluded that In film grown at a deposition rate of 2.7 nm/sec (Sample-B2) has proved itself an optimized film having morphological properties like low surface roughness, densely packed, continuous and non-porous. Thus, the surface morphological results of In thin-film have shown a good consistency with earlier reported best results where the In films were prepared by the electrodeposition and pulsed laser deposition (PLD) growth techniques [22,35]. Thus, the morphological properties of thermally grown In thin-film make it suitable for HgCdTe-based IR device fabrication.

4.3.3. Energy dispersive x-ray (EDX): compositional analysis

The elemental composition of the thermally evaporated In film was performed using the EDX technique. The resultant EDX spectra of In/HgCdTe interfaces prepared at different deposition rates (Sample-C1: rate of 1.4 nm/sec, Sample-C2: rate of 2.7 nm/sec, and Sample-C3: rate of 15 nm/sec) are shown in Fig. 4.3(a, b and c).

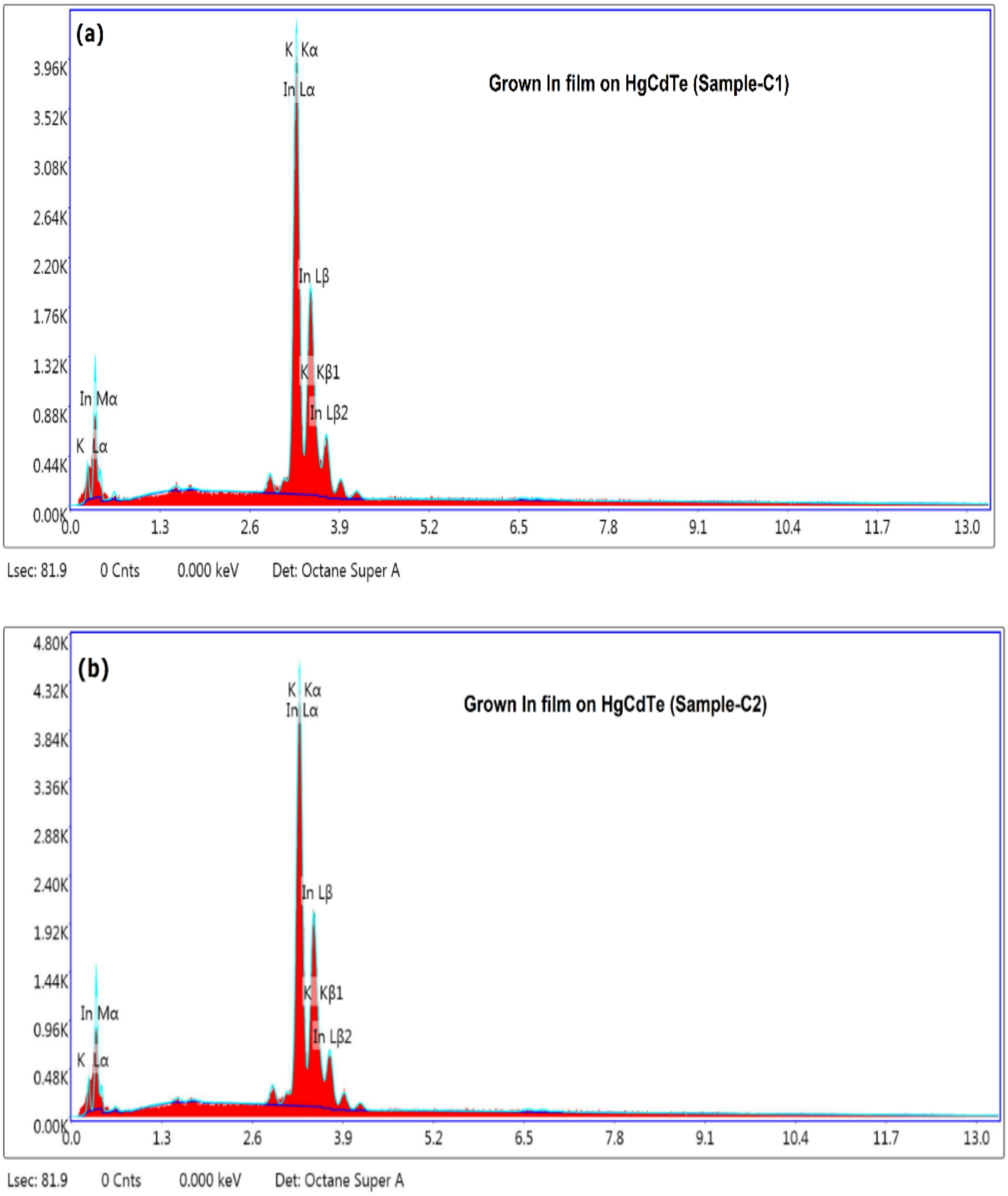

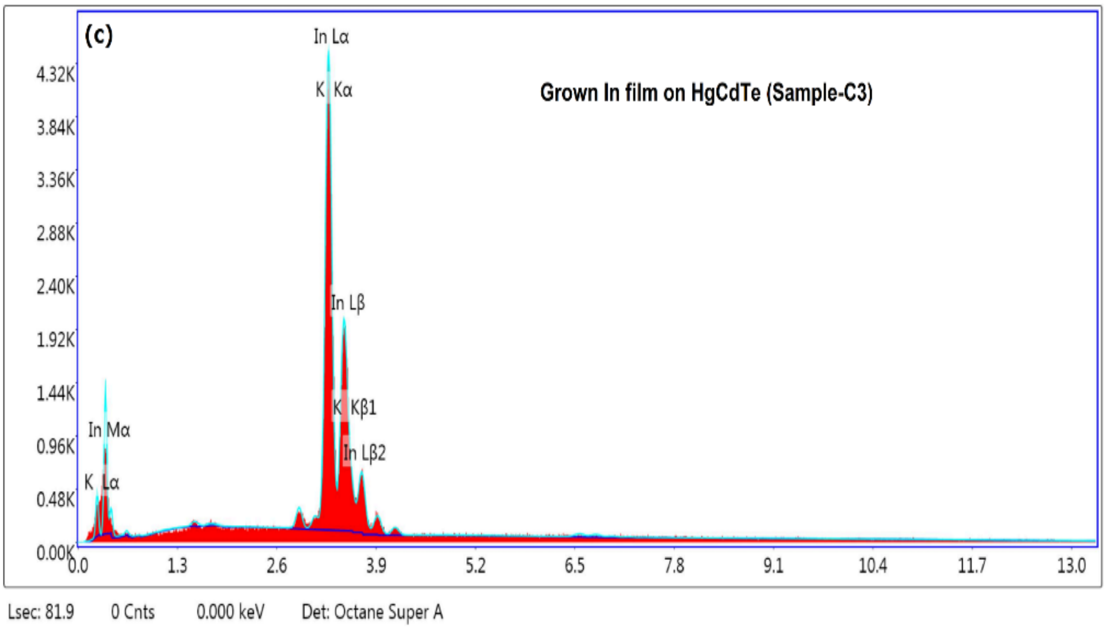

Figure 4.3. EDX spectra of thermally evaporated In films on various HgCdTe samples with different deposition rates (a) with 1.4 nm/sec (Sample-C1), (b) 2.7 nm/sec (Sample-C2) and (c) 15 nm/sec (Sample-C3).

The spectrum of Sample-C1 (Fig. 4.3a) has displayed two peaks of indium (In) and potassium (K) elements, respectively. Similarly, Sample-C2 (Fig. 4.3b) and Sample-C3 (Fig. 4.3c) have also exhibited similar peaks of indium (In) and potassium (K) elements at the same energy positions. The comparison of all three spectra (Sample-C1, Sample-C2, and Sample-C3) states that thermally grown In films of all the samples have a maximum amount of In with a negligible amount of K element. EDX results of In/HgCdTe interfaces produced at various deposition rates have been listed in Table 4.3. Fig. 4.3(a, b, and c) and Table 4.3 indicate that Sample-C2 has relatively more elements of In (atomic: 97.89 %, weight: 90.81 %) than Sample-C1 and Sample-C3. It is concluded that the purity of Sample-C2 is relatively higher than that of Sample-C1 and Sample-C3. The presence of K-element peaks (negligible intensities) in the spectra of all three Samples (C1, C2 & C3) may be due to contamination of the semiconductor (HgCdTe) surface with oily things during sample preparation.

Table 4.3: A comparative analysis of EDX results for grown In film on HgCdTe Samples (C1, C2, and C3) at different deposition rates.

Sr. No.	Sample-C1 (Rate: 1.4 nm/sec)		Sample-C2 (Rate: 2.7 nm/sec)		Sample-C3 (Rate: 15 nm/sec)	
Element	Atomic (%)	Weight (%)	Atomic (%)	Weight (%)	Atomic (%)	Weight (%)
In L	97.79	90.58	97.89	90.81	97.06	88.75
K K	2.21	9.42	2.11	9.19	2.94	11.25
Total	100	100	100	100	100	100

Thus, elemental analysis of three Samples (C1, C2 & C3) expresses that a relatively pure film may be grown at the deposition rate of 2.7 nm/sec, which can be treated as the optimized deposition rate. The analysis further confirmed the desired elemental composition of grown In thin film on the HgCdTe substrate. Hence, the thermally evaporated In thin films have shown an excellent agreement with the best-reported In films so far [21,28].

4.3.4. Scanning electron microscopy (SEM) analysis

SEM measurement technique was used to investigate the microstructural features (surface topology) of In/HgCdTe. The resultant SEM images (at various scales and magnifications) of the In films grown on HgCdTe samples with different deposition rates (Sample-C1: rate of 1.4 nm/sec, Sample-C2: rate of 2.7 nm/sec, and Sample-C3: rate of 15 nm/sec) are shown in Figs. 4.4, 4.5, and 4.6, respectively. Fig. 4.4(a, b, and c) displays the features of Sample-C1, which reflect that the deposited In film is dense, continuous, and uniform.

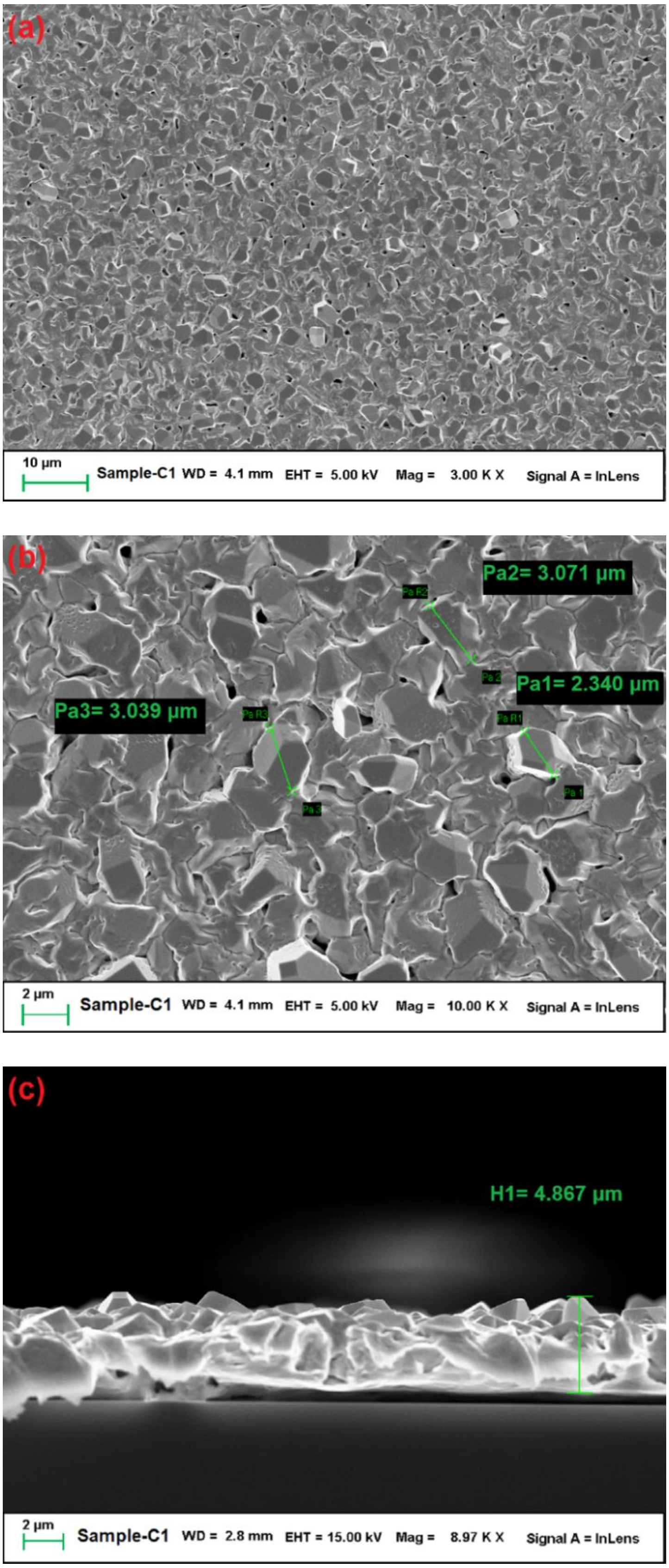

Figure 4.4. SEM images with different scales and magnifications of In thin films grown on HgCdTe Sample-C1 at a deposition rate of In-1.4 nm/sec: (a) 10 μm and 3.00 KX, (b)

particle size measured at 2.0 μm and10.00 KX and (c) cross-sectional view of In thin film with film height of 2μm and 8.97 KX.

SEM images revealed that the film is made from different interconnected particles of random shapes (spherical, hexagonal, and conical) and probably some voids (negligible) are also presented within the film. Fig. 4.4(b) shows the measured size of some typical particles, which ranges from 2.34 - 3.07 μm.

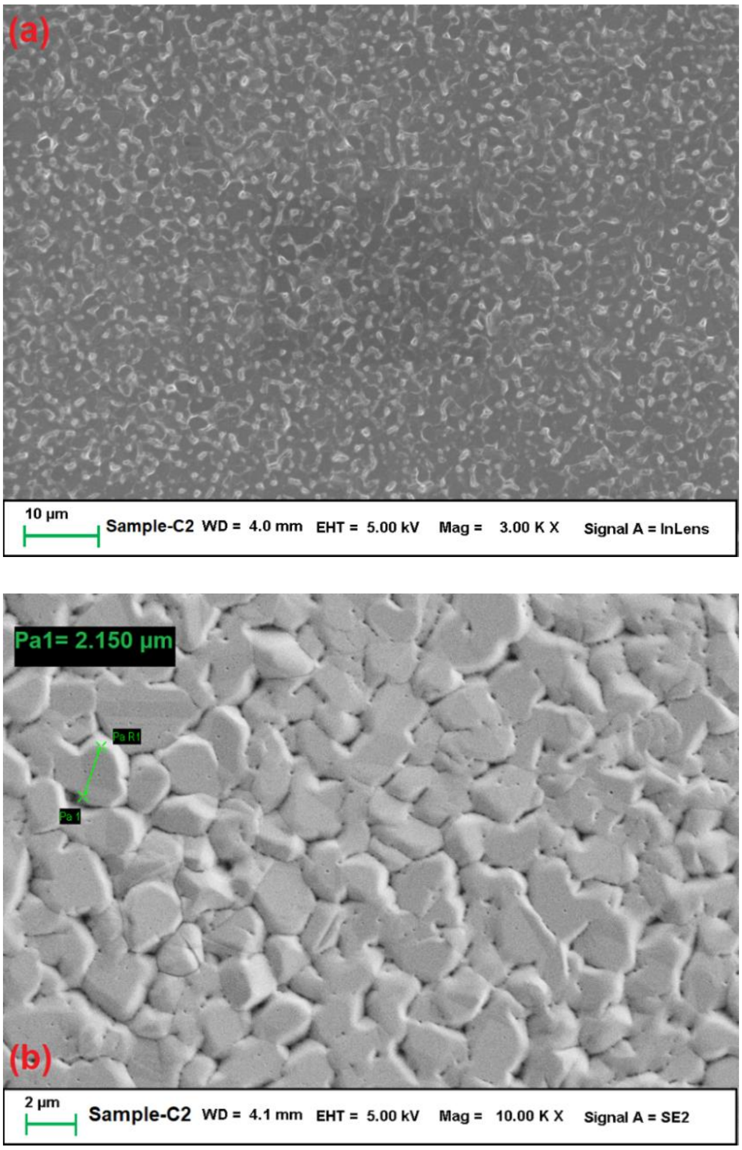

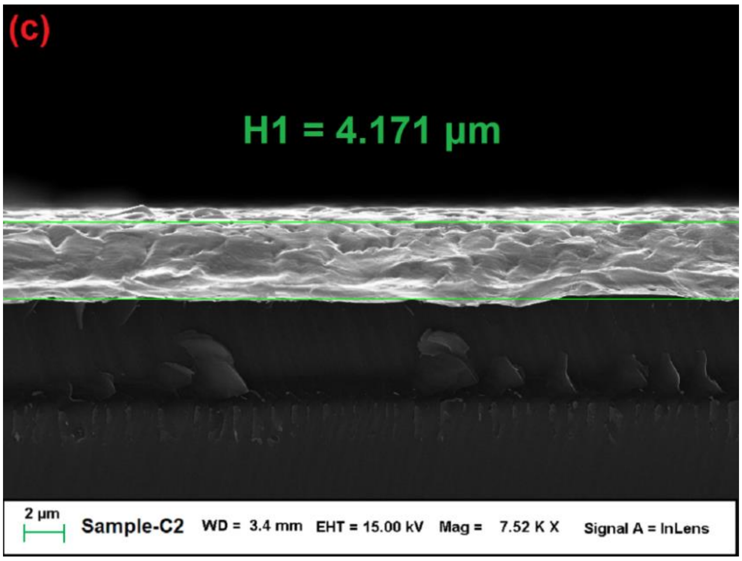

Figure 4.5. SEM images with various scales/magnifications of In thin films grown on HgCdTe Sample-C2 at a deposition rate of In-2.7 nm/sec: (a) 10 µm and 3.00 KX, (b) particle size measured at 2 µm and 10.00 KX and (c) cross-sectional view of In thin film with film height at 2.0 µm and 7.52 KX.

Fig. 4.5(a, b, and c) and Figs. 4.6(a, b, and c) represent the microstructural features of Sample-C2 and Sample-C3, respectively, and predict that the deposited In films are uniform, dense, and continuous forms. The obtained particle size for Samples-C2 (Fig. 4.5b) and Sample-C3 (Fig. 4.6b) through SEM analysis are 2.15 µm and 53.70 nm, respectively. Further, the comparison states that all the Samples (C1, C2 & C3) are dense, continuous, and uniform, but Sample-C3 is slightly superior in density, continuity, and uniformity than Sample-C1 and Sample-C2. The presence of more defects (trenches or voids) in the Sample-C3 surface may degrade the quality of the thin film in terms of increasing the porosity and roughness of the film. Sample-C2 is more densely packed, continuous, uniform, and free from defects (negligible voids or trenches) than Sample-C1, which also has some voids (negligible) on its surface. The cross-sectional view of Samples-C1 indicates mixed growth (preferential 2D-layer and 3D-islands) of the film across the HgCdTe surface.

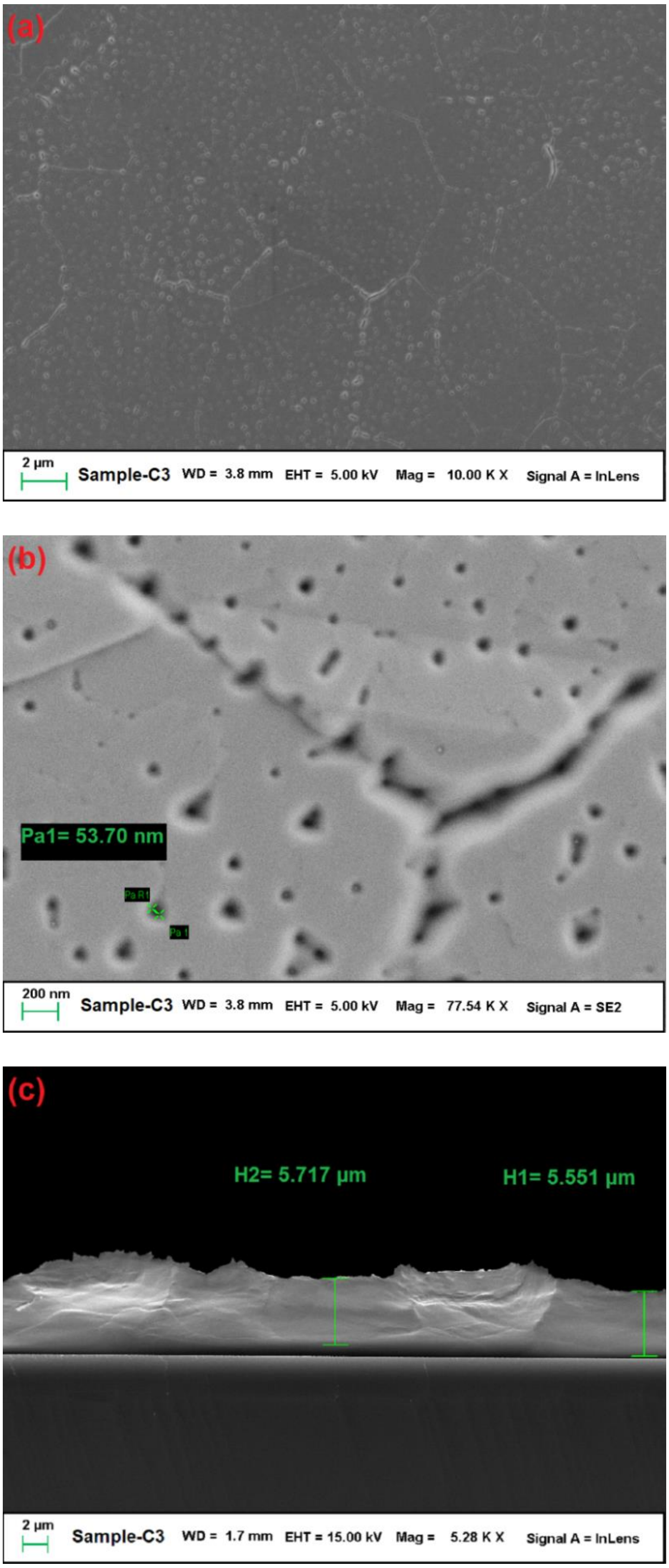

Figure 4.6. SEM images with various scales/magnifications of In thin films deposited on HgCdTe Sample-C3 at the deposition rate of 15 nm/sec: (a) 2 µm and 10.00 KX, (b)

particle size measured at 200 nm and 77.54 KX and (c) cross-sectional view of In thin film with film height at 2µm and 5.28 KX.

The cross-sectional view of Sample-C1 (Fig. 4.4c) displays the thickness of the grown thin film equal to 4.87 µm, which is quite close to the actual thickness of the produced film (4.5 ± 0.5 µm) measured by a quartz crystal monitor. On the other hand, in Samples (C2 and C3), the island growth is dominated by preferential 2D-layer growth, which means the development of In clusters occurs along the lateral direction. The evaluated heights of In films for Sample-C2 and Sample-C3 are 4.17 µm and 5.55 - 5.72 µm, respectively, as shown in the cross-sectional view of Figs. 5c and 6c are also close to the actual height of the grown film (4.5 ± 0.5 µm) measured by a quartz crystal monitor. Thus, the film height of Sample-C2 (measured by SEM) is relatively closer to the actual height of the grown film than the Samples (C1 and C3). The particle size of the Sample-C2 (deposition rate of 2.7 nm/sec) is also close to the early reported result of In film [22]. The surface coverage and close contact formation among the clusters increase with the increasing thickness of In film.

Thus, the Sample-C2 prepared by the deposition rate of 2.7 nm/sec achieved all the desired microstructural properties (film height, particle size, continuity, uniformity, high density, and voids or trenches-free film, smooth step coverage, minimum grain boundaries, etc.) therefore can be treated as an optimized deposition rate condition and further used for the fabrication of TLM structure and In bumps. The microstructural quality of the thermally grown In thin film is comparable to the reported In metal films [22,28,30].

4.3.5. Microstructural analysis of In bumps (grown at an optimized deposition rate of 2.7 nm/sec)

A test-structure configuration (In bumps/n-HgCdTe, the thickness of In bumps: 4.5 ± 0.5 µm) was fabricated on HgCdTe Sample-G1 to examine the effectiveness of the optimized In films for the IR photodetector technology. The In bumps of thickness 4.5 ± 0.5 µm were grown on this sample at an optimized deposition rate of 2.7 nm/sec. The SEM measurement technique was employed to find out the microstructural features of indium bumps (In film), and the resultant SEM images (at various scales and magnifications) of the HgCdTe-based structure are shown in Fig. 4.7(a, b, c, and d). The features of In bumps (In film) at different scales/magnification are highlighted in Fig. 4.7(a and b). All the deposited In bumps look circular, flat, uniform, and dense. The measured particle size for a typical In bump was equal to 2.77 µm (Fig. 4.7b), and it has shown a reasonable agreement to the grain size of plane In film (Sample-C2: grown at 2.7 nm/sec) evaluated by SEM. The particle size value is also comparable to the early reported values of In bumps [19].

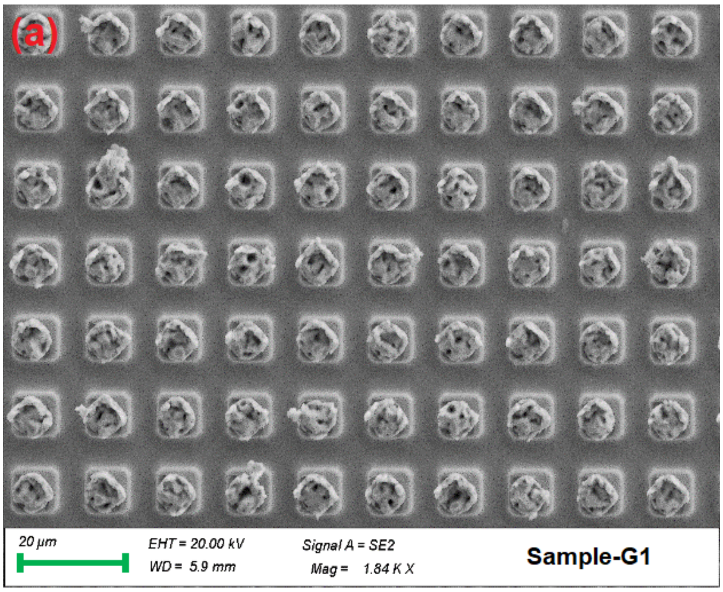

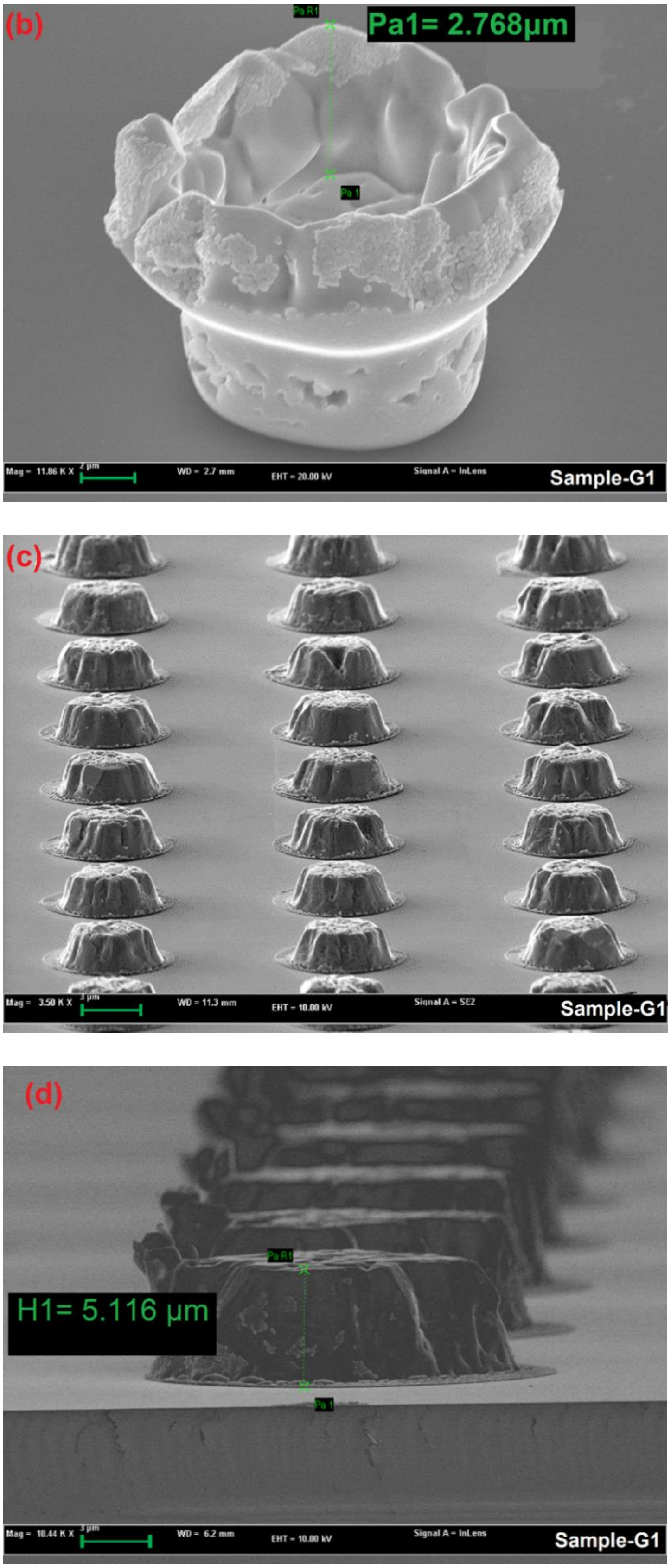

Figure 4.7. Microstructural analysis using SEM technique of grown In bumps on HgCdTe Sample-G1 with an optimized deposition rate of 2.7 nm/sec at various

scales/magnifications: (a) front-view of In bumps at 20 μm and 1.84 KX, (b) particle size of In bump by front-view at 2 μm and 11.86 KX, (c) cross-sectional view of In bumps at 3.0 μm and 3.50 KX and (d) height of In bumps by the cross-sectional view at 3μm and 10.44 KX.

The In bumps at various scales are displayed in Fig. 4.7(c, d), according to which the grown In bumps are uniform in height (thickness) and dia. The measured height (thickness: 5.12 μm) of In bumps, as shown in Fig. 4.7(d), is nearly equal to the actual thickness (4.5 ± 0.5 μm) of the grown In bumps, which is controlled by a quartz crystal monitor. Since the uniformity of height/thickness of In bumps has an essential role in deciding the quality of fabricated In bump arrays as reported in the literature [36]. Consequently, uniform and tall In bumps with desired particle size and optimum thickness (height) were achieved, which indicates that the thermal evaporation method (used for In bump growth) is well-established. These types of In bumps are generally favoured in the IRFPA fabrication technology, which enhances the long-term stability and reliability of the detectors.

The thermally-grown In bumps (Sample-G1) have all the microstructural properties (desired film height and particle size, bumps with uniform dia and height, high density, etc.) required for IR detector fabrication. Thus, the microstructural quality (topography) of In bumps is comparable to the reported In bumps for fabricating IR focal plane arrays [17,19,36-39]. Therefore, IR detectors of nominal size, high density, and high reliability could be fabricated using these optimized In bumps.

4.3.6. Electrical characteristics of In films

The In thin films were grown on HgCdTe Sample-G2 at an optimized deposition rate to fabricate TLM structure to find the electrical properties of grown In thin film. Subsequently, I-V/resistance measurements of In/n/p-HgCdTe-based TLM structure were performed. The fabricated TLM structure has five contact pads of the same area (100 × 200 µm^2: length -L and width-W of the contact pads remain the same) and different interpad spacing d1, d2, d3, and d4 (where the values of interpad spacing between adjacent contact pads are d1-25 µm, d2-50 µm, d3-100 µm, and d4-200 µm), as shown in the schematic diagram (Fig. 4.8). The resistances between the pairs of all adjacent contact pads of TLM structure were measured. A resistance vs. interpad separation plot was obtained to estimate the sheet resistance (R_{sh}) and transfer length (L_T). The resultant values of R_{sh} and L_T were used to evaluate the other parameters like contact resistance (R_c) and specific contact resistance (ρ_c). I-V measurements of TLM structures were also performed to examine the behaviour of the contacts.

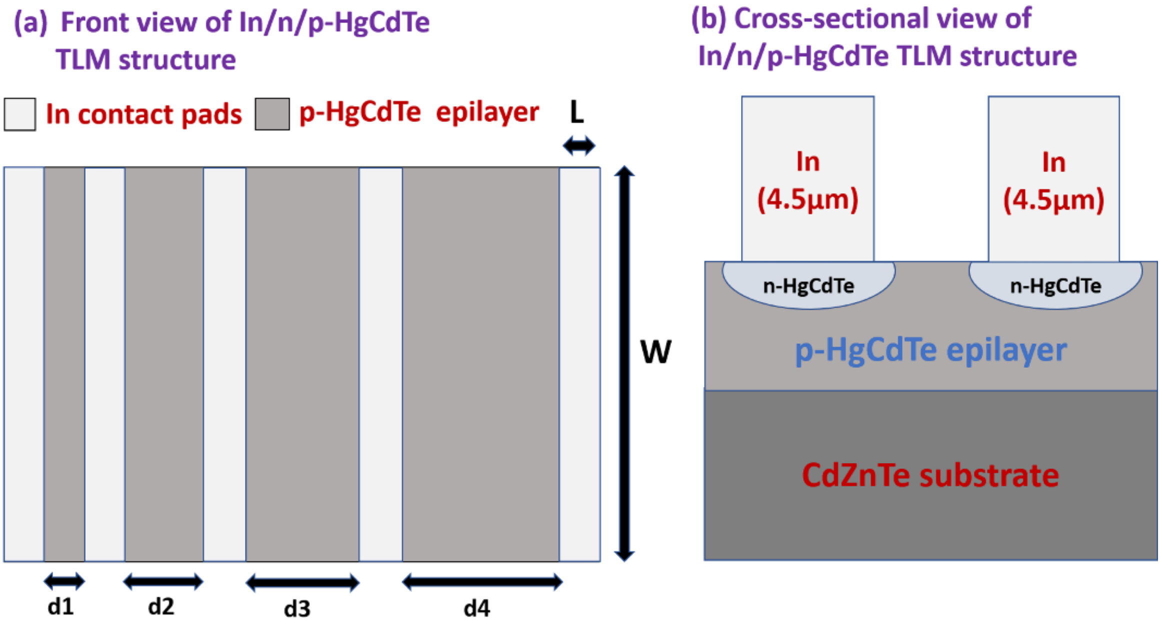

Figure 4.8. Schematic diagram of HgCdTe Sample-G2 based TLM structure. Front view of fabricated TLM structure (a) with five contact-pads of the same length (L= 100 µm), same width (W=200 µm) and interpad spacing for contacts are d1-25 µm, d2-50 µm, d3-100 µm and d4-200 µm. Cross-sectional view (b) with a configuration of In/ n/p-HgCdTe and x=0.29.

The measured resistance R_T for a pair of TLM structure contact pads (length L, width W, and interpad spacing d) can be given by Eq. 4.6 [9,40,41].

$$R_T = R_{semi} + 2R_c = R_{sh}\frac{d}{W} + 2\frac{R_{sh}L_T}{W} \tag{4.6}$$

The parameters L_T, $R_{sh,}$ $R_{semi,}$ and R_c represent transfer length, sheet resistance, the resistivity of the semiconductor, and contact resistance, respectively. The transfer length can be evaluated using Eq. 4.7 [9,40,41].

$$L_T = \sqrt{\left(\frac{\rho_c}{R_{sh}}\right)} \tag{4.7}$$

The relation among contact resistance R_c, specific contact resistance $\rho_{c,}$ and transfer length L_T can be expressed by Eq. 4.8 [9,40,41].

$$\rho_c = R_{sh}L_T \Rightarrow R_c = \frac{\rho_c}{L_T W} = \frac{R_{sh}\,L_T}{W} \tag{4.8}$$

To evaluate R_c and ρ_c of the ohmic planar contact Eqs. 4.9, 4.10, and 4.11 were used [9,40,41]. Since R_c for an ohmic planar contact is defined as:

$$R_c = \frac{R_{sh}\cdot L_T}{W}\coth\left({}^{L}\!/_{L_T}\right) \approx \frac{\rho_c}{L_T W}\coth\left({}^{L}\!/_{L_T}\right) \tag{4.9}$$

The limiting cases modify the value of R_c, which is given in the simplified form as follows:

- Short contact Limit (L«L_T, no significant current penetration in metal contact) →

  $$\coth\left({}^{L}\!/_{L_T}\right) \approx {}^{L}\!/_{L_T} \text{ then } R_c = \frac{\rho_c}{LW} \Rightarrow \rho_c = R_c LW \tag{4.10}$$

- Long contact Limit (L»L_T, significant current transport into the metal contact) →

  $$\coth\left({}^{L}\!/_{L_T}\right) \approx 1 \text{ then } R_c = \frac{\rho_c}{L_T W} \Rightarrow \rho_c = R_c L_T W \tag{4.11}$$

4.3.7. TLM measurement and analysis

The total resistance R_T of HgCdTe Sample-G2 based TLM structure (configuration: In/n/p-HgCdTe) was measured for all the pairs of adjacent contact pads at 80 ± 3 K.

Subsequently, a plot of total resistance R_T *vs*. interspacing (d) was constructed as shown in Fig. 4.9. Eqs. 4.6-4.11 and Fig. 4.9 were used to estimate the electrical parameters (R_c, L_T, R_{sh}, and ρ_c), and the evaluated values of electrical parameters are listed in Table 4.4.

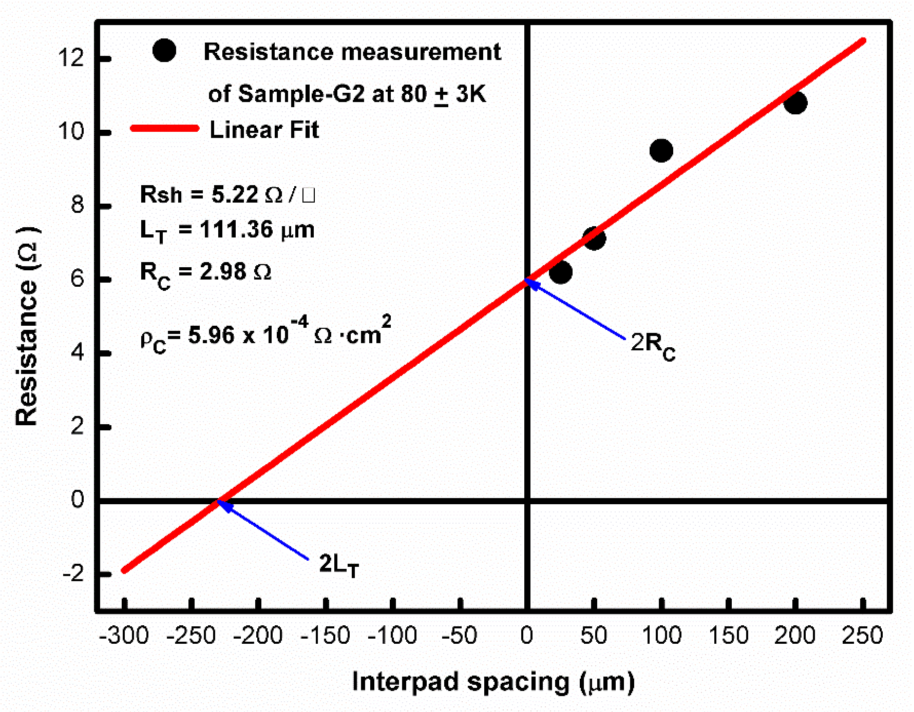

Figure 4.9. The resistance *vs*. interpad spacing curve of HgCdTe Sample-G2 based TLM structure (configuration: In/ n/p-HgCdTe & x = 0.29) was used to estimate contact resistance and other electrical parameters of the thermally grown In film.

Table 4.4: The calculated values of electrical parameters for the HgCdTe-based TLM structure fabricated at optimized deposition rate of 2.7 nm/sec (Sample-G2; configuration: In/ n/p-HgCdTe, x=0.29).

Sr. No.	R_{sh} (Ω/□)	Rc (Ω)	L_T (μm)	ρ_c (Ω·cm^2)
TLM Structure	5.22	2.98	111.36	5.96 x 10^{-4}

The value of ρ_c for In based TLM structure (Sample-G2) is 5.96 × 10^{-4} $\Omega\cdot cm^2$ and is comparable and favourable to the early reported values of low specific contact resistance of In films (10^{-3}-10^{-5} $\Omega\cdot cm^2$), where various combination of metals such as In/ n-HgCdTe, In/HgTe/n-HgCdTe, Mo/In/n-HgCdTe, Mo/Au/n-HgCdTe, Ti/HgTe/n-HgCdTe, Ti/Au/PEDOT: PSS/n-HgCdTe, Ti/Pt/Au/n-HgCdTe, Au/HgTe/n-HgCdTe were used to achieve these low contact resistance for $Hg_{1-x}Cd_xTe$ (where x = 0.28 and 0.30) substrate [2,4,5,8-10,42]. The ρ_c of In film has also shown a good agreement with the ρ_c of In-metal contacts used to develop CdTe-based IR detectors and MoS_2-based high-performance optoelectronic devices [7,15].

The probable reasons for achieving low specific contact resistance for the In/n-HgCdTe interface may be related to sample surface conditions and pre-deposition chemical treatments. Possibly, the first reason is the formation of a thin interfacial layer (few nm) on the HgCdTe sample due to the bombarding of the sample into oxygen plasma before In film deposition, which may have reduced the number of interface states (In/n-HgCdTe interface) responsible for rectifying behaviour of the contact [4,5,9,40,42]. Consequently, the second possible reason for low specific contact resistance may be the inward diffusion of In into the HgCdTe near-surface region, which enhances the HgCdTe-doping concentration (due to the distribution of ionized donors, the doping density becomes relatively higher than the bare HgCdTe, which reduces the width of a potential barrier) and responsible for creating the metal contacts with low specific contact resistance [4,5,42]. The third responsible factor for high contact resistance may be the presence of features like pinholes, contaminations, non-uniform thickness, and impurity in the grown In films which can create difficulty in generating the desired electrical characteristics. The obtained features of EDX, AFM, and SEM analysis confirm that originated In films are uniform, pure, and dense. The film also has desired grain size and minimum roughness. Hence, the charges will easily move across the In/n-HgCdTe interface because of minimum blocking effects in their path and the achieved specific contact resistance of the grown In contact will be low [4,5,43,44].

I–V measurements were performed to realize the current-transportation mechanism of the In/n-HgCdTe interface and behaviour of thermally grown metal contact. Fig. 4.10 shows the I–V characteristic of fabricated TLM structure (Sample-G2) measured at 80 ± 3K and displays that the grown In contacts have ohmic behaviour on n-type HgCdTe. Thus, the I-V features of thermally grown In films are reliable and similar to that of metals/n-HgCdTe interfaces used for IR photodetectors with linear I-V characteristics and ohmic behaviour [2,4,9,40].

The current transport mechanism of the In/n-HgCdTe interface, for HgCdTe (x = 0.30 and at temperature 77 K) substrate realizes the current flow in the In/n-HgCdTe contacts because of thermionic field emission (following two types of current-transport mechanisms simultaneously, namely quantum field emission tunnelling and thermionic emission) for the doping concentration ranging from 3.5×10^{16} to 1.6×10^{18} cm^{-3} [4].

The dependence of specific contact resistance (R_c) within the above-two regimes is well defined. The R_c is independent of the doping density (concentration) in the thermionic emission regime. It is a function of the reciprocal exponential carrier concentration root in quantum field tunnelling. High doping concentration creates a narrow depletion layer (thin potential barrier) so that the e^- can pass the potential barrier with a high tunnelling probability. Since the parameters of the HgCdTe-based TLM structure (composition x=0.29, doping concentration: 1×10^{16} $cm^{-3,}$ and I-V measurement temperature: 80 ± 3K) are identical to the reported structures [2,4,9] and hence the current transport in the fabricated In/n-HgCdTe interface most probably occurs due to significant tunnelling and negligible thermionic emission. Thus, the properties of thermally grown In films are suitable to generate an ohmic contact on the n-HgCdTe surface and it could be used in HgCdTe based IR photodetector fabrication.

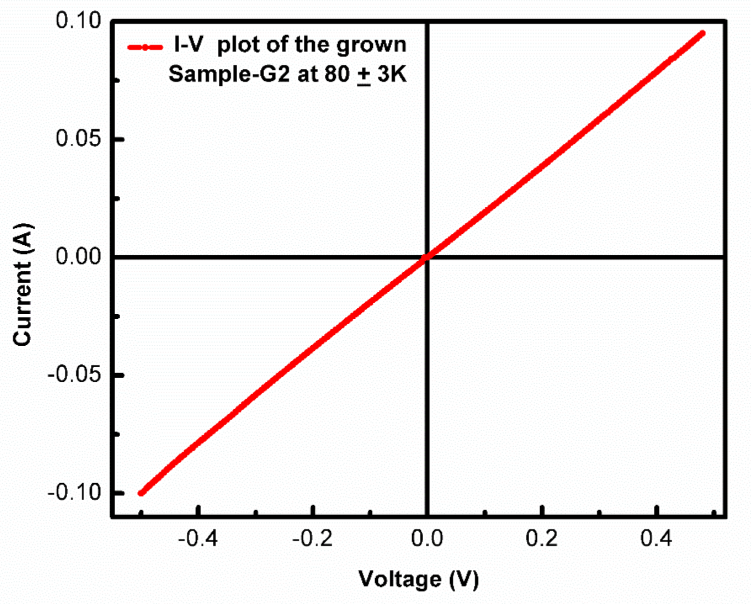

Figure 4.10. I–V characteristics of thermally evaporated TLM structure (Sample-G2, configuration: In/ n/p-HgCdTe, x=0.29) at 80 ± 3 K.

4.3.8. Testing of adhesion and compatibility of In films for HgCdTe-based device fabrication

The tape test shows that thermally grown In films have good adhesion on the HgCdTe substrate and the films are well compatible with the photolithography (PLG) lift-off process of HgCdTe-based detector fabrication.

4.4. Conclusions

The investigation of thermally grown Indium (In) thin films over the HgCdTe surface (substrate) was presented. The properties of grown In films were examined by various characterization techniques to obtain the optimized In film. The polycrystalline In film with a typical tetragonal phase (bcc lattice) and preferred orientation (101) was revealed through structural analysis. The morphological and elemental characterizations indicate that the grown films are uniform, densely packed, smooth with low roughness, and highly pure. The evaluated particle size and film height are 2.15 μm and 4.17 μm, respectively. These optimized indium films were further utilized to form In bumps/HgCdTe and TLM structures (configuration: In/n/p-HgCdTe) for investigating their usefulness in the HgCdTe-based IR detector fabrication process. The indium bumps with optimum particle size, uniform diameter, and height were achieved. In/n-HgCdTe interface has shown linear I-V characteristics (ohmic behaviour) and attained specific contact resistance ρ_c is $5.96 \times 10^{-4}\ \Omega\cdot\text{cm}^2$. The grown In films are adhesive and have shown good compatibility with the photolithography (PLG) lift-off process of HgCdTe-based structure-fabrication. Hence, the evaluated parameters (structural, morphological, compositional, microstructural, and electrical) of the In concluded that this could be utilized as the most appropriate material for creating ohmic n-contact and indium-bumps HgCdTe-based IR photodetector fabrication technology.

References

[1] C. L. Tan, H. Mohseni, Emerging technologies for high performance infrared detectors, Nanophotonics 7 (2018) 169–197.

[2] Z. Tsybrii, Y. Bezsmolnyy, K. Svezhentsova, M. Vuichyk, I. Lysiuk, M. Apatska, M. Smolii, N. Dmytruk, S. Bunchuk, K. Andreeva, F. Sizov, HgCdTe/CdZnTe LPE epitaxial layers: from material growth to applications in devices, J. Cryst. Growth 529 (2019) 125295.

[3] A. Raisanen, D.J. Peterman, A. Wall, S. Chang, G. Haugstad, X. Yu., and A. Franciosi, Yb diffusion barriers at Hg1-x CdxTe interfaces with Al, In, and Cr, Solid State Commun. 71 (1989) 585-589.

[4] P. W. Leech, G. K. Reeves, Specific contact resistance of indium ohmic contacts to n-type Hg1-x CdxTe, J. Vac. Sci. Technol. A 10 (1992) 105.

[5] W. E. Spicer, Metal contacts on Hg1−xCdxTe, J. Vac. Sci. Technol. A 8 (1990) 1174.

[6] Y. X. Wang and P. H. Holloway, Indium ohmic contacts to n-ZnSe, Vacuum 43 (1992) 1149 -1151.

[7] S. Nozaki and A. G. Milnes, Specific contact resistivity of indium contacts to n - type CdTe, J. Electron. Mater. 14 (1985) 137-155.

[8] P. Leech, G. K. Reeves, Properties of HgTe as a contact layer to n-Hg1-xCdxTe, Semicond. Sci. Technol. 8 (1993) 2097.

[9] V. Srivastav, R. Pal, B. L. Sharma, V. Mittal, V. Gopal, and H.P. Vyas, Electrical Properties of Titanium-HgCdTe Contacts, J. Electron. Mater. 34 (2005) 225–231.

[10] P.Y. Emelie, E. Cagin, J. Siddiqui, J.D. Phillips, C. Fulk, J. Garland, and S. Sivananthan, Electrical Characteristics of PEDOT: PSS Organic Contacts to HgCdTe, J. Electron. Mater. 36 (2007) 841–845.

[11] M. Zandian, J. M. Arias, R. Zucca, R. V, Gil, and S.H. Shin, HgCdTe double heterostructure injection laser grown by molecular beam epitaxy, Appl. Phys. Lett. 59 (1991) 1022-1024.

[12] K. M. Kang, J. M. Jo and J. S. Kwak, H. Kim, Y. S. Kim, C. Sone and Y. Park, In/ITO Ohmic Contacts to Ga-face and N-face n-GaN for InGaN-based Light-emitting Diodes, J. Korean Phys. Soc. 55 (2009) 318-321.

[13] S. Y. Moon, J. H. Son, K. J. Choi, J. L. Lee, and H. W. Jang, Indium as an efficient ohmic contact to N-face n-GaN of GaN-based vertical light emitting diodes, Appl. Phys. Lett. 99 (2011) 202106.

[14] S. Palimar, K. V. Bangera, G. K. Shivakumar, Study of the doping of thermally evaporated zinc oxide thin films with indium and indium oxide, Appl. Nanosci. 3 (2013) 549-553.

[15] B.K. Kim, T.H. Kim, D.H. Choi, H. Kim, K. Watanabe, T. Taniguchi, H. Rho, J.J. Kim, Y.H. Kim and M.H. Bae, Origins of genuine Ohmic van der Waals contact between indium and MoS2, NPJ 2D Mater. Appl. 5 (2021) 9.

[16] R. Kay, R. Bean, K. Zanio, C. Ito and D. McIntyre, HgCdTe Photovoltaic detectors on Si Substrates, Appl. Phys. Lett. 51 (1987) 2211.

[17] P. Kozłowski, K. Czuba, K. Chmielewski, J. Ratajczak, J. Branas, A. Korczyc, K. Regi ´nski, A. Jasik, Indium-Based Micro-Bump Array Fabrication Technology with Added Pre-Reflow Wet Etching and Annealing, Materials 14 (2021) 6269.

[18] P. Castelein, F. Marion, J.L. Martin, J. P. Baylet, N. Moussy, O. Gravrand, A. Durand, J.P. Chamonal and G. L. Destefanis, Megapixel HgCdTe MWIR focal plane array with a 15- µm pitch, Infrared Technology and Applications XXIX, Proc. of SPIE, 5074 (2003) 52-59.

[19] J. Jiang, S. Tsao, T. O'Sullivan, M. Razeghi, G. J. Brown, Fabrication of indium bumps for hybrid infrared focal plane array applications, Infrared Phys.Technol.45 (2004) 143–151.

[20] M. Singh and Y.K. Vijay, Electrical, optical and structural properties of indium-antimonide (In-Sb) bilayer film structure, Indian J. Pure Appl. Phys.42 (2004) 610-614.

[21] Q. Huang, G. Xu, Y. Yuan, X. Cheng and L. Luo, Development of indium bumping technology through AZ9260 resist electroplating, J. Micromech. Microeng. 20 (2010) 055035.

[22] P. Lobaccaro, A. Raygani, A. Oriani, N. Miani, A. Piotto, R. Kapadia, M. Zheng, Z. Yu, L. Magagnin, D. C. Chrzan, R. Maboudian, and A. Javey, Electrodeposition of High-Purity Indium Thin Films and Its Application to Indium Phosphide Solar Cells, J. Electrochem. Soc. 161 (2014) D794-D800.

[23] B. Majeed, P. Soussan, P. L. Boterf, P. Bouillon, Microbumping technology for hybrid IR detectors, 10µm pitch and beyond, 2014 IEEE 16th Electronics Packaging Technology Conference (EPTC), 43624540 (2014) 453-457.

[24] R. K. Bhan, V. Dhar, Recent infrared detector technologies, applications, trends and development of HgCdTe based cooled infrared focal plane arrays and their characterization, Opto-electron. Rev. 27 (2019) 174–193.

[25] X. Zhang, C. Meng, W. Zhang, Y. Lv, J. Si, Q. Meng, Design rule of indium bump in infrared focal plane array for longer cycling life, Infrared Phys. Technol. 76 (2016) 631–635.

[26] V. S. Meena, M. S. Mehata, Thermally grown Indium (In) thin-film for creating ohmic contact and In-bumps for HgCdTe-based IR detectors, Appl. Surf. Sci. 596 (2022)153501.

[27] R. S. Parra, P. J. George, G.G. Sa´nchez, A. J. Gonza´lez, L. Ban˜os, P. K. Nair, Optical and electrical properties of Pbs + In thin films subjected to thermal processing, J. Phys. Chem. Solids 61 (2000) 659–668.

[28] P. N. Bartlett, D. A. Cook, C. H. (Kees) de Groot, A. L. Hector, R. Huang, A. Jolleys, G. P. Kissling, W. Levason, S. J. Pearce and G. Reid, Non-aqueous electrodeposition of p-block metals and metalloids from halometallate salts, RSC Adv. 3 (2013) 15645–15654.

[29] R. Das and R. K. Soni, Synthesis and surface-enhanced Raman scattering of indium nanotriangles and nanowires, RSC Adv. 7 (2017) 32255–32263.

[30] S. R. Kumar, B. Prajapati, S. K. Tiwari & V. K. Tiwari, Growth and characterization of copper, indium and copper-indium alloy films non-aqueous method of electrodeposition, Indian J. Pure Appl. Phys. 46 (2008) 198-203.

[31] K. Ulutaş, D. Değer, N. Kalkan, S. Yıldırım, Y. G. Çelebi, Y. Iskarlatos, M. L. Öveçoğlu and A. Genç, Structural properties of In-In2O3 composite films, IOP Conf. Ser.: Mater. Sci. Eng. 15 (2010) 012095.

[32] R. P. Reed, C. N. McCowan, R. P. Walsh, L. A. Delgado and J. D. McColskey, Tensile Strength and Ductility of Indium, Mater. Sci. Eng. A, 102 (1988) 227-236.

[33] G. Lee, J. Y. Kim, A. S. Budiman, N. Tamura, M. Kunz, K. Chen, M. J. Burek, J. R. Greer, T. Y. Tsui, Fabrication, structure and mechanical properties of indium nanopillars, Acta Mater. 58 (2010) 1361-1368.

[34] S. E. Al Garni, A. F. Qasrawi, Effect of Indium nano-sandwiching on the structural and optical performance of ZnSe films, Results Phys. 7 (2017) 4168-4173.

[35] M. A. Hafez and H. E. Elsayed-Ali, Femtosecond pulsed laser deposition of indium on Si (100), J. Laser Micro Nanoeng. 1 (2006) 44-47.

[36] H. Qiuping, X. Gaowei, Q. Gang, Y. Yuan, and L. Luo, Electroplated indium bump arrays and the bonding reliability, J. Semicond. 31 (2010) 116004.

[37] H. Yuyang, Z. Yuxiang, Y. Zhizhen, C. Guoxin, H. C. Liu, B. Lifeng, Y. Hui, and Z. Yaohui, Indium bump array fabrication on small CMOS circuit for flip-chip bonding, J. Semicond. 32 (2011) 115014.

[38] A. M. Biktashov, N. B. Kuzmin, A. G. Paulish, Indium Bumps Investigation for the Flip-chip Assembly, International Workshops and Tutorials on Electron Devices and Materials (EDM), 10583331 (2006) 35-37.

[39] Y. Tian, C. Liu, D. Hutt, B. Stevens, Electrodeposition of Indium for Bump Bonding, 2008 58th Electronic Components and Technology Conference (ECTC), 21632652 (2008) 2096-2100.

[40] A. Singh, A. K. Shukla, S. Jain, B. S. Yadav, R. Pal, Electrical characteristics of electroless gold contacts on p-type Hg1-xCdxTe, Mater. Sci. Semicond. Process. 26 (2014) 294–300.

[41] T. Abbas, L. Slewa, Transmission line method (TLM) measurement of (metal/ZnS) contact resistance, Int. J. Nanoelectron. Mater. 8 (2015) 111-120.

[42] T. V. Blank and Y. A. Goldberg, Mechanisms of Current Flow in Metal–Semiconductor Ohmic Contacts, Semiconductors 41 (2007) 1263–1292.

[43] V. Krishnamurthy, A. Simmons, C.R. Helms, Oxide interfacial layers in Au ohmic contacts to p-type Hg1-x CdxTe, Appl. Phys. Lett. 56 (1990) 925.

[44] V. S. Meena, M. S. Mehata, Investigation of grown ZnS film on HgCdTe substrate for passivation of infrared photodetector, Thin Solid Films 731 (2021) 138751.

Chapter 5

Structural, compositional, morphological and electrical characteristics of thermally evaporated Au Ohmic contact on p-type HgCdTe substrate

5.1. Introduction

Infrared (IR) detectors have become very useful in defence, medical science, astronomy, meteorology, earth, and planetary remote-sensing, etc. [1-5]. There are various IR materials available in the modern world like mercury cadmium telluride (HgCdTe), quantum well-infrared photo detectors (QWIP: GaAs/AlGaAs), type-II super lattices (T2SL), etc. However, HgCdTe material's unique properties (electrical and optical) established it as the most popular material among the available IR materials for the development of third-generation infrared sensors (like a multicolour detector, avalanche photodiode, and high-temperature operation), which could be fulfilled the current and future technology requirements [2-8]. Two major factors can affect the performance and reliability of HgCdTe-based IR photodetectors: (i) the nature of the metal/HgCdTe contact interface (the metal contacts must have Ohmic behaviour bearing low contact resistance & linear current-voltage curve) and (ii) features of metal/HgCdTe contact interface like uniformity, reproducibility, reliability, and long-lasting steadiness in a high working temperature, etc. [8-11]. The properties of HgCdTe material, like its delicate nature (weak Hg–Te bond) and the stability of HgCdTe concerning time & temperature, might also be problematic factors for generating desired Ohmic metal contacts.

******Part of this work has been published in* ***Optical Materials 141 (2021) 113943(Elsevier)****.*

The surface treatment and metal-deposition techniques play a vital role in realizing the excellent performance of IR detectors. The metal deposition process may have various probabilities like decomposition of HgCdTe in the surface layer (especially mercury telluride: HgTe), interdiffusion of metal into the HgCdTe, outward-diffusion of HgCdTe elements from the deposited metal layer, etc. The energetic metal atoms (energy of atoms: several eV) may create impurity levels on the HgCdTe surface because of their diffusion into HgCdTe, whereas an accumulation region at the HgCdTe-metal interface is generated due to easy out-diffusion of weakly bonded Hg atoms from HgCdTe. This reaction may result in degradation of contact**,** timely surface dissociation, and thermal-stability variation during packaging and detector usage. Therefore, metal contact formation on HgCdTe at room temperature is another significant factor in the instability of the contacts. The formation of Cd vacancies and excess Te at the HgCdTe surface during the surface treatment (chemical etching of HgCdTe using HBr and Br_2 solution) is also responsible for the performance of the IR detector. The surface treatment is essential before the metal deposition on the HgCdTe substrate because the physical properties of metal contacts strongly depend on the surface-treatment method and metal-deposition technique, as reported [5,8,11-13].

The interfacial reactions of HgCdTe with different metals or semiconductors over layers have an essential role in deciding the nature of metal/MCT interfaces of the IR devices. The overlayer can be classified into four categories: ultra-reactive (Ti, Yb, Sm, and Sn), reactive (Al, In, Cr, and Si) and intermediate (Ge, Ag, Cu, Pt, and Pd), and unreactive (Au and Sb). The behaviour of over-layer metals/HgCdTe interface can be affected by factors like Sample history, surface preparation, wet etching, etc. [9,11,14-16]. Various metals are utilized to form contacts on HgCdTe, like Al, Ag, Cu, Ti, Pd, Pt, Ge, and HgTe. Metals (Ag, Cu, Pd, Pt, Sb, and Ge) demonstrate rectifying behaviour, whereas metals (Au and Al) have created nearly ohmic contacts. HgTe metal generates contact with Ohmic nature, but high-cost and complicated growth equipment (metal-organic chemical vapour deposition and molecular beam epitaxy techniques) are required to grow this metal. Also, the deposition temperature is high enough to alter the properties of the HgCdTe substrate. Ti and the organic contacts PEDOT: PSS (3, 4-polyethylene dioxythiophene: polystyrene sulfonate) can also be applied to form n and p-type Ohmic contact on HgCdTe [9,11,16-19]. The ohmic contacts on the HgCdTe were created using the metals (Au/Sn, Au/In) by ion beam sputtering and deposition methods [18-21]. Generally, Au is used for Ohmic contact formation in p-type HgCdTe substrates, but it (creating Ohmic contact on p-HgCdTe) is a very challenging task. The ohmic contact for the p-HgCdTe substrate can be accomplished by adopting the low-temperature deposition method, high adhesion, low contact resistance, etc. [5,12,13].

Researchers [5,8,9,22] have made efforts to fulfill these shortcomings. V. Krishnamurthy *et al.* [22] have conveyed the Ohmic behaviour of the HgCdTe/Au interface with low contact resistance where the Au contact was prepared using electroless and thermal evaporation growth techniques. Vanya *et al.* [8] have applied a multilayer metal scheme (Ti/Pt/Au) to fabricate the HgCdTe photoconductive detector. The metal contacts (TLM structure) produced through DC sputtering deposition technique have exhibited an Ohmic behaviour at low and room temperatures. A recent report [5] states that various IR detectors could be fabricated (like discrete detectors and multielement focal plane arrays: FPAs) with Mo/Au and Mo/In-based Ohmic metallic contacts, where the metals have been grown by thermal evaporation and magnetron sputtering deposition techniques. Another report [9] claimed to rectify the issues of high contact resistance, which may affect the performance of large format/fine pitch detector arrays. The low contact resistance for the electroless Au/HgCdTe interface was reported [9]. Although reports [5,8,9] show the utility of Au Ohmic contacts in the HgCdTe-IR photodetector fabrication and thoroughly discussed the electrical properties of these Ohmic contacts. All the other issues, like compositional, morphological, and structural properties, etc., were not covered as these are equally important for a better understanding of the electrical behaviour of Au/HgCdTe contacts. Some reports [23-25] have involved all these belongings to study AuTiAlTi/AlGaN/GaN contact (HFET structure), Ta/Ti/Ni/Au/n-GaN contact, and Pt/Re/Au/p-GaN interface. These reports [23-25] cover only the issues related to Au metal contacts grown on other substrates except for HgCdTe.

In the present work, an attempt has been made to address all the aspects like structural, compositional, morphological, and electrical properties of thermally evaporated Au metal thin film on p-type HgCdTe substrate. Since all these properties have an important role in achieving good quality ohmic contacts (for Au/p-HgCdTe interfaces) and that is necessary for the fabrication of higher format HgCdTe IR detectors with optimum performance. The grown Au films were evaluated using different characterization techniques such as X-ray diffraction (XRD), energy dispersive x-ray (EDX), atomic force microscopy (AFM), scanning electron microscopy (SEM), etc. The resulting optimized Au films were further employed in fabricating the “Transfer length method (TLM)” structure having configuration (Au/p-HgCdTe). Subsequently, the current-voltage (I-V)/resistance measurement for the fabricated TLM structure was performed to find out the electrical properties of the Au film, through which the specific contact resistance of Au-metal contacts was revealed. Thus, the thermally evaporated Au film could be an effective and appropriate ohmic contact metal for HgCdTe IR photodetector fabrication.

5.2. Experimental section

5.2.1. Preparation of HgCdTe surface and deposition of Au film

The p-$Hg_{1-x}Cd_xTe$ epitaxial layers were grown on CdZnTe (111) lattice-matched substrate through the in-house liquid phase epitaxy (LPE) growth method. A Te-rich melt/solution in a specified ratio (i.e. Hg:0.71, Cd:0.29 and Te elements, where composition x: 0.29) was put into a tube fixed in the furnace and this melt was converted into a homogeneous one through heating it at the temperature of 490 °C > the HgCdTe growth temperature: 475 °C. Subsequently, the melt was cooled to a temperature of 475 °C, and CdZnTe substrates were put into this melt for some time of 30-40 min. Resultantly, HgCdTe epilayers with the parameters (dimensions: 30×30 mm^2, thickness: 18-20μm**,** composition x: 0.29**,** carrier-concentration: 1×10^{16} cm^{-3}**,** mobility: 416 cm^{-2} V^{-1}s^{-1}) were originate. Four HgCdTe epilayers, namely A, B, C, and D, with the aforesaid parameters (dimensions: 30×30 mm^2, thickness: 18-20μm) have been used for the investigation of Au films. The reasonable/desired dimension (10μm) of these HgCdTe epilayers (A, B, C, and D) was achieved by mechanical polishing, which was performed with the Al_2O_3 (alumina powder: 0.05 μm). Successively, the solution of (I_2: KI: $C_2H_6O_2$) :: (1g: 4g: 10 ml) and KOH was applied for the chemical-mechanical polishing of the epilayers to achieve oxide free surface with good morphology. Then, the epilayer was washed and dried using de-ionized (DI) water and highly pure $N_{2,}$ respectively. Out of these four, three epilayers (A, B, and C) were diced into pieces of the same dimensions 30×15 mm^2 (namely Samples A1, A2, B1, B2, C1, and C2) where Samples (A1, A2, B1, and B2) were used in many growth experiments (of various deposition rates) to achieve an optimized Au thin film. Then characterization techniques such as XRD, EDX, and non-contact sheet resistance measurement were utilized to examine the grown films. To execute this study, a standard and conventional cleaning procedure (which includes 5 min heating of Samples in each chemical sequentially, i.e., in trichloroethylene, acetone, and methanol) was adopted to clean the surface of epilayer A (A1 and A2). Samples were carried out through a chemical etching process (for 20 sec using 0.1% bromine in methanol solution) followed by successive washing (with DI water) and drying (with highly pure N_2) processes, respectively. Sequentially baking samples at 90 °C (to remove the residual water content/environmental moisture from the sample's surface) for 5 minutes were also performed. Before Au film deposition, the quality of the HgCdTe Samples (A1 and A2) surface was examined through microscopic and ellipsometry observations to ensure a defect and contamination-free surface. These samples were immediately transported into the vacuum chamber (coating unit model: HHV 20F10) and the source material Au (purity: 99.99%) was put into a molybdenum boat. After achieving the required pressure of the order of 6×10^{-7} Torr within the vacuum chamber, the Au film (thickness: 200 ± 5 nm) deposition on Samples (A1 and A2) was accomplished at the parameters (deposition rate: 3Å/sec; evaporation current: 97-109 A), while the source to sample (substrate) distance was fixed at 30 cm. The rate of deposition and film thickness was monitored by an auto rate controller (attached with a quartz crystal monitor). The process of Au thin-film growth was performed at 25 °C (room temperature). Epilayer B (Samples B1 and B2) was also carried out through a similar treatment (cleaning, etching, washing, baking, etc.) given to the epilayer-A (Samples A1 and A2). Au films of the same thickness were grown on Samples (B1 and B2) at the deposition rate: 10 Å/sec, with evaporation currents of 122-130 A. The non-contact sheet resistance measurement has established the desired value of conductivity (5.12×10^5 mho/cm) for the Au films grown at a higher deposition rate: 10 Å/sec. Afterward, XRD, as well as EDX characterization techniques, have also realized the higher deposition rate of Au films with the desired structural parameters (cubic structure) and composition (purity). Thus, the deposition rate (Au: 10Å/sec) has been optimized for Au film deposition on the HgCdTe substrate. Subsequently, the optimized deposition parameters were used for further investigations of epilayer-C (Samples C1 and C2) and epilayer-D (Sample-D). Au films (thickness: 200 ± 5 nm) on Samples (C1 and C2) were grown at the optimized process parameters (pressure: 6×10^{-7}

Torr, deposition rate-10Å/sec, and the evaporation current: 122-130 A) to discover the morphological and microstructural features of films. The optimized Au-films were further utilized to study the electrical characteristics of HgCdTe (Sample-D) based TLM structure. The fabrication of TLM structure on Sample-D was started with the similar processing steps of the other three Samples, A, B, and C (like chemo-mechanical polishing, prolonged cleaning, chemical etching, etc.) followed by the microscopic and ellipsometry observations, which confirm the defect and contamination-free surface of Sample-D. A photolithography process was executed to generate the desired TLM pattern on Sample-D. Subsequently, a descum-process for Sample-D was performed by bombarding the sample in an oxygen plasma (pressure: 10^{-1} - 10^{-2} Torr, power: 100 W, O_2 flow rate: 200 ml/minute) for approximately 30 sec. After this, Au thin film (thickness: 200 ± 5 nm) was deposited on Sample-D at the chamber pressure of 6×10^{-7} Torr, and then a photolithography lift-off process (using acetone) was performed to produce the resulting TLM structure.

5.2.2. Characterization techniques

XRD diffractometer (Model: Analytical B.V.-X'Pert PRO MRD, CuKα-source with λ: 0.1542 nm**)** was used to evaluate the structural properties of grown Au films. The resulting X-ray diffractograms of Au films were attained at the parameters of grazing angle of 3° and 2θ of 20-85°). AFM (Model-5600LS, Agilent Technologies) system has realized the morphological statistics of thermally grown Au-films. Microstructural and compositional findings of Au films originated from a FESEM (attached with an EDX Spectrometer, Model-Carl Zeiss SUPRA, working voltage: 5-20 kV) characterization technique. A cryo-prober of Keithley Parametric analyzer (Model: 4200 having integrated 4200-CUV card**)** was utilized for current-voltage (I-V)/resistance measurements of the fabricated TLM structure (configuration: Au/p-HgCdTe), and I-V characteristic for the test-structure was recorded at a temperature of 80 ± 3 K.

5.3. Results and discussion

5.3.1. Structural analysis

XRD measurements of the Au/p-HgCdTe samples grown by various deposition rates (Sample-A1: 3 Å/sec, Sample-B1: 10 Å/sec) have been performed to assess the structural properties of the Au-film, and the resulting diffractograms are shown in Fig. 5.1(a,b). Sample-A1 exhibited five diffraction peaks at 2θ values of 38.30°, 44.46°, 64.70°, 77.70°, and 81.90° (Fig. 5.1a), which could be assigned to (111), (200), (220), (311) and (222) planes of Au fcc-structure, respectively [26-29]. Sample-B1 displays five similar diffraction peaks, but some of the peaks are slightly shifted towards the lower 2θ values (Fig. 5.1b) relative to Sample-A1 (Fig. 5.1a). The diffraction peaks of Sample-B1 along the 2θ axis are 38.26°, 44.46°, 64.66°, 77.70° and 81.86°, respectively. These peaks are associated with the planes (111), (200), (220), (311), and (222) of a typical Au *fcc*-structure (JCPDS no. 04-0784), as reported in the literature [26-29].

The diffraction peak Au (111) of the Samples (A1) and (B1**)** is relatively more intense than the other four peaks, as shown in Fig. 5.1(a, b). The cubic and polycrystalline Au films with the preferred orientation Au (111) were confirmed for the HgCdTe Samples (A1 and B1). The measured FWHM values for the dominant peak Au (111) of the samples (Sample-A1: 0.0062 rad and Sample B1: 0.0057 rad) indicate that the crystallinity of Samples-B1 has been upgraded. Since the crystallinity of the films is related to the FWHM of the diffraction peak and according to that the diffraction peak with low FWHM is more crystalline than the diffraction peak of high FWHM. Thus, Sample-B1 (rate-10 Å/sec) is slightly more crystalline than Sample-A1 (rate-3 Å/sec) because of its relatively low value of FWHM than Sample-A1. The XRD plots (Samples

A1 and B1) also state that the peak intensity varies with the increasing deposition rate. Two diffraction peaks, Au (220) and Au (311) of Sample-B1 (rate- 10 Å/sec) are relatively more intense than the corresponding peaks of Sample-A1 (rate- 3 Å/sec). So, the increased peak intensity is also accountable for the higher crystallinity of Sample-B1 (rate-10 Å/sec), which was grown at a relatively higher deposition rate than Sample-A1 (rate-3 Å/sec).

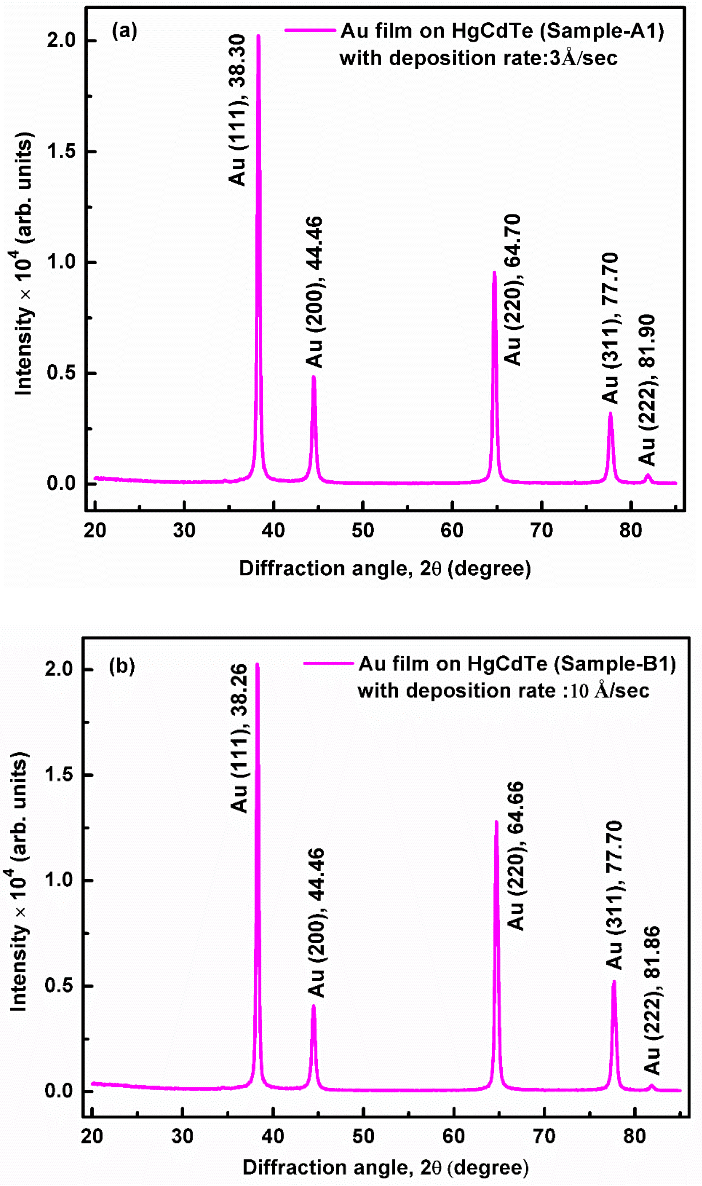

Figure 5.1. XRD patterns of Au films grown over HgCdTe Samples (A1 and B1) at deposition rates of Au-3 Å/sec (a) and Au-10 Å/sec (b).

Thus, the developed Au thin film of Sample-B1 (rate-10 Å/sec) has shown a good agreement with the early reported thermally evaporated Au film [27].

The well-known Eq. 5.1 (relation between the first-order Bragg's equation and the d-spacing formula) was used to evaluate the lattice constant (a) of Au film:

$$a = \frac{\lambda\sqrt{h^2+k^2+l^2}}{2\sin\theta} \tag{5.1}$$

Here λ and θ represent the x-ray wavelength and diffraction angle, respectively, while h, k, and l are the miller indices of a crystal plane. The average grain size (D) estimation for the Au film was done using the well-known Debye-Scherrer formula (Eq. 5.2) as follows:

$$D = \frac{0{\cdot}94\lambda}{\beta\cos\ \theta} \tag{5.2}$$

Here, β is the FWHM (full-width at half-maximum) of the diffraction peaks, and θ is the diffraction angle. Strain (ε) of the thin film can be expressed as the ratio of $(\mathrm{a}-\mathrm{a}_0)/\mathrm{a}_0$, wherever a and a_0 represent the lattice constants of thermally grown Au film and standard Au material. Eq. 5.3 was used to evaluate the strain (*ε)* of Au film.

$$\varepsilon = \frac{\beta}{4\tan\theta} \tag{5.3}$$

The estimated structural parameters (β: FWHM, a: lattice-constant, D: Average crystallite- size**,** ε: strain) evaluated with XRD parameters **(**2θ**,** diffraction-peaks and lattice-plane**)** are listed in Table 5.1. A good agreement between the obtained experimental and theoretical (standard) values of the lattice constant was obtained.

Hence, the properties of Au film and standard/bulk Au material are the same. The structural parameters (D: Average grain size, **ε**: strain) of thermally grown films are also comparable and acceptable to the reported Au films [26,27]. It demonstrates the validation of the conventional/established thermal evaporation technique, which could generate the Au metal films of desired crystalline quality**.** Thus, structural parameters (Table 5.1) of both the Au films (Samples A1 and B1) verify that a relatively higher crystalline film can be obtained at a deposition rate of 10 Å/sec, and it was treated as the optimized deposition rate.

Table 5.1: Calculated structural parameters of Au film (Samples A1 and B1) for the dominant plane (111).

Structural parameters	**Estimated values for Sample-A1 (Rate: 3 Å/sec)**	**Estimated values for Sample-B1 (Rate: 10 Å/sec)**
2θ (degree)	38.30	38.26
Lattice plane (hkl)	(111)	(111)
FWHM, β (rad)	0.0062	0.0057
Lattice-constant, a (Å)	4.071	4.075
Average grain size, D (nm)	24.91	27.06
Strain, **ε**	0.0044	0.0041

5.3.2. Elemental analysis

The EDX characterization technique was used to perform the elemental analysis of the thermally evaporated Au thin film grown over the HgCdTe substrate. The resultant EDX spectra of Au/p-HgCdTe samples prepared at different deposition rates (Sample-A2: 3 Å/sec; Sample-B2: 10 Å/sec) are shown in Fig. 5.2 (a and b). Fig. 5.2(a) represents the EDX spectrum of Sample-A2 (rate: 3 Å/sec), containing the peaks of carbon (C), phosphorous (P), and gold (Au) elements, respectively. The elements P and C are minimal, while the high peak intensity of the Au element shows its maximum contribution to the thermally grown film. Similarly, Sample-B2 (rate: 10 Å/sec) displays the Au and P elements peaks, as shown in Fig. 5.2(b), where the contribution of Au within the grown film is maximum except for a minor proportion of the P element.

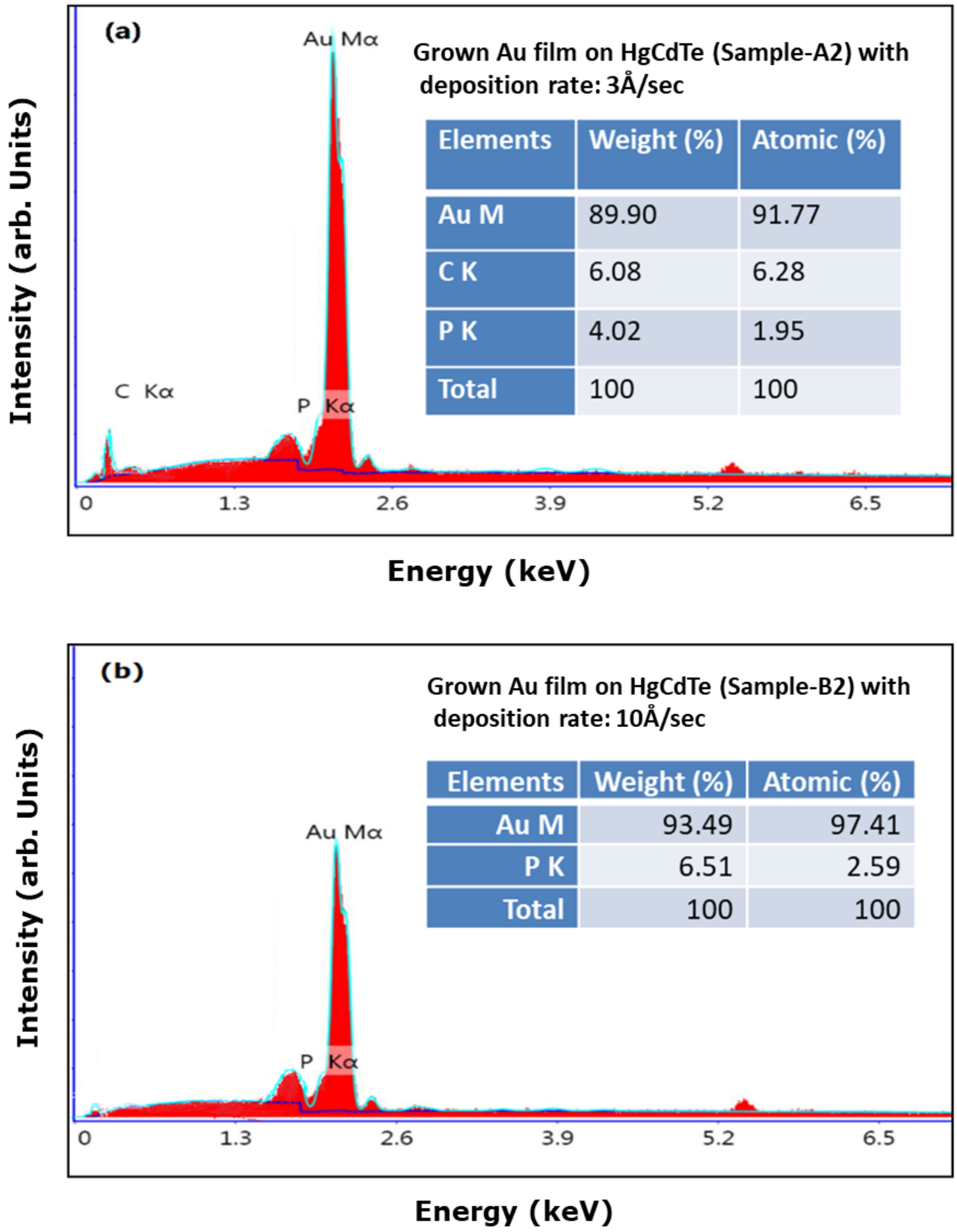

Elements	Weight (%)	Atomic (%)
Au M	89.90	91.77
C K	6.08	6.28
P K	4.02	1.95
Total	100	100

Elements	Weight (%)	Atomic (%)
Au M	93.49	97.41
P K	6.51	2.59
Total	100	100

Figure 5.2. EDX-SEM images and spectrum of thermally deposited Au film on HgCdTe Samples (A2 and B2) at deposition rates of Au-3 Å/sec (a) and Au-10 Å/sec (b).

The EDX results of Au film grown on HgCdTe samples (Sample-A2: 3 Å/sec; Sample-B2: 10 Å/sec) at various deposition rates (rate: 3 Å/sec, rate: 10 Å/sec) are listed in Table 5.2. Although Sample-B2 has a relatively more amount of element P (weight: 6.51 %, atomic: 2.59 %) than Sample-A2, which may affect the purity of Au film, a more proportion of Au element (weight: 93.49 %, atomic: 97.41%) has been achieved in the Sample-B2 compared to Sample-A2 (weight: 89.90 %, atomic: 91.77 %). Accordingly, the purity of Sample-B2 (in terms of Au element ratio) is enhanced since the contaminating element-C is not present in its spectrum. Some other peaks of negligible intensities have also been observed in EDX spectra of Samples A2 and B2, which may arise due to traces of atmospheric water vapours and carbon adhesive used during EDX sample preparation.

Table 5.2: Comparison of EDX results of Au films grown on HgCdTe Samples (A2 and B2) at different deposition rates.

Sr. No.	**Sample-A2** **(Rate: 3 Å/sec)**		**Sample-B2** **(Rate: 10 Å/sec)**	
Elements	**Weight (%)**	**Atomic (%)**	**Weight (%)**	**Atomic (%)**
Au M	89.90	91.77	93.49	97.41
C K	6.08	6.28	-	-
P K	4.02	1.95	6.51	2.59
Total	100	100	100	100

Thus, the elemental analysis of Samples-A2 and B2 demonstrated that a relatively pure Au film might be produced at the deposition rate: 10 Å/sec and it was considered the optimized deposition rate. The thermally grown high-purity thin film on HgCdTe substrate with desired Au element was confirmed through this EDX analysis and showed excellent agreement with several reports of Au films [23,30-35]. This highly pure Au film is very helpful in generating a contact of low specific contact resistance on the HgCdTe substrate since any impurity within the Au contact can affect the performance (in terms of degraded quality of the film) of the IR detector.

5.3.3. Surface morphology

The morphology of thermally evaporated Au film on HgCdTe Sample-C1 was investigated using the AFM measurement. Since soft, fragile, and adhesive samples like HgCdTe may face problems (related to friction, electrostatic force, and adhesion) during this measurement. Therefore, AFM scans of thermally grown Au thin film (Sample-C1) were performed in a relevant mode (intermittent or tapping mode with high resolution) at the desired parameters like temperature (20-25 °C) and humidity (40-45 %).

The obtained AFM images (2D and 3D) and the linear image profile of Sample-C1 (Au thin film thickness: 250 nm, scanning area: 2.0 μm × 2.0 μm) are shown in Fig. 5.3(a, b, and c). Accordingly, it can be estimated that thermally grown Au film is very dense and uniform. Several highly-dense islands within the film are interconnected via minor and paddy-like granules, as shown in Fig. 5.3(a, c). The measured RMS (root-mean-square) roughness of Au thin film is 4.19 ± 0.02 nm. The linear profile (Fig. 5.3b) indicates that the average lateral diameter and grains (particles) heights of the grown films are 35-85 and 6-15 nm, respectively. The lateral diameter (AFM) is comparable to the average crystallite size (D: 24.91-24.91 nm) evaluated through XRD measurement. Thus, the evaluated surface morphological parameters (lateral grain diameter, lateral height, and RMS surface-roughness**)** of thermally-evaporated Au film were found very close to the Au films (thickness: 10-150 nm) reported in the literature [27,36-41].

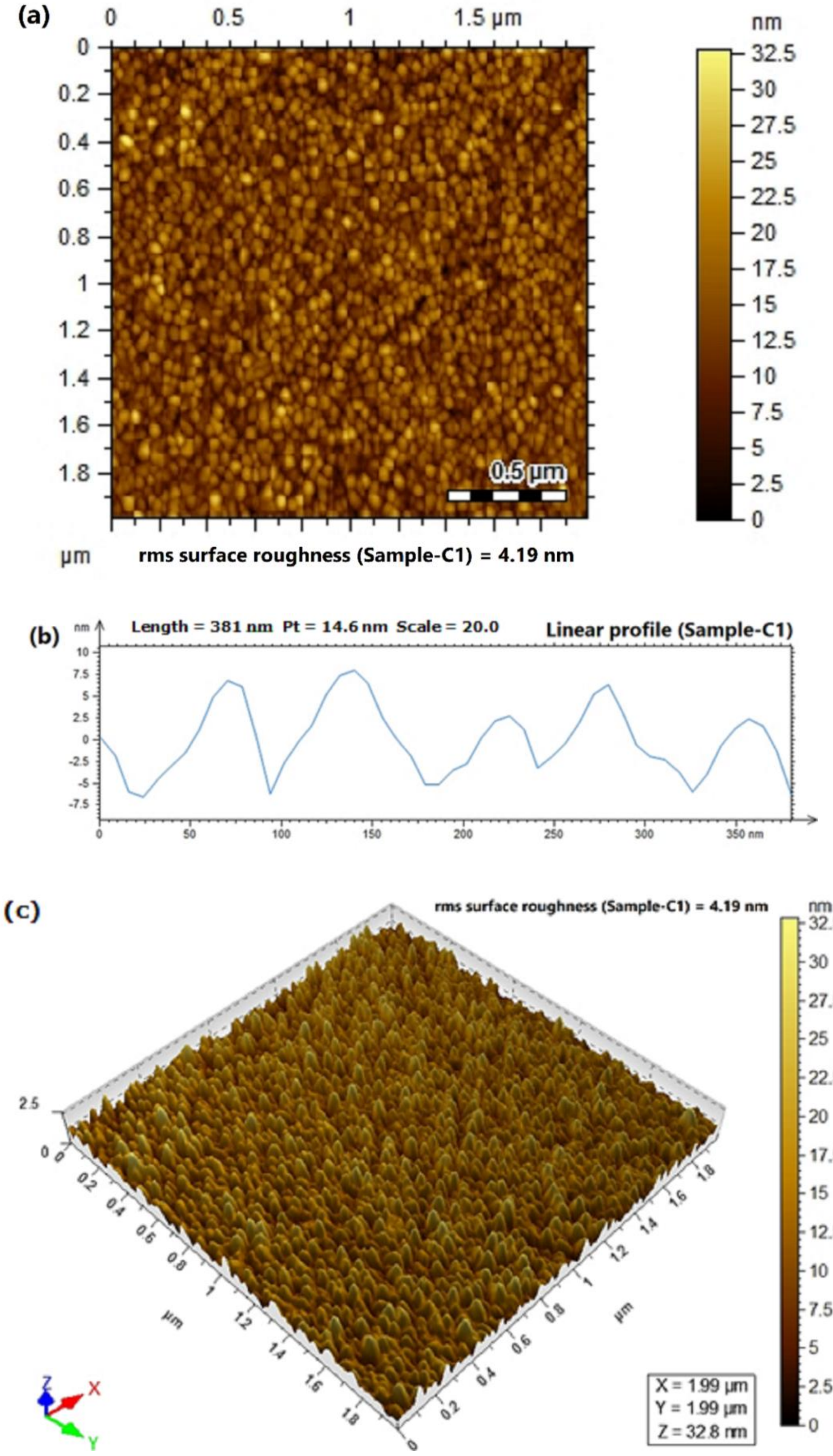

Figure 5.3. 2D and 3D AFM images (2 µm × 2 µm) of grown Au film on HgCdTe Sample-C1 along with their linear profile: 2D image (a), linear profile (b) and 3D image (c).

Thermally grown Au film has low surface roughness and is very useful in creating the Au-based interface (Au/p-HgCdTe) with low specific contact resistance since the charges can easily transport through this interface because of the least blocking effects in their path. This estimation has been validated through the electrical properties where the Au/p-HgCdTe interface of low specific contact resistance is achieved. Consequently, the achieved morphological results (uniform, densely packed, and low roughness) of Au thin film might be very suitable for HgCdTe-based IR detectors.

5.3.4. Microstructural analysis

Since the long-lasting stability of a thin metal film is responsible for the performance of IR devices in an extreme environment, it may depend upon the features of the grown metal film. Therefore, it is essential to minimize the undesirable microstructural features (like cracks, voids, hollows, defects, more grain boundaries, etc.) of the deposited metal film since their existence can degrade the performance of the fabricated device. Accordingly, the thickness of Au film (200 nm) was optimized to achieve a highly dense and conducting film with minimum defects (cracks) and voids. SEM measurement technique (an effective and frequently used analytical tool for studying the semiconductor device surface, cross-sectional and failure analysis, etc.) was used to investigate the microstructural features of grown Au-film on Sample-C2. The SEM images (at various scales and magnifications) of measured Sample-C2 are shown in Fig. 5.4(a, b, and c). Fig. 5.4a (1.0 µm, 100 Kx) discloses that the deposited Au film appears dense, continuous, and uniform, excluding one spot within the surface of the film. Fig. 5.4b (200 nm, 77.31 Kx) and Fig. 5.4c (100 nm, 301.82 Kx) revealed that the film is mainly made from interconnected nanoparticles of spherical shape. Still, some hexagonal nanoparticles also exist within the film.

Thus, the most familiar and necessary topographies of Au particles were achieved. The size of a typical nanoparticle is 24.86 nm (Fig. 5.4c), and it shows a fair agreement with the grain size evaluated through AFM. The cross-sectional view of the Au thin film is shown in Fig. 5.4d (200 nm, 102.18 Kx), which has realized the flat and discrete Au clusters (islands) within the deposited film.

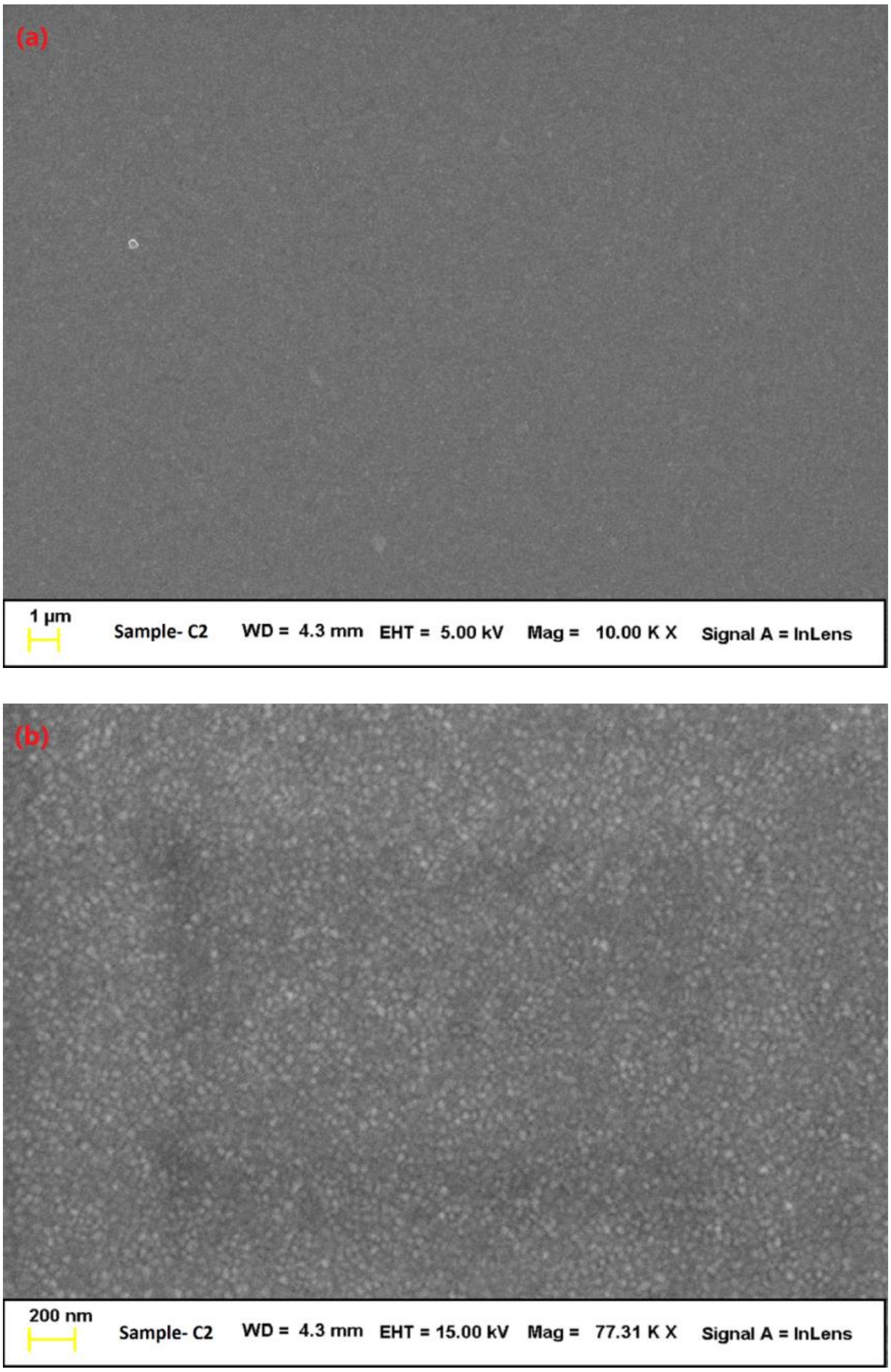

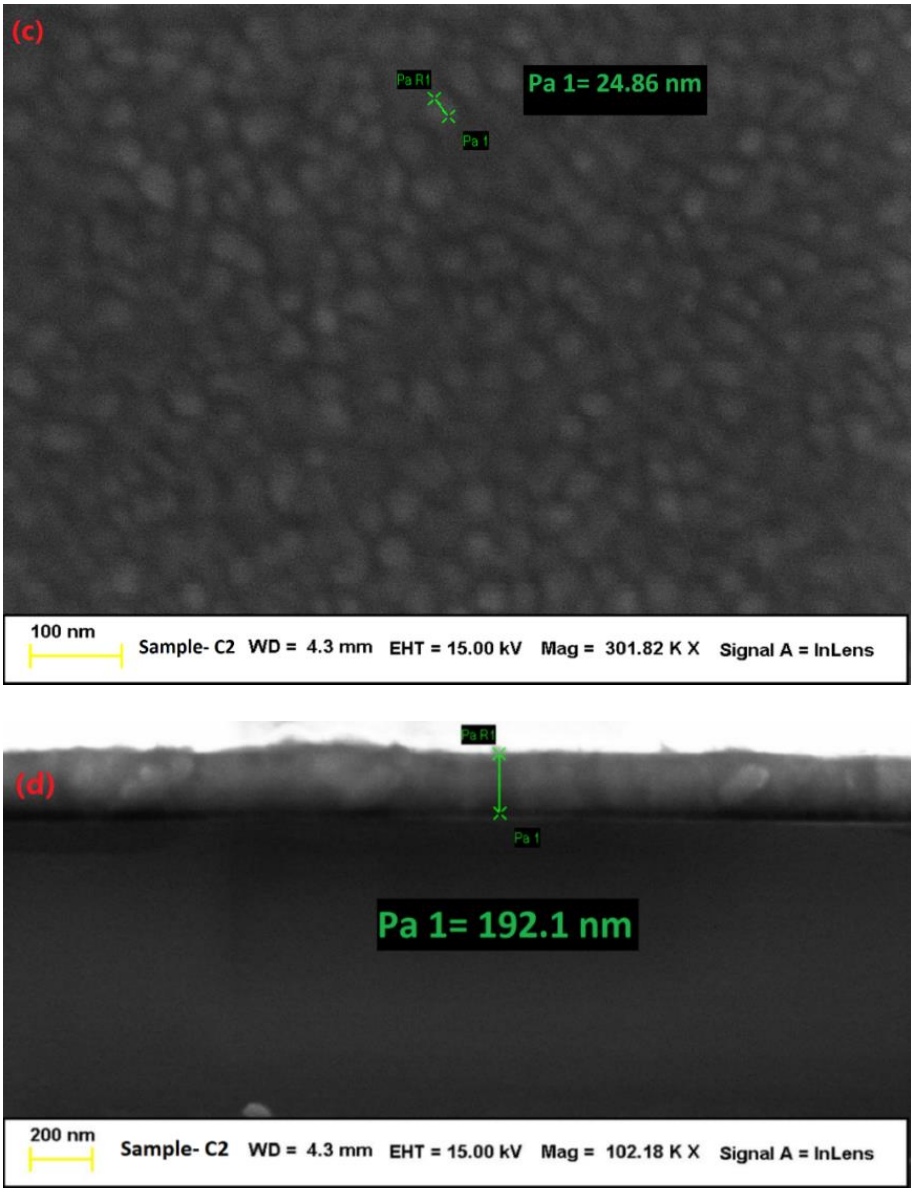

Figure 5.4. SEM images of grown Au film on HgCdTe Sample-C2 at various scales/ magnifications of 1 µm, 10.00 KX (a) 200 nm, 77.31 KX (b) 100 nm, 301.82 KX (c) and cross-sectional view of Au thin film at 200 nm, 102.18 KX (d).

It may be predicted from this cross-sectional view that a preferential growth of the Au cluster occurs along the vertical direction. The increasing surface coverage/close contact formation among the clusters leads to extra adsorption since this (adsorption) is a surface phenomenon that depends upon the surface area/coverage. A more number of adsorbing sites will be available in the case of increasing surface area. Thus, this adsorption phenomenon is responsible for the growth of film in a vertical direction only since the boundary of the moving cluster suppresses the adjacent (lateral) thin-film growth. The estimated thickness (height) of the grown thin film is 192.10 nm (Fig. 5.4d), and it was found to be approximately equal to the actual thickness (200 nm) monitored by the auto-rate controller.

Hence, the microstructural findings of thermally grown Au thin films have shown excellent agreement with the best-reported results [30-32,36,42,43]. Thus, the SEM is an effective and reasonable analyzing tool to evaluate the quality of grown metal films. The SEM analysis of grown Au film also validates thermal evaporation as an optimized deposition technique, creating the Au thin film of desired and perfect topography without any cracks over the surface. The thermally grown Au thin film (smooth step coverage, columnar growth, negligible voids, and tighter metallurgical grain boundaries) is comparable to the reported Au metal films used for HgCdTe-based IR detector fabrication [20]. Therefore, the Au film could be beneficial in creating the ohmic contacts of low contact resistance necessary for developing extremely reliable HgCdTe IR detectors of high-performance, high-density, and minor dimensions.

5.3.5. Electrical responses of Au thin film

I-V/resistance measurement of HgCdTe Sample-D based TLM structure (Au/p-HgCdTe) was executed to find the electrical properties of grown Au thin film. The TLM pattern has eight contact pads of the same area of 100 × 200 μm^2 (length L=100 μm and width W= 200 μm of all the contact pads are identical) and varying interpad spacing, d1- 50 μm, d2- 100 μm, d3-150 μm, d4 - 200 μm, d5 - 250 μm, d6 - 300 μm and d7 - 350 μm respectively (spacing between adjacent contact pads is varied) as demonstrated in the schematic of fabricated TLM structure (Fig. 5.5). Resistances between all the adjacent contact pads were measured, and a plot of resistance versus interpad spacing (separation) was constructed to evaluate sheet-resistance R_{sh} and transfer-length L_T.

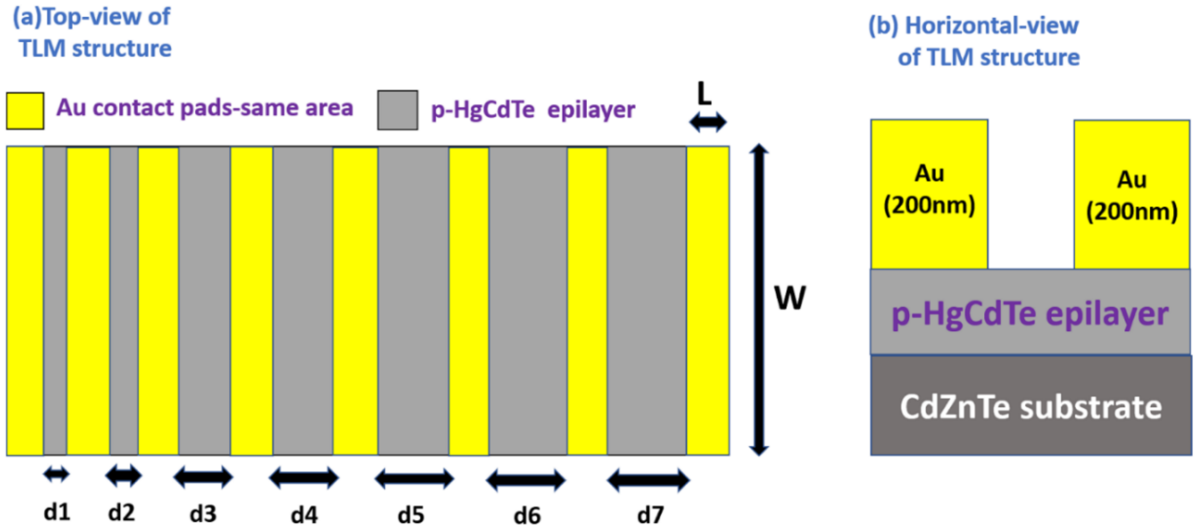

Figure 5.5. Schematic of the fabricated TLM-structure (a) top-view: there are eight contact pads of identical length and width (L= 100 µm and W=200 µm) in the fabricated structure and (b) horizontal-view: it represents the single part of the structure with a configuration of Au/p-HgCdTe & x=0.29.

Subsequently, these resultant values of R_{sh} and L_T were further applied to estimate the other resistive parameters like contact resistance (R_c) and specific contact resistance (ρ_c), respectively. I-V measurement for the fabricated TLM structure (contact pads) was also carried out to examine the electrical behaviour of the Au/p-HgCdTe interface. The total resistance (R_T) measured for all the pairs of consecutive contact pads (interpad spacing, d) is given by using Eq. 5.4, and the transfer length is defined by Eq. 5.5 [8,9,44].

$$R_T = R_{semi} + 2R_c = R_{sh}\frac{d}{W} + 2\frac{R_{sh}L_T}{W} \tag{5.4}$$

$$L_T = \sqrt{\left(\frac{\rho_c}{R_{sh}}\right)} \tag{5.5}$$

The relation among R_c, ρ_c, and L_T can be expressed by Eq. 5.6, whereas the R_c and ρ_c of an ohmic planar contact are given by Eqs. 5.7, 5.8, and 5.9 [8,9,44].

$$\rho_c = R_{sh}L_T \Rightarrow R_c = \frac{\rho_c}{L_T W} = \frac{R_{sh}\,L_T}{W} \tag{5.6}$$

Since contact resistance for an Ohmic planar contact is given by**:**

$$R_c = \frac{R_{sh} \cdot L_T}{W} \coth(L|L_T) \approx \frac{\rho_c}{L_T W} \coth(L|L_T) \tag{5.7}$$

There are two limiting cases in the above Eq., which make the simplified form of R_c as mentioned as follows:

(i) Short contact limit ($L \ll L_T$) → $\coth(L|L_T) \approx L/L_T$ then $R_c = \frac{\rho_c}{LW} \Rightarrow \rho_c = R_c L W$ (5.8)

(ii) Long contact limit ($L \gg L_T$) → $\coth(L|L_T) \approx 1$ then $R_c = \frac{\rho_c}{L_T W} \Rightarrow \rho_c = R_c L_T W$ (5.9)

TLM structure measurement and analysis

The total resistances R_T for all the pairs of adjacent contact pads of the TLM structure (Sample-D: as-deposited and annealed) were measured at 80 ± 3 K since low-temperature measurements are suitable for the operation of fabricated devices. The plots of total resistance R_T vs. interpad spacing d were constructed, as demonstrated in Fig. 5.6(a, b).

The Eqs. 5.4 - 5.9 were used to evaluate the electrical parameters (R_c, L_T, R_{sh}, and ρ_c) of Au/p-HgCdTe-based TLM structure (as-deposited and annealed), and the calculated values are summarised in Table 5.3. The evaluated specific contact resistance (ρ_c) of the as-deposited and annealed TLM test structures are 2.73×10^{-3} **Ω**·cm^2, 7.11×10^{-4} **Ω**·cm^2, respectively. These resultant values of specific contact resistance (ρ_c) are relatively better than the reported results of Au/p-HgCdTe contacts [9,17]. Thus, thermally grown Au film can be used to fabricate HgCdTe-based IR detectors for creating an interface with low specific contact resistance [8,9,17,19].

The most probable reasons for realizing the low specific contact resistance for Au/HgCdTe interface are associated with the sample surface condition, pre-deposition chemical treatments, and post-deposition annealing [8,9,22,33,45]. The first possible reason for low Ohmic contact resistance is the effect of the thin interfacial oxide layer (say few Å, it works as a barrier layer for Au diffusion into HgCdTe during the deposition of Au metal) on the HgCdTe surface. It is formed due to bombarding the sample in oxygen plasma for 30 sec before the deposition of Au film on the HgCdTe samples.

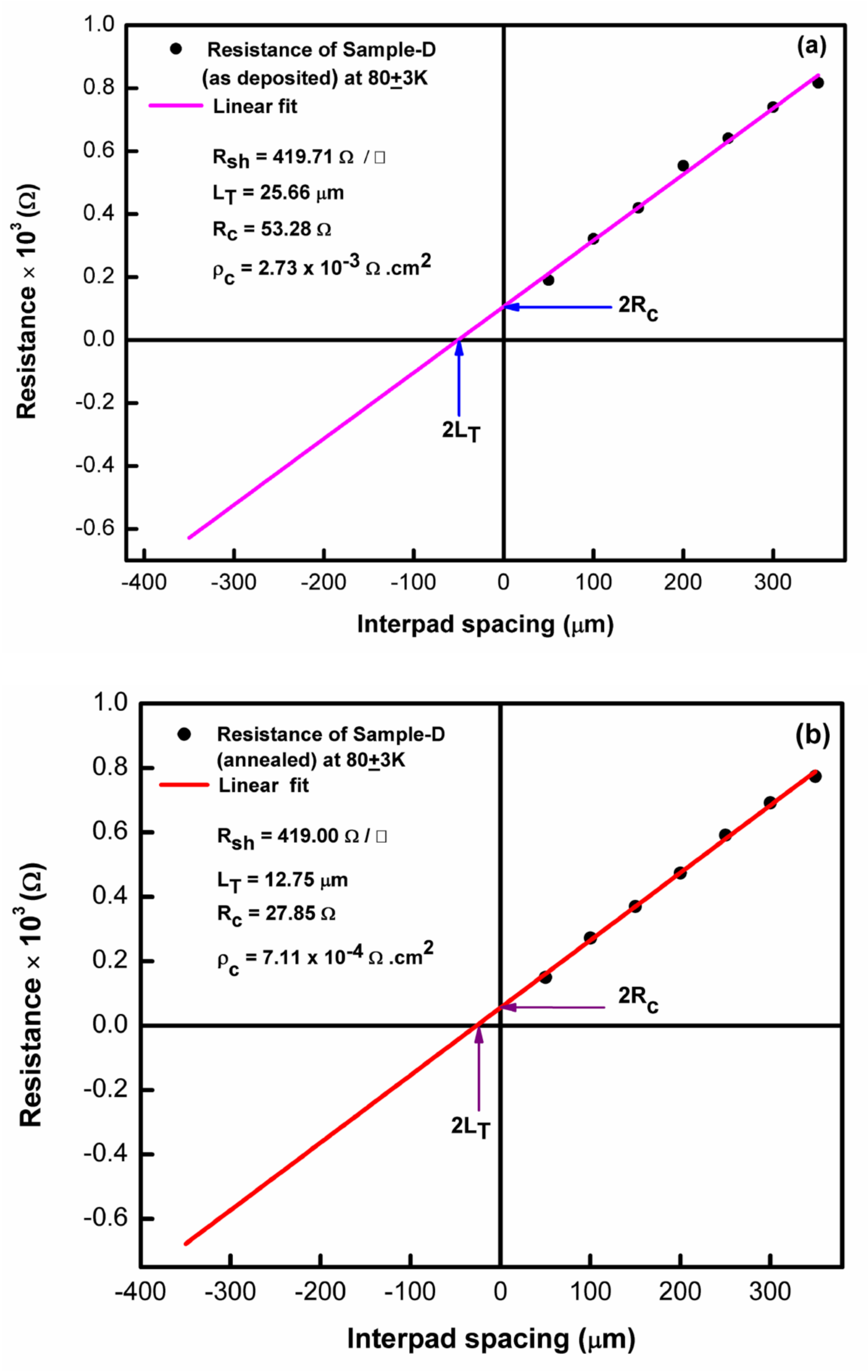

Figure 5.6. Total resistance versus interpad spacing plots for the as-deposited and annealed contact-pads of Sample-D (TLM structure configuration: Au/p-HgCdTe & x =

0.29) recorded at 80 ± 3 K: (a) plot for as-deposited contacts and (b) plot for annealed contacts. The plots were utilized to evaluate the contact resistance and other electrical parameters of grown Au contacts.

Table 5.3: Electrical parameters of the Sample-D (TLM test-structure configuration: Au/p-HgCdTe, x=0.29 and Au film with optimized deposition rate-10 Å/sec) evaluated from its TLM measurement (test-structure: as deposited and annealed) performed at 80 ± 3 K.

Parameters	**Sample-D (TLM test structure)**	
	As deposited	**Annealed**
Sheet resistance R_{sh} (Ω/□)	419.71	419.00
Contact resistance Rc (Ω)	53.28	27.85
Transfer length L_T (μm)	25.66	12.75
Specific contact resistance ρ_c ($\Omega\cdot cm^2$)	2.73×10^{-3}	7.11×10^{-4}

Many interface states on the Au/p-HgCdTe interface (due to an interaction between the deposited Au metal and the HgCdTe Sample) are accountable for the Fermi-level pinning near the conduction-band minima which generate the rectifying contacts of high-value specific contact resistance. Accordingly, the thin interfacial oxide layer reasonably reduces the number of interfaces states by minimizing the diffusion of Au into HgCdTe and a low specific contact resistance: 2.73×10^{-3} $\Omega\cdot cm^2$ for the as-deposited Au/p-HgCdTe interface (Fig. 5.6a). An annealing treatment for Au-based TLM structure (Sample-D) was given for 2h at 80 ^{o}C. It was found that the value of specific contact resistance for the annealed Sample-D (TLM structure) became 7.11×10^{-4} $\Omega.cm^2$, which is relatively low than the as-deposited Sample-D (TLM pattern). The thermal annealing of as-deposited Sample-D (TLM contacts) has further reduced the number of interface states (although the plasma treatment has already reduced these interface states but those are still high to create Fermi level pinning) of the Au/p-HgCdTe interface and accordingly, a relatively low specific contact resistance for the annealed TLM structure (Fig. 5.6b) was achieved [8,9,22,46]. The second responsible factor for low specific contact resistance is associated with the surface morphology and grown film/HgCdTe surface compositions. Since the undesirable features (pinholes, contaminations, defects, scratches, non-uniform thickness, and non-stoichiometric composition) in the film/substrate surface can generate difficulties in achieving the desired electrical characteristics of the device. The HgCdTe Sample-D (TLM-structure) achieved a defect and contamination-free surface because of various effective surface treatments (like chemo-mechanical polishing and chemical etching) applied to this sample. Also, the produced Au films are uniform, pure, and dense. The films also have minimum roughness and the preferred size of particles. The aforementioned features are discussed in EDX, AFM, and SEM analysis. Hence, these belongings of HgCdTe surface/Au film direct that charges will quickly move through the Au/p-HgCdTe interface due to minimum blocking effects in their path. This is the second factor responsible for the low value of specific contact resistance/improved Ohmic nature of the Au/p-HgCdTe interface. The grown Au film has all the desired features (morphological and compositional) necessary to fabricate good-quality IR detectors with low specific contact resistance [22,33,45,46].

I-V characteristics provide the behaviour of Au metal contact and the mechanism of current transport in the Au/p-HgCdTe interface. The resultant I–V curves (realized at 80 $\pm$ 3K) of the Au/p-HgCdTe interface (Sample-D: as-deposited and annealed) are shown in Fig. 5.7. It was found that Au-contacts (TLM structure: as-deposited and annealed) exhibited nearly Ohmic behaviour since Au-contacts are not purely Ohmic and some rectifying features in these contacts were observed. Hence, the I-V characteristics of the thermally grown Au films are consistent and comparable to the reported structures [9,16,17,19] in which different metals like Au, PEDOT: PSS, Au/Pt/Ti, electroless Au, and HgTe/Ti were used to develop the HgCdTe based IR photodetectors with good Ohmic contacts [8,9,16,17,19].

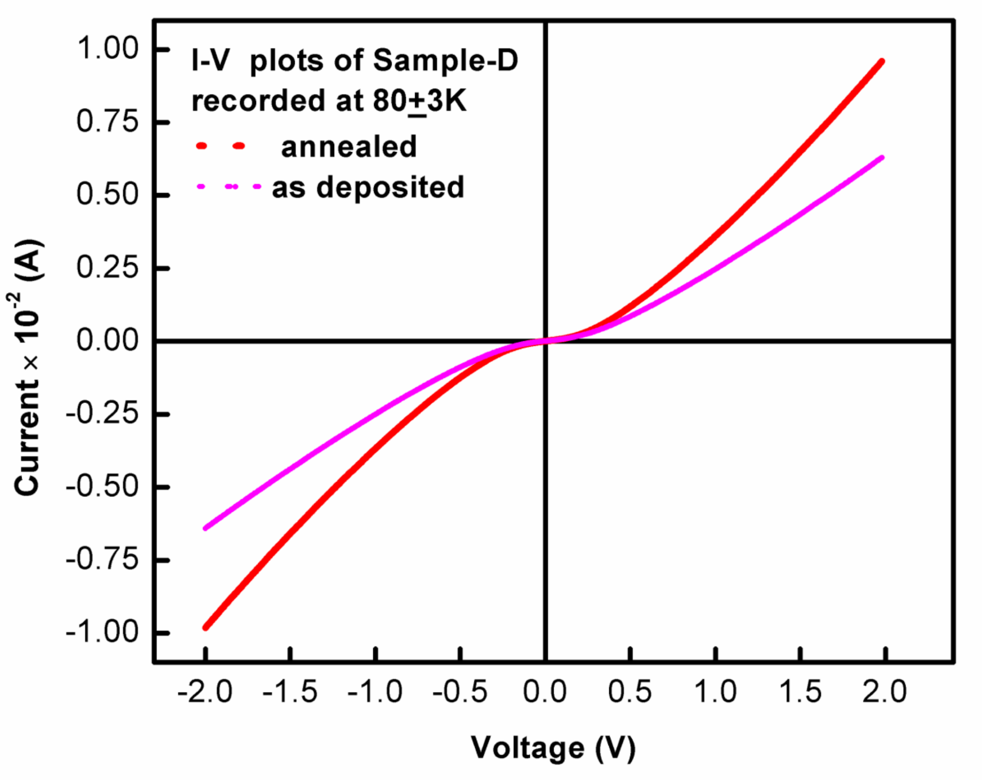

Figure 5.7. I–V measurements for the as-deposited and annealed contacts of the Sample-D based TLM structure (configuration: Au/p-HgCdTe, x = 0.29) performed at a temperature of 80 ± 3 K: plots of as-deposited and annealed structures. The plots show the behaviour of the Au/p-HgCdTe interface.

The reasons which may be accountable for generating Au/p-HgCdTe interface (of as-deposited and annealed TLM structures) with Ohmic nature (linear I-V plot) are deliberated. The first reason for Ohmic behaviour is the effect of the plasma descum process on the HgCdTe surface before Au metal deposition that has reasonably reduced the number of interface states on the Au/p-HgCdTe interface and I-V plot of the as-deposited Au contact (Fig.5.7) is ohmic except having some partial rectifying nature. Fermi level pinning occurring near the conduction-band minimum (due to some interface states presented on the Au/p-HgCdTe interface after the plasma descum process) is responsible for the partially-rectifying I-V plot of the as-deposited Au Ohmic contact (Fig.5.7). I-V plot of the annealed Au- contact (Sample-D) is also ohmic with partial rectifying nature. Since the thermal annealing treatment applied on the as-deposited Sample-D has not improved its ohmicity (except for a slight improvement) so considerably but the current of the annealed Sample-D (Fig. 5.7) is increased relative to the current of as-deposited Sample-D (Fig. 5.7).

Consequently, the specific contact resistance of as-deposited Au contact (Sample-D) is reduced after its thermal annealing (Fig. 5.6b) and this annealed Au/p-HgCdTe interface (Fig.5.7) has shown slightly improved ohmic behaviour than the as-deposited Au/p-HgCdTe interface (Fig.5.7). The second answerable factor for making Ohmic contact is the long-term stability of Au contact, which is affected because of its cluster growth mechanism, high diffusion coefficient, and poor adhesion. The in/out-diffusion (the grown metal/HgCdTe elements) processes that occur at the time of metal-deposition/post-deposition can be minimized through the thin interfacial oxide layer (created by plasma descum process) and low-temperature deposition process. Au films were carried out through a tape test that established their strong adhesion on the HgCdTe surface/epilayer. These films were also found compatible with the photolithography process of IR detector fabrication (i.e. desired TLM structure’s patterns were defined on the HgCdTe substrate via photolithography masking process followed by depositions of Au thin films. Consequently, photolithography lift-off processes were performed to generate the desired patterns of Au/p-HgCdTe-based TLM structures, and no interruptions were encountered during these processes). Au film favours the factor of stability since it has the features like minimum defects (due to a thin interfacial oxide layer), a low-temperature deposition process, and strong adhesion, and it is essential to develop IR detectors with Ohmic electrical contacts [5,8,9,18,26,47-49]. Thus, an excellent Ohmic contact (low specific contact resistance and long-lasting stability) can be generated by using the Au film with desired properties (like the cubic structure of preferred orientation Au (111), high purity, defects free, lower roughness, small grain, strong adhesion, etc.) and proper control over the unit processing steps (like HgCdTe surface preparation, surface treatment, deposition conditions, and annealing treatments).

5.4. Conclusion

The present work offers the essential features of thermally grown Au thin films on the mercury cadmium telluride (HgCdTe) substrate. Various characterization techniques were applied to realize the optimized Au film. The cubic and polycrystalline Au films of preferred orientation (111) were confirmed by structural analysis. The elemental and morphological characteristics expressed that the grown films are pure, uniform, highly dense, and have low roughness of 4.19 ± 0.02 nm. The evaluated grain size and film heights were 24.86 nm and 192.1 nm, respectively. The optimized Au films were further employed to create the TLM structure with configuration (Au/p-HgCdTe) for examining their utility in the HgCdTe-based IR detector fabrication. Au/p-HgCdTe interfaces (as-deposited and annealed) displayed Ohmic characteristics while the specific contact resistance **(**ρ_c) for the as-deposited and annealed Au/p-HgCdTe interfaces are 2.73×10^{-3} **Ω**$\cdot$cm^2 and 7.11×10^{-4} **Ω**.cm^2, respectively. Thermal annealing (contacts annealed for 2h at 80 ^{o}C in the air) has reduced the value of specific contact resistance (ρ_c) by about one order as the specific contact resistance (ρ_c=7.11×10^{-4} **Ω**.cm^2) of the annealed Au contact is relatively low than the specific contact resistance (ρ_c=2.73×10^{-3} **Ω**$\cdot$cm^2) of as-deposited contact. The grown Au films have good adhesion to the HgCdTe substrate and are compatible with the photolithography process used in IR detector fabrication. Hence, Au metal could be the most appropriate material to develop the reproducible and thermally stable p-Ohmic contact on HgCdTe IR detectors**.**

References

[1] C. Downs, T. Vandervelde, Progress in Infrared Photodetectors Since 2000, Sensors 13 (2013) 5054–5098.

[2] A. Rogalski, Recent progress in infrared detector technologies, Infrared Phys. Technol. 54 (2011) 136–154.

[3] C. L. Tan, H. Mohseni, Emerging technologies for high performance infrared detectors, Nanophotonics 7 (2018) 169–197.

[4] W. Lei, J. Antoszewski, L. Faraone, Progress, challenges, and opportunities for HgCdTe infrared materials and detectors, Appl. Phys. Rev. 2 (2015) 041303.

[5] Z. Tsybrii, Y. Bezsmolnyy, K. Svezhentsova, M. Vuichyk, I. Lysiuk, M. Apatska, M. Smolii, N. Dmytruk, S. Bunchuk, K. Andreeva, F. Sizov, HgCdTe/CdZnTe LPE epitaxial layers: from material growth to applications in devices, J. Cryst. Growth 529 (2019) 125295.

[6] A. Rogalski, Infrared detectors: Status and trends, Prog. Quantum Electron. 27 (2003) 59– 210.

[7] A. Rogalski, J. Antoszewski, L. Faraone, Third-generation infrared photodetector arrays, J. Appl. Phys. 105 (2009) 91101.

[8] V. Srivastav, R. Pal, B. L. Sharma, V. Mittal, V. Gopal, and H. P. Vyas, Electrical Properties of Titanium-HgCdTe Contacts, J. Electron. Mater. 34 (2005) 225–231.

[9] A. Singh, A. K. Shukla, S. Jain, B. S. Yadav, R. Pal, Electrical characteristics of electroless gold contacts on p-type Hg1_xCdxTe, Mater. Sci. Semicond. Process. 26 (2014) 294–300.

[10] V. Srivastav, R. Pal, and V. Venkataraman, Modelling of room temperature current-voltage measurements on homo-junction HgCdTe diodes exhibiting nonequilibrium effects, J. Appl. Phys. 111 (2012) 033112.

[11] P. Capper, J. Garland, Mercury Cadmium Telluride Growth, Properties and Application: Structure and Electrical Characteristics of Metal/MCT Interfaces, John Wiley & Sons Ltd., U. K., 1st Edition (2011) 340–356.

[12] W. E. Spicer, D. J. Friedman, and G. P. Carey, The electrical properties of metallic contacts on $Hg_{1-x}Cd_xTe$, J. Vac. Sci. Technol. A 6 (1988) 2746.

[13] W. E. Spicer, Metal contacts on $Hg_{1-x}Cd_xTe$, J. Vac. Sci. Technol. A 8 (1990) 1174.

[14] G. D. Davis, W. A. Beck, Y.W. Mo, D. Kilday, and G. Margaritondo, Interfacial interactions between (HgCd)Te and Ti, an ultrareactive metal, J. Appl. Phys. 61 (1987) 5191.

[15] G. D. Davis, J. T. McKinley, D, G. Kilday, and G. Margaritondo, Effects of Al and Ti interlayers on Sb/(HgCd)Te interface behaviour, J. Appl. Phys. 65 (1989) 3435.

[16] W. A. Beck, G. D. Davis, and A. C. Goldberg, Resistance and 1/f noise of Au, Al, and Ge contacts to (HgCd)Te, J. Appl. Phys. 67 (1990) 6340.

[17] P.Y. Emelie, E. Cagin, J. Siddiqui, J.D. Phillips, C. Fulk, J. Garland, and S. Sivananthan, Electrical Characteristics of PEDOT: PSS Organic Contacts to HgCdTe, J. Electron. Mater. 36 (2007) 841–845.

[18] Y. Tang, Jia Jia, H. Qiao, Y. Zhang, X. Li, Application of Au/Sn in the formation of p-HgCdTe photoconductive detectors electrodes, 6th International Symposium on Advanced Optical Manufacturing and Testing Technologies: Optoelectronic Materials and Devices for Sensing, Imaging, and Solar Energy, Proc. of SPIE, 8419 (2012) 84190Z.

[19] P. W. Leech and G. K. Reeves, Low resistance ohmic contacts to n-$Hg_{1-x}Cd_xTe$ using a HgTe cap layer, Infrared Detectors–Materials, Processing, and Devices, Proc. of Mat. Res. Soc. Symp., 299 (1994) 978-1-107-40952-1.

[20] D. Qian, J. Jia, Y. Tang, F. Liu, X. Ma, L. Zhang, F. Liu, B. Ye, H. Qiao, L. Zhu, X. Li, The evaluation of curved extended electrodes for off-area bonding of HgCdTe photoconductive detectors, International Symposium on Photoelectronic Detection and Imaging 2011: Advances in Infrared Imaging and Applications, Proc. SPIE,8193 (2011) 81932E.

[21] P. W. Leech, G. K. Reeves, Specific contact resistance of indium ohmic contacts to n-type Hg_{1-x} Cd_x Te, J. Vac. Sci. Technol. A 10 (1992) 105.

[22] V. Krishnamurthy, A. Simmons, C. R. Helms, Oxide interfacial layers in Au ohmic contacts to p-type Hg_{1-x} Cd_x Te, Appl. Phys. Lett. 56 (1990) 925.

[23] M. W. Fay, G. Moldovan, P. D. Brown, I. Harrison, J. C. Birkbeck, B. T. Hughes, M. J. Uren, and T. Martin, Structural and electrical characterization of AuTiAlTi/AlGaN/GaN ohmic contacts, J. Appl. Phys. 92 (2002) 94.

[24] A. Motayed, K. A. Jones, M. A. Derenge, M. C. Wood, D. N. Zakharov, Z. Liliental-Weber, D. J. Smith, A.V. Davydov, W. T. Anderson, A. A. Iliadis, and S. N. Mohammad, Electrical, microstructural, and thermal stability characteristics of Ta/Ti/Ni/Au contacts to n- GaN, J. Appl. Phys. 95 (2004) 1516.

[25] V. R. Reddy, Study of the electrical, structural and surface morphological characteristics of Pt/Re/Au ohmic contacts on p-type GaN, Mater. Chem. Phys. 93 (2005) 286–290.

[26] I. Dutta, C. B. Munns, G. Dutta, An X-ray diffraction (XRD) study of vapor deposited gold thin films on aluminum nitride (A1N) substrates, Thin Solid Films 304 (1997) 229-238.

[27] N. Mahmoodi, A. I. Rushdi, J. Bowen, A. Sabouri, C. J. Anthony, P. M. Mendes, and J. A. Preece, Room temperature thermally evaporated thin Au film on Si suitable

for application of thiol self-assembled monolayers in micro/nano-electro-mechanical-systems sensors, J. Vac. Sci. Technol. A 35 (4), (2017) 041514.

[28] A. Dandapat, S. Pramanik, S. Bysakh and G. De, Boat-like Au nanoparticles embedded mesoporous c-Al2O3 films: an efficient SERS substrate, J. Nanopart. Res. 15 (2013) 1804.

[29] G. Geng, P. Chen, B. Guan, Y. Liu, C. Yang, N. Wang and M. Liu, Sheetlike gold nanostructures/graphene oxide composites via a one-pot green fabrication protocol and their interesting two-stage catalytic behaviors, RSC Adv.7 (2017) 51838-51846.

[30] T. S. T. Amran, M. R. Hashim, N. K. A. Al-Obaidi, H. Yazid and R. Adnan, Optical absorption and photoluminescence studies of gold nanoparticles deposited on porous silicon, Nanoscale Res. Lett. 8 (2013) 35.

[31] N. Azizah, U. Hashim, M. K. M. Arshad, S. C. B. Gopinath, S. Nadzirah, M. A. Farehanim, M. F. Fatin, A. K. M. Muaz, A. R. Ruslinda and RM Ayub, Analysis study of single gold nanoparticle system of interdigitated device electrodes (IDES) by using energy-dispersive X-ray (EDX) ARPN J. Eng. Appl. Sci. 11 (2016) 14.

[32] C. Benazzouz, N. Benouattas, S. Iaiche, A. Bouabellou, Study of diffusion at surface of multilayered Cu/Au films on monocrystalline silicon, Nucl. Instrum. Methods Phys. Res. Sect. B 213 (2004) 519–522.

[33] J. Sun, L. Fu, Z. Nie, Y. Shi, L. Yapeng, The effect of chemical polishing on the interface structure and electrical property of Au/$Cd_{0.9}$ $Zn_{0.1}$Te contact, Appl. Phys. A 115 (2013) 1309-1316.

[34] T. E. Novelo, G. M. Alonzo-Medina, P. Amézaga-Madrid, and R. D. Maldonado, Surface Morphology and Electrical Resistivity in Polycrystalline Au/Cu/Si (100) System, J. Nanomater. 2079204 (2017) 1-8.

[35] M. Deura, H. Fukuyama, Formation of SiC layer by carbonization of Si surface using CO gas, J. Cryst. Growth 434 (2016) 77-80.

[36] B. Chen, M. Mokume, C. Liu and K. Hayashi, Structure and localized surface plasmon tuning of sputtered Au nano-islands through thermal annealing, Vacuum 110 (2014) 94-101.

[37] T. Rerek, L. Skowronski, R. Szczesny, M.K. Naparty, B. Derkowska-Zielinska, The effect of the deposition rate on morphology, opto-electronic properties and formation intermetallic compounds of Au-Sn alloys, J. Alloys Compd. 849 (2020) 156041.

[38] Y. Kalachyova, O. Lyutakov, A. Solovyev, P. Slepička and V. Švorčík, Surface morphology and optical properties of porphyrin/Au and Au/porphyrin/Au systems, Nanoscale Res. Lett. 8, 547 (2013) 1-10.

[39] F. Ruffino, V. Torrisi, G. Marletta, M. G. Grimaldi, Atomic force microscopy investigation of the kinetic growth mechanisms of sputtered nanostructured Au film on mica: towards a nanoscale morphology control, Nanoscale Res. Lett. 6 (2011) 112.

[40] O. Akogwua, D. Kwabi, S. Midturi, M. Eleruja, B. Babatope, W.O. Soboyejo, Large strain deformation and cracking of nanoscale gold films on PDMS substrate, Mater. Sci. Eng., B 170 (2010) 32–40.

[41] A. Toma, B. Š. Batič, D. Chiappe, C. Boragno, U. Valbusa, M. Godec, M. Jenko, and F. B. Mongeot, Patterning polycrystalline thin films by defocused ion beam: The influence of initial morphology on the evolution of self-organized nanostructures, J. Appl. Phys. 104 (2008) 104313.

[42] M. Walther, D. G. Cooke, C. Sherstan, M. Hajar, M. R. Freeman, and F. A. Hegmann, Terahertz conductivity of thin gold films at the metal-insulator percolation transition, Phys. Rev. B 76 (2007) 125408.

[43] J. Siegel, O. Lyutakov, V. Rybka, Z. Kolská, V. Švorčík, Properties of gold nanostructures sputtered on glass, Nanoscale Res. Lett. 6 (2011) 96.

[44] L. Basset, W. Favre, O. Bonino, J. Sudre, G. M´enard, J.-P. Vilcot, In depth analysis of transfer length method application on passivated contacts under illumination, Sol. Energy Mater. Sol. Cells 230 (2021) 111255.

[45] R. Nokhwal, V. Srivastav, A. Goyal, B. L. Sharma, S. A. Hashmi, and R. K. Sharma, Surface Studies on HgCdTe Using Non-aqueous Iodine-Based Polishing Solution, J. Electron. Mater. 46 (2017) 6795–6803.

[46] T. V. Blank and Y. A. Goldberg, Mechanisms of Current Flow in Metal–Semiconductor Ohmic Contacts, Semiconductors 41 (2007) 1263–1292.

[47] V. S. Meena, M. S. Mehata, Investigation of grown ZnS film on HgCdTe substrate for passivation of infrared photodetector, Thin Solid Films 731 (2021) 138751.

[48] A. K. Saini, V. Srivastav, S. Gupta, B. L. Sharma, M. Asthania, N. Singh, S. K. Gaur, V. S. Meena, R. Thakur, Chanchal, V. Sharma, R. K. Sharma, Improvement of Electrical properties of ZnS/CdTe-HgCdTe interface by (NH4)2S treatment, Infrared Phys. Technol. 102 (2019) 102988.

[49] V. S. Meena, M. S. Mehata, Thermally grown Indium (In) thin-film for creating Ohmic contact and In-bumps for HgCdTe-based IR Detectors, Appl. Surf. Sci. 596 (2022) 153501.

Chapter 6

Synthesis and characterization of four-layer anti-reflection coating stacks (ZnS and YF_3 thin films) for HgCdTe-based mid-wave infrared detectors

6.1. Introduction

Infrared (IR) photodetectors are widely employed in various scientific and technical fields, including night vision, thermal imaging, military target detection, IR-guided missile systems, defence technologies, biomedical sensing, remote sensing, tracking, and meteorological monitoring. Several materials, namely mercury cadmium telluride (HgCdTe), quantum-well infrared photodetector (QWIP), type-II superlattices (T2SL), InSb, PbSnTe, and Si; have been used to fabricate the IR detectors but HgCdTe is the popular and leading infrared detector-material that has the unique fundamental properties like mature growth technology, availability of wide-band lattice-matched substrates, large absorption coefficients, high quantum efficiencies, moderate dielectric constant and thermal expansion of coefficient, etc. Another important feature of $Hg_{1-x}Cd_xTe$ material is its adjustable/wide optical band gap (since HgCdTe material of different band gap/ spectral regions can be generated via the specific tuning of cadmium (Cd) concentration during the growth of this material). The HgCdTe material with spectral regions of 1-30 µm (cut-off wavelength λ_c =1-30 µm) has been realized [1-4].

Part of this work has been published in **Materials Science in Semiconductor Processing 163 (2023) 107556 (Elsevier).*

The most significant spectral bands lying in the aforesaid wavelength range are designated as short-wave infrared (SWIR: 1-3 µm), mid-wave infrared (MWIR: 3-5 µm) and long-wave infrared (LWIR: 8-14 μm), which have been used in the fabrication of multi-spectral (SWIR, MWIR, LWIR) HgCdTe IR detectors. The MWIR (3–5 μm) window/ atmospheric transmission window is considered the best appropriate window that can detect hot objects (like military-related targets, missiles, troops, airfields, aircraft, vehicle engines, and factories, which have their surface temperatures within the range of 700 °C) having different radiating characteristics (temperature or emissivity/both) relative to general terrain where this window is used in thermal imaging systems for the detection process [5-10]. MWIR is also helpful for identifying objects in all environmental conditions (like fog, tropical, arctic, oil, desert, sand, storm, and oceanic), weather tracking, night vision, and multiple defence technology. The MWIR detector system (3.6 – 4.9 μm) has a band-selection filter that can choose the desired spectral region to gather certain information in this region. HgCdTe-based high-performance (high quantum efficiencies, responsivity, and detectivity) infrared focal plane arrays (IRFPAs) working in the MWIR range are the key component of space tracking & surveillance system (STSS) and missile guidance systems. Thus, the continuing enhancement of the IR detector's performance and minimizing cost have been the major research attention in the last decade [10-13].

Most frequently used HgCdTe FPAs with backside-illuminated configuration (designated backside illuminated IRFPAs) are the hybridized assembly consisting of a two-dimensional (2D) HgCdTe detector array and an identical 2D array of input circuits (a Si-based readout integrated circuit (ROIC) which are bonded (electrically, thermally, and mechanically) to each other with the help of indium bumps. HgCdTe detectors are grown on various substrates like Si, GaAs, CdTe, and cadmium zinc telluride (CdZnTe), but the CdZnTe is the most popular substrate for the growth of HgCdTe-epilayer since it has the best lattice matching with HgCdTe material [1,5-7,9,14,15]. The performance of the HgCdTe-based IR detector depends on the amount of incident IR radiation reaching the active area of the HgCdTe-based IR detector. HgCdTe detectors (grown on bulk CdZnTe substrates and with backside-illuminated configuration) have an optical path along which the incident IR radiation traverse firstly to thick transparent CdZnTe substrate (for IR radiation) and lastly to the absorbing layer of HgCdTe IR detector. The CdZnTe material of high refractive index (2.7) relative to the air (1.0) will reflect about one-fourth (21%) of incident IR light from the air/CdZnTe or air/HgCdTe interface because of the high Fresnel reflection. Therefore, only three-fourths (79%) of incident IR radiation can reach the active area of HgCdTe based IR device where the creation of electron-hole pair takes place. Thus, the loss of incident signal/incident IR flux (due to reflections) at the air/CdZnTe interface (IR substrate-CdZnTe) results in low-performance HgCdTe IR detectors (lower detector quantum efficiency, limits the sensitivity/responsivity, high detector noise, and cross-talk) and it generates poor image contrast or blind image [1,5,9,10,15].

The anti-reflection coating (ARC) is one of the important factors that can minimize the reflection losses at the air/CdZnTe interface to enhance the performance of HgCdTe IR detectors since it has already been used to generate the highly demanding optoelectronic devices/optical components of maximum performance [1,5-7,9,10,13-15]. However, it is still challenging to attain a high-performance AR coating stack within MWIR optical region since a few ARC materials/designs (namely, SiO_2/TiO_2, $Ge/HfO_2/YF_3$-BaF_2 (IR-F625) based multilayer, $SiO_2/Ge/SiO_2$, $ZnS/Al_2O_3/Ge$, ZnS/CdS, $MgF_2/ZnS/MgF_2$, Ge/ZnS/Ge/ZnS, ZnS/ThF_4, ZnS/YF_3, YF_3/ZrN, YbF_3/ZnS, etc. are available in this spectral region, which has been utilized to realize the minimum reflectance with a low reflection loss on various IR substrates like Si, Ge, GaAs, GaP, InP, chalcogenide glass, ZnSe, and zinc sulphide (ZnS) [8,10-13,16-22,23-26,27-30].

Among these ARC designs, the ZnS/YF_3-based multilayer design (4-layers, 6-layers, 7-8 layers) is a seldom used design that can minimize the reflectance of IR substrates. Recently, Matsuoka et al. [23] demonstrated a four-layer ARC design (thickness-2.485 μm) on an InP substrate with reflection ≤1.0% within the spectral range: 7–12 μm where the ARC stack was made from YF_3 (low refractive index: nL) and ZnS (high refractive index: nH) coating materials respectively. The HgCdTe IR detectors of good spectral response (minimum reflection)/high performance (absolute QE: 80-95 %) are developed using the ARC structures/designs [4,9,14,18]. Consequently, ZnS-based single-layer ARC was used to fabricate a good performance/(increased quantum efficiency) back-illuminated HgCdTe photovoltaic detector (MCT-epilayer grown on GaAs substrate) with a cut-off wavelength of 6 μm. A four-layer [9] ARC (CdTe /Si_3N_4/BaF_2 /diamond) with minimum reflection/high optical quality/excellent bond strength contributed to develop high-performance HgCdTe detectors (grown on CdZnTe substrate) operating in the LWIR (8–12 μm) spectral region. Moth-eye textured nanostructure ARC (height/thickness: 4.0 μm)/5-layer ARC microstructures (ZnS/Ge, thickness: 1.53-3.4 μm) were applied to a CdZnTe window for fabricating the HgCdTe FPA of minimum reflection (1%) within the LWIR (7-13 μm) range that is simpler/more effective than the reported [7] multilayer ARC (25 layers, thickness-10 μm) with minimum reflection. The novel dual-band SWS microstructure (thickness: 2.2 μm deep) also showed a minimum reflection loss of 2 % within MWIR/LWIR bands [1,5,7].

The performance of IR detectors depends on the ARC structure's properties like high stability (no performance degradation within solar radiation/harsh environment), durability/high adhesion/better bond strength (temperature variation during the thermal cycling is responsible for adhesion loss that is responsible for the disastrous failure of IR cameras), minimum inherent stress (because of different thermal expansion coefficients of materials within AR coating stack), etc. Hence, the AR coatings must be grown at a temperature smaller than optimum to achieve the ARC film with minimum stress, adequate adhesion, and high density [1,2,7,14-20]. So, a few reports on ZnS/YF_3-based ARC design (HgCdTe-CdZnTe assembly or CdZnTe substrate) with minimum reflectance is available for the MWIR region. Recently, Saini *et al.* [31] have developed a thermally evaporated double-layer ARC structure (YF_3/ZnS/CdZnTe-HgCdTe) for CdZnTe-HgCdTe assembly using ZnS/YF_3 materials that offered a reflectance of 2 % within the MWIR (3.0 - 4.5 µm) range. However, this ARC design is very useful (with a minimum number of layers, minimum thickness, and good adhesion) for HgCdTe IR detector development [32]. It would be more effective/fruitful if it covered the other belongings like structural, morphological, compositional, and microstructural properties.

In the presented work, a thermally-evaporated four-layer AR coating film stack (configuration: YF_3/ZnS/YF_3/ZnS/CdZnTe-HgCdTe) with a relatively low total thickness and minimum reflectance/transmission has been generated, and the factors, e.g., structural, morphological, compositional, microstructural and optical properties were examined. The created ARC film stack accomplishes the goal of achieving the maximum incident photo-signal/IR signal on the CdZnTe substrate within the targeted MWIR spectral region, which will be highly beneficial in the fabrication of high-performance IR detectors for the current as well as futuristic technological requirements.

6.2. ARC design approach and selection of materials

The anti-reflection coating design for the targeted MWIR (3.2 - 5.3 µm) wavelength range was established based on a comprehensive search method, reverse engineering, and numerous experimentations [8,10-13,23,25-27,29-31,33]. The best multilayer ARC design/ growth (for targeted spectral range) may face many problems like a large number of layers with a large thickness (accountable for generating a high level of integrated stress energy, and this high stress creates flaking/delamination/thickness-error in the grown ARC layer) and searching a combination of coating materials (with refractive indices near to external medium and substrate) that covers the full spectral range of CdZnTe substrate. The realization of such an ARC multilayer also necessitates the co-evaporation of these coating materials. Therefore, the best probable AR coating design [13,23,25,27,29] for CdZnTe substrate was established through a set of parameters (refractive indices, lowest number of coating layers with optimized/minimum optical thicknesses and least production cost) to attain the goal of minimum reflection in targeted MWIR spectral-regions. This ARC structure/design (which contains alternative material layers of low/high refractive indices) is based on a simple/standard coating design (Lockhart design) proposed by Lockhart and King in 1947 [8,12,30].

The criterion of coating material selection is associated with their refractive index values, transparency within the spectral range, physical stability, and compatibility with the interface. Zinc sulphide (ZnS) and yttrium fluoride (YF_3) coating materials are involved in the proposed ARC stack design where ZnS serve as a high refractive index (nH) material and YF_3 has the role of a low refractive index (nL) material. ZnS/YF_3-based ARC stack design (with desired features: transmission/reflection) for HgCdTe-CdZnTe assembly is achieved at the optimized/minimum thicknesses and refractive indices of individual coating material layers [8,12,24,28,30] as shown in Table 6.1.

ZnS is a material with a refractive index of 2.25 and a transmission spectrum (0.4 -14 µm) free from major absorption. It is a suitable aspirant for optical elements/electro-optical applications within SWIR (0.9-2.5 µm), MWIR (3-5 µm), and LWIR (7.5-10.5 µm) bands because of its properties like easy availability in large quantity, high purity, good surface hardness, and robustness [29,30,34]. YF_3 is an appropriate AR coating material with a refractive index and transmission spectrum range of 1.5, 0.3-12.5 µm, respectively. Although fluoride layers are well-known for their porosity/water adsorption, which affects the transmittance/durability of the coating (since absorption of liquid water occurs in the IR range) yet adsorption/absorption of water can be reduced by growing the thick outer YF_3 layer. Both the materials (ZnS and YF_3) are deposited by thermal evaporation, but substrate temperature may create problems during the ARC deposition. The optimal substrate temperature for ZnS deposition is (20-50°C), which is relatively low than the substrate temperature of YF_3 deposition (40-65°C) [8,12,24-30].

Table 6.1. Design four-layer ARC film stacks of different coating materials (the physical thicknesses and refractive indices of individual coating layers).

Layer sequence	Coating material	Role of an individual layer	Refractive index at 4 μm	Physical thickness (nm)
1st	ZnS	High refractive index (H)	2.2	91 ± 0.4
2nd	YF_3	Low refractive index (L)	1.5	207 ± 0.6
3rd	ZnS	High refractive index (H)	2.2	91 ± 0.4
4th	YF_3	Low refractive index (L)	1.5	310 ± 0.8
HgCdTe/CdZnTe assembly				Massive
The total thickness of ARC layers				699 ± 2.2 nm

6.3. Experimental methods

6.3.1. HgCdTe surface-preparation and ARC film deposition

The proposed study (design/development) of ARC thin film-stack was executed through the use of p-type $Hg_{1-x}Cd_xTe$ epilayers (grown over lattice-matched CdZnTe substrates) and an in-house growth method viz. liquid phase epitaxy (LPE) was applied to produce the epilayers. The thermal evaporation vacuum technique was applied to develop the proposed ARC stack. Two epilayers, A and B, with specifications (thickness: 10 µm, sizes: 30×30 mm^2, composition x =0.29, mobility: 416 cm^{-2} V^{-1} s^{-1}, carrier-concentration: 1×10^{16} cm^{-3}), were utilized to complete the whole study. The mechanical/chemical-mechanical polishing process on the backside (i.e., CdZnTe) of the HgCdTe epilayers (A and B) was accomplished through an alumina powder (0.05 µm), and the (I_2: KI: $C_2H_6O_2$) : (1g: 4g: 10 ml) solution as well as few drops of KOH. The HgCdTe-CdZnTe assembly (epilayers: A and B) was washed and dried with de-ionized (DI) water and extremely pure N_2 exhaustively. They were divided into fragments of equal sizes, 10×10 mm^2 (namely A1, A2, A3, B1, B2, and B3). Samples A1 and A2 were carefully cleaned using a standard/prolonged cleaning process (samples were heated for 5-2 min sequentially in trichloroethylene, acetone, and methanol, respectively). Afterward, these samples were washed, dried, and successfully finished 10 min baking (at 90 °C). The microscopic observations/ellipsometry measurements confirmed the defect and contamination-free surface of the samples. The samples (A1 and A2) were immediately transferred into the vacuum chamber of the thermal evaporation coating unit (model: HHV 20F10). Evaporant materials (ZnS and YF_3 having purity: 99.999 %) were also put into separate molybdenum (Mo) boats and the distance of the source to the sample was kept at 30 cm. The coating units vacuum chamber was evacuated to an ultimate pressure of 2 × 10^{-7} Torr and samples were preheated for a time of 30 min to improve the adhesion and humidity resistance (by reducing the contaminations like humidity, oxides, and traces of chemicals, etc.) of such AR coating stacks. The sample's temperature was monitored by a thermocouple. Later, the deposition process of the four-layer ARC stack (film thickness: 699 ± 2.6 nm, configuration: ZnS/YF_3/ZnS/YF_3) formation was accomplished at the parameters listed in Table 6.2. The four layers of ZnS/YF_3 materials are deposited sequentially on the backside of HgCdTe-CdZnTe assembly (i.e., on CdZnTe) at the specified parameters (shown in Table 6.2), where the deposition rate and film thickness are measured via quartz crystal monitor /an in-built auto rate controller. The four-layer ARC (ZnS/YF3/ZnS/YF3) film-stack deposition process was completed at room temperature (21°C). Samples B1 and B2 were also passed through similar processes (cleaning and inspection of sample surface) adopted for Samples A1 and A2. Successively, the four-layer ARC stacks (films) of similar specifications (thickness: 699 ± 2.6 nm, configuration: $ZnS/YF_3/ZnS/YF_3$) were grown on the backsides (CdZnTe) of these samples at the same deposition parameters mentioned in Table 6.2. Afterward, the first set of Samples A1 and A2 (deposited ARC film-stacks) was examined through the X-ray diffractometer (XRD), atomic force microscope (AFM), energy dispersive X-ray (EDX) spectrometer, and scanning electron microscope (SEM), respectively. Continuously, it was revealed that these ARC films hold all the essential properties (structural: cubic structure, morphological: highly dense film with low roughness, compositional: purity, and microstructural: optimum grain size) that an ideal ARC film must retain. The identical results (structural: cubic structure, morphological: highly dense film with low roughness, compositional: purity, and microstructural: optimum grain size) were found for the second set of Samples B1 and B2. Thus, the process of ARC film deposition is repeatable/optimized, and the effectiveness of the optimized ARC film stack will further be examined through Samples A3 and B3.

All the treatments (like prolonged cleaning, washing, drying, baking, etc.) were followed for Sample-A3 (HgCdTe-CdZnTe assembly), similar to Samples A1, A2, B1, and B2. The microscopic/ellipsometry measurements confirmed that Sample-A3 (HgCdTe-CdZnTe) has a defect and contamination-free surface. Now the deposition of the four-layer ARC stack (film thickness: 699 ± 2.6 nm, configuration: ZnS/YF_3/ZnS/YF_3) on the backsides (CdZnTe) of Sample-A3 was accomplished at the parameters similar to Samples A1, A2, B1, and B2. The reflectance of Sample-A3 (without ARC film-stack)/Sample-A3 (with four-layer ARC film-stack) was measured using the Fourier Transform Infrared (FTIR) spectrometer. The repeatability of reflectance for the HgCdTe-CdZnTe assembly was examined by growing an identical ARC film stack on the Sample-B3 and measuring its reflectance through the FTIR. In this continuation, Sample-B3 was passed through processes (like prolonged cleaning, washing, drying, baking, surface quality examination, etc.) similar to Samples A1, A2, A3, B1, and B2.

Table 6.2. The deposition parameters of four-layer ARC film stacks and sequence of individual coating-layer in the ARC film stacks.

Coating material and layer-sequence	Deposition rate (Å/sec)	Evaporation current (A)	Thickness (nm)
ZnS (1st)	2 ± 0.2	77-82	91 ± 0.5
YF_3 (2nd)	5 ± 0.5	92-99	207 ± 0.7
ZnS (3rd)	2 ± 0.2	78-86	91 ± 0.5
YF_3 (4th)	5 ± 0.5	92-103	310 ± 0.9
HgCdTe/CdZnTe assembly			massive
The total thickness of ARC layers			699 ± 2.6 nm

The ultimate vacuum of 2.0×10^{-7} Torr was achieved within the deposition chamber. Then ARC film-stack of the same specifications (thickness: 699 ± 2.6 nm, configuration: ZnS/YF_3/ZnS/YF_3) was deposited on the backside (CdZnTe) of Sample-B3. FTIR has shown the same reflectance level for Sample B3, so the ARC film-stack formation process is repeatable and reliable.

6.3.2. Characterization techniques

The XRD system (model: analytical B.V.-X'Pert PRO MRD (material research diffractometer), source: CuKα with λ = 0.154 nm) was utilized to evaluate the structural properties of thermally evaporated four-layer ARC film stacks. The surface morphology of grown ARC film stacks was achieved by the AFM (model: 5600LS, Agilent Technologies) system. The FESEM (model: Carl Zeiss SUPRA55VP attached by Oxford Instrument X-MAX EDX Spectrometer, operational voltage: 5-20 kV) instrument was used to assess the microstructural and compositional findings of ARC film stacks. The reflectance measurements of the ARC film-stacks (HgCdTe-CdZnTe assembly without ARC film-stack, HgCdTe-CdZnTe assembly with ARC film-stack and configuration: $YF_3/ZnS/YF_3/ZnS/CdZnTe$-HgCdTe) were completed successfully through the FTIR Spectrometer (make: Varian, model: 680-IR, range = 0.5-100 μm, resolution = 0.01 cm^{-1}) at a temperature of 300 ± 3 K (room temperature).

6.4. Results and discussion

6.4.1. XRD measurement

The structural properties of thermally evaporated Samples-A1 and B1 (CdZnTe-HgCdTe assemblies) with ARC film-stacks (configuration: $ZnS/YF_3/ZnS/YF_3$) were assessed through XRD measurement. The resultant diffractograms (XRD patterns) of both the samples (Fig. 6.1(a): Sample-A1 ($ZnS/YF_3/ZnS/YF_3$), Fig. 6.1(b): Sample-B1 ($ZnS/YF_3/ZnS/YF_3$)) are shown in Fig. 6.1. XRD pattern of Sample-A1 (Fig. 6.1a: four-layer ARC stack with a configuration of $ZnS/YF_3/ZnS/YF_3$) has exhibited the diffraction peaks at $2\theta = 23.78^\circ$, 27.14°, 47.50°, 56.54° and 65.82° corresponding to the diffraction planes (011), (111), (301), (222) and (232) those are related with the standard YF_3

material of cubic primitive structure (JCPDS no. 70-1935). Similarly, the diffraction peaks at $2\theta = 28.62^{\circ}$, 47.62°, 56.94°, and 77.38° could be assigned to the diffraction planes (111), (220), (311) and (331) of a standard/bulk ZnS material with cubic fcc structure (JCPDS no. 650309). Two overlapping peaks, YF_3(301)/ZnS(220) and YF_3(222)/ZnS (311), were also observed within the ARC film-stack (composite made from the combined phases of ZnS/YF_3/ZnS/YF_3 films) those are indicating towards the lattice diffusion occurs during the deposition of alternate layers of four-layer ARC film-stack. Some peaks of the four-layer ARC film-stack are not so sharp, and this shows the partial amorphous nature of the polycrystalline ARC film-stack. Comparing these experimental results with the standard JCPDS cards of ZnS and YF3 single films reveals that no extra peaks (of any crystalline compound) are present within the XRD pattern of the four-layer ARC film-stack grown on Sample-A1. ARC film-stack (Sample-A1: ZnS/YF_3/ZnS/YF_3) was found with two original phases of ZnS (cubic fcc) and YF_3 (cubic primitive) materials, which are polycrystalline (partial amorphous) in nature.

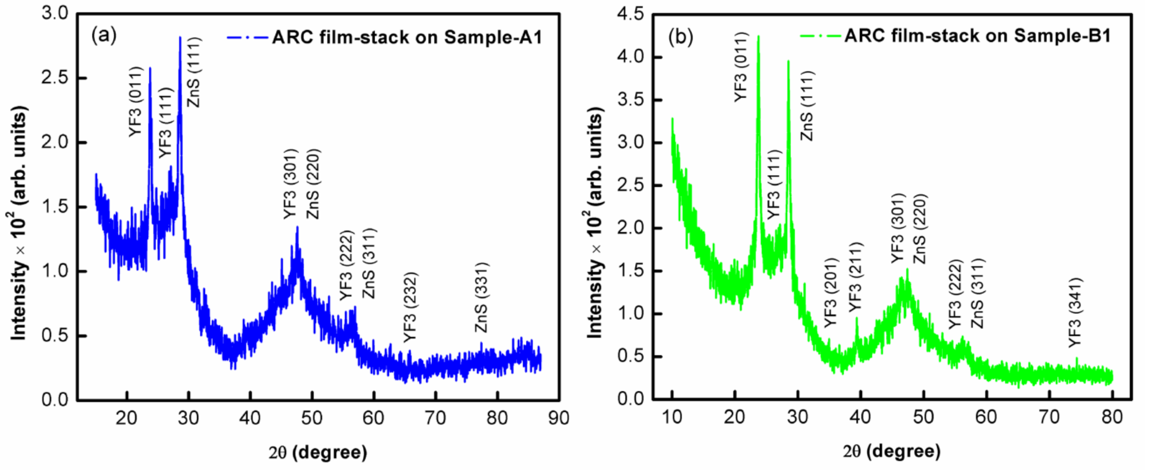

Figure 6.1. XRD patterns of thermally grown ARC thin film stacks (ZnS/YF_3/ZnS/YF_3) on Samples A1 and B1 (CdZnTe-HgCdTe assemblies).

As a result, Sample-A1 (ZnS/YF_3/ZnS/YF_3) has shown a similar tendency of ARC thin-film formation as reported in the literature [26,35,36].

Sample-B1 was identified with the diffraction peaks (011), (111), (201), (211), (301), (222), and (341) planes (Fig. 6.1b), which could be associated with diffraction peaks $2\theta = 23.75^{\circ}$, 27.17°, 34.97°, 39.37°, 47.50°, 56.20° and 74.32° of the standard YF_3 material with a typical cubic primitive structure (JCPDS no. 70-1935). Moreover, Sample-B1 (Fig. 6.1b) has displayed the diffraction peaks $2\theta = 28.52^{\circ}$, 47.62°, and 56.20° corresponding to (111), (220), and (311) planes of standard ZnS material with a typical cubic fcc structure (JCPDS no. 650309). The Sample-B1 (four-layer ARC film-stack: composite made from the combined phases of $ZnS/YF_3/ZnS/YF_3$ films) has also shown an overlapping of YF_3 (301)/ZnS (220) and YF_3 (222)/ZnS (311) diffraction peaks similar to Sample-A1 (but a slight shift in their positions has been observed) that directs to a lattice diffusion during the growth of alternate layers of four-layer ARC film-stack. The polycrystalline ARC film stack (Sample-B1) of partial amorphous nature was confirmed and had some less sharp peaks. No other crystalline compounds (no extra peaks) are noticed within the diffraction pattern of Sample-B1. The existence of both initial phases of ZnS (cubic fcc) and YF_3 (cubic primitive) within the ARC film-stack of Sample-B1 was confirmed by XRD, and it has a similar trend of ARC thin-film formation as reported in the literature [26,35,36].

Both the ARC film-stacks (Samples-A1 and B1) have identical XRD patterns (Fig. 6.1a, b) except for some minor differences. The four same peaks, i.e., YF_3 (011), YF_3 (111), YF_3 (301), and YF_3 (222), are observed within the diffractogram of both Samples-A1 and B1. The peak YF_3 (232) is present within Sample-A1, but it is absent from the XRD pattern of Sample-B1. On the other hand, three diffraction peaks, YF_3 (201), YF_3 (211), and YF_3 (341), are detected in the diffractogram of Sample-B1 but do not exist within the XRD pattern of Sample-A1. XRD patterns of Samples A1 and B1 do not comprise all the desired diffraction peaks similar to standard materials ZnS and YF3.

The differences may arise due to a small variation in growth conditions (rate, film thickness, and substrate temperature) and the quality of the CdZnTe-HgCdTe surface. Samples A1 and B1 have presented a good coincidence (2θ and (hkl) plane) with the standard films of ZnS (JCPDS no. 650309) and YF3 (JCPDS no. 70-1935). Various formulae (from Eqs. 6.1 to 6.3) were used for evaluating the structural parameters of Samples A1 and B1.

The lattice constant (a) of ZnS (cubic fcc) and YF_3(cubic primitive) were calculated using Eq. 6.1 [34] as given below:

$$a = \frac{\lambda \sqrt{h^2+k^2+l^2}}{2 \sin \theta} \tag{6.1}$$

where $\frac{\lambda}{2 \sin \theta} = d$

Here, λ: wavelength of x-ray, θ: angle of diffraction; h, k, and l: miller indices of corresponding crystal planes and d: interplanar spacing.

The average crystallite size (D) of ZnS and YF_3 films was evaluated through the well-known Debye Scherrer formula [26,32,34] given in Eq. 6.2 as follows:

$$D = \frac{0.94 \lambda}{\beta \cos \theta} \tag{6.2}$$

Here, β: FWHM of diffraction peaks (evaluated values of β are displayed in Table 6.3) and θ: diffraction angle.

The stress of ZnS and YF_3 films can be calculated by Eq. 6.3 [32,34].

$$\sigma_s = \frac{Y(a-a_o)}{2a_o\gamma} \tag{6.3}$$

where *Y*: Young's modulus (values of *Y* are in GPa; *Y* (ZnS) = 75 GPa and *Y* (YF_3) = 51 GPa), *a*: lattice constant originate via XRD technique (values for ZnS and YF3 films are shown in Table 3), a_0: lattice constant of standard /bulk material (a_0(ZnS) = 5.406 Å, a_0 (YF_3) = 5.385 Å) and γ: Poisson's ratio (γ(ZnS) = 0.28, γ(YF_3) = 0.33) of a material.

Table 6.3 displays the calculated structural parameters of Samples A1 & B1 (β: FWHM, a: lattice constant, D: Average crystallite size, and stress: σ), which were evaluated for the preferred orientation planes ZnS (011) and YF_3 (111), respectively. The experimentally-measured XRD parameters (2θ, diffraction peaks, and lattice planes) of Samples A1 & B1 were used to estimate structural parameters.

Table 6.3. Estimated structural parameters of Samples A1 & B1 (four-layer ARC film-stacks) for the preferred orientation planes ZnS (111) and YF_3 (011) of grown ARC film-stacks.

Structural parameters	**Sample-A1**		**Sample-B1**	
	(ZnS)	(YF_3)	(ZnS)	(YF_3)
2θ (degree)	28.62	23.78	28.52	23.75
Lattice plane (hkl)	(111)	(011)	(111)	(011)
FWHM β, (radian)	0.0045	0.0068	0.0047	0.0071
The lattice constant, a (Å)	5.404	5.292	5.421	5.299
Average crystallite size, D (nm)	32.98	21.77	31.75	20.71
Stress σ (GPa)	0.049	1.334	0.371	1.234

Table 6.3 indicates that all the structural parameters (β: FWHM, a: lattice constant, D: Average crystallite size and stress: σ(YF3)) of Samples A1 & B1 have nearly equal values, but a deviation in the stress of ZnS film for both the Samples A1 & B1 (σ(ZnS) of the Sample-B1 is slightly higher than the σ(ZnS) of Sample-A1) is observed. Probably the difference between bulk versus measured lattice constants ($a-a_{0=}$ 0.015 Å) for the Sample-B1 (bulk lattice constant a_0 = 5.406 Å and measured lattice constant a=5.421 Å) is slightly higher than that of Sample-A1 ($a-a_{0=}$ 0.002 Å, where a_0 = 5.406 Å and measured lattice constant a=5.404 Å) that is accountable for the increased stress of grown ZnS film over the Sample-B1, as per the Eq. 6.3. This comparison of the

structural parameters of both the Samples-A1 and B1 also reveals the repeatability of four-layer ARC stack fabrication-process. Therefore, the thermally evaporated four-layer ARC stacks (HgCdTe-CdZnTe/ZnS/YF_3/ZnS/YF_3) with the realized structural parameters (presence of standard phases of ZnS and YF_3 materials) could be acceptable and favorable for the development of HgCdTe-based MWIR detectors.

6.4.2. AFM analysis

The surface morphological properties of thermally evaporated ARC film-stacks (on Samples A1 and B1, the configuration of ARC film-stacks: HgCdTe-CdZnTe/ZnS/YF_3/ZnS/YF_3) were evaluated via AFM measurement technique where the scanning of Samples A1 and B1 (ARC film-stacks: HgCdTe-CdZnTe/ZnS/YF_3/ZnS/YF_3) were performed in tapping mode. The resultant AFM image profiles (2D and 3D) of both the ARC film-stacks (thickness 699 ± 2.6 nm, scanning area: 5.0 μm × 5.0 μm) are shown in Fig. 6.2(a, b). The grown ARC film-stacks (over Sample-A1 and Sample-B1) are uniform, dense, and continuous (Fig. 6.2a,b). Several high-density islands (maize-shaped islands), interconnected 2D layers, and nanoclusters were observed within these ARC film stacks. Sample-A1 and Sample-B1 were found with the root-mean-square (RMS) roughness values 1.82 ± 0.12 nm and 1.40 ± 0.09 nm, respectively. The morphology of both the Samples (A1 and B1) appears similar except for having a minor deviation in their rms surface roughness. The measured roughness of Sample-A1 (1.82 ± 0.12 nm) is slightly higher than that of Sample-B1 (1.40 ± 0.09) nm. The difference in surface-roughness for the samples (A1 and B1) may be associated with the variation of deposition rate (probably Sample-A1 has a slightly lower deposition rate than Sample-B1), and it has created the ARC film-stack of higher surface-roughness over the Sample-A1.

Thus, the process of ARC film-stack growth (Samples A1 and B1) has shown good repeatability. The comparative analysis of the Samples (A1 and B1) revealed the optimized ARC film stacks with reasonable/favourable morphological belongings (like low roughness, high packing density, continuity, non-porosity, and good repeatability). The surface morphology (low surface roughness) not only affects the anti-reflective character of the AR coating but also supports achieving the hydrophobic surface of the AR coating.

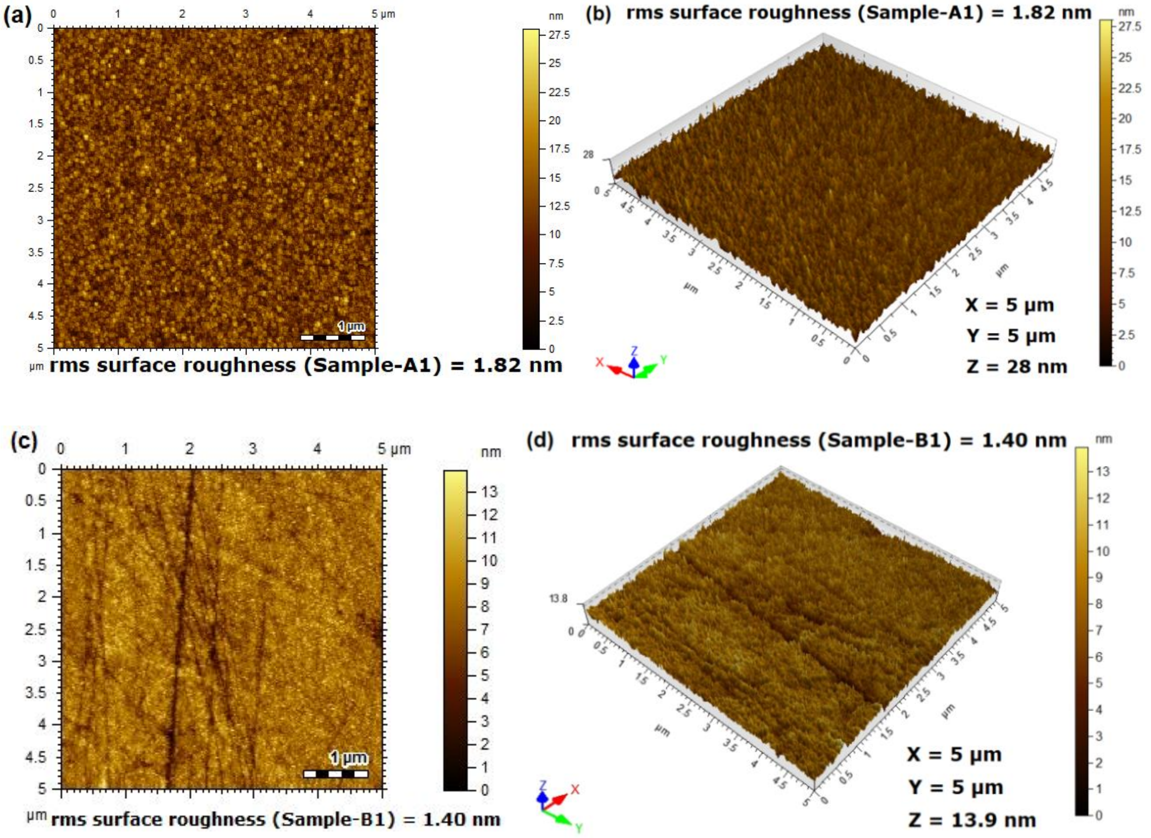

Figure 6.2. AFM images (showing surface morphologies) of ARC thin film stacks grown on different CdZnTe-HgCdTe Samples (A1 and B1). 2D image of Samples A1 and B1 (a,c) and 3D image of Samples A1 and B1 (b,d).

The low surface roughness [25,32,34,37-40] is an essential parameter responsible for the quality/performance of the ARC film-stacks (in terms of reflectance since ARC layers with low surface roughness can ensure low reflectance) and the reflectance measurement results of the four-layer ARC stacks have validated this fact where the fabricated ARC film-stacks (Samples-A1 and B1) of low surface roughness were found with desired low reflectance-2%. The humidity test/boiling water test of ARC stacks did not indicate peeling/cracking/physical degradation within the film stacks. This probably happens due to the hydrophobic behaviour of ARC stacks with low surface roughness. Thus, the ARC film stacks with optimum morphological properties (low surface roughness) might be appropriate for developing high-performance HgCdTe IR detectors.

6.4.3. EDX measurement

The EDX technique was applied to find the elemental composition of thermally evaporated four-layer ARC film stacks. Fig. 6.3(a and b) represent the EDX spectra of ARC film stacks grown on Sample-A2 and Sample-B2, respectively. The peaks of elements zinc (Zn), sulphur (S), yttrium (Y), and fluorine (F) were observed within the EDX spectrum of Sample-A2 (Fig. 6.3a). Also, similar peaks of zinc (Zn), sulphur (S), yttrium(Y), and fluorine (F) elements at the same energy points were detected within the spectrum of Sample-B2 (Fig. 6.3b). EDX results of thermally grown ARC film stacks (Samples-A2 and B2) are itemized in Table 6.4. Fig. 6.3 (a, b) and Table 6.4 direct that the compositional parameters of both Samples-A2 and B2 are identical except for having a minor variation in the atomic/weight % of the constituent elements (Zn, S, Y, and F).

The difference between the EDX results/spectra of both the ARC film stacks (Samples A2 and B2) may occur because of slight variation in their film-thickness, surface roughness, electron interaction volume (i.e., the volume of electron beam interaction with the film/substrate during EDX measurement) and nature of sample/substrate. SEM/AFM measurement results validate this estimation since the film-thickness/surface-roughness variations have been observed. EDX results/spectra of both the ARC film stacks (Samples A2 and B2) also consist of the same/single elements (Zn) at different energy positions since the Zn element is mainly identified by the energy peak with high intensity (corresponds to L_α=1.012 eV) and hence it is marked as high intensity/low energy peak in the resultant EDX spectra. On the other hand, the other peaks with low intensity/high energy appearing in the EDX spectrum are associated with the peaks of K-shell. As a result, the elements (Zn) appear for different energies and are marked in the spectrum except for having low intensity. The four-layer ARC film stacks (Sample-A2 and B2) originated with the desired elements, but some peaks of Cd and Te elements (negligible intensities) were also recorded in their spectra which may be generated because of the interaction of high energy EDX beam with the Samples (CdZnTe) surface [4,32,33]. The compositional analysis has created highly pure ARC film stacks (Samples A2 & B2) with good repeatability, and those can be treated as optimized ARC film stacks.

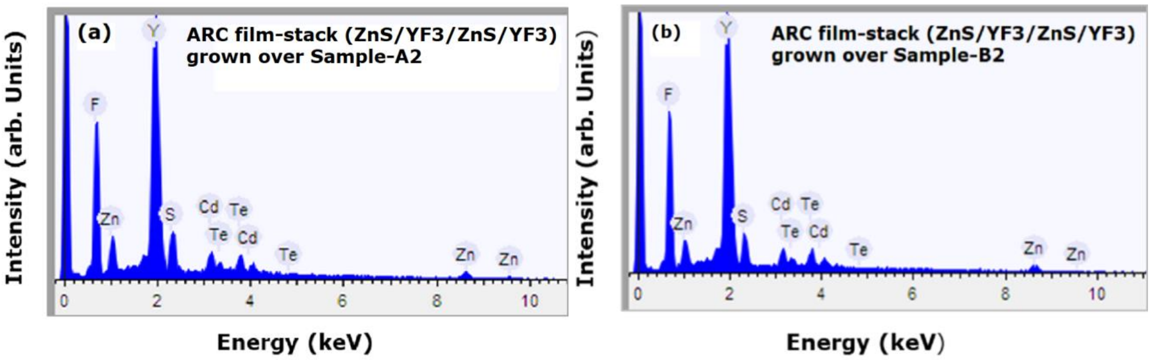

Figure 6.3. Elemental analysis (EDX spectra) of thermally evaporated ARC film stacks on Samples A2 and B2. (a) EDX spectrum of Sample-A2 and (b) EDX spectrum of Sample-B2.

Hence, the thermally evaporated ARC film stacks with high purity could be advantageous for the fabrication of high-performance IR detectors [32, 34] since any impurity within the film affects the elemental ratios of desired grown materials, which can degrade the optical property (reflected signal)/performance of the fabricated HgCdTe-based IR detectors.

Table 6.4. EDX results of thermally grown four-layer ARC film stacks on CdZnTe-HgCdTe Samples (A2 and B2).

Sr. No.	Sample-A2		Sample-B2	
Elements	Atomic %	Weight %	Atomic %	Weight %
Fluorine	74.33	40.59	75.95	41.99
Sulphur	4.03	3.72	3.01	2.80
Zinc	3.68	6.88	2.63	5.01
Yttrium	14.81	37.86	15.62	40.41
Cadmium	1.48	4.81	1.35	4.43
Tellurium	1.67	6.14	1.44	5.36
Total	100	100	100	100

6.4.4. SEM analysis

The microstructural properties of thermally grown four-layer ARC film-stacks (on CdZnTe-HgCdTe Samples-A2 and B2) were evaluated through the SEM characterization technique. The resulting SEM images of Samples A2 and B2 (at various scales and magnifications) are demonstrated in Fig. 6.4(a, b, c, d, e, f, g, and h). The front view of thermally grown Sample-A2 (Fig. 6.4a, b) shows that the ARC film-stack is uniform, continuous, and highly dense. The film stack resembles a cauliflower comprising several random-shaped particles (spherical, hexagonal, and conical) and some interconnecting trenches. The measured particle size for Sample-A2 (Fig. 6.4b) ranged from 24.83 - 36.17 nm. Fig. 6.4(c, d) displays the cross-sectional view of Sample-A2 that has revealed the thickness (height) of four-layer ARC film-stacks: ZnS (88.3 nm)/YF_3 (212.6 nm)/ZnS (94.8 nm)/YF_3 (316.4 nm) and it is reasonably near to the thickness of ARC film-stack: ZnS (91 nm)/YF_3 (207 nm)/ZnS (91 nm)/YF_3 (310 nm) measured through a quartz crystal monitor. Similarly, the microstructural features of Sample-B2 (four-layer ARC film-stack) are highlighted in Fig. 6.4(e, f, g, and h), indicating that the deposited ARC film-stack is uniform, continuous, and densely packed. The Sample-B2 (Fig. 6.4e, f) also gives the impression of cauliflower (the structure of the ARC film-stack has several randomly shaped particles as well as some interconnecting trenches) similar to Sample-A2 and the particle size for this Sample-B2 (Fig. 6.4f) was found between 23.67 to 35.49 nm. The cross-sectional view of Sample-B2 displayed in Fig. 6.4(g, h) reveals the thickness (height) of four-layer ARC film-stacks: ZnS (87.9 nm)/YF_3 (210.8 nm)/ZnS (93.2 nm)/YF_3 (315.7 nm) and it is very near to real thickness of the deposited ARC film-stack: ZnS (91 nm)/YF_3 (207 nm)/ZnS (91 nm)/YF_3 (310 nm).

Subsequently, the comparison of Samples A2 and B2 conveys that both the ARC film-stacks are identical (highly dense, uniform, continuous, and negligible trenches) except for a slight deviation in the values of grain size (Sample-A2 has a larger grain size than the Sample-B2) that is related to the variation of deposition-rate and thickness. According to a well-known fact, the grain size increases with increasing thickness and decreasing deposition rate. The resultant values of particle sizes (grain sizes) of Sample-A2 (24.83 - 36.17 nm) and B2 (23.67-35.49 nm) validate the fact described above that the grain size of Sample-A2 is marginally high relative to the grain size of Sample-B2. Since Sample-A2 (712.1 nm) is relatively thicker than Sample-B2 (707.6 nm) and may also have a lower deposition rate than Sample-B2, the ARC film-stacks (Samples A2 and B2) have presented good repeatability (in terms of microstructural findings like density, uniformity, continuity, and presence of negligible trenches, etc.), and may be treated as the optimized ARC film-stack [22,26,41] with desired film thickness. Since the reflectance depends on the film thickness, a small thickness variation can change the reflectance level of the ARC film-stack/IR detector performance, which might be favorable in fabricating low-pitch/high-format IR detectors.

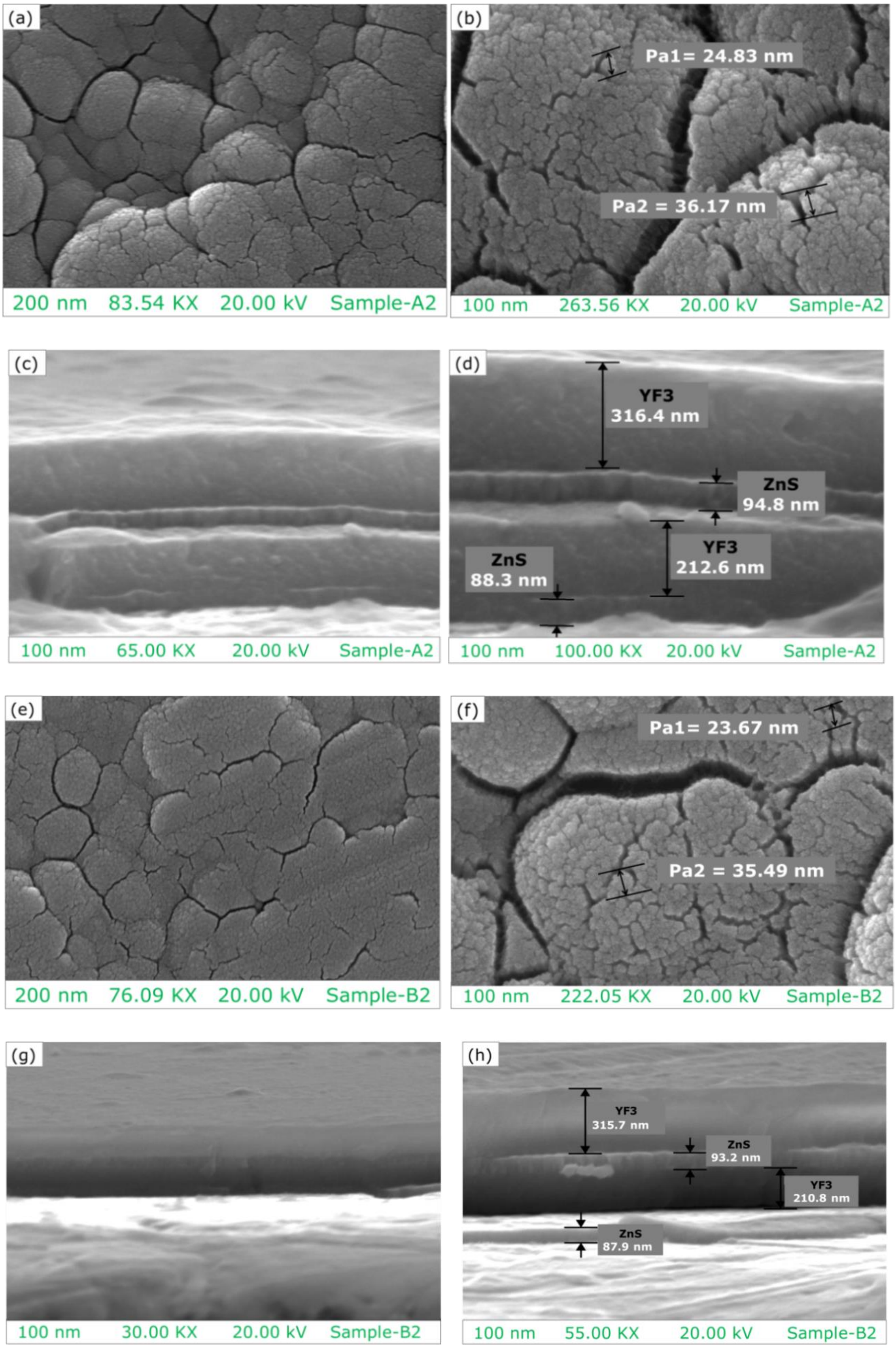

Figure 6.4. Microstructural analysis (SEM images) of thermally grown ARC film-stacks on CdZnTe-HgCdTe Samples (A2 and B2) at various scales/magnifications: (a) front-

view of Sample-A2 (ARC film-stack) at 200 nm and 83.54 KX, (b) particle size of Sample-A2 (ARC film-stack) via front-view at 100 nm and 263.56 KX, (c) cross-sectional view of Sample-A2 (ARC film-stack) at 100 nm and 65.00 KX and (d) height of individual layers in ARC film-stack (Sample-A2, configuration: ZnS /YF_3/ZnS YF_3) via its cross-sectional view at 100 nm and 100.00 KX, (e) front-view of Sample-B2 (ARC film-stack) at 200 nm and 76.09 KX, (f) particle size of Sample-B2 (ARC film-stack) via front-view at 100 nm and 222.05 KX, (g) cross-sectional view of Sample-B2 (ARC film-stack) at 100 nm and 30.00 KX and (h) height of individual layers in ARC film-stack (Sample-B2, configuration: ZnS /YF_3/ZnS YF_3) via its cross-sectional view at 100 nm and 55.00 KX.

6.4.5. Optical properties (reflectance via FTIR measurement)

The optimized ARC films were used to develop the four-layer ARC structures on the HgCdTe-CdZnTe assembly (configuration: YF_3/ZnS/YF_3/ZnS/CdZnTe-HgCdTe) for evaluating their optical properties (in terms of reflectance). Fig. 6.5 represents the schematic diagram of a backside-illuminated HgCdTe-CdZnTe assembly (without ARC film/with ARC film-stack) where the IR radiation is coming to the backside of this assembly (on the CdZnTe side). The thicknesses (as per theoretical design) of individual layers of ARC film-stack (ZnS (91 nm)/YF_3 (207 nm)/ZnS (91 nm)/YF_3 (310 nm)) are displayed in Fig. 6.5 (schematic diagram) and Table 1. Reflectance measurements of these HgCdTe-CdZnTe structures (without ARC film/with ARC film-stack) were accomplished via FTIR spectrometer at 300 K (room temperature) because of the non-availability of an FTIR measurement setup operating at the temperature of 80 K. Although, HgCdTe based IR detectors work at a temperature of 80 K but the theoretical design of ARC film-stack [8,31,33] has been prepared accordingly for the working temperatures 80 and 300 K. The HgCdTe-CdZnTe-based theoretical study [31] reflects that no considerable change occurs in the values of reflections at different temperatures 80 and 300 K, but only a relative shift in the cut-off wavelength for these curves was observed where the cut-off wavelength (corresponding to 80 K) was higher than the cut-off wavelength at 300 K [8,31].

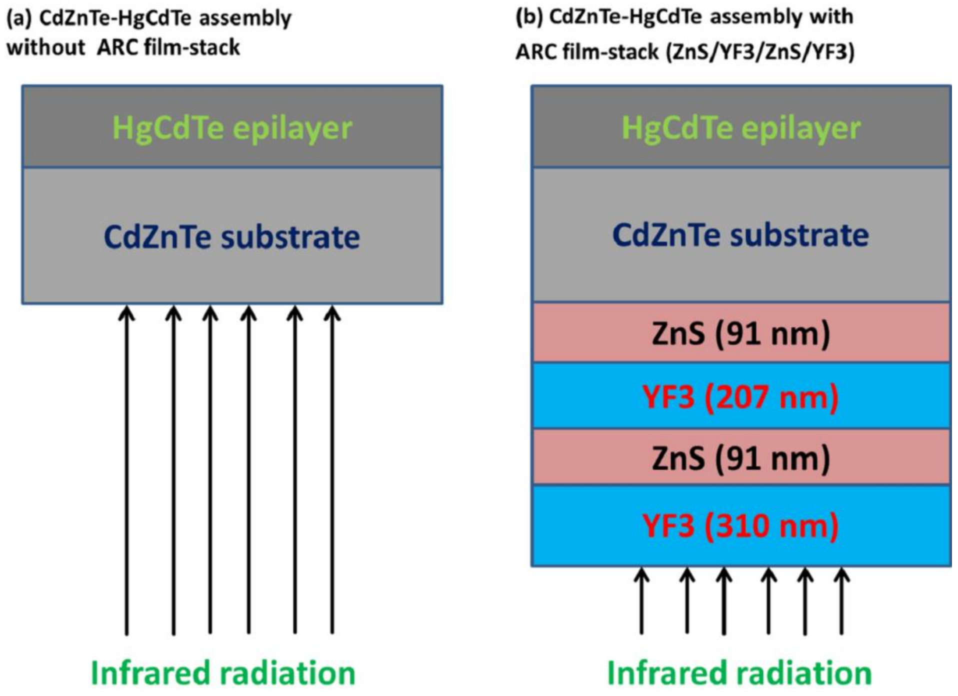

Figure 6.5. Schematic diagram of CdZnTe-HgCdTe (Samples A3 and B3) based ARC film-stacks :(a) CdZnTe-HgCdTe assembly without ARC stack and (b) CdZnTe-HgCdTe assembly with four-layer ARC stack with a configuration YF_3/ZnS/YF_3/ZnS/CdZnTe-HgCdTe and x=0.29.

Since the HgCdTe epilayer absorbs all the incident IR flux/radiation in the MWIR (i.e., 3-5 µm) spectral region and hence the FTIR measurements (which is not possible in the transmittance mode) of grown ARC stacks have been performed in the reflectance mode. The reflectance versus wavelength curves for Samples A3 and B3 are presented in Fig. 6.6 (a, b, c, d, e, and f). Fig. 6.6 (a, b) displays the measured values of reflectance for the Sample-A3 (without ARC: HgCdTe-CdZnTe and with four-layer ARC film-stack: YF_3/ZnS/YF_3/ZnS/CdZnTe-HgCdTe) in the targeted MWIR (3.2- 4.3 µm) spectral range.

The bare Sample-A3 (without ARC) has shown average reflectance of 22.2% (Fig. 6.6a), and it is reduced to 4.9-5.6% (Fig. 6.6b) with a four-layer ARC film-stack (ZnS (91 nm)/YF_3 (207 nm)/ZnS (91 nm)/YF_3 (310 nm)), while the minimum reflectance 0.3% occurs at 4 µm. Similarly, Sample-B3 (without ARC: HgCdTe-CdZnTe) has displayed an average reflectance of 22.5% (Fig. 6.6c) in the MWIR (3.2- 4.3 µm) spectral range, which is decreased to 3.9-5.1 % (Fig. 6.6d) using four-layer ARC film-stack (ZnS / YF_3 / ZnS / YF_3) of the same thickness and its reflectance minimum 0.3% is achieved at 4 µm in the reflectance spectrum.

HgCdTe-CdZnTe Samples (Sample A3: 22.2 % and Sample B3: 22.5%) with an identical reflectance value of 0.3% were found, covering the whole spectral range (3.2-4.3 µm) of MWIR detectors. The decrease in reflection for both Samples (A3: 21.9 %, B3: 22.3 %) is nearly the same except for a slight deviation. This discrepancy in the reflectance values [8,10,12,25,26,29,42] could be associated with a minor thickness difference between two ARC film-stacks (errors in tooling factor-calibration and ARC film growth monitoring), deviation in packing density of grown samples, and uncertainty in FTIR measurement (due to low reflectance level, temperature variation, and calibration error) of the fabricated ARC stacks. The comparative analysis of Samples A3 and B3 (Fig. 6.6e: without ARC film, Fig. 6.6f: with ARC film-stack) reveals that ARC film-stacks have reduced the reflection of bare CdZnTe-HgCdTe assembly.

The measured reflectance of both the ARC stacks (Samples A3 and B3) did not thoroughly cover the designed spectral region (MWIR: 3.2-5.3 µm) but showed the reflectance only in the spectral region of 3.2-4.3 µm (i.e., a relative shift in the cut-off wavelengths of the measured and designed ARC stacks were found) since as per the ARC stack-design (MWIR, temperature: 80 K) the cut-off wavelength must be present at 5.3 µm (80 K), but in the measured reflectance-curves it was revealed at 4.3 µm (300 K) that occurs due to the temperature difference of the measured and designed ARC film-stacks. Thus, Samples A3 and B3 have shown good repeatability in terms of reflectance. Hence the created ARC film-stacks with minimum reflectance and repeatability might be highly useful to produce the high-performance HgCdTe-based IR detectors (in terms of high quantum efficiency, low noise, low cross-talk, high image contrast, and long-term stability) which are utilized in space tracking & surveillance system (STSS), thermal imaging system, night vision devices, and missile guidance systems.

The theoretically evaluated reflectance curves/design of CdZnTe-HgCdTe assembly (with four-layer ARC stack, configuration: YF_3/ZnS/YF_3/ZnS/CdZnTe-HgCdTe; curves evaluated at the temperatures 300 and 80 K) were generated [8,27,30,31,33], which are shown in Fig. 6.7 (a-d). The theoretically evaluated reflectance curve (at 300 K: Fig. 6.7a) shows a reflectance of 3.8 - 6.2 % in the MWIR (3.2- 4.3 µm) spectral range with a minimum reflectance value of 0.9 % at the wavelength 4.2 µm. Similarly, the theoretical reflectance curve (Fig. 6.7c) evaluated at the temperature of 80 K show reflectance values in the range of 4.1 - 6.3 % for the MWIR (3.2- 5.3 µm) spectral range with a minimum of 1.7 % at the corresponding wavelength of 4.3 µm. Fig. 6.7(b) shows a comparison of the theoretical curve (evaluated at 300 K) with the experimentally measured reflectance curves (Samples A3 and B3 at 300 K). Accordingly, the experimental reflectance values of Samples-A3 have shown a better match with the theoretically evaluated values, while the experimental reflectance curve of Sample-B3 also has a quite close match with the theoretical curve but lesser than Sample-A3. This variation may occur due to the better surface quality (low surface roughness, fewer defects/impurities) and relatively small thickness of Sample-A3 (CdZnTe substrate) than the Sample-B3 (CdZnTe substrate). Fig. 6.6 (a and c) also validate that the reflectance of Sample A3 is lower than that of Sample B3.

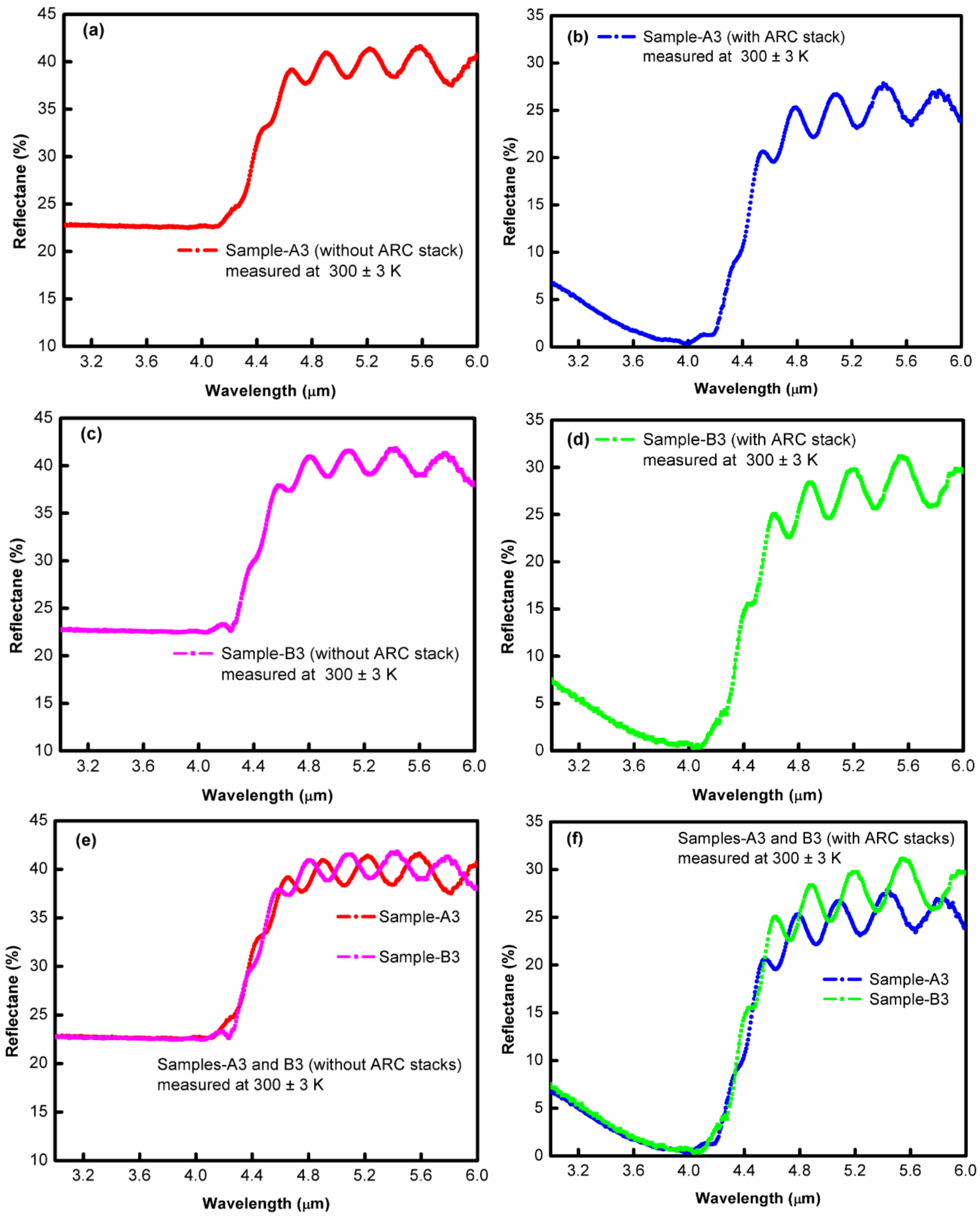

Figure 6.6. Reflectance spectra of the Samples A3 and B3 (without ARC film-stack/with ARC film-stack, x=0.29) at 300 ± 3 K: (a) Sample-A3 (CdZnTe-HgCdTe assembly) without ARC stack, (b) Sample-A3 (CdZnTe-HgCdTe assembly) with four-layer ARC stack having a configuration of YF_3/ZnS/YF_3/ZnS/CdZnTe-HgCdTe, (c) Samples-B3 (CdZnTe-HgCdTe assembly) without ARC stack, (d) Samples-B3 (CdZnTe-HgCdTe assembly) with four-layer ARC stack having a configuration of

$YF_3/ZnS/YF_3/ZnS/CdZnTe$-HgCdTe, (e) comparative curves of Samples-A3 and B3 (CdZnTe-HgCdTe assembly) without ARC stack, (f) comparative curves of Samples-A3 and B3 (CdZnTe-HgCdTe assembly) with four-layer ARC stacks having a configuration of $YF_3/ZnS/YF_3/ZnS/CdZnTe$-HgCdTe.

Correspondingly, the comparison of Samples A3 and B3 (reflectance curves measured at 300 K) with the theoretical reflectance curve/design at 80 K is shown in Fig 6.7(d), which is not so significant, but it has been done for just seeing the reflectance trend/behaviour in both the curves. It also reveals that the experimental reflectance curves (Samples A3 and B3) are very close to the theoretical reflectance curve/design (evaluated at 300 K) except for a relative shift in the cut-off wavelength (since the theoretical reflectance curve owns its cut-off wavelength at 5.3 µm and the experimental reflectance curves (Samples A3 and B3) exhibit their cut-off wavelengths at 4.3 µm) occurs because of the temperature difference existing between the experimentally measured curves and theoretically evaluated curves/designs. Accordingly, the comparative analysis validates the theoretical designs of a four-layer ARC film stack created over the CdZnTe-HgCdTe assembly.

The developed four-layer ARC film-stack (CdZnTe-HgCdTe assembly) with low relative total thickness has shown better performance (in terms of reflectance) than the early reported double-layer ARC film-stack [31] since probably the ARC film-stack created with more number of layers has lower internal stress and better adhesion comparative to double-layer ARC film. Hence, parameters like the number of layers, internal stress, and adhesion can affect the performance of the ARC stack. Thus, the developed ARC film-stack (structure: with minimum no. of layers, low relative total thickness, low internal stress, and low reflectance within the targeted MWIR spectral range) exhibited a fair agreement with the early published ARC schemes [2,15,18,27, 30,43] of the HgCdTe IR detectors and hence this could be most favourable and appropriate in the fabrication of high-performance IR detectors (minimum reflectance, high quantum efficiency, low-noise, high stability, and low cross-talk) of futuristic as well as current technological requirements.

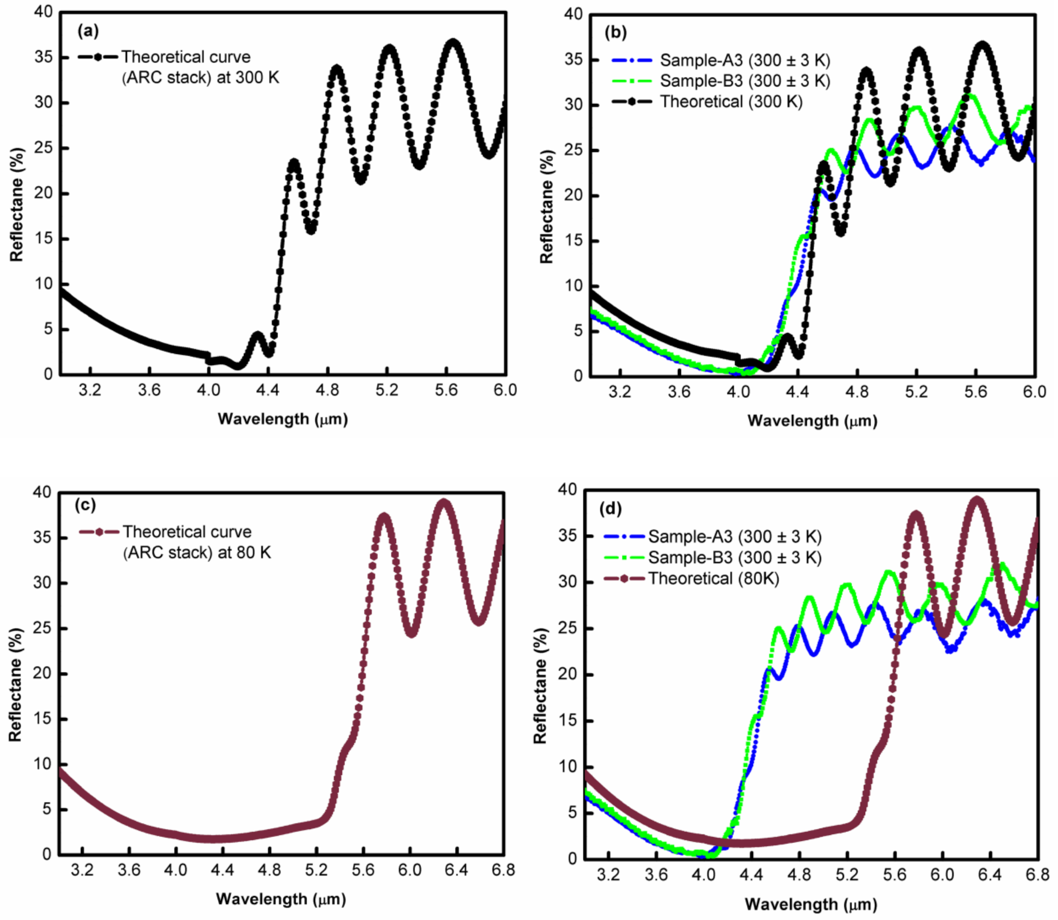

Figure 6.7. Comparison of the experimentally observed reflectance curves of the Samples A3 and B3 (four-layer ARC film-stack, x=0.29 and temperature: 300 ± 3 K) with the theoretically obtained reflectance curves of CdZnTe-HgCdTe assembly (four-layer ARC stack, configuration: YF_3/ZnS/YF_3/ZnS/CdZnTe-HgCdTe; temperatures: 300 and 80 K). Theoretical reflectance curve at 300 K (a), experimental reflectance curves (Samples-A3 and B3) and theoretical curve at temperature 300 K (b) and theoretical reflectance curve at 80 K (c), experimental reflectance curves (Samples A3 and B3 at 300 ± 3 K) and theoretical reflectance curve at temperature 80 K (d).

6.4.6. Examination of adhesion and environmental durability

The reliability, environmental durability, and adhesion of the AR coating film-stack (structure) are the factors that play a significant role in creating the production-level CdZnTe-HgCdTe-based ARC technology. The quality (reliability/durability) of the AR coatings depends upon their packing density/adhesion, which is greatly affected due to the presence of humidity within the ARC films. Since the packing density of thermally evaporated AR coatings (deposited at room temperature) is relatively low because of absorbed environmental water molecules responsible for generating voids within the films, the packing density and the overall quality of AR coatings can be increased considerably if the film's deposition occurs at a relatively high temperature. The molecules of coating materials have high surface mobility at this high temperature, producing highly-dense films with high resistance to humidity/chemicals [10,12,20,26,34]. Hence, in the present research work, a preheating of CdZnTe-HgCdTe assembly was performed at a high temperature to enhance the quality of four-layer AR coatings. The reliability and durability of the ARC deposited samples (four-layers AR coatings) were inspected using three tests (the tape-peeling test: to decide the bonding quality between the CdZnTe surface and four-layers AR coating stack, water solubility test, and humidity-test: to know the effect of water/humidity on the durability of the four-layers AR coatings) as mentioned below:

(1) **Tape-test:** A scotch tape (more than 6 cm in length) was applied to the sample surface, and then a force was applied to the end of the tape from the CdZnTe sample surface. Peel the tape off the sample's surface along its total length. No small segments of ARC films were lifted off through scotch tape.

(2) **Water solubility test:** The grown sample (AR coatings) was put into boiling DI water/acetone for 5 min, but no indication of peeling, cracking, or any physical degradation within the AR coating was perceived.

(3) **Humidity test**: The grown samples (AR coatings) were put into humid conditions (Time: 24 h, Relative humidity: 95–100%, temperature-49 °C), but no effects of humidity were realized on the ARC film-stacks.

All the samples (CdZnTe-HgCdTe) have successfully passed the reliability and durability tests. The grown ARC stacks (structures) have good adhesion, high packing density, and high resistance to environmental humidity/water/chemicals. Thus, these tests prove the high reliability/durability of the fabricated AR coating stacks, which can be utilized in humid and nautical environments.

6.5. Conclusions

The present research work has disclosed all the aspects of thermally-evaporated four-layer anti-reflection coating (ARC) film-stacks (based on ZnS and YF3 coating materials with configuration: ZnS/YF3/ZnS/YF3 and optimized thickness of 699 ± 2.6 nm) on the HgCdTe-CdZnTe assembly (i.e., CdZnTe substrate exists on the backside of this assembly and it is the base-material for HgCdTe epilayer growth). The properties of grown ARC film-stacks were examined through numerous characterization techniques, namely XRD, AFM, EDX, and SEM analysis. The polycrystalline ARC film-stacks (partial amorphous nature and minimum stress) were found with cubic zinc-blende phase and preferred orientation (111). ARC film-stacks with the desired surface morphology (good uniformity, high density, and low rms roughness: 1.40-1.82 nm), elemental composition (high purity), and micro-structural features (average grain size: 23.67- 36.17 nm, thickness: 707.6-712.1 nm) was realized. Henceforward, the optimized ARC films were further used to produce two ARC film-stacks/structures (with identical configuration: YF3/ZnS/YF3/ZnS/CdZnTe-HgCdTe and remarkably thin film-thickness) for examining their effectiveness. Subsequently, FTIR measurements of both the ARC film-stacks/structures (HgCdTe-CdZnTe/ZnS/YF3/ZnS/YF3) have shown the reflection of the order of less than 1.0 % within the targeted MWIR (3.2 - 4.3 μm) wavelength range, which has also been supported by the theoretically estimated results. Thus the process of ARC film-stack fabrication is repeatable and reproducible. Various tests (tape test, water solubility test, and humidity test) have also validated the reliability/durability of the fabricated AR coating film-stack/structure (in terms of good adhesion, high packing density, and high resistance to environmental humidity/water/chemicals) that can be utilized in a humid environment. Thus, the four-layer ARC film-stacks are the most effective and suitable reflection agents that could be used to fabricate high-performance HgCdTe-based IR detectors.

References

[1] A. Rogalski, Competitive technologies of third generation infrared photon detectors, Opto-electron. Rev. 14 (2006) 84-98.

[2] N. Vanamala, K. C. Santiago, and N. C. Das, Enhanced MWIR absorption of HgCdTe (MCT) via plasmonic metal oxide nanostructures, AIP Adv. 9 (2019) 025113.

[3] F. Li, J. Deng, J. Zhou, Z. Chu, Y. Yu, X. Dai, H. Guo, L. Chen, S. Guo, M. Lan & X. Chen, HgCdTe mid-Infrared photo response enhanced by monolithically integrated meta lenses, Sci. Rep. 10 (2020) 6372.

[4] S. L. Price and P. R. Boyd, Overview of compositional measurement techniques for HgCdTe with emphasis on IR transmission, energy dispersive x-ray analysis and optical reflectance, Semicond. Sci. Technol. 8 (1993) 842-859.

[5] A. K. Sood, A. W. Sood, R. E. Welser, G. G. Pethuraja, Y. R. Puri, X. Yan, D. J. Poxson, J. Cho, E. F. Schubert, N. K. Dhar, D. L. Polla, P. Haldar, J. L. Harvey, Development of nanostructured anti-reflection coatings for EO/IR sensor and solar cell applications, Mater. sci. appl. 3 (2012) 22914.

[6] A. Rogalski, Optical detectors for focal plane arrays, Opto-electron. Rev. 12 (2004) 221–245.

[7] B. D. MacLeod and D. S. Hobbs, Long life, high performance anti-reflection treatment for HgCdTe Infrared Focal Plane Arrays, Infrared technology and applications XXXIV, Proc. of SPIE 6940 (2008) 69400Y.

[8] A. Ghosh, A. S. Upadhyaya, Broad band anti-reflection coating on zinc sulphide simultaneously effective in SWIR, MWIR and LWIR regions, Infrared Phys. Technol. 52 (2009) 109-112.

[9] Q. J. Liao X. N. Hu, The Study of Improving the Performance of HgCdTe Photovoltaic Detectors with Antireflection Coating, 2006 Joint 31st International

conference on infrared millimeter waves and 14th international conference on terahertz electronics, IEEE Xplore, 23524110 (2006) 132-132.

[10] M. Bhatt, B. B. Nautiyal, P. K. Bandyopadhyay, High efficiency anti-reflection coating in MWIR region (3.6–4.9 μm) simultaneously effective for germanium and silicon optics, Infrared Phys. Technol. 53 (2010) 33-36.

[11] M. Moayedfar and M.K. Assadi, Various types of anti-reflective coatings (ARCs) based on the layer composition and surface topography: a review, Rev. Adv. Mater. Sci. 53 (2018) 187-205.

[12] M. B. Kala, P. K. Bandyopadhyay, B. B. Nautiyal, Thorium free anti-reflection coating in MWIR region on silicon optics, Infrared Phys. Technol. 55 (2012) 409.

[13] A. Yenisoy, C. Yesilyaprak, K. Ruzgar, and S. Tuzemen, Ultra-broad band anti-reflection coating at mid wave infrared for high efficient germanium optics, Opt. Mater. Express 9 (2019) 3123-3131.

[14] N. D. Akhavan, G. A. Umana-Membreno, R. Gu, J. Antoszewski, L. Faraone, Design principles for high QE HgCdTe infrared photodetectors for eSWIR applications, J. Electron. Mater. 51 (2022) 4742–4751.

[15] A. I. D’Souza, E. Robinson, P. S. Wijewarnasuriya, and M. G. Stapelbroek, Spectral response model of backside-illuminated HgCdTe detectors, J. Electron. Mater. 40 (2011) 1657-1662.

[16] A. Bahrami, S. Mohammadnejad, N. J. Abkenar, S. Soleimaninezhad, Optimized single and double layer anti-reflection coatings for GaAs solar cells, Int. J. Renew. Energy Res. 3 (2013) 80-83.

[17] M. R. Hantehzadeh, M. Ghoranneviss, A. H. Sari, F. Sahlani, A. Shokuhi, M. Shariati, Antireflection coating on InP for semiconductor detectors, Thin Solid Films 515 (2006) 547–550.

[18] V. Gopal, Effect of anti-reflection coating on the performance of 0.1 eV HgCdTe photoconductive detectors, Infrared Phys. 23 (1983) 307-310.

[19] O. Duyar, H. Z. Durusoy, Design and preparation of anti-reflection and reflection optical coatings, Turk. J. Phys. 28 (2004) 139-144.

[20] G. Zhang, J. Zhao, M. A. Green, Effect of substrate heating on the adhesion and humidity resistance of evaporated MgF2 /ZnS anti-reflection coatings and on the performance of high-efficiency silicon solar cells, Sol. Energy Mater. Sol. Cells 51 (1998) 393-400.

[21] P. Nubile, Analytical design of anti-reflection coatings for silicon photovoltaic devices, Thin Solid Films 342 (1999) 257-261.

[22] H. K. Raut, V. A. Ganesh, A. S. Nair and S. Ramakrishna, Anti-reflective coatings: A critical, in-depth review, Energy Environ. Sci. 4 (2011) 3779-3804.

[23] A. Yenisoy, C. Yeşilyaprak, S. Tüzemen, High efficient ultra-broadband anti-reflection coating on silicon for infrared applications, Infrared Phys. Technol. 100 (2019) 82-86.

[24] S. F. Hasan and S. N. Turki, Design of an anti-reflection coating for mid- wave infrared regions in the range (3000-5000) nm, Int. J. Appl. Innov. Eng. Manag. 2 (2013) 96-100.

[25] R. Z. Moghadam, H. Ahmadvand , M. Jannesari, Design and fabrication of multi-layers infrared anti-reflection coating consisting of ZnS and Ge on ZnS substrate, Infrared Phys. Technol. 75 (2016) 18-21.

[26] M. Gholampour, A. Miri, S. I. Karanian and A. Mohammadi, Design and fabrication of multi-layers infrared anti-reflection nanostructure on ZnS substrate, Acta Phys. Pol. A 136 (2019) 527-530.

[27] F. Lemarquis, G. Marchand, and C. Amra, Design and manufacture of low-absorption ZnS–YF_3 anti-reflection coatings in the 3.5-16 µm spectral range, Appl. Opt. 37 (1998) 4239-4244.

[28] W. Lei, J. Antoszewski, and L. Faraone, Progress, challenges, and opportunities for HgCdTe infrared materials and detectors, Appl. Phys. Rev. 2 (2015) 041303.

[29] C. L. Tan and H. Mohseni, Emerging technologies for high performance infrared detectors, Nanophotonics 7 (2018) 169–197.

[30] Y. Matsuoka, S. Mathonneire, S. Peters, and W. T. Masselink, Broadband multilayer anti-reflection coating for mid-infrared range from 7 µm to 12 µm, Appl. Opt. 57 (2018) 1645-1649.

[31] A. K. Saini, A. Singh, V. S. Meena, S. K. Gaur, R. Pal, Design and development of double-layer anti-reflection coating for HgCdTe based mid-wave infrared detector, Mater. Sci. Semicond. Process. 147 (2022) 106749.

[32] V. S. Meena, M. S. Mehata, Thermally grown Indium (In) thin-film for creating ohmic contact and In-bumps for HgCdTe-based IR detectors, Appl. Surf. Sci. 596 (2022)153501.

[33] W. Pan, J. Liu, Z. Zhang, R. Gu, A. Suvorova, S. Gain, H. Wang, Z. Li, L. Fu, L. Faraone, W. Lei, Large area van der Waals epitaxy of II-VI CdSe thin films for flexible optoelectronics and full-color imaging, Nano Res. 15 (2022) 368-376.

[34] V. S. Meena, M. S. Mehata, Investigation of grown ZnS film on HgCdTe substrate for passivation of infrared photodetector, Thin Solid Films 731(2021)138751.

[35] M. H. Ehsani, R. Z. Moghadam, H. R. Dizaji, P. Kameli, Surface modification of ZnS films by applying an external magnetic field in vacuum chamber, Mater. Res. Express 4 (2017) 096408.

[36] N. Tajik, M.H. Ehsani, R. Z. Moghadam, H. R. Dizaji, Effect of GLAD technique on optical properties of ZnS multilayer antireflection coatings, Mater. Res. Bull. 100 (2018) 265-274.

[37] A. T. Salih, A. A. Najim, M. A. H. Muhi, K. R. Gbashi, Single-material multilayer ZnS as anti-reflective coating for solar cell applications, Opt. Commun. 388 (2017) 84-89.

[38] H. Shimomura, Z. Gemici, R. E. Cohen, and M. F. Rubner, Layer-by-layer-assembled high-performance broad band anti-reflection coatings, ACS Appl. Mater. Interfaces 2 (2010) 813-820.

[39] A. Belosludtsev, N. Kyzas, A. Selskis, R. Narbutiene, Design, preparation and characterization of anti-reflective coatings using oxynitride films, Opt. Mater. 98 (2019) 109430.

[40] A. Behranvand, M. D. Darareh, M. Jannesari, M. Mahdavi, Design and fabrication of PbTe/BaF_2 hydrophobic high-efficiency broad-band anti-reflection coating on Ge substrate in long-wave infrared region, Infrared Phys. Technol. 92 (2018) 163-165.

[41] X. Ligang, H. Junhui, Antifogging and anti-reflection coatings fabricated by integrating solid and mesoporous silica nanoparticles without any post-treatments, ACS Appl. Mater. Interfaces 4 (2012) 3293-3299.

[42] M. López, H. Hofer, K. D. Stock, J. C. Bermúdez, A. Schirmacher, F. Schneck, and S. Kück, Spectral reflectance and responsivity of Ge- and InGaAs-photodiodes in the near-infrared: measurement and model, Appl. Opt. 46 (2007) 7337-7344.

[43] J. Schuster and E. Bellotti, Numerical simulation of cross-talk in reduced pitch HgCdTe photon-trapping structure pixel arrays, Opt. Express 21 (2013) 14712.

Chapter 7

Summary and future scope

7.1 Summary

In the present research work, thin films of ZnS (passivation), indium (as ohmic n-contact/detector-ROIC interconnector), Au (ohmic p-contact), and ZnS/YF_3 (four-layer AR coating to minimize IR signal reflectance) were synthesized using thermal evaporation technique. Consequently, the characterization techniques like X-ray diffraction, atomic force microscopy (AFM), scanning electron microscope (SEM), energy-dispersive X-ray analysis (EDX), surface profiler (Dektak), ellipsometry, microscopy, and non-contact sheet resistance measurement were used to created (after evaluating their properties) the optimized films. The effectiveness/usefulness of these optimized films were further examined by fabricating numerous test structures/devices such as metal-insulator-semiconductor (MIS) with the configuration of Au-Cr/ZnS/p-HgCdTe, In bumps/HgCdTe structure, transfer length method (TLM) structure (configuration: In/n/p-HgCdTe), TLM structure with Au/p-HgCdTe and ARC film-stack (configuration: YF_3/ZnS/YF_3/ZnS/CdZnTe-HgCdTe). Furthermore, the characterization techniques scanning electron microscope (SEM), capacitance-voltage (C-V)/current-voltage (I-V) measurements, and Fourier transform infrared (FTIR) spectroscopy were used to verify the suitability of the fabricated structures/devices for IR detector fabrication; which might be the corresponding applications of these thin films.

The whole thesis entitled "*Investigation of thin films properties for HgCdTe based infrared detector*" is divided into seven chapters and organized as follows:

Chapter 1 includes all the scientific information related to the discovery of IR radiation, IR materials/detectors & their applications, past/present scenario of HgCdTe-based IR detector technology (HgCdTe as IR detector/material: unique properties, growth technology, progress, and limitations); structure, working and fabrication technology. The chapter also comprises the applications/roles of various thin films (ZnS, Indium, Cr-Au, and ZnS/YF_3-based ARC film-stack) in HgCdTe-based IR detector fabrication and a short literature review of all these films. The motivation behind the proposed research and the findings have also been included in this chapter.

Chapter 2 presents an overview of the experimental and characterization techniques utilized to accomplish the proposed objectives of the thesis. The experimental techniques/methodology involves the sample preparation, different deposition techniques to grow the proposed thin films, and an exhaustive description of the applied thermal evaporation technique (experimental set-up and thin film growth mechanism) for the growth of various thin films. The main characterization techniques which were utilized for evaluating the properties of grown thin films are X-ray diffraction (XRD) measurement, atomic force microscopy (AFM), scanning electron microscope (SEM), energy-dispersive X-ray analysis (EDX), capacitance-voltage (C-V)/current-voltage (I-V) measurements, Fourier transform infrared (FTIR) spectroscopy, surface profiler (Dektak), ellipsometry, microscopy and non-contact sheet resistance measurement. All these characterization techniques have been thoroughly designated in this chapter.

Chapter 3 describes the study of the thermally evaporated ZnS films on the HgCdTe substrate. The structural, morphological, compositional, and electrical properties of the samples were evaluated through various techniques like XRD, AFM, EDX analysis, and CV measurement. The film has good adhesion with the HgCdTe surface (verified by scotch tape) and it is also compatible with the PLG lift-off process of the device fabrication. The ZnS films have shown all the essential qualities (structural, morphological, compositional, and electrical) of a good passivation film. Thus, it could be an effective passivation agent for the HgCdTe-based IR photodetector. [*]Part of this work has been published in ***Thin Solid Films 731 (2021) 138751 (Elsevier).***

Chapter 4 covers the investigation of thermally grown indium (In) thin films over the HgCdTe substrate/surface. Numerous characterization techniques such as XRD, AFM, EDX, and SEM were utilized to examine the structural, morphological, compositional, and microstructural properties of grown In films; which have realized the optimized In film. Subsequently, these optimized indium films were used in the formation of In bumps/HgCdTe structure and TLM structure (configuration: In/n/p-HgCdTe) to explore their efficacy in the HgCdTe-based IR detector fabrication process. SEM characterization has produced the indium bumps with optimum microstructural parameters (particle size, uniform diameter, and height) while I-V measurement revealed the In/n-HgCdTe interface of ohmic nature. The grown In films are adhesive and well-compatible with the photolithography lift-off process. Therefore, the In could be utilized as the most appropriate material for generating ohmic n-contact and indium-bumps to the HgCdTe-based IR photodetector.[*]Part of this work has been published in ***Applied Surface Science 596 (2022)153501 (Elsevier)***.

Chapter 5 contains all the essential features of thermally grown Au thin films as p-Ohmic contact on the mercury cadmium telluride (HgCdTe) substrate. The optimized Au film was realized via the use of several characterization techniques namely XRD, EDX, AFM, and SEM, respectively. Consequently, the optimized Au films were employed to generate the TLM structure with configuration: Au/p-HgCdTe for examining their usefulness in the HgCdTe-IR detector fabrication. An Au/p-HgCdTe interface was characterized by I-V measurement which has demonstrated ohmic behaviour. The grown Au thin films have good adhesion with the HgCdTe substrate and those are compatible with the photolithography process of IR detector fabrication. Henceforth, Au metal could be the most suitable material to develop reproducible and thermally stable p-ohmic contact on HgCdTe IR detectors. Part of the research work has been published in ***Optical Materials 141 (2023) 113943.***

Chapter 6 encloses all the aspects of the thermally-evaporated four-layer anti-reflection coating (ARC) film-stack (configuration: $ZnS/YF_3/ZnS/YF_3$ and optimized thickness: 699 ± 2.6 nm) over the HgCdTe-CdZnTe assembly. The optimized ARC films were attained after evaluating the structural, morphological, compositional, and microstructural properties of grown ARC film-stacks using numerous characterization techniques like XRD, AFM, EDX, and SEM, respectively. The optimized ARC films were further applied for generating two ARC film-stacks/structures of an identical configuration: $YF_3/ZnS/YF_3/ZnS/CdZnTe$-HgCdTe and the same film thickness. Then, FTIR measurements realized the repeatable/reproducible ARC film-stacks with reflection$\leq$1.0 % within the targeted MWIR (3.2 - 4.3 µm) wavelength range. Tape-test, water solubility test, and humidity test have also validated the reliability/durability (in terms of good adhesion, high packing density, and high resistance to environmental humidity/water/chemicals) of the AR coating film-stack. Hence, the four-layer ARC film-stacks are the most effective and proper reflection agents that could be used to develop high-performance HgCdTe-based IR detectors. Part of the research work has been published in ***Materials Science in Semiconductor Processing 163 (2023) 107556.***

7.2 Future scope of the research work

Considering the aforesaid facts that the developed devices/structures (via utilization of various optimized thin films) might be very useful in the HgCdTe-based IR detector fabrication but several signs of progress which may be accomplished in the future are itemized as follow:

- Comparative study of ZnS passivation layers with different/varying thicknesses to realize an optimized passivation layer with the desired properties (which has a minimum value of surface leakage current/dark current: fixed charge density, interface state, slow state density, oxide charges) and consequently, examine the effectiveness/usefulness of the optimized passivation layer in IR detector fabrication through fabricating an MIS structure/device using this passivation film.

- The effect of $(NH_4)_2S$ treatment on the properties of the ZnS passivation layer: for that one ZnS passivation layer can be grown over the HgCdTe substrate which has been given with $(NH_4)_2S$ treatment before performing deposition while the other ZnS passivation layer can be grown over the HgCdTe substrate that has not given $(NH_4)_2S$ treatment. Accordingly, various characterization techniques can be used to evaluate the properties of both the passivation layers for achieving an optimized passivation layer that might be suitable in the fabrication of an HgCdTe-based IR detector.
- To realize an In/n-HgCdTe interface (TLM structure) with relatively low specific contact resistance and ohmic nature so that high-performance IR detectors (easy current transport and high photocurrent) could be developed.
- Investigation of the In-bumps of varying thicknesses to find out the effect of thickness on the properties (uniformity, grain size, stress, mismatch of thermal expansion of coefficient, defects, etc.) of these In bumps and its relation with the IR detector performance.
- Study the properties of Au films having different thicknesses and find out an optimal film (that has desired uniformity, grain size, stress, defects, surface roughness, adhesion, etc.) that could be utilized in the fabrication of an IR detector.
- Creation of an ohmic Au/p-HgCdTe interface with relatively low specific contact resistance that might be useful for high-performance IR detectors.
- Development of dual-band (spectral regions: MWIR and LWIR) and multi-band (spectral regions: SWIR, MWIR, and LWIR) high-performance ARC film-stacks that could be used for the fabrication of corresponding IR detectors.

- Growth of aforesaid thin films by other deposition techniques like e-beam evaporation and atomic layer deposition for achieving the thin films with relatively good features, which may be suitable in the fabrication of HgCdTe-based IR detectors.

Thus, this chapter summarizes the major findings of the thesis. Exhaustive understanding of various thin film properties, the role of these thin films in HgCdTe-based IR detector technology, the interconnection of detector performance with varying properties of numerous thin films, and finally future scope of the work.